

UC San Diego

UC San Diego Electronic Theses and Dissertations

Title

Spectroscopic Investigations into Nascent and Aged Sea Spray Aerosol

Permalink

<https://escholarship.org/uc/item/0vg3t9cm>

Author

Trueblood, Jonathan

Publication Date

2018

Peer reviewed|Thesis/dissertation

UNIVERSITY OF CALIFORNIA SAN DIEGO

Spectroscopic Investigations into Nascent and Aged Sea Spray Aerosol

A dissertation submitted in partial satisfaction of the requirements for the degree of Doctor of
Philosophy

in

Chemistry

by

Jonathan V. Trueblood

Committee in charge:

Professor Vicki H. Grassian, Chair
Professor Ertugrul Cubukcu
Professor Robert “Skip” Pomeroy
Professor Kimberly A. Prather
Professor M. Dale Stokes
Professor Mike Tauber

2018

Copyright

Jonathan V. Trueblood, 2018

All rights reserved

The Dissertation of Jonathan V. Trueblood is approved, and is acceptable in quality and form for publication on microfilm and electronically:

Chair

University of California San Diego

2018

DEDICATION

To the dinosaurs.

They seemed to have a pretty good thing going for that brief 180 million years.

EPIGRAPH

How do you look at a plant that isn't built yet? I don't know. Lieutenant Zumwalt, who was always coming around with me because I had to have an escort everywhere, takes me into this room where there are these two engineers and a loooooong table covered with a stack of blueprints representing the various floors of the proposed plant.

I took mechanical drawing when I was in school, but I am not good at reading blueprints. So they unroll the stack of blueprints and start to explain it to me, thinking I am a genius. Now, one of the things they had to avoid in the plant was accumulation. They had problems like when there's an evaporator working, which is trying to accumulate the stuff, if the valve gets stuck or something like that and too much stuff accumulates, it'll explode. So they explained to me that this plant is designed so that if any one valve gets stuck nothing will happen. It needs at least two valves everywhere.

Then they explain how it works. The carbon tetrachloride comes in here, the uranium nitrate from here comes in here, it goes up and down, it goes up through the floor, comes up through the pipes, coming up from the second floor, bluuuurp going through the stack of blueprints, down up-down-up, talking very fast, explaining the very, very complicated chemical plant.

I'm completely dazed. Worse, I don't know what the symbols on the blueprint mean! There is some kind of a thing that at first I think is a window. It's a square with a little cross in the middle, all over the damn place. I think it's a window, but no, it can't be a window, because it isn't always at the edge. I want to ask them what it is.

You must have been in a situation like this when you didn't ask them right away. Right away it would have been OK. But now they've been talking a little bit too long. You hesitated too long. If you ask them now they'll say, "What are you wasting my time all this time for?"

What am I going to do? I get an idea. Maybe it's a valve. I take my finger and I put it down on one of the mysterious little crosses in the middle of one of the blueprints on page three, and I say, "What happens if this valve gets stuck?" -- figuring they're going to say, "That's not a valve, sir, that's a window."

So one looks at the other and says, "Well, if that valve gets stuck --" and he goes up and down on the blueprint, up and down, the other guy goes up and down, back and forth, back and forth, and they both look at each other. They turn around to me and they open their mouths like astonished fish and say, "You're absolutely right, sir."

So they rolled up the blueprints and away they went and we walked out. And Mr. Zumwalt, who had been following me all the way through, said, "You're a genius...I want to know how, how do you do that?"

I told him you try to find out whether it's a valve or not.

--Richard Feynman, *Surely You're Joking, Mr. Feynman!*

TABLE OF CONTENTS

SIGNATURE PAGE.....	iii
DEDICATION	iv
EPIGRAPH	v
TABLE OF CONTENTS	vi
LIST OF FIGURES	xi
LIST OF TABLES	xvi
ACKNOWLEDGMENTS.....	xvii
VITA	xxiii
ABSTRACT OF THE DISSERTATION.....	xxv
Chapter 1 An Introduction to Sea Spray Aerosol.....	1
1.1 Atmospheric Aerosols and the Earth's Climate	1
1.1.1 Climate Impacts of Aerosols	1
1.1.2 Sources of Aerosols	1
1.2 Marine Aerosols.....	4
1.2.1 Composition and Formation of MA	4
1.2.2 Biological Control of SSA Chemical Composition.....	6
1.3 The Chemistry of SSA	6
1.3.1 Heterogeneous Reactions of SSA with Trace Atmospheric Gases.....	7
1.3.2 Photochemical Reactions at Atmospherically Relevant Air-Water Interfaces	8
1.4 Generation and Analysis of Aerosols.....	11
1.4.1 Experimental Methods to Generate and Collect SSA.....	13
1.4.2 Analysis	14
1.5 Synopsis and Goal of this Thesis	19
1.6 Figures.....	21
1.7 References.....	29
Chapter 2 Investigating the Impact of Ocean Biology on the Chemical Composition and Climate-Relevant Properties of SSA Using Single Particle Raman Spectroscopy	35
2.1 Synopsis	35
2.2 Introduction.....	36
2.3 Methods.....	39
2.3.1 IMPACTS Experiment and Generation of an Indoor Phytoplankton Bloom	39
2.3.2 Collection of SSA for Off-Line Analysis	40
2.3.3 Generation of Aerosol Standards from Aqueous Solution	40

2.3.4	Chemicals and standards used in the spectroscopic analysis of individual SSA Particles.....	41
2.3.5	Raman Spectra Collection	41
2.3.6	Compound Identification in SSA.....	41
2.3.7	Analysis of Chemical Composition of IN Particles	42
2.4	Results.....	43
2.4.1	Identifying the Molecular Diversity of SSA.....	43
2.4.2	Connection Between Biological Activity and SSA Composition.....	47
2.4.3	Connection to Climate: IN Properties of SSA	51
2.5	Conclusions.....	52
2.6	Acknowledgements.....	53
2.7	Figures.....	55
2.8	References.....	67
Chapter 3 Heterogeneous Chemistry of Lipopolysaccharides with Gas-Phase Nitric Acid: Reactive Sites and Reaction Pathways		73
3.1	Synopsis	73
3.2	Introduction.....	73
3.2.	Experimental Methods	75
3.2.1	Sources and Purity of Compounds.	75
3.2.2	Model Systems Sample Preparation	75
3.2.3	Reaction of Sea Spray Aerosol and Model Systems with Nitric Acid Vapor.....	75
3.2.4	Micro-Raman Spectroscopy of Authentic Sea Spray Aerosols and Model System Particles.....	76
3.2.5	Verification of Model System LPS Reactivity Using ATOFMS and XPS.....	76
3.2.6	Determination of Relative Reactivities for LPS and NaCl with HNO ₃	77
3.3	Results and Discussion.....	77
3.3.1	Reaction of Authentic SSA Particles.....	77
3.3.2	Reaction of LPS Particles	78
3.3.3	Investigation of LPS Reactive Sites	79
3.3.4	Extension of Reaction Mechanism to other Aerosol Types.....	80
3.3.5	Acid/Base Properties of LPS	81
3.3.6	Relative Product Formation and Rates NaCl Compared to LPS	83
3.4	Conclusions.....	84
3.5	Acknowledgements.....	85
3.6	Figures.....	86
3.7	Supporting Information.....	93

3.7.1	Micro-Raman Spectroscopy of Authentic SSA and Model System Particles	93
3.7.2	Molecular Structure and Reactivity of LPS and its Constituents	93
3.7.3	Micro-Raman Spectroscopy of Nitrate Salts	93
3.7.4	Reactivity of Carboxylate and Phosphate Groups	93
3.7.5	Gas Phase Acid/Base Characteristics of Selected Proxy Molecules	94
3.7.6	Supporting Information Figures	95
3.7.7	Supporting Information Tables.....	101
3.8	References.....	102
Chapter 4 The Old and the New: Aging of Sea Spray Aerosols and Formation of Secondary Marine Aerosol Through OH Oxidation Reactions.....		
4.1	Synopsis	106
4.2	Introduction.....	107
4.3	Methods.....	109
4.3.1	Mesocosm Experiment	109
4.3.2	Oxidation of SSA and VOCs via OH Exposure	110
4.3.3	Off-line sampling of Nascent SSA and Marine Aerosols Exposed to OH Radicals (PAM-Derived MA)	111
4.3.4	Micro-Raman Spectroscopy of Supermicron Nascent SSA and PAM-Derived MA 111	
4.3.5	Atomic Force Microscopy-Photo-Thermal Infrared Spectroscopy of Submicron Nascent SSA and PAM-Derived MA	111
4.3.6	Online sampling of Submicron Nascent SSA and PAM-Derived MA.....	112
4.4	Results and Discussion.....	112
4.4.1	Biological Activity of Seawater.....	112
4.4.2	Formation of Secondary Marine Aerosols (SMA)	113
4.4.3	Fragmentation Reactions and Loss of Organic Matter in PAM-Derived MA.....	114
4.4.4	Proposed Reaction Mechanism.....	115
4.5	Conclusions.....	117
4.6	Acknowledgments.....	117
4.7	Figures.....	119
4.8	Supporting Information.....	128
4.8.1	Supporting Information Figures	128
4.9	References.....	129
Chapter 5 Shedding Light on Photosensitized Reactions within Marine-Relevant Organic Thin Films		
5.1	Synopsis	132
5.2	Introduction.....	132

5.3	Experimental Methods	135
5.3.1	Chemicals and Production of m-DOM	135
5.3.2	TOC Analysis	136
5.3.3	Analysis of Photosensitized Reactions with Nonanoic Acid.....	136
5.3.4	Analysis of Molecular Composition of Photosensitizers.....	137
5.4	Results.....	139
5.4.1	Analysis of Photosensitized Reactions of Three Different Photosensitizers with NA 139	
5.4.2	Comparison of m-DOM and Humic Acid Molecular Composition and Chromophores.....	144
5.5	Conclusions.....	146
5.6	Acknowledgements.....	148
5.7	Figures.....	149
5.8	Tables.....	153
5.9	Supporting Information.....	156
5.9.1	Supporting Information Figures	156
5.9.2	Supporting Information Tables.....	159
5.10	References.....	160
Chapter 6	Design and Validation of an LED Incoherent Broadband Cavity Enhanced Absorption Spectrometer (LED-IBCEAS) for the Detection of Nitrogen Oxides	163
6.1	Synopsis	163
6.2	Introduction.....	164
6.2.1	Sources of Atmospheric Nitrous Acid.....	164
6.2.2	Methods for HONO Detection.....	165
6.2.3	Long Path Absorption Based Spectroscopic methods	166
6.3	Theory of LED-IBCEAS	167
6.3.1	Absorption Spectroscopy and Beer's Law.....	167
6.3.2	Differential Optical Absorption Spectroscopy (DOAS).....	168
6.3.3	LED-IBCEAS	169
6.4	Design and Validation of LED-IBCEAS	170
6.4.1	Design and Hardware	170
6.4.2	Validation of Instrument.....	172
6.5	Conclusions and Future Work.....	174
6.6	Acknowledgements.....	175
6.7	Figures.....	176
6.8	Supporting Information.....	186

6.8.1	Supporting Information Figures	186
6.9	References.....	187
Chapter 7	Conclusions and Future Work	190
7.1	Synopsis	190
7.2	Chapter 2 Summary	190
7.3	Chapter 3 Summary	191
7.4	Chapter 4 Summary	192
7.5	Chapter 5 Summary	193
7.6	Chapter 6 Summary	194
7.7	Future Studies	194
7.8	References.....	197

LIST OF FIGURES

Figure 1.1: Direct and indirect effects of aerosol particles in the atmosphere	21
Figure 1.2: Radiative forcing (RF) and effective radiative forcing (ERF) of climate change between 1750 and 2011. RF and ERF quantify the change in the Earth's radiative balance due to anthropogenic influences.....	22
Figure 1.3: Size-resolved organic mass fraction of sea spray aerosol measured in clean marine conditions as a function of aerosol diameter	23
Figure 1.4: Raman spectra of individual SSA particles analyzed with micro-Raman spectroscopy for several different particle types, along with optical images, individual spectra, and spectra maps in the insets.....	24
Figure 1.5: Image of the 30-meter-long wavechannel used during the 2014 IMPACTS experiment in the Hydraulics Laboratory at Scripps Institution of Oceanography	25
Figure 1.6: Marine Aerosol Reference Tank (MART).....	26
Figure 1.7: Schematic of the atomizer assembly block. Adapted from TSI, Inc.....	27
Figure 1.8: Block diagram of the Raman spectrometer used in the studies described herein. The system is equipped with a 532 nm laser and 10x, 50x, and 100X objective lenses. An environmental cell (Linkam) allows for temperature and RH control of samples	28
Figure 2.1: Experimental setup during the IMPACTS research intensive	55
Figure 2.2: Six types of Raman signatures observed for 560-1000 nm and 1.8-3.2 μm sized SSA particles collected on a quartz substrate during the month-long IMPACTS mesocosm experiment.. ..	56
Figure 2.3: A) Raman spectra obtained for standards of short-chain fatty acids. B) χ^2 plots showing the statistical relationship between each standard spectra of short-chain saturated fatty acids to that of a representative SSA particle collected during the mesocosm.....	57
Figure 2.4: A) Raman spectra obtained for standards of long-chain saturated and unsaturated fatty acids. B) χ^2 plots showing the statistical relationship between each standard spectra of long-chain saturated fatty acids and alcohols and phospholipids to that of the single SSA particle collected during the mesocosm.....	58
Figure 2.5: A) Raman spectra obtained for standards of free saccharides and amino sugars. B) χ^2 plots showing the statistical relationship between each standard spectra of free saccharides to that of the single SSA particle collected during the mesocosm	59
Figure 2.6: A) Comparison of Raman spectra obtained from the analysis of biofilm collected from the mesocosm and that for a single particle from SSA collected during the mesocosm with Raman spectra resembling that of siliceous material (Figure 2.2e). B) χ^2 plot showing the statistical relationship between the standard spectra of the biofilm and that of the single SSA particle.....	60

Figure 2.7: A) Comparison of Raman spectra obtained from the analysis of a standard of lipopolysaccharide and a single particle from SSA collected during the mesocosm with Raman spectra resembling that of polysaccharides. B) χ^2 plot showing the statistical relationship between the standard spectra of LPS and sodium alginate to that of the single SSA particle 61

Figure 2.8: Changes in the composition of individual (a) submicron (0.56–1.00 μm) and (b) supermicron (1.8–3.2 μm) particles within SSA collected on different days throughout the mesocosm. 62

Figure 2.9: Degradation pathways of diatoms and bacteria leading to organic species that are transported from seawater to SSA particles as either film or jet drops. Boxes with a dashed outline were not directly observed in this work, but are shown here as a precursor to classes of compounds that were observed. 63

Figure 2.10: Timeline of A) ice nucleating particle (INP) number concentrations and B) chlorophyll a concentrations. The yellow highlighted region indicates the day when ICR were collected for Raman analysis 64

Figure 2.11: Timeline of A) ice nucleating particle (INP) number concentrations and B) chlorophyll a concentrations. The yellow highlighted regions indicates the days when ICR were collected for Raman analysis 65

Figure 2.12: Relative contributions of particle types for ice crystal residuals (ICR) on specific days of A) IMPACTS experiment B) MART experiment. C) Shows the corresponding spectra for each particle type. 66

Figure 3.1: Optical image of SSA particles collected on a substrate following exposure to HNO_3 . Besides particles identified as reacted salt particles, another class was identified as a nitric acid reacted lipopolysaccharide (LPS) particle from micro-Raman spectroscopy 86

Figure 3.2: Experimental data for liposaccharide exposed to gas phase nitric acid in three different experiments. A) micro-Raman spectroscopy of substrate deposited LPS aerosol particles from aqueous solution, B) XPS data of the N1s binding energy region for LPS powder, and C) ATOFMS average spectra of atomized aqueous solutions of LPS 87

Figure 3.3: Basic components of LPS that could react with gas phase nitric acid. The phosphate and carboxylate sites are highlighted red and blue, respectively, and are found in the Lipid A and inner core oligosaccharide regions 88

Figure 3.4: Raman spectra of different isolated portions of LPS before (blue) and after (red) exposure to HNO_3 89

Figure 3.5: Raman spectra of individual particles composed of A) DPPA, B) sodium palmitate, C) sodium nonanoate, and D) sodium butyrate before (left) and after (right) exposure to HNO_3 90

Figure 3.6: A) NaCl and B) LPS particle Raman spectra of the ν_1 nitrate stretching region as a function of HNO_3 exposure time. The nitrate peak increased with time for both particle types... 91

Figure 3.7: Nitric acid can react with different components of SSA as summarized above. (1) is the well-known chloride displacement reaction. Other reactive sites within the bioaerosols, in particular that of LPS, include carboxylate (2) and phosphate (3) groups. 92

Figure 3.8: Optical image of SSA particles collected on a substrate following exposure to HNO₃. Raman spectra are shown for three of these particles. 95

Figure 3.9: Raman spectra of the three HNO₃ reacted model systems (blue) compared to reacted real sea spray aerosol (red). The model systems are aerosolized samples of A) NaCl, B) LPS, and C) palmitic acid. 96

Figure 3.10: Chemical structure of model systems used A) lipopolysaccharide, B) Kdo₂-Lipid A, C) Lipid A, and D) DPPA. 97

Figure 3.11: Raman spectra of atomized A) sodium nitrate, B) potassium nitrate, C) magnesium nitrate, and D) calcium nitrate from aqueous solutions..... 98

Figure 3.12: Raman spectra of a sodium nitrate particle at 20% and 76% relative humidity. The frequency of the $\nu_1(\text{NO}_3^-)$ vibrational mode changes from 1068 at 20% RH to 1052 cm⁻¹ at 76% RH. 99

Figure 3.13: Full Raman spectra collected following reaction of HNO₃ with DPPA and three carboxylate model systems..... 100

Figure 4.1: Dissolved organic carbon (DOC), heterotrophic bacteria counts, and chlorophyll-a (Chl) throughout the bloom. 119

Figure 4.2: AMS-derived mass size distributions and corresponding curve fits for nascent and PAM-derived marine aerosol. Results show that PAM-derived marine aerosol have a greater contribution of particles in the size range from ~50 to 500 nm, indicating the formation of SMA. 120

Figure 4.3: Curve fits of the AMS-derived mass size distributions of organic signals for PAM-derived marine aerosol on different days of the experiment. 121

Figure 4.4: Particle counts (top) and amplitude images (bottom) as carried out by AFM for PAM-derived marine aerosol on 9/01 and 9/05..... 122

Figure 4.5: A) AFM amplitude image of a particle with a volume equivalent diameter of 250 nm. B) FTIR spectra taken at the particle core (black) and on the shell (blue). C) 3D height image of a particle with a volume equivalent diameter of 70 nm. D) Chemical map of the particle in panel C taken at 2930 cm⁻¹. 123

Figure 4.6: Relative fractions of particles that were identified as organic, burnt/fluorescing, or sea salt across all days for particles ranging from 1.8-3.2 μm , classified using Raman spectroscopy. Particles were classified according to a method previously described in literature 124

Figure 4.7: Violin plot of the integrated area from 2700 to 3100 cm⁻¹ for of all particles classified as the most common particle type in nascent SSA and PAM-derived MA. The width of each plot represents the number of particles with a given integrated area intensity..... 125

Figure 4.8: Proposed reaction mechanism for loss of organic mass from marine aerosols containing simple amino sugars and amino acids such as alanine upon exposure to OH radicals. Gaseous products are highlighted in red while condensed phase products are in blue..... 126

Figure 4.9: Difference spectrum (PAM versus non-PAM marine aerosol) of the average of the normalized spectra of the most abundant particle type for supermicron SSA across all days analyzed 127

Figure 4.10: Comparison of spectra of the most common particle type in supermicron particles across all days (red) with alanine (blue) and sialic acid (green). 128

Figure 5.1: Select regions of ATR-FTIR difference spectra (final-initial) of 60-minute non-irradiated (gray lines) and irradiated (colored lines) NA in the presence of A) BBA; B) HA and C) m-DOM. Spectra were collected every 10 minutes. Lines become increasingly light with increased time..... 149

Figure 5.2: Excitation-emission matrices of A) humic acid and B) m-DOM. 150

Figure 5.3: ATR-FTIR spectra of A) humic acid and B) m-DOM extracted from a lab-grown phytoplankton culture. Peak assignments are listed in Table 4.1..... 151

Figure 5.4: Relative abundance of each molecular class in humic acid and m-DOM as determined by HESI-LIT-Orbitrap MS analysis calculated according to section 4.3.4..... 152

Figure 5.5: ATR-FTIR spectra of thin films of each of the photosensitizer model systems studies in this experiment. An in-depth analysis of the humic acid and m-DOM spectra is given in Section 4.4.2..... 156

Figure 5.6: ATR-FTIR spectra of nonanoic acid and each of the systems containing a thin film of photosensitizer with nonanoic acid. Peak assignments for nonanoic acid are shown in Table 4.3. 157

Figure 5.7: Signal detected (counts) for select products upon analysis by HESI-LIT-Orbitrap MS analysis in positive (left) and negative (right) mode of irradiated (light colored), non-irradiated (dark colors), and water blanks (grey) of A) NA in the presence of BBA, B) NA in the presence of humic acid, and C) NA in the presence of m-DOM..... 158

Figure 6.1: Block diagram of the LED incoherent broadband cavity enhanced absorption spectrometer constructed for detection of gas-phase HONO. 176

Figure 6.2: Schematic of the circuit board, power supplies, and MyRIO control. The computer interacts with the MyRIO through Labview to control the power supply of the LED and Peltier cooler and to give temperature readout of the thermocouples..... 177

Figure 6.3: Image of the custom-built mount consisting of an aluminum base tooling plate that can be swiveled in x and y directions. The mount has a cavity filled with lens tube and a lens for collimation of LED light not the optical cavity..... 178

Figure 6.4: Flow chart for determination of differential absorption coefficients and absorber concentrations using the LED-IBCEAS-DOAS method..... 179

Figure 6.5: Calculated Rayleigh extinction coefficient for A) helium and B) nitrogen. 180

Figure 6.6: LED transmitted intensity through the cavity filled with helium and with nitrogen. 181

Figure 6.7: Calculated mirror reflectivity as a function of wavelength..... 182

Figure 6.8: A) Literature NO₂ absorption cross section before and B) after convolution to the resolution of our spectrometer..... 183

Figure 6.9: LED transmitted intensity through the optical cavity filled with nitrogen or NO₂. . 184

Figure 6.10: (Top) Resulting fit of the measured absorption coefficient for NO₂ compared with the results from the literature of a mixture of NO₂ with HONO (bottom). 185

Figure 6.11: High resolution absorption cross section of NO₂ from literature..... 186

LIST OF TABLES

Table 3.1: Thermodynamic Properties and Molecular Structures of Chosen LPS Proxy Biomolecules.	101
Table 5.1: Signal strength and enrichment ratios for select products as detected by MS analysis for samples of various photosensitizers in the presence of NA.	153
Table 5.2: Peak assignments of ATR-FTIR spectra of humic acid and m-DOM.....	154
Table 5.3: Molecular characteristics of humic acid and m-DOM as determined by HESI-LIT-Orbitrap MS analysis.....	155
Table 5.4: Peak assignments of nonanoic acid.....	159

ACKNOWLEDGMENTS

As I reach the conclusion of this fun, crazy, unexpected, at times insanely frustratingly difficult, and yet ultimately rewarding journey that is graduate school, I am struck by just how much help and support I received along the way. Stretching all the way back to the beginning of my M.S. studies, I've spent 7 years and have literally traveled across the entire country, from North Carolina, to Iowa, to California to complete this degree. Each place has been unique in its own way, but the one constant throughout it all was the presence of friends, colleagues, and mentors that made this achievement possible.

Technically, this journey began much earlier; way back in high school and perhaps even grade school. I was (and arguably still am) a pretty weird kid. To the teachers that were patient with me and my weird antics, who chose to see the positives in me rather than focusing on the flaws, and who believed in me and encouraged me, I say "thank you." The world needs more of you.

I also owe much to all of my professors throughout the past decade, including those from Dordt, North Carolina State University, University of Iowa, and UCSD. The knowledge they shared with me is the foundation upon which my research and this dissertation is built. I would like to especially thank my committee members at the University of Iowa and here at UCSD: Dr. Scott Shaw, Dr. Alexei Tivanski, Dr. Betsy Stone, Dr. Mark Young at Iowa, and Dr. Mike Tauber, Dr. Ertugral Cubukcu, Dr. Dale Stokes, Dr. Kim Prather, and Dr. Skip Pomeroy here at UCSD. Thank you for your answers to my seemingly endless list of questions and for your support throughout these years.

Moving to California in the middle of my degree was a bit more challenging than I expected. I owe a huge thank you to all of the staff that helped me get settled in at UCSD. Specifically, Edgar Diaz, Carmen Alfaro, and Monica Castrejon for being so helpful all the time. I realize that's a vague 'thank you', but they answered so many questions and helped me in so many different situations that I simply can't list them all. Thank you to John Lasky at the stock room for

not getting too angry at me when I would inevitably forget to return the keys to various rooms. Thank you to Amy Tran, Erica Lennard, Jeanine Sun Kolinko, and Jeff Rances for answering my endless list of last-minute, obscure financial and student enrollment questions that I always had. Jeff also once bailed me out when I had 50 undergraduate students who wanted to review before a final exam and no room to teach them in. To all of the staff at Iowa and UCSD: there are so many things you all do on a daily basis that make the universities run smoothly. Thank you.

The construction of the LED-IBCEAS has been an extremely challenging and fun task. I've learned so much beyond the realm of chemistry throughout the process. However, I would have never come close to putting the instrument together had it not been for Joe Mayer, Joey Manson, Frank Cardon, and Dr. Mark Young. Their support in helping me design and construct the instrument was invaluable. I basically came to Frank and Joe with with a drawing of a square on a piece of blank paper and said "I want to make a cavity enhanced spectrometer to detect nitrogen oxides" and somehow we ended up with this amazing instrument. This is no doubt due to their knowledge and expertise. I should also thank Samantha Doyle for taking the time out of writing her own thesis to help me with the instrument's optical alignment. I'd probably still be sitting in the lab trying to align the LED had it not been for her.

None of the research I've conducted these past years would have been possible had it not been for my advisor, Dr. Vicki Grassian. Dr. Grassian for took a chance and gave me an opportunity even though I didn't have an official background in chemistry. It has been a joy working for her, as she has been patient with me during the times I have struggled to fill in the gaps of my chemistry knowledge. She was also never more than one email away, no matter how busy she was. This kind of support from an advisor is hard to come by and I am extremely lucky to have had such a patient, knowledgeable, and effective advisor.

I am also incredibly grateful to have been surrounded by such a knowledgeable and helpful cohort. Thank you to all my fellow graduate students, particularly those in CAICE, and those who

took part in the 2016 IMPACTS experiment. IMPACTS was a crazy month and it never would never have been so successful had it not been for all of the amazing students. I'd like to specifically thank Dr. Camille Sultana and Dr. Chris Lee for their amazing work in preparing the intensive. Of course there are countless collaborators that I must thank as well, including Dr. Xiaofei Wang, Mitch Santander, Dr. Christina McCluskey, and my undergraduate mentees Dylan Power, Jackie Dowling, and Neyen Romano.

In graduate school your second family are your fellow group members. I have been blessed to have an amazing second family in the Grassian Group. First and foremost, thank you to Dr. Olga Laskina for being the best mentor anyone could ask for during my first two years at Iowa. I could always count on her to answer every question I had with patience, kindness, and clarity. Olga really taught me how to troubleshoot instruments, which is perhaps one of the most important skills one can have in graduate school. A huge thank you to the other senior members of the Grassian Group that showed me the ropes when I first arrived: specifically, Dr. Charith Nanayakkara and Dr Aruni Gankanda. I had a lot of trouble with the heterogenous chemistry mixing chamber but they helped me to finally figure it out.

I'm also incredibly grateful to the post docs in the Grassian group that were a source of knowledge and friendship. It was a pleasure working and publishing with Dr. Armando Estillo. He was always positive and encouraging to everyone in the lab. Dr. Rich Cochran was also a pleasure to work with and was a seemingly endless source of knowledge regarding MS techniques. I always enjoyed talking hockey with him, so long as we weren't talking about the Blackhawks winning. Thanks to Dr. Natalia Gonzalez-Pech for suggesting I try out Clubes de Mexico, and for her many tips on daily life for when I travel to Latin America. Finally, I'd like to thank Dr. Mona Shrestha for her friendship and for being in charge of the UCSD Marketplace and putting in the bazillion orders I requested.

The Grassian Group at UCSD has been a blast. Mike Alves has been a great colleague and friend. His knowledge of MS is impressive and I have no doubt he will do big things in the near future. I should also thank him for all the times he shared his candy with me. Our Friday night game nights with Victor Or were always fun. A shout out to Liora for buying the package so we could play NYT crosswords every day. They gave me 30 minutes (sometimes longer...) of respite during many hectic days. Ellen Coddens has been a great friend since Iowa. I'm especially thankful to her for agreeing to look after Peaches while I'm in South America. Thank you to everyone else in the Grassian Group, past and present for being such wonderful friends and a joy to work with. Also, thank you for not murdering me during the final month of my thesis writing when I inexplicably developed a nervous tic of clearing my throat every 30 seconds.

I am forever grateful for the endless support of my friends and family. Thank you to my mom and dad for instilling the value of an education in me at a young age, for teaching me to always ask questions, to never give up, and to always do what's right. Thank you to all of the friends I have made along the way in North Carolina, Iowa, and California. I still miss my old friends back in Raleigh: Matthew Johnson, Brett Gantt, Kyle Dawson, Addison English, Summer Finck, and everyone else—you know who you are!

Thank you to my friends back in Iowa. To the Longfellow Ultimate crew: one of the hardest parts about leaving Iowa was not being able to play frisbee with you guys anymore. It was always a much needed outlet after a long day in the lab. Lying in the grass on a cool summer night after several games and chatting with you guys a memory I will always hold dearly. Summers in Iowa really are unlike anything else.

Thank you to my roommates/friends: Jake Grant, Chad Gilmer, Justin Carter, Alex Nilors, Eric Sletten, and Mike Tylka. I will always cherish the memories of our crazy winter nights out on the town in frozen Iowa City. I still miss karaoke, free bass at Blue Moose, pizza at Mesa, Saturday morning Premier League, and some of the other stories I probably can't mention here. I miss you

guys like crazy. Hopefully one day in the future we can meet up at Bojames one last time for some of that world class beer.

Finally, thank you to my best friends Josh Ryks and Kenny Gradert. There were many times where I didn't think I was going to make it through to the finish line for various reasons. But each time I felt like giving up, you guys were there to either listen, offer advice, or just encourage me to keep going. They say there's only a handful of people in your life that you can count on to always be there for you no matter what. You guys definitely fit into that rare group.

So many people have helped me throughout this journey, that were I to individually thank every one of them, I think the length of this dissertation would double. I apologize to anyone I have left off this list. Please know I am incredibly grateful for your support. Finally, to all of my friends and family, I want to say thank you for being patient with me through these past few years. Graduate school is hard. There are times where the stress from the work makes it easy to develop a kind of tunnel vision. There have been many times I've found myself too focused on my own issues to the point that I've forgotten about the needs and wants of my friends and family. For this I apologize, and again say thank you for offering such invaluable support. I could not have done this without you.

A portion of Chapter 2 is reproduced with permission from the American Chemical Society: Wang, X., Sultana, C. M., Trueblood, J. V., Hill, T. C. J., Malfatti, F., Lee, C., Laskina, O., Moore, K. A., Beall, C. M., McCluskey, C. S., Cornwell, G. C., Zhou, Y., Cox, J. L., Pendergraft, M. A., Santander, M. V., Bertram, T. H., Cappa, C. D., Azam, F., DeMott, P. J., Grassian, V. H., Prather, K. A. Microbial Control of Sea Spray Aerosol Composition: A Tale of Two Blooms, *ACS Central Science*, 1 (3), 124-131, 2015. The dissertation author was an investigator and co-author of this paper.

A portion of Chapter 2 is reproduced with permission from: Cochran, R. E., Laskina, O., Trueblood, J. V., Estillore, A. D., Morris, H. S., Jayarathne, T., Sultana, C. M., Lee, C., Lin, P., Laskin, J., Laskin, A., Dowling, J. A., Qin, Z., Cappa, C. D. Bertram, T. H., Tivanski, A. V., Stone, E. A., Prather, K. A., Grassian, V. H. Molecular Diversity of Sea Spray Aerosol Particles: Impact of Ocean Biology on Particle Composition and Hygroscopicity, *Chem*, 2 (5), 655-667, 2017. The dissertation author was an investigator and co-author of this paper.

A portion of Chapter 2 is reproduced with permission from: McCluskey, C. S., Hill, T. C. J., Sultana, C. M., Laskina, O., Trueblood, J. V., Santander, M. V., Beall, C. M., Michaud, J. M., Kreidenweis, S. M., Prather, K. A., Grassian, V. H., DeMott, P. J. A Mesocosm Double Feature: Insights into the Chemical Make-up of Marine Ice Nucleating Particles, *Journal of the Atmospheric Sciences*, 75 (7), 2405-2423, 2018. The dissertation author was an investigator and co-author of this paper.

Chapter 3 is reproduced with permission from: Trueblood, J. V., Estillore, A. D., Lee, C., Dowling, J. A., Prather, K. A., Grassian, V. H. Heterogeneous Chemistry of Lipopolysaccharides with Gas-Phase Nitric Acid: Reactive Sites and reaction Pathways, *JPC A*, 120 (32), 6444-6450, 2016. The dissertation author was the primary investigator and author of this paper.

Chapter 4 is in preparation: Trueblood, J. V., Wang, X., Or, V. W., Alves, M. R., Santander, M., Prather, K. A., Grassian, V. H. The Old and the New: Aging of Sea Spray Aerosols and Formation of Secondary Marine Aerosol Through OH Oxidation Reactions. The dissertation author was the primary investigator and author of this paper.

Chapter 5 is in preparation: Trueblood, J. V., Alves, M., Power, D., Santander, M., Cochran, R., Prather, K. A., Grassian, V. H. Shedding Light on Photosensitized Reactions within Marine-Relevant Organic Thin Films. The dissertation author was the primary investigator and author of this paper.

The dissertation author was the primary investigator and author of the work in Chapter 6.

VITA

2011	Bachelor of Arts, Physics, Dordt College
2011-2013	Teaching Assistant, Department of Atmospheric Science, North Carolina State University
2011-2013	Research Assistant, North Carolina State University
2013	Master of Science, Atmospheric Science, North Carolina State University
2013-2015	Teaching Assistant, Department of Chemistry, University of Iowa
2013-2015	Research Assistant, University of Iowa
2016-2018	Research Assistant, University of California San Diego
2018	Teaching Assistant, Department of Chemistry, University of California, San Diego
2018	Doctor of Philosophy, Chemistry, University of California, San Diego

PUBLICATIONS

- Trueblood, J. V.**, Alves, M., Power, D., Sauer, J., Cochran, R., Prather, K. A., Grassian, V. H. (2018). Shedding light on marine relevant photosensitizing reactions. *Manuscript Prep.*
- Trueblood, J. V.**, Wang, X., Santander, M., Alves, M., Prather, K. A., Grassian, V. H. (2018). Interplay between ocean biological activity and aging via oxidation with hydroxyl radical on the chemical composition of sea spray aerosols. *Manuscript Prep.*
- Deane, G. B., Cochran, R. E., Jayarathne, T., Stokes, M. D., Forestieri, S. D., Wang, X., Sultana, C. M., Lee, C., Laskina, O., **Trueblood, J. V.**, Morris, H. S., Ray, K. K., Lee, H. D., Burrows, S. DeMott, P. J., Tivanski, A. V., Bertram, T. H., Prather, K. A., Grassian, V. H., Cappa, C. D., Stone, E. A. (2018). A mechanistic model for the size-dependent transfer of organic matter to sea spray aerosol. *Science, in review.*
- McCluskey, C. S., Hill, T. C. J., Laskina, O., **Trueblood, J. V.**, Santander, M. V., Beall, C. M., Sultana, C. M., Michaud, J. M., Prather, K. A., Grassian, V. H., DeMott, P. J. (2018). A mesocosm double feature: revealing the identity of marine ice nucleating particles. *Journal of the Atmospheric Sciences, in review.*
- Cochran, R. E., Laskina, O., **Trueblood, J. V.**, Estillore, A. D., Morris, H. S., Jayarathne, T., Sultana, C. M., Lee, C., Lin, P., Laskin, J., Dowling, J. A., Qin, Z., Cappa, C. D., Bertram, T. H., Tivanski, A. V., Stone, E. A., Prather, K. A., Grassian, V. H. (2017). Molecular diversity of sea spray aerosol particles: impacts of ocean biology on particle composition and hygroscopicity. *Chem*, 2(5), 655-667.

- Trueblood, J. V.**, Estillore, A. D., Lee, C., Dowling, J., Prather, K. A., Grassian, V. H. (2016). Heterogeneous chemistry of lipopolysaccharides with gas-phase nitric acid: reactive sites and reaction pathways. *Journal of Physical Chemistry A*, *120*, 6444-6450.
- Estillore, A. D., **Trueblood, J. V.**, Grassian, V. H. (2016). Atmospheric chemistry of bioaerosols: heterogeneous and multiphase reactions with atmospheric oxidants and other trace gases. *Chemical Science*, *7*, 6604-6616.
- Chen, T. H, Wang, L., **Trueblood, J. V.**, Grassian, V. H., Cohen, S. M. (2016). Poly(isophthalic acid)(ethylene oxide) as a macromolecular modulator for metal-organic polyhedral. *Journal of American Chemical Society*, *138*, 9646-9654.
- Wang, X., Sultana, C. M., **Trueblood, J. V.**, Hill, T. C. J., Malfatti, F., Lee, C., Laskina, O., Moore, K. A., Beall, C. M., McCluskey, C. S., Cornwell, G. C., Zhou, Y., Cox, J. L., Pendergraft, M. A., Santandar, M. V., Bertram, T. H., Cappa, C. D., Azam, F., DeMott, P. J., Grassian, V. H., Prather, K. A. (2015). Impact of bacterial enzymatic activity on organic enrichment in sea spray aerosol: a tale of two blooms. *ACS Central Science*, *1*, 124-131.
- Ault, A. P., Guasco, T. L., Baltrusaitis, J., Ryder, O. S., **Trueblood, J. V.**, Collins, D. B., Ruppel, M. J., Cuadra-Rodriguez, L. A., Prather, K. A., Grassian, V. H. (2014). Heterogeneous reactivity of nitric acid with nascent sea spray aerosol: large differences observed between and within individual particles. *Journal of Physical Chemistry Letters*, *5*, 2493-2500.
- Allen, D. R., Douglass, A. R., Manney, G. L., Strahan, S. E., Krosschell, J. C., **Trueblood, J. V.**, Nielsen, J. E., Pawson, S., and Zhu, Z. (2011). Modeling the frozen-in anticyclone in the 2005 arctic summer stratosphere. *Atmospheric Chemistry and Physics*, *11*, 4557-4576.

FIELDS OF STUDY

Major Field of Study: Chemistry

Studies in Atmospheric and Physical Chemistry

Professor Vicki H. Grassian

ABSTRACT OF THE DISSERTATION

Spectroscopic Investigations into Nascent and Aged Sea Spray Aerosol

by

Jonathan V. Trueblood

Doctor of Philosophy in Chemistry

University of California San Diego, 2018

Professor Vicki H. Grassian, Chair

Atmospheric aerosols directly impact the Earth's climate by scattering and absorbing solar radiation and indirectly by altering the microphysical properties of clouds. Aerosols formed over the oceans, termed marine aerosols, consist of secondary marine aerosols (SMA) formed upon the oxidation of gas phase species and of primary sea spray aerosols (SSA) that are directly emitted from the surface of the ocean. The climate relevant properties of primary SSA are determined by their size and chemical composition, both of which are functions of the ocean's biological activity as well as atmospheric heterogeneous reactions with trace gas species and photochemical aging reactions. This dissertation investigates the impacts of each of these processes on the chemical complexity of SSA by conducting fundamental laboratory studies involving spectroscopic probing of various SSA systems ranging from simple, single component model systems to authentic SSA produced using an indoor ocean-atmosphere facility that replicates the chemical and biological complexity of the ocean and SSA. First, we identified the various chemical species found in SSA and linked their size and temporal changes to the biological activity of the ocean. Next, we used our improved understanding of the molecular speciation of SSA to look in-depth at the atmospheric reactions that alter the chemical and physical properties of SSA, including the heterogeneous reaction with gas phase nitric acid and OH radicals, as well as photosensitized reactions with chromophoric species. We found that the chemical complexity of SSA due to the organic and biological components alters their reactivity and introduces alternative pathways beyond those previously acknowledged. Finally, to aid in future experiments of photochemical aging reactions of SSA, we constructed and validated an LED incoherent broadband cavity enhanced absorption spectrometer (LED-IBCEAS) to detect various nitrogen oxides (e.g., NO₂ and HONO). The findings presented in this dissertation improve our understanding of the various chemical and biological controls on the climate relevant properties of SSA, and can ultimately be used to improve the performance of regional and global climate models.

Chapter 1 An Introduction to Sea Spray Aerosol

1.1 Atmospheric Aerosols and the Earth's Climate

Gases and aerosols are the two main components of the Earth's atmosphere. Aerosols are defined as any solid or liquid particle suspended in a gas, and range in size from a few nanometers to tens of microns.¹ This broad definition underscores the chemical and physical heterogeneity of atmospheric aerosols, which is a result of their wide ranging sources, formation mechanisms, and atmospheric aging processes. The importance of aerosols was noted at least as far back as 1500 by Leonardo da Vinci, when he stated "...as I say, the atmosphere assumes this azure hue by reason for the particles of moisture which catch the rays of the sun."² In the more than 500 years since then, the understanding of the role aerosols play in the Earth system has increased greatly. Presently, aerosols are known to have substantial impacts on air quality, visibility, human health, biogeochemical cycles, atmospheric chemistry, and global climate.^{1,3}

1.1.1 Climate Impacts of Aerosols

The total aerosol impact on global climate is highly complex and multifaceted, with effects broadly classified as either direct or indirect (Figure 1.1). Aerosols directly alter the Earth's climate by scattering and absorbing solar radiation, which have cooling and warming effects on the atmosphere, respectively. The ability of an aerosol to scatter light is largely determined by its size and refractive index,¹ with increasing aerosol diameters linked to more efficient scattering. However, a complicating factor in determining an aerosol's light-scattering ability is that its size is not static throughout its lifetime and can change due to any number of physical and chemical processes, including coagulation, heterogeneous and photochemical reactions, and the uptake of water at the particle's surface.

In terms of absorbing properties, aerosol chemical composition is the guiding principle.⁴ As with scattering, the absorbing properties of aerosols are difficult to model due to the sheer number of chemical structures of which they are composed as well as the countless factors that alter them. For example, the carbonaceous components of aerosols are known to exist as any number of a wide range of molecular compositions, each with unique light-absorbing properties; from colorless organics such as carboxylic acids, to brown carbon composed of humic-like substances (HULIS), to highly absorbing black carbon consisting primarily of soot.⁵

Aerosols indirectly affect climate due to their ability to serve as cloud condensation nuclei (CCN) and ice nuclei (IN), both of which are critical to the formation of clouds and the occurrence of precipitation.¹ The cloud formation process begins when air rises and subsequently cools due to adiabatic expansion. With cooling, the saturation vapor pressure decreases, causing the air to become supersaturated with respect to water vapor. However, due to the existence of an intermediate maximum in the Gibbs free energy, supersaturation ratios of over 400% are required before water vapor will undergo a homogeneous phase change and condense into a liquid droplet. As CCN, aerosols provide a surface upon which water vapor can condense at much lower supersaturation ratios, allowing for the eventual formation of cloud droplets in conditions found in the Earth's atmosphere. Similarly, at low temperatures, aerosols can also serve as IN, by providing a surface or nucleus upon which ice crystals can form.

The number and type of aerosols available to serve as CCN or IN alters the microphysical and radiative properties of clouds. For example, in environments with high numbers of CCN, water is distributed among more cloud droplets, resulting in a greater number of smaller sized droplets. This has a dual effect on the resulting cloud, giving it a higher reflectivity, or albedo,⁶ as well as a longer lifetime due to the resulting delayed onset of precipitation.⁷ Together, these indirect effects lead to a cloud that more efficiently scatters radiation for a longer period of time.⁸

The ability of an aerosol particle to serve as CCN or IN is determined by its size and chemical composition.⁹ However, due to gaps in the knowledge of their physical and chemical characteristics, the CCN/IN activity of aerosols is ill-defined and therefore poorly represented in climate models. Currently, the single largest uncertainty in global radiative forcing is due to the aerosol indirect effect (Figure 1.2). It is therefore obvious that to improve regional and global climate models, an improved understanding of aerosol chemical composition, relevant aging processes, and their links to climate relevant properties such as CCN/IN activity is needed.¹⁰⁻¹³ Such improvements are the goal of the research presented in this thesis.

1.1.2 Sources of Aerosols

As previously mentioned, aerosols originate from a wide variety of sources and formation mechanisms, each with unique lifetimes, sizes, and chemical and physical properties. Depending on their specific formation mechanism, aerosols can be broadly classified as either primary or secondary in nature. Primary aerosols are directly emitted from natural sources such as windborne dust, sea spray, volcanos, and forests,¹ as well as anthropogenic sources including combustion of fuels, metal working, and biomass burning.³ Secondary aerosols are formed through the chemical reactions between gas-phase species and the subsequent nucleation or condensation of the resulting low volatility product species.^{1,14} Examples of secondary aerosol precursor gases that undergo oxidation include biogenic volatile organic compounds (VOCs) released by trees in terrestrial regions, dimethyl sulfide (DMS) released by marine phytoplankton, and sulphur dioxide (SO₂) from volcanos.¹⁴ The formation of secondary organic aerosols (SOA) from organic precursor gases is a particularly active area of research, as it is estimated that 10⁴-10⁵ different organic compounds can contribute to SOA formation and growth.¹⁵

1.2 Marine Aerosols

The portion of atmospheric aerosols that come from the Earth's oceans are termed marine aerosols (MA). A brief glance at a map of the Earth offers a clue as to why MA are so important: as oceans cover two-thirds of the surface of the planet, MA make up one of the largest fluxes of aerosol particles in the atmosphere.^{10,16} Further adding to their importance is the fact that the remote marine regions in which MA are formed are quite clean, with ambient aerosol concentrations as low as <100 per cubic cm.¹⁶ As a result, the microphysical properties of clouds in these regions are exceptionally sensitive to the characteristics of available CCN and any changes they may undergo. Finally, in order to model anthropogenic aerosol impacts on climate, an improved baseline of natural aerosols such as MA is needed.¹⁷ Together, these factors point to the need for improved understanding of the number, size, and chemical composition of MA, which will allow for a better understanding of climate over a significant portion of the Earth.

1.2.1 Composition and Formation of MA

Great strides have been made in determining the chemical composition of MA since the 1960s when it was first discovered that organic matter was incorporated into submicron MA.¹⁸ While it is presently understood that in addition to inorganic salt, there is an important organic component of MA,¹⁹⁻²² the mixing state, chemical fractionation, and impact of production mechanism on organic enrichment all remain poorly characterized.²³ Before further discussing the specific gaps in MA knowledge, a brief introduction to their production mechanism is first given below.

As alluded to in the previous section, marine aerosols can be classified as either primary sea spray aerosol (SSA) or secondary marine aerosol (SMA), depending on their production mechanism. Primary SSA is produced when bubbles become entrained in the water column by breaking waves. During their rise to the surface, the bubbles scavenge various surface-active

molecules, bringing them to the uppermost 1-1000 μm of the ocean surface. This small, yet critically important region of the ocean is known as the sea surface microlayer (SML) and is unique due to its ability to concentrate dissolved and particulate organic matter (DOM and POM, respectively) at the air-water interface where they can undergo further chemical and photochemical processing.

In addition to exposing DOM and POM to sunlight and various reactive trace gases, the air-water interface is important as it allows for the efficient transfer of surface-active species into the atmosphere as aerosols upon the bursting of bubbles. The bubble bursting process at the SML consists of a two-step mechanism. As the bubble initially breaks, there is a retraction and disintegration of the thin fluid film that caps the bubble. The film drops that result from this process are typically small (diameters less than 300 nm) and are composed largely of surface-active organics. Next, as water fills into the cavity left by the bursting bubble, a reactionary jet drop is ejected. It was long assumed that jet drops largely resulted in the formation of SSA with diameters greater than 2 μm . Furthermore, since jet drops originate from bulk water, the organic components of these SSA were believed to be more water soluble than film drops. However, a recent study has shown that jet drops also contribute to the submicron SSA population (~20-43%), with a chemical composition that is unique from those formed by film drops.²⁴ As will be discussed in Section 1.4 of this chapter, accurate representation of this complex process is required to generate relevant model systems for experimental studies.^{10,25}

The resulting view of primary SSA afforded by the understanding of the bubble bursting process is that SSA particles directly ejected from the ocean with diameters greater than 1 micron are composed largely of salts and biological material, while submicron particles are dominated by insoluble organic matter such as polysaccharides, lipids, and proteins.^{19,25,20,26,22,21} It is also generally understood that as particle size decreases, their organic mass fraction increases, with

organics contributing up to 75% of SSA particle mass in the size range of 50-150 nm as shown in Figure 1.3.^{11,19,22}

In addition to primary SSA, marine aerosols are also classified as secondary marine aerosols (SMA), which are formed upon the release and subsequent oxidation of precursor gas species. Perhaps the most well-known SMA precursor species is dimethylsulfide (DMS), which is produced upon enzymatic cleavage of dimethylsulfoniopropionate (DMSP) released by phytoplankton. Several pathways for DMS oxidation exist, each depending on the oxidant (e.g., OH or NO₃). For example, the abstraction pathway of DMS leads to the formation of SO₂, which eventually leads to production of sulfate (SO₄²⁻) particles either directly from the gas phase or in cloud droplets. The link between the biogenic production of DMS and subsequent SMA has intrigued scientists for decades, leading to considerable research efforts in determining the overall climate impacts and validity of the proposed mechanisms and feedback loops.²⁷⁻³²

To date, DMS is the only biologically-driven SMA precursor used in global models,^{33,34} despite the consensus that other VOCs are needed to explain SMA observations in marine regions. Indeed, other SMA precursor gases of marine origin exist and have recently been increasingly investigated, including isoprene, iodine, dicarboxylic acids, and biogenic alkyl amines.^{35,36,37} Still, considerable uncertainties regarding the formation (i.e., SMA precursor gases, oxidation pathways, link to biological activity, etc.) and climate impacts of SMA in marine regions persist.³⁷

1.2.2 Biological Control of SSA Chemical Composition

The organic matter scavenged by bubbles rising in the water column (and eventually emitted to the atmosphere) originates from the various complex metabolic activities of phytoplankton, bacteria, and viruses, otherwise collectively known as the microbial loop. For this reason, attempts have been made to link chlorophyll-a (chl-a) concentration, a common proxy for biological activity, to the chemical composition of SSA in large scale climate models.³⁸⁻⁴⁰ However,

such attempts have yielded mixed results, with some studies indeed finding a link between organic fraction of SSA and chl-a for monthly and seasonal time scales,^{26,37} with others reporting no differences.^{41,42} These conflicting results suggest that the understanding of the link between the ocean's biological activity and SSA chemical composition needs improving; a need that is specifically addressed by the research presented in Chapter 2 of this thesis.

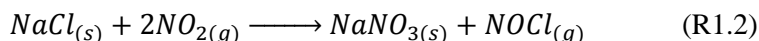
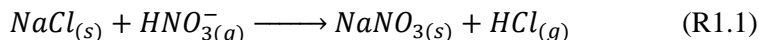
1.3 The Chemistry of SSA

Unfortunately, a solid understanding of how the ocean's microbial loop and the various transfer processes alter the chemical composition of SSA is not alone sufficient to determine how SSA impact climate. This is because the generation of nascent SSA is only the first step in an aerosol's journey through the atmosphere, which can last anywhere from seconds to days. During this time, SSA particles can undergo a wide range of aging processes which drastically alter their chemical and physical composition, thereby considerably changing their climate relevant properties. The following section introduces a few of these processes, with focus on those that are the topic of the studies described in this thesis.

1.3.1 Heterogeneous Reactions of SSA with Trace Atmospheric Gases

1.3.1.1 Reactions with HNO_3

An important class of SSA aging reactions are multiphase, or heterogeneous reactions, in which trace gas-phase species react with solid or liquid-phase SSA particles. A well-known set of heterogeneous reactions of SSA is that between NaCl and nitrogen oxides, which yield nitrate salt products and cause depletion of chloride within the particle due to the formation of gaseous HCl:



These reactions are particularly important in atmospheric chemistry due to the loss of nitrogen oxides from the gas phase as well as the subsequent changes to SSA properties.^{43,44,45}

As SSA have an organic component in addition to inorganic salts such as NaCl, numerous studies have attempted to better understand the role of organic coatings on such reactions.^{43,46,47} Despite these studies, a disconnect remains between field observations and lab results due to the use of simple systems that fail to properly replicate the composition and associated reactivity of SSA.^{43,48,49} Reducing the gap between simple lab studies and highly complex field observations of SSA is one of the main goals of the Center for Aerosol Impacts on Chemistry of the Environment (CAICE), an NSF-funded Center of Chemical Innovation (CCI). For example, a 2011 research intensive by CAICE analyzed HNO₃-reacted SSA particles produced from natural seawater using an ocean-atmosphere facility. Throughout the study, large ranges in particle reactivity with HNO₃ were observed on a particle-to-particle basis (Figure 1.4).⁵⁰ These results further underscored the importance of SSA chemical heterogeneity in such reactions, as well as the need to generate and study representative lab systems that accurately mimic SSA when conducting reaction studies.

Finally, as outlined in a recent review paper, SSA have been shown to contain biologically derived molecules which can also undergo heterogenous reactions with trace gases.⁵¹ The specific pathways of these reactions as well as the reactants involved are still poorly understood. As such, Chapter 3 of this thesis focuses on the effect of the presence of organic species and various biological components on the reactivity of SSA particles with the trace gas HNO₃.

1.3.1.2 Reactions with OH

Hydroxyl (OH) radicals are among the most reactive of all atmospheric oxidants and are thus sometimes colloquially referred to as the detergents of the atmosphere. Unsurprisingly, this has led to numerous studies of the reaction of OH radicals with other gas phase species. For instance, it has long been known that OH radicals react with VOCs to produce secondary organic

aerosols.¹⁴ However, while gas phase OH reactions have been extensively studied, only recently has attention been given to the heterogeneous reactions of gas phase OH on condensed phase organic aerosols, specifically simple saturated and unsaturated hydrocarbon species.⁵²

The reaction pathway for the OH-initiated oxidation of simple saturated organic aerosols as it is currently understood begins with hydrogen abstraction and is followed by the formation of a reactive oxygenated species (ROS). The reaction pathway then branches into two different mechanisms which leads to either the formation of oxygenated low volatility species through functionalization reactions or the formation of higher volatility species and a concomitant reduction in particle mass due to volatilization through fragmentation reactions. However, studies differ on the extent to which functionalization vs fragmentation pathways dominate in aerosols, with some studies finding functionalization the dominant pathway,^{53,54} while others indicate the fragmentation pathway is of greater importance.⁵⁵⁻⁵⁹ These conflicting results highlight the need for more studies on the OH-initiated oxidation of aerosol particles to determine the relevant pathways.

Furthermore, very little work has been done on the effect of OH reactions on SSA, with studies to date focusing on terrestrial and biomass burning sources. Since SSA has a unique chemical composition different from that of terrestrial aerosols, it is expected to exhibit different reactivities and pathways. Chapter 4 describes a study aimed at further improving the understanding of the role of OH reactions on the total marine aerosol composition by investigating the effect of OH-initiated heterogeneous aging reactions on primary SSA chemical composition as well as the formation of secondary marine aerosol (SMA) through OH-initiated homogeneous oxidation reactions of volatile organic compounds.

1.3.2 Photochemical Reactions at Atmospherically Relevant Air-Water Interfaces

In addition to various reactive trace gases, radiation from the sun can also initiate chemical reactions. When a molecule absorbs a photon of sufficient energy, its electrons transition into an

excited state. From there, the electronically excited molecule can undergo non-reactive relaxation via photophysical processes such as fluorescence, phosphorescence, and non-radiative transitions. Alternatively, the excited molecule can relax through reactive photochemical processes, including dissociation (photolysis), isomerization, rearrangement, ionization, or take part in direct or photosensitized reactions with other molecules. While homogenous gas-phase photochemical reactions in the atmosphere have been studied extensively, less is known about light driven reactions in the condensed phase, specifically those at the organic-rich air-water interface of aerosols, cloud droplets, and the sea surface microlayer. A brief introduction to two different photochemical reactions relevant to SSA are given in the following sections.

1.3.2.1 Photosensitized Reactions at Marine-Relevant Air-Water Interfaces

As noted above, dissolved organic matter (DOM) and particulate organic matter (POM) are enriched at air-water interfaces, including lakes, oceans, and aerosol surfaces. Due to its favorable position at the air-water interface, DOM can undergo a multitude of aging processes, including photochemical reaction upon absorption of sunlight. The fraction of DOM that absorbs radiation in the UV and visible range of the spectrum is termed chromophoric dissolved organic matter (CDOM). Upon irradiation, photoexcited molecules within CDOM undergo any one of the number of pathways outlined above.

Numerous studies have investigated the photosensitizing capability of triplet CDOM in the bulk phase, finding that photoexcited triplet state DOM degrades aqueous phase organic compounds, leading to the formation of alcohols, aldehydes, and ketones.⁶⁰ More recently, there has been increasing interest in the role of CDOM in photosensitized reactions that occur at the air-water interface where intermediate radical species are more likely to interact with one another due to their high concentration. Irradiation of simple model system photosensitizers (e.g., benzoyl benzoic acid (BBA)) with organic substrates such as nonanoic acid have been found to produce

functionalized and unsaturated gas and condensed phase products.⁶¹⁻⁶³ Such products are of particular interest due to their ability to serve as secondary organic aerosol precursors.

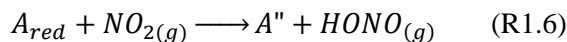
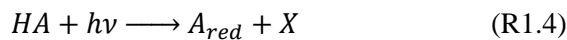
The total pool of DOM in marine environments (termed m-DOM) accounts for one of the largest carbon reservoirs on Earth (662 Pg).⁶⁴ Since a portion of the massive m-DOM pool consists of chromophoric species (m-CDOM), there is an abundance of molecules available to serve as photosensitizers in these regions. However, studies investigating potential photosensitized reactions at the air-water interface in marine environments have to date only been conducted using simple model system photosensitizers (e.g., BBA), or systems not representative of those found in the open ocean (e.g., humic acid of terrestrial origin). As such, the extent to how effective m-DOM, and its associated fraction of m-CDOM, serves as a photosensitizer remains poorly understood. Furthermore, the specific chromophores and processes responsible for m-CDOM's absorption characteristics are still a matter of debate.⁶⁵ For these reasons, analysis of photosensitized reactions involving more realistic model system photosensitizers need to be performed to ascertain the relevance of such reactions at the air-water interface of marine environments. This is the focus of the research described in Chapter 5.

1.3.2.2 Photoproduction of HONO

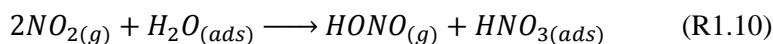
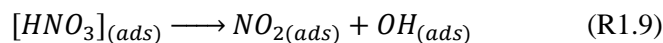
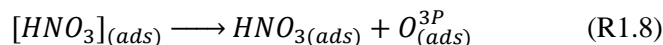
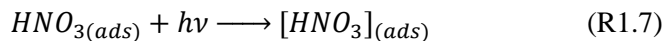
Nitrous acid (HONO) is a key atmospheric trace gas due to its harmful health effects and its role in the formation of hydroxyl (OH) radicals. There are currently five known pathways for the formation of HONO in the atmosphere: direct emission, homogeneous gas-phase reactions, heterogeneous reactions, surface photolysis, and biological processes. However, despite being the focus of many studies since the 1970s, a complete understanding of the formation mechanisms of HONO, especially during the daytime, remains elusive.⁶⁶

Recently, photosensitized reactions have gained interest as a potential pathway for the production of HONO. For example, previous work studies have proposed the following HONO

formation mechanism involving the photosensitized reduction of NO₂ on surfaces containing the photosensitizer humic acid:⁶⁷



In the proposed mechanism, humic acid (HA) is in activated Reaction 1.4 and either deactivates with an oxidant (X) via Reaction 1.5 or reduces gaseous NO₂ to form HONO in Reaction 1.6. In addition to photosensitized reactions, direct photolysis formation pathways have been proposed involving adsorbed HNO₃/particulate nitrate:⁶⁶



These pathways for HONO formation (i.e., direct photolysis of adsorbed HNO₃/NO₃⁻, and photosensitized reactions of NO₂ with HULIS) require further characterization at aerosol surfaces to improve agreement between modeled and observed HONO concentrations. Specifically, studies investigating the impact of surface water content, chemical composition of organic photosensitizers, aerosol aging, emission of VOCs from aerosol surface, pH, and varying irradiation regimes (i.e., UVA vs UVB) on relevant HONO formation mechanisms are needed. With this in mind, an incoherent broadband cavity enhanced absorption spectrometer (IBCEAS) was designed and constructed to monitor the presence of gaseous HONO, allowing for further investigation of the various pathways for HONO formation. Chapter 6 of this thesis describes the

construction and validation of a lab-built IBCEAS, and, after showing some preliminary data with this system, presents a discussion of potential future experiments.

1.4 Generation and Analysis of Aerosols

As Section 1.3 has shown, more studies of SSA need to be conducted to fill in the gaps regarding their chemical composition and reactivity. One approach to this is through analysis of SSA during field studies, in which instruments are brought to the ocean on ships or airplanes to track aerosols and conduct experiments in-situ. However, due to the complexity of the ocean-atmosphere system, the always-occurring process of aerosol aging, and the ubiquity of anthropogenic contributions, attaining meaningful results from field studies can be difficult.⁶⁸ Alternatively, while simple lab studies allow for the removal of such complicating factors, the simple model systems used are often poor mimics in terms of replicating the chemical complexity of authentic SSA. The Center for Aerosol Impacts on Chemistry of the Environment (CAICE) seeks to overcome the weaknesses of both approaches while maximizing their advantages by bringing the ocean into the lab. The following sections briefly introduce the methods used by CAICE to generate SSA and the instruments used to probe them.

1.4.1 Experimental Methods to Generate and Collect SSA

1.4.1.1 Generation of Authentic SSA

While in-lab generation of authentic SSA is a considerably more complicated process than the production of simple model systems, it is highly advantageous in that it produces single particles that are representative of SSA found in the real marine boundary layer. The key to generating authentic SSA is replicating ocean biological/chemical complexity and accurately mimicking the bubble formation/bursting process. The next two sections briefly describe methods for accomplishing this.

The first step to generating authentic SSA with accurate chemical complexity in the lab setting is accurately mimicking the microbial loop which produces the various chemical species found in the ocean.⁶⁹ This is accomplished by spiking filtered seawater with F/2 nutrient medium to induce phytoplankton blooms. Doing so allows for accurate replication of microbial loop processes that occur in marine environments, affording more realistic SSA composed of biogenically derived chemical species.

Having mimicked the biological complexity of the ocean, authentic SSA can then be reproduced by generating bubbles with size distributions similar to those found in the ocean. Two different methods were used in the studies outlined in this thesis. The first and most robust method for aerosol production is the use of an ocean-atmosphere facility that houses a 30-meter long waveflume channel.²⁵ Figure 1.5 shows the waveflume. Breaking waves were generated by using a hydraulic paddle, and the resulting SSA was sampled either using off-line or on-line methods.

A second and slightly less complicated method for SSA generation is through the use of a Marine Aerosol Reference Tank (MART). In MARTs, a plunging waterfall system is used to generate bubbles in the bulk water with size distributions similar to those found in the ocean, allowing for formation of SSA that are representative of authentic SSA found over the ocean. Figure 1.6 shows the MART.⁷⁰ For size-resolved collection of authentic SSA particles generated in waveflume and MART experiments, SSA were impacted onto substrates using a micro-orifice uniform deposit impactor (MOUDI) operating at a flow rate of ~30 lpm and with size cuts at .056, 0.10, 0.18, 0.32, .56, 1.0, 1.8, 3.2, 5.6, 10, 18 μm .

1.4.1.2 Formation of Simple SSA Model Systems: Atomizer, Thin Films

To conduct simple experiments and aid in identification of molecular species present in lab generated authentic SSA, simple model systems were generated using a commercial TSI atomizer which aerosolized particles from an aqueous solution. Figure 1.7 shows the atomizer assembly

block. The atomizer works by creating a high-velocity jet by using compressed air from a commercial dry air generator pushed through a small orifice. As the compressed air moves through the orifice, liquid is drawn into the atomizer assembly block from the solution and is subsequently aerosolized by the jet. Large droplets are removed upon impaction on the wall opposite the jet and are drained back into the atomizer bottle. Aerosols are sent then through a fitting at the top of the atomizer with the air flow, where they are then passed through diffusion dryers to be dried to ~5% RH. Aerosols particles were impacted directly onto substrates by placing the substrate in the line of the aerosol flow on the surface of the impactor installed on the front of a differential mobility analyzer (DMA).

In addition to model system aerosol particles, thin films of organics were used to study the reactivity of organic-rich aerosol interfaces. Thin films were created by dissolving solid samples in organic solvent and evaporating off the solvent, leaving behind a thin film. While these two methods are much simpler than those described in the previous section, they are useful in building up a library of compounds for analysis of complicated authentic SSA and can also be used in targeted, specific experiments.

1.4.2 Analysis

A range of analytical techniques have been used for the analysis of SSA. A brief overview of the techniques most relevant to this thesis is next given, with details of supplementary analysis methods given in the appropriate chapters.

1.4.2.1 Raman Spectroscopy

Aerosols can be examined either by measuring many particles at once (i.e., bulk analysis), or by analyzing individual particles one at a time. While more time consuming, single particle analysis is useful in that it reveals chemical constituents, as well as phase and mixing state. Currently, a need exists for more studies at the single particle level as global climate models that

include primary SSA do not account for single particle variability, an oversight that hinders their accuracy.^{71,72} Raman vibrational spectroscopy is a well-established analysis technique that can be used to acquire vibrational spectra of single SSA particles, allowing analysis of their chemical composition. A classical description of the Raman scattering principle is next briefly given.

Upon irradiation by an electromagnetic wave, the electron cloud and nuclei of a molecule are shifted in opposite directions, causing the formation of an induced dipole moment, μ_{ind} . The strength of the induced dipole moment is described by Equation 1.1:

$$\mu_{ind} = \alpha E \quad (\text{Eq1.1})$$

where α is the polarizability and E is the magnitude of the oscillating electromagnetic wave, which is described as:

$$E = E_o \cos(2\pi\nu_o t) \quad (\text{Eq1.2})$$

where ν_o is the frequency of the wave. Substituting this equation into the equation describing the induced dipole moment gives:

$$\mu_{ind} = \alpha E_o \cos(2\pi\nu_o t) \quad (\text{Eq1.3})$$

This equation shows that the induced dipole oscillates at a frequency equal to the incident electromagnetic wave and is responsible for the elastically scattered light observed. However, if internal vibrational modes exist that alter the polarizability of the molecule, additional frequencies are seen. The polarizability of a molecule can be approximated by a Taylor series expansion:

$$\alpha = \alpha_o + \left(\frac{\delta\alpha}{\delta Q_k}\right)_0 Q_k + \dots \quad (\text{Eq1.4})$$

where α_o is the polarizability of the molecule at equilibrium position. As a molecule vibrates, the physical displacement Q_k of its atoms about their equilibrium position can be expressed as:

$$Q_k = Q_k^0 \cos(2\pi\nu_k t) \quad (\text{Eq1.5})$$

where Q_k^0 is the max displacement and ν_k is the frequency of vibration of the atoms. Equation 1.4 can be substituted back into Equation 1.3 to give an expanded description of the induced dipole of a vibrating molecule:

$$\mu = \alpha_o E_o \cos(2\pi\nu_o t) + \left(\frac{\delta\alpha}{\delta Q_k} \right)_0 Q_k^0 \cos(2\pi\nu_k t) E_o \cos(2\pi\nu_o t) \quad (\text{Eq1.6})$$

After application of the trigonometric identity for the product of two cosines, Eq.1.6 can be further simplified as:

$$\mu = \alpha_o E_o \cos(2\pi\nu_o t) + \frac{1}{2} E_o Q_k^0 \left(\frac{\delta\alpha}{\delta Q_k} \right)_0 [\cos(2\pi(\nu_o + \nu_k)t) + \cos(2\pi(\nu_o - \nu_k)t)] \quad (\text{Eq1.7})$$

This equation shows that the induced dipole moment oscillates at three frequencies. The first component is still due to elastically scattered light (i.e., Rayleigh scattering), and has a frequency unchanged from the incident electromagnetic wave. The latter two terms are due to inelastic Raman scattering and are shifted to higher and lower frequencies (i.e., anti-stokes and stokes shifts, respectively). For a vibration to be Raman active, it must cause a change in the polarizability of the molecule.

The Raman instrument used throughout the studies described here is a Labram HR Evolution Raman Spectrometer (Horiba). A block diagram of the spectrometer is shown in Figure 1.8. The spectrometer is equipped with a 532 nm laser and an Olympus optical microscope with 10x, 50x, and 100x magnification objective lenses. The laser spot diameter, and thus the spatial resolution of the Raman spectrometer, is related to the wavelength of the laser and the numerical aperture of the objective according to Equation 1.8:

$$D_{laser} = 1.22 \left(\frac{\lambda}{NA} \right) \quad (\text{Eq1.8})$$

According to this equation, the maximum spatial resolution of our system is ~700 nm when the 0.90/100x objective is used with the 532 nm laser. The system has been further augmented with an environmental chamber to allow for temperature and relative humidity (RH) control. Furthermore, both off-line and on-line mixing chambers have been designed to allow samples to be exposed to reactive gases.

1.4.2.2 Attenuated Total Reflectance-Fourier Transform Infrared Spectroscopy

Infrared vibrational (IR) spectroscopy is a popular technique that is often used complementary to Raman spectroscopy. While the Raman effect is a two-photon scattering process that requires a change in polarizability of the molecule, IR vibrational transitions are one-photon absorption processes that require a change in the dipole moment of a molecule. Because of the different selection rules, the two methods are often used together to attain a complete picture of the vibrational modes of a given molecule.

Analysis of thin films representative of thick organic coatings present at the SML and aerosol interface was conducted using a variant of IR spectroscopy termed attenuated total reflectance-Fourier transform infrared spectroscopy (ATR-FTIR). This method is based on the principle of total internal reflection of IR radiation at the boundary between two media. Briefly, a light beam is sent through a crystal that is coated in sample. As the light beam propagates through the optically dense crystal, it undergoes total internal reflection when it approaches the sample at an angle of incidence greater than the critical angle. Upon reflection, an evanescent wave is sent into the sample, with an electric field amplitude that decays exponentially with propagation distance. In regions of the IR spectrum where the sample absorbs energy, the evanescent wave is attenuated, leading to a decrease in the IR beam's intensity. After multiple reflections, the IR beam is eventually passed back out of the ATR crystal and to a detector, where changes in the spectrum

are measured. The resulting signal decrease is due to absorbance by the sample and can be described according to Beer's law:

$$A = \epsilon lc = \epsilon n d_p \quad (\text{Eq1.9})$$

where ϵ is the molar absorption coefficient, d_p is the penetration depth, and n is the number of internal reflections at the ATR element interface.⁷³ The penetration depth of the electric field is defined as the distance required to decrease the amplitude to e^{-1} of its value at the surface, which is given by:

$$d_p = \frac{\lambda}{2\pi n_1 n_2 (\sin^2 \theta - n_{21}^2)^{1/2}} \quad (\text{Eq1.10})$$

where λ is the wavelength of the light, n_1 is the index of refraction of the optically dense medium, n_2 is the index refraction of the optically rare medium, $n_{21} = n_2/n_1$, and θ is the angle of incidence. For an AMTIR crystal, this gives a penetration depth of 1.46 μm . As such, ATR-FTIR is a useful probe for studying the interfacial region of samples and is one of the main methods used in the studies of reactions at the aerosol interface described in Chapter 5.

1.4.2.3 Additional Analysis Techniques

In addition to Raman and ATR-FTIR, additional analysis was conducted using several analytical techniques including X-ray photoelectron spectroscopy (XPS), ultra-high resolution mass spectrometry (MS), and aerosol time of flight mass spectrometry (ATOFMS), among others. Each of these techniques are further described in the appropriate chapters.

1.5 Synopsis and Goal of this Thesis

In this chapter, several gaps in knowledge regarding SSA and the motivation for reducing them have been introduced. Furthermore, experimental methods to generate and analyze SSA relevant to the studies in this thesis have been introduced. The remaining chapters serve to describe

the studies that were performed with the aim of improving the understanding regarding the topics discussed in this introduction. Specifically, the thesis is focused on the following considerations and is organized as follows:

Chapter 2: What are the molecular species found in SSA? How does changing ocean biology alter the chemical composition of SSA? How do the changes in SSA chemical composition alter their climate relevant properties, such as their ability to serve as IN?

Chapter 3: How do organic coatings and the presence biologically derived organic matter in SSA alter their reactivity and reaction pathway with HNO₃?

Chapter 4: What are the products of photosensitized reactions between simple model system photosensitizers and nonanoic acid? How do complex model system photosensitizers differ from simple model system photosensitizers?

Chapter 5: How does exposure to OH radicals alter the chemical composition of SSA?

Chapter 6: Outlines the design and construction of an LED-IBCEAS and discusses future experiments aimed at determining HONO sources.

Chapter 7: Summarizes the findings of each chapter and discusses gaps of knowledge that remain as well as future and ongoing studies.

1.6 Figures

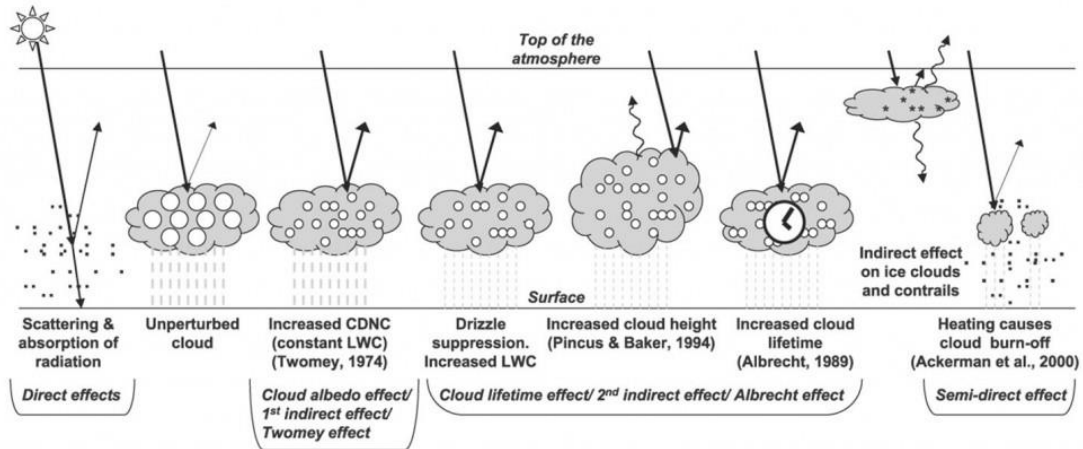


Figure 1.1: Direct and indirect effects of aerosol particles in the atmosphere. Image reprinted from Forster, P., V. Ramaswamy, P. Artaxo, T. Berntsen, R. Betts, D.W. Fahey, J. Haywood, J. Lean, D.C. Lowe, G. Myhre, J. Nganga, R. Prinn, G. Raga, M. Schulz and R. Van Dorland, 2007: Changes in Atmospheric Constituents and in Radiative Forcing. In: Climate Change 2007: The Physical Science Basis. Contribution of Working Group I to the Fourth Assessment Report of the Intergovernmental Panel on Climate Change [Solomon, S., D. Qin, M. Manning, Z. Chen, M. Marquis, K.B. Averyt, M. Tignor and H.L. Miller (eds.)]. Cambridge University Press, Cambridge, United Kingdom and New York, NY, USA.

Radiative forcing of climate between 1750 and 2011
Forcing agent

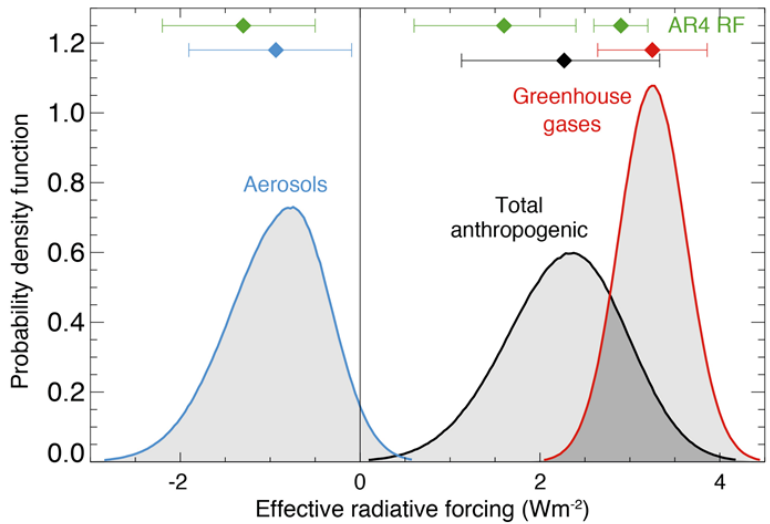
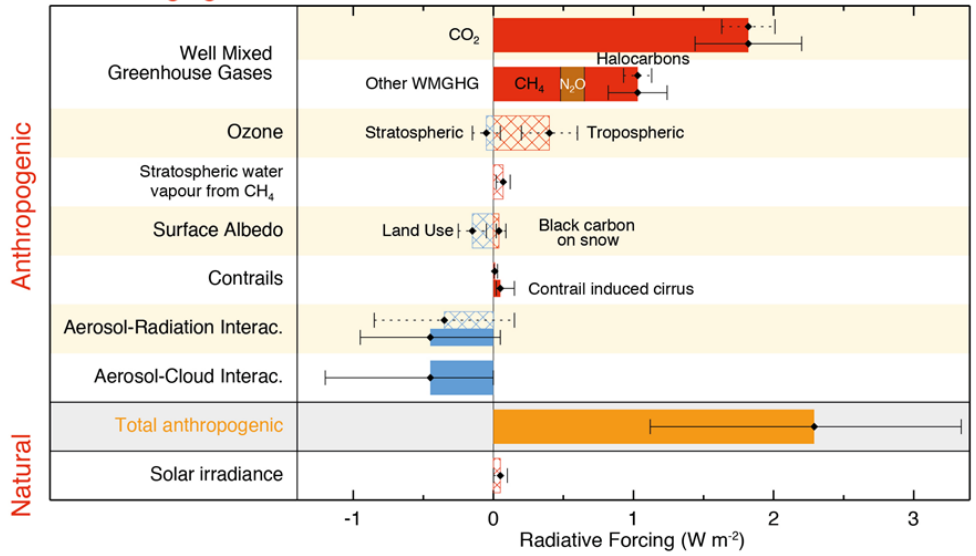


Figure 1.2: Radiative forcing (RF) and effective radiative forcing (ERF) of climate change between 1750 and 2011. RF and ERF quantify the change in the Earth's radiative balance due to anthropogenic influences. RF keeps all surface and tropospheric conditions fixed, while ERC calculations allow physical variables to respond to perturbations, except for those related to the ocean and sea ice. The top graph shows the RF (solid) and ERF (hatched) of various agents. The bottom plot shows the probability density functions for the ERF of aerosol, greenhouses gases, and total influence. Image adapted from Stocker, T.F., D. Qin, G.-K. Plattner, M. Tignor, S. K. Allen, J. Boschung, A. Nauels, Y. Xia, Bex, V., Midgley, P. M, in *Climate Change 2013: The Physical Science Basis*. Contribution of Working Group I to the Fifth Assessment Report of the Intergovernmental Panel on Climate Change; Stocker, T.F., D. Qin, G.-K. Plattner, M. Tignor, S. K. Allen, J. Boschung, A. Nauels, Y. Xia, Bex, V., Midgley, P. M., Eds.; Cambridge University Press: Cambridge, United Kingdom and New York, NY, USA, **2013**.

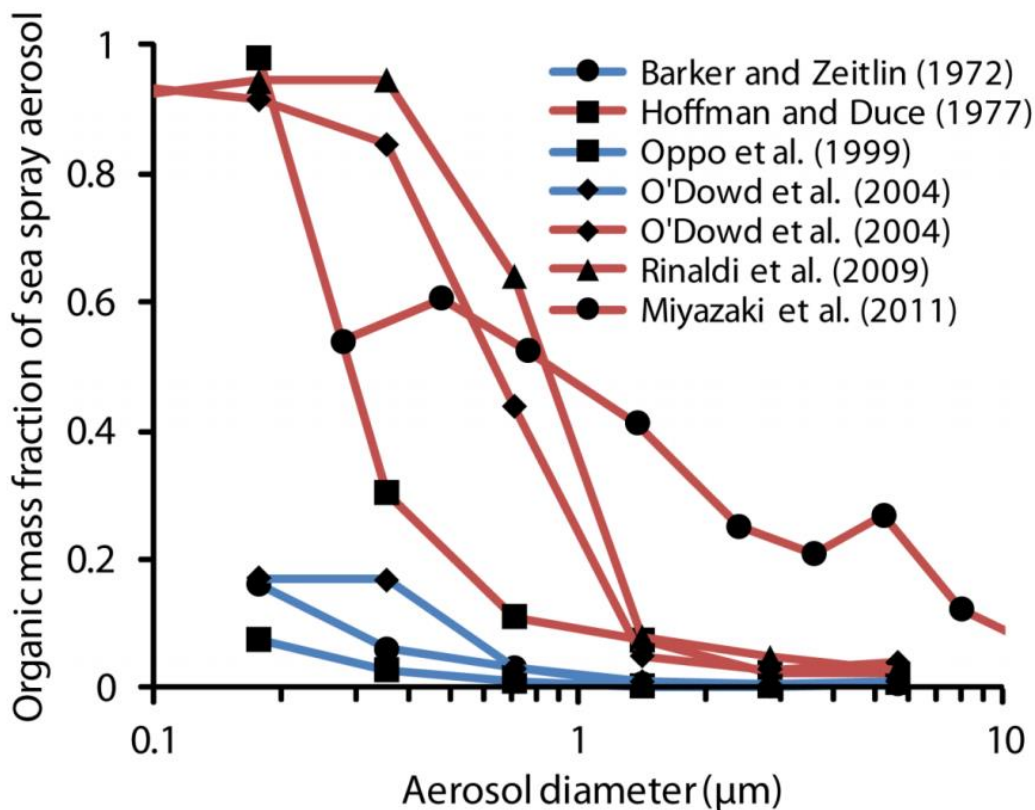


Figure 1.3: Size-resolved organic mass fraction of sea spray aerosol measured in clean marine conditions as a function of aerosol diameter. Blue lines represent measurements taken during periods of low biological activity while red lines represent periods of high biological activity. Image reprinted from Gantt, B.; Meskhidze, N. The Physical and Chemical Characteristics of Marine Primary Organic Aerosol : A Review. *Atmos. Chem. Phys.* **2013**, *13* (8), 3979–3996.

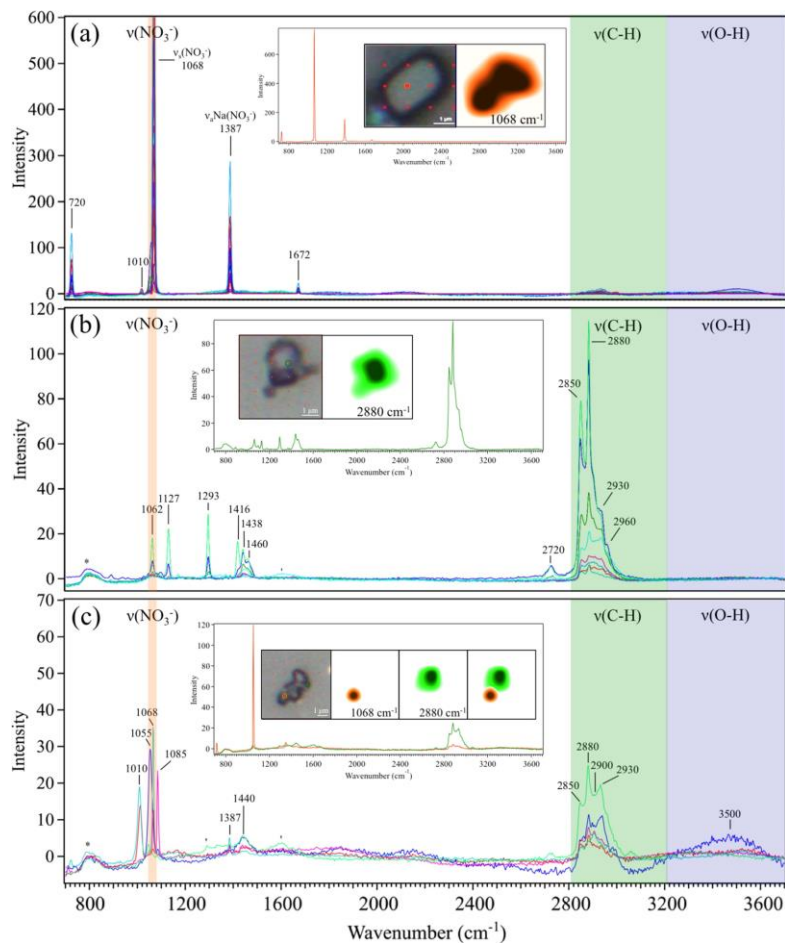


Figure 1.4: Raman spectra of individual SSA particles analyzed with micro-Raman spectroscopy for several different particle types, along with optical images, individual spectra, and spectra maps in the insets. The larger colored circles on the optical images indicate the locations of the particle that the laser beam interrogated for each of the spectra shown in the inset. The smaller dots represent the grid that defines the points used for spectral maps. These spectra of particles exposed to nitric acid show different particle types. (a) Particles with high reactivity as indicated by an intense signal for the symmetric stretch of the nitrate ion at 1068 cm^{-1} , along with other nitrate vibrations. These particles also show minimal intensity in the C–H stretching region, indicating small amounts of organic species present within these particles. (b) Particles with high intensity due to organic species, as shown by the large intensity in the C–H stretching region indicating high levels of organics associated with the particle but minimal signal associated with the nitrate ion. These particles have low reactivity. (Note: Although there is a peak at 1062 cm^{-1} close to the NO_3^- region, it is most likely due to vibrations associated with the organic species within these particles, e.g., C–C stretches, C–O stretches, and/or methyl deformations, associated with the organic species present as its intensity correlates with other peaks due to organics from 1100 to 1500 cm^{-1} .) (c) Particles with both peaks associated with organic species and a nitrate anion, indicating particles with intermediate reactivity. Spectral maps are shown for the $\nu_s(\text{NO}_3^-)$ mode (1068 cm^{-1}) and $\nu(\text{C-H})$ mode at 2880 cm^{-1} . For these particles, spectral maps along with the optical image show phase segregation between the nitrate and organic species within the particle. * designates the quartz substrate, and ' designates a small amount of graphitic carbon from sample damage by the laser.



Figure 1.5: Image of the 30-meter-long wavechannel used during the 2014 IMPACTS experiment in the Hydraulics Laboratory at Scripps Institution of Oceanography. The wavechannel was filled with filtered seawater and spiked with nutrients to produce a phytoplankton bloom. Aerosols were generated using a hydraulic paddle on the left end of the channel. A plank was used to mimic a beach upon which wave broke, producing SSA. Generated SSA were collected from a manifold for off-line and on-line analysis.

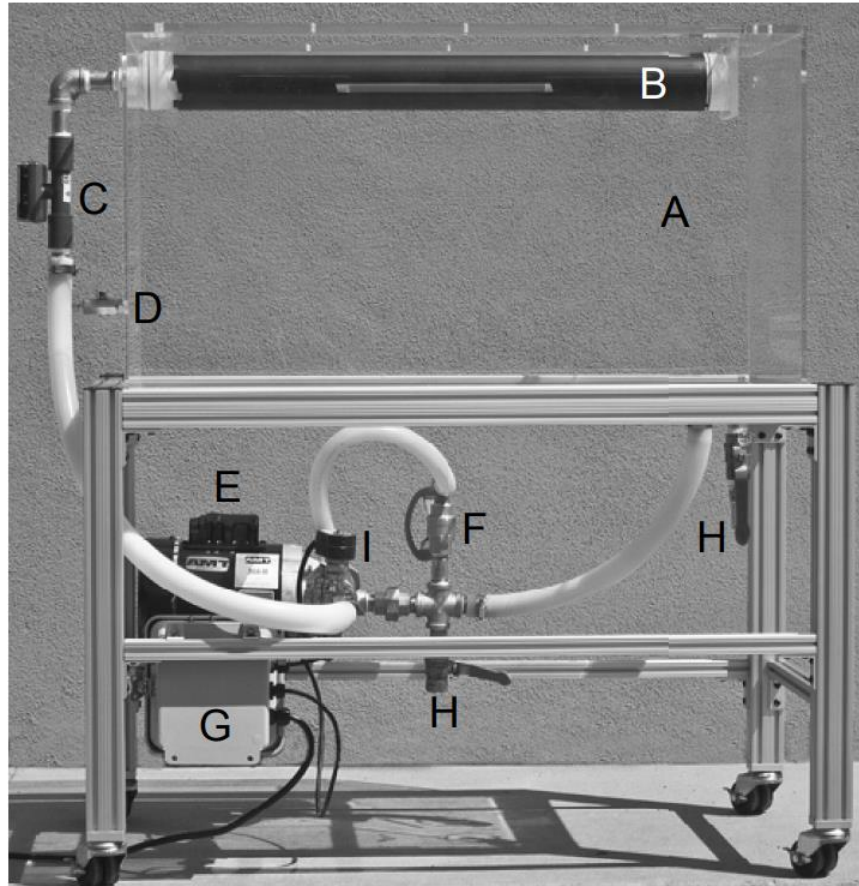


Figure 1.6: Marine Aerosol Reference Tank (MART). The 210 L plexiglass tank (A) is approximately 1 m in the longest dimension. (B) The internal water distribution assembly is o-ring sealed with central spillway slot. Inside the assembly is a secondary diffuser tube (not visible) for evenly distributing the water along the spillway. (C) Flow meter. (D) Tank water sampling spigot. (E) 1/3 HP centrifugal pump. (F) Flow shunt control valve. (G) Timing relay control box. (H) Tank drain and purge valves. (I) Solenoid valve. Reprinted from Stokes, M. D.; Deane, G. B.; Prather, K.; Bertram, T. H.; Ruppel, M. J.; Ryder, O. S.; Brady, J. M.; Zhao, D. A Marine Aerosol Reference Tank System as a Breaking Wave Analogue for the Production of Foam and Sea-Spray Aerosols. *Atmos. Meas. Tech.* **2013**, 6 (4), 1085–1094.

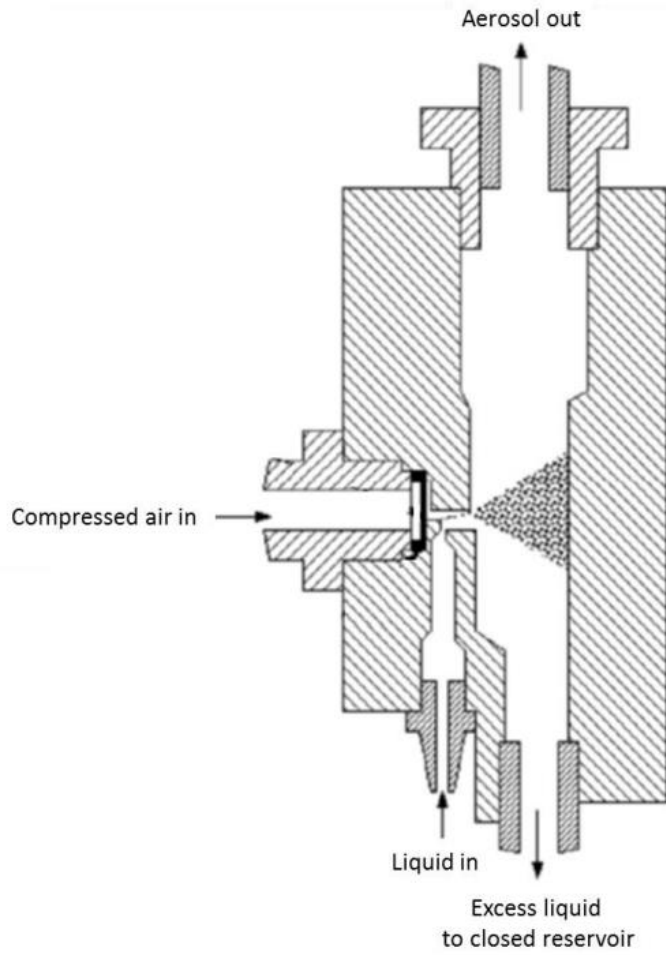


Figure 1.7: Schematic of the atomizer assembly block. Adapted from TSI, Inc.

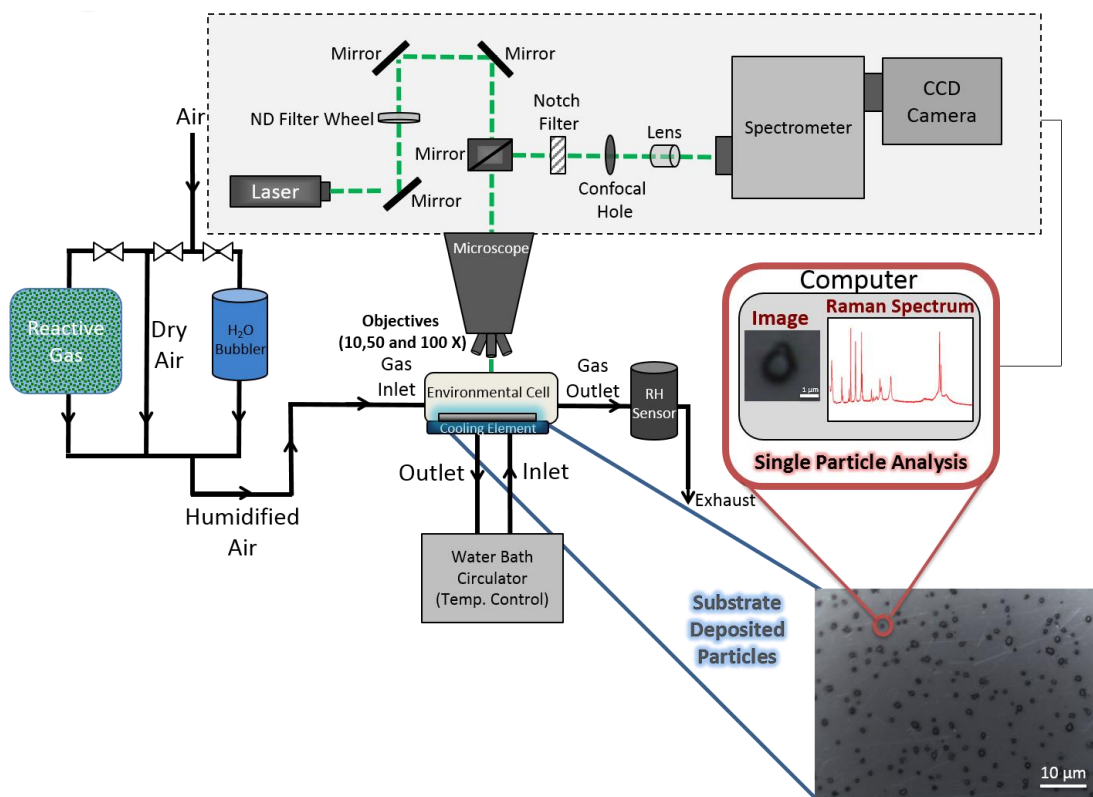


Figure 1.8: Block diagram of the Raman spectrometer used in the studies described herein. The system is equipped with a 532 nm laser and 10x, 50x, and 100X objective lenses. An environmental cell (Linkam) allows for temperature and RH control of samples. Furthermore, samples can be exposed to reactive gases either on-line or in an off-line mixing chamber (not shown).

1.7 References

- (1) Pandis, S. N.; Seinfeld, J. H. *Atmospheric Chemistry and Physics*, 2nd ed.; John Wiley & Sons, Inc.: Hoboken, 2006.
- (2) da Vinci, L. *The Notebooks of Leonardo Da Vinci*; Richter, J. P., Ed.; Dover Publications: Mineola, 1970.
- (3) Pöschl, U. Atmospheric Aerosols: Composition, Transformation, Climate and Health Effects. *Angew. Chemie - Int. Ed.* **2005**, *44* (46), 7520–7540.
- (4) Andreae, M. O.; Gelencs, A.; Box, P. O.; Veszpr, H.-. And Physics Black Carbon or Brown Carbon? The Nature of Light-Absorbing Carbonaceous Aerosols. **2006**, 3131–3148.
- (5) Pöschl, U. Aerosol Particle Analysis: Challenges and Progress. *Anal. Bioanal. Chem.* **2003**, *375* (1), 30–32.
- (6) S. Twomey. The Influence of Pollution on the Shortwave Albedo of Clouds. *J. Atmos. Sci.* **1977**, *34*, 1150–1152.
- (7) Rosenfeld, D. Suppression of Rain and Snow by Urban and Industrial Air Pollution. **2000**, 287 (March), 1793–1796.
- (8) Albrecht, B. A. Fractional Cloudiness. *Science (80-.)*. **1989**, *245* (4923), 1227–1230.
- (9) Mcfiggans, G.; Artaxo, P.; Baltensperger, U.; Coe, H.; Facchini, M. C.; Feingold, G.; Fuzzi, S.; Gysel, M.; Laaksonen, A.; Lohmann, U.; Mentel, T. F.; Murphy, D. M.; O'Dowd, C. D.; Snider, J. R.; Weingartner, E. And Physics The Effect of Physical and Chemical Aerosol Properties on Warm Cloud Droplet Activation. **2006**, 2593–2649.
- (10) de Leeuw, G.; Andreas, E. L. L.; Anguelova, M. D. D.; Fairall, C. W. W.; Lewis, E. R. R.; Dowd, C. O. O.; Schulz, M.; Schwartz, S. E. E. Production Flux of Sea Spray Aerosol. *Rev. Geophys.* **2011**, No. 2010, 1–39.
- (11) Dowd, C. D. O.; Langmann, B.; Varghese, S.; Scannell, C.; Ceburnis, D.; Facchini, M. C. A Combined Organic-Inorganic Sea-Spray Source Function. **2008**, *35* (October 2007), 1–5.
- (12) Carslaw, K. S.; Boucher, O.; Spracklen, D. V; Mann, G. W.; Rae, J. G. L.; Woodward, S.; Kulmala, M. And Physics A Review of Natural Aerosol Interactions and Feedbacks within the Earth System. **2010**, 1701–1737.
- (13) Long, M. S.; Keene, W. C.; Kieber, D. J.; Erickson, D. J.; Maring, H. And Physics A Sea-State Based Source Function for Size- and Composition-Resolved Marine Aerosol Production. **2011**, 1203–1216.
- (14) Kroll, J. H.; Seinfeld, J. H. Chemistry of Secondary Organic Aerosol: Formation and Evolution of Low-Volatility Organics in the Atmosphere. *Atmos. Environ.* **2008**, *42* (16), 3593–3624.
- (15) Goldstein, A. H.; Galbally, I. E. Known and Unexplored Organic Constituents in the Earth's Atmosphere. *Environ. Sci. Technol.* **2007**, *41* (5), 1514–1521.
- (16) Andreae, M. O.; Rosenfeld, D. Earth-Science Reviews Aerosol – Cloud – Precipitation Interactions . Part 1 . The Nature and Sources of Cloud-Active Aerosols. **2008**, *89*, 13–41.

- (17) Hoose, C.; Kristjánsson, J. E.; Iversen, T.; Kirkevåg, A.; Seland; Gettelman, A. Constraining Cloud Droplet Number Concentration in GCMs Suppresses the Aerosol Indirect Effect. *Geophys. Res. Lett.* **2009**, *36* (12), 1–5.
- (18) Blanchard, D. C. The Electrification of the Atmosphere by Particles from Bubbles in the Sea. *Prog. Oceanogr.* **1963**, *1* (1254), 73–202.
- (19) Facchini, M. C.; Rinaldi, M.; Decesari, S.; Carbone, C.; Finessi, E.; Mircea, M.; Fuzzi, S.; Ceburnis, D.; Flanagan, R.; Nilsson, E. D.; de Leeuw, G.; Martino, M.; Woeltjen, J.; O'Dowd, C. D. Primary Submicron Marine Aerosol Dominated by Insoluble Organic Colloids and Aggregates. *Geophys. Res. Lett.* **2008**, *35*, 1–5.
- (20) Cavalli, F.; Facchini, M. C. C.; Decesari, S.; Mircea, M.; Emblico, L.; Fuzzi, S.; Ceburnis, D.; Yoon, Y. J.; O'Dowd, C. D.; Putaud, J. P. Advances in Characterization of Size-Resolved Organic Matter in Marine Aerosol over the North Atlantic. *J. Geophys. Res. D Atmos.* **2004**, *109* (24), 1–14.
- (21) Ceburnis, D.; Garbaras, A.; Szidat, S.; Rinaldi, M.; Fahrni, S.; Perron, N.; Wacker, L.; Leinert, S.; Remeikis, V.; Facchini, M. C.; Prevot, A. S. H.; Jennings, S. G.; Ramonet, M.; O'Dowd, C. D. Quantification of the Carbonaceous Matter Origin in Submicron Marine Aerosol by ¹³C and ¹⁴C Isotope Analysis. *Atmos. Chem. Phys.* **2011**, *11*, 8593–8606.
- (22) Keene, W. C. C.; Maring, H.; Maben, J. R. R.; Kieber, D. J. J.; Pszenny, A. A. P. A. P.; Dahl, E. E. E.; Izaguirre, M. A. A.; Davis, A. J. J.; Long, M. S. S.; Zhou, X.; Smoydzin, L.; Sander, R. Chemical and Physical Characteristics of Nascent Aerosols Produced by Bursting Bubbles at a Model Air-Sea Interface. *J. Geophys. Res. Atmos.* **2007**, *112*, 1–16.
- (23) Gantt, B.; Meskhidze, N.; Meskhidze, B. G. and N. The Physical and Chemical Characteristics of Marine Primary Organic Aerosol : A Review. *Atmos. Chem. Phys.* **2013**, *13* (8), 3979–3996.
- (24) Wang, X.; Deane, G. B.; Moore, K. A.; Ryder, O. S.; Stokes, M. D.; Beall, C. M.; Collins, D. B.; Santander, M. V.; Burrows, S. M.; Sultana, C. M.; Prather, K. A. The Role of Jet and Film Drops in Controlling the Mixing State of Submicron Sea Spray Aerosol Particles. *Proc. Natl. Acad. Sci.* **2017**, *114* (27), 6978–6983.
- (25) Prather, K. A.; Bertram, T. H.; Grassian, V. H.; Deane, G. B.; Stokes, M. D.; Demott, P. J.; Aluwihare, L. I.; Palenik, B. P.; Azam, F.; Seinfeld, J. H.; Moffet, R. C.; Molina, M. J.; Cappa, C. D.; Geiger, F. M.; Roberts, G. C.; Russell, L. M.; Ault, A. P.; Baltrusaitis, J.; Collins, D. B.; Corrigan, C. E.; Cuadra-Rodriguez, L. A.; Ebben, C. J.; Forestieri, S. D.; Guasco, T. L.; Hersey, S. P.; Kim, M. J.; Lambert, W. F.; Modini, R. L.; Mui, W.; Pedler, B. E.; Ruppel, M. J.; Ryder, O. S.; Schoepp, N. G.; Sullivan, R. C.; Zhao, D. Bringing the Ocean Into the Laboratory to Probe the Chemical Complexity of Sea Spray Aerosol. *Proc. Natl. Acad. Sci. U. S. A.* **2013**, *110* (19), 7550–7555.
- (26) O'Dowd, C. D.; Facchini, M. C.; Cavalli, F.; Ceburnis, D.; Mircea, M.; Decesari, S.; Fuzzi, S.; Yoon, Y. J.; Putaud, J.-P. Biogenically Driven Organic Contribution to Marine Aerosol. *Nature* **2004**, *431* (7009), 676–680.
- (27) Andreae, T. W.; Andreae, M. O.; Schebeske, G. Biogenic Sulfur Emissions and Aerosols over the Tropical South Atlantic: 1. DMS in Seawater and in the Atmospheric Boundary Layer. *J. Geophys. Res.* **1994**, *99* (D11), 22,819–822,829.

- (28) Andreae, M. O.; Elbert, W.; de Mora, S. J. Biogenic Sulfur Emissions and Aerosols over the Tropical South Atlantic: 3. Atmospheric Dimethylsulfide, Aerosols and Cloud Condensation Nuclei. *J. Geophys. Res.* **1995**, *100* (D6), 11335.
- (29) Bates, T. S.; Charlson, R. J.; Gammon, R. H. Evidence for the Climatic Role of Marine Biogenic Sulphur. *Nature* **1987**, *329* (6137), 319–321.
- (30) Gondwe, M.; Krol, M.; Gieskes, W.; Klaassen, W.; de Baar, H. Correction to “The Contribution of Ocean-Leaving DMS to the Global Atmospheric Burdens of DMS, MSA, SO₂, and NSS SO₄⁼.” *Global Biogeochem. Cycles* **2003**, *17* (4), n/a-n/a.
- (31) Sunda, W.; Kieber, D. J.; Kiene, R. P.; Huntsman, S. An Antioxidant Function for DMSP and DMS in Marine Algae. *Nature* **2002**, *418* (6895), 317–320.
- (32) Quinn, P. K.; Bates, T. S. The Case against Climate Regulation via Oceanic Phytoplankton Sulphur Emissions. *Nature* **2011**, *480* (7375), 51–56.
- (33) Boucher, O.; Moulin, C.; Belviso, S.; Aumont, O.; Bopp, L.; Cosme, E.; Von Kuhlmann, R.; Lawrence, M. G.; Pham, M.; Reddy, M. S.; Sciare, J.; Venkataraman, C. DMS Atmospheric Concentrations and Sulphate Aerosol Indirect Radiative Forcing: A Sensitivity Study to the DMS Source Representation and Oxidation. *Atmos. Chem. Phys.* **2003**, *3* (1), 49–65.
- (34) Bopp, L.; Aumont, O.; Belviso, S.; Monfray, P. Potential Impact of Climate Change on Marine Dimethyl Sulfide Emissions. *Tellus Ser. B-Chemical Phys. Meteorol.* **2003**, *55* (1), 11–22.
- (35) Meskhidze, N.; Nenes, A. Phytoplankton and Cloudiness in the Southern Ocean. *Science* (80-.). **2006**, *314*, 1419–1423.
- (36) Sellegri, K.; Pey, J.; Rose, C.; Culot, A.; DeWitt, H. L.; Mas, S.; Schwier, A. N.; Temime-Roussel, B.; Charriere, B.; Saiz-Lopez, A.; Mahajan, A. S.; Parin, D.; Kukui, A.; Sempere, R.; D'Anna, B.; Marchand, N. Evidence of Atmospheric Nanoparticle Formation from Emissions of Marine Microorganisms. *Geophys. Res. Lett.* **2016**, *43*, 6596-6603.
- (37) Rinaldi, M.; Decesari, S.; Finessi, E.; Giulianelli, L.; Carbone, C.; Fuzzi, S.; Dowd, C. D. O.; Ceburnis, D.; Facchini, M. C. Primary and Secondary Organic Marine Aerosol and Oceanic Biological Activity: Recent Results and New Perspectives for Future Studies. **2010**, *2010*.
- (38) Vignati, E.; Facchini, M. C.; Rinaldi, M.; Scannell, C.; Ceburnis, D.; Sciare, J.; Kanakidou, M.; Myriokefalitakis, S.; Dentener, F.; Dowd, C. D. O. Global Scale Emission and Distribution of Sea-Spray Aerosol: Sea-Salt and Organic Enrichment. *Atmos. Environ.* **2010**, *44* (5), 670–677.
- (39) Spracklen, D. V; Arnold, S. R.; Sciare, J.; Carslaw, K. S.; Pio, C. Globally Significant Oceanic Source of Organic Carbon Aerosol. **2008**, *35*, 1–5.
- (40) Partanen, A.; Dunne, E. M.; Bergman, T.; Laakso, A.; Kokkola, H.; Ovadnevaite, J.; Sogacheva, L.; Baisnée, D. Global Modelling of Direct and Indirect Effects of Sea Spray Aerosol. **2014**, 11731–11752.
- (41) Quinn, P. K.; Bates, T. S.; Schulz, K. S.; Co, D. J.; Frossard, A. A.; Russell, L. M.; Keene, W. C.; Kieber, D. J. Contribution of Sea Surface Carbon Pool to Organic Matter Enrichment

in Sea Spray Aerosol. **2014**, 7 (March), 228–232.

- (42) Bates, T. S.; Quinn, P. K.; Frossard, A. A.; Russell, L. M.; Hakala, J.; Petäjä, T.; Kulmala, M.; Covert, D. S.; Cappa, C. D.; Li, S.; Hayden, K. L.; Nuaaman, I.; McLaren, R.; Massoli, P.; Canagaratna, M. R.; Onasch, T. B.; Sueper, D.; Worsnop, D. R.; Keene, W. C. Measurements of Ocean Derived Aerosol off the Coast of California. *J. Geophys. Res.* **2012**, *117*, 1–13.
- (43) Abbatt, J. P. D.; Lee, A. K. Y.; Thornton, J. A. Quantifying Trace Gas Uptake to Tropospheric Aerosol: Recent Advances and Remaining Challenges. *Chem. Soc. Rev.* **2012**, *41*, 6555–6581.
- (44) Gard, E. E.; Kleeman, M. J.; Gross, D. S.; Hughes, L. S.; Allen, J. O.; Morrical, B. D.; Ferguson, D. P.; Dienes, T.; Ga, M. E.; Johnson, R. J.; Cass, G. R.; Prather, K. A. Direct Observation of Heterogeneous Chemistry in the Atmosphere. *Science* **1998**, *279* (February), 1184–1187.
- (45) Ault, A. P.; Guasco, T. L.; Ryder, O. S.; Baltrusaitis, J.; Cuadra-Rodriguez, L. A.; Collins, D. B.; Ruppel, M. J.; Bertram, T. H.; Prather, K. A.; Grassian, V. H. Inside versus Outside: Ion Redistribution in Nitric Acid Reacted Sea Spray Aerosol Particles as Determined by Single Particle Analysis. *J. Am. Chem. Soc.* **2013**, *135* (39), 14528–14531.
- (46) Donaldson, D. J.; Vaida, V. The Influence of Organic Films at the Air-Aqueous Boundary on Atmospheric Processes. *Chem. Rev.* **2006**, *106* (4), 1445–1461.
- (47) Nishino, N.; Hollingsworth, S. A.; Stern, A. C.; Roeselova, M.; Tobias, D. J.; Finlayson-pitts, B. J. Individual and Mixed Alkyl Self-Assembled. **2014**, 2358–2367.
- (48) Kolb, C. E.; Cox, R. A.; Abbatt, J. P. D.; Ammann, M.; Davis, E. J.; Donaldson, D. J.; Garrett, B. C.; George, C. And Physics An Overview of Current Issues in the Uptake of Atmospheric Trace Gases by Aerosols and Clouds. **2010**, 10561–10605.
- (49) Liu, Y.; P., C. J.; Wang, H.; Laskin, A. Kinetic Study of Heterogeneous Reaction of Deliquesced NaCl Particles with Gaseous HNO₃. *J. Phys. Chem. A* **2007**, *111*, 10026–10043.
- (50) Ault, A. P.; Guasco, T. L.; Baltrusaitis, J.; Ryder, O. S.; Trueblood, J. V.; Collins, D. B.; Ruppel, M. J.; Cuadra-Rodriguez, L. A.; Prather, K. A.; Grassian, V. H. Heterogeneous Reactivity of Nitric Acid with Nascent Sea Spray Aerosol: Large Differences Observed between and within Individual Particles. *J. Phys. Chem. Lett.* **2014**, *5* (15), 2493–2500.
- (51) Estillore, A. D.; Trueblood, J. V.; Grassian, V. H. Atmospheric Chemistry of Bioaerosols: Heterogeneous and Multiphase Reactions with Atmospheric Oxidants and Other Trace Gases. *Chem. Sci.* **2016**.
- (52) George, I. J.; Abbatt, J. P. D. Heterogeneous Oxidation of Atmospheric Aerosol Particles by Gas-Phase Radicals. *Nat. Chem.* **2010**, *2* (9), 713–722.
- (53) Kessler, S. H.; Nah, T.; Daumit, K. E.; Smith, J. D.; Leone, S. R.; Kolb, C. E.; Worsnop, D. R.; Wilson, K. R.; Kroll, J. H. OH-Initiated Heterogeneous Aging of Highly Oxidized Organic Aerosol. *J. Phys. Chem. A* **2012**, *116* (24), 6358–6365.
- (54) George, I. J.; Vlasenko, A.; Slowik, J. G.; Broekhuizen, K.; Abbatt, J. P. D. Heterogeneous Oxidation of Saturated Organic Aerosols by Hydroxyl Radicals: Uptake Kinetics,

- Condensed-Phase Products, and Particle Size Change. *Atmos. Chem. Phys.* **2007**, *7* (16), 4187–4201.
- (55) Molina, M. J.; Ivanov, A. V.; Trakhtenberg, S.; Molina, L. T. Atmospheric Evolution of Organic Aerosol. *Geophys. Res. Lett.* **2004**, *31* (22), 1–5.
- (56) Kroll, J. H.; Donahue, N. M.; Jimenez, J. L.; Kessler, S. H.; Canagaratna, M. R.; Wilson, K. R.; Altieri, K. E.; Mazzoleni, L. R.; Wozniak, A. S.; Bluhm, H.; Mysak, E. R.; Smith, J. D.; Kolb, C. E.; Worsnop, D. R. Carbon Oxidation State as a Metric for Describing the Chemistry of Atmospheric Organic Aerosol. *Nat. Chem.* **2011**, *3* (2), 133–139.
- (57) Kessler, S. H.; Smith, J. D.; Che, D. L.; Worsnop, D. R.; Wilson, K. R.; Kroll, J. H. Chemical Sinks of Organic Aerosol: Kinetics and Products of the Heterogeneous Oxidation of Erythritol and Levoglucosan. *Environ. Sci. Technol.* **2010**, *44* (18), 7005–7010.
- (58) Lim, C. Y.; Browne, E. C.; Sugrue, R. A.; Kroll, J. H. Rapid Heterogeneous Oxidation of Organic Coatings on Submicron Aerosols. *Geophys. Res. Lett.* **2017**, *44* (6), 2949–2957.
- (59) Kroll, J. H.; Smith, J. D.; Che, D. L.; Kessler, S. H.; Worsnop, D. R.; Wilson, K. R. Measurement of Fragmentation and Functionalization Pathways in the Heterogeneous Oxidation of Oxidized Organic Aerosol. *Phys. Chem. Chem. Phys.* **2009**, *11*, 8005–8014.
- (60) Clark, C.; Zika, R. Marine Organic Photochemistry: From the Sea Surface to Marine Aerosols. *Mar. Chem.* **2000**, *5*, 1–33.
- (61) Ciuraru, R.; Fine, L.; Pinxteren, M. Van; D’Anna, B.; Herrmann, H.; George, C. Unravelling New Processes at Interfaces: Photochemical Isoprene Production at the Sea Surface. *Environ. Sci. Technol.* **2015**, *49* (22), 13199–13205.
- (62) Tinel, L.; Rossignol, S.; Bianco, A.; Passananti, M.; Perrier, S.; Wang, X.; Brigante, M.; Donaldson, D. J.; George, C. Mechanistic Insights on the Photosensitized Chemistry of a Fatty Acid at the Air/Water Interface. *Environ. Sci. Technol.* **2016**, *50* (20), 11041–11048.
- (63) Fu, H.; Ciuraru, R.; Dupart, Y.; Passananti, M.; Tinel, L.; Rossignol, S.; Perrier, S.; Donaldson, D. J.; Chen, J.; George, C. Photosensitized Production of Atmospherically Reactive Organic Compounds at the Air/Aqueous Interface. *J. Am. Chem. Soc.* **2015**, *137* (26), 8348–8351.
- (64) Hansell, D.; Carlson, C.; Repeta, D.; Schlitzer, R. Dissolved Organic Matter in the Ocean: A Controversy Stimulates New Insights. *Oceanography* **2009**, *22* (4), 202–211.
- (65) Sharpless, C. M.; Blough, N. V. The Importance of Charge-Transfer Interactions in Determining Chromophoric Dissolved Organic Matter (CDOM) Optical and Photochemical Properties. *Environ. Sci. Process. Impacts* **2014**, *16* (4), 654–671.
- (66) Spataro, F.; Ianniello, A. Sources of Atmospheric Nitrous Acid: State of the Science, Current Research Needs, and Future Prospects. *J. Air Waste Manage. Assoc.* **2014**, *64* (11), 1232–1250.
- (67) Stemmler, K.; Ndour, M.; Elshorbany, Y.; Kleffmann, J.; D’Anna, B.; George, C.; Bonn, B.; Ammann, M. Light Induced Conversion of Nitrogen Dioxide into Nitrous Acid on Submicron Humic Acid Aerosol. *Atmos. Chem. Phys.* **2007**, *7* (16), 4237–4248.
- (68) Quinn, P. K.; Collins, D. B.; Grassian, V. H.; Prather, K. A.; Bates, T. S. Chemistry and

Related Properties of Freshly Emitted Sea Spray Aerosol. *Chem. Rev.* **2015**, *115* (10), 4383–4399.

- (69) Pomeroy, L.; leB. Williams, P.; Azam, F.; Hobbie, J. The Microbial Loop. *Oceanography* **2007**, *20* (2), 28–33.
- (70) Stokes, M. D.; Deane, G. B.; Prather, K.; Bertram, T. H.; Ruppel, M. J.; Ryder, O. S.; Brady, J. M.; Zhao, D. A Marine Aerosol Reference Tank System as a Breaking Wave Analogue for the Production of Foam and Sea-Spray Aerosols. *Atmos. Meas. Tech.* **2013**, *6* (4), 1085–1094.
- (71) Jaeglé, L.; Quinn, P. K. K.; Bates, T. S. S.; Alexander, B.; Lin, J.-T. T. Global Distribution of Sea Salt Aerosols: New Constraints from in Situ and Remote Sensing Observations. *Atmos. Chem. Phys.* **2011**, *11* (2004), 3137–3157.
- (72) Russell, L. M.; Bahadur, R.; Ziemann, P. J. Identifying Organic Aerosol Sources by Comparing Functional Group Composition in Chamber and Atmospheric Particles. **2011**, *108* (9).
- (73) Hase, M.; Scheffelmaier, R.; Hayden, S.; Rivera, D. Quantitative in Situ Attenuated Total Internal Reflection Fourier Transform Infrared Study of the Isotherms of Poly(sodium 4-Styrene Sulfonate) Adsorption to a TiO₂ Surface over a Range of Cetylpyridinium Bromide Monohydrate Concentration. *Langmuir* **2010**, *26* (8), 5534–5543.

Chapter 2 Investigating the Impact of Ocean Biology on the Chemical Composition and Climate-Relevant Properties of SSA Using Single Particle Raman Spectroscopy

2.1 Synopsis

The impacts of sea spray aerosol (SSA) on climate are critically linked to the size and chemical composition of the individual particles that make up the overall SSA population. While the organic fraction of SSA has been characterized from a bulk perspective, a lack of knowledge of remains regarding the chemical composition of single particle SSA, how SSA composition changes with ocean biological activity, and how those changes impact SSA climate relevant properties, such as their ability to serve as ice nucleating (IN) particles. To address these uncertainties, CAICE conducted the Investigation into Marine PArticle Chemistry and Transfer Science (IMPACTS) research intensive during the summer of 2014. The intensive took place at the Scripps Institution of Oceanography and made use of an indoor ocean-atmosphere facility that consisted of a wave flume filled with 3,400 gallons of natural seawater which was spiked with nutrients to generate a phytoplankton bloom. This setup allowed for accurate representation of ocean biological and chemical complexity, as well as the generation of authentic SSA isolated from anthropogenic and terrestrial sources.

During the month-long IMPACTS study which spanned two successive phytoplankton blooms, SSA and seawater properties were analyzed using a suite of off-line and on-line instruments. This chapter describes the role of single particle Raman microspectroscopy in the analysis of SSA during the IMPACTS research intensive. First, I describe efforts to deconvolute the composition of freshly emitted SSA by characterizing the classes of organic compounds and specific molecules within individual SSA particles. Raman analysis showed that the diversity of

molecules within the organic fraction varied between sub and supermicron sized particles, with contributions from fatty acids, free saccharides/amino sugars, polysaccharides, and siliceous material. Using these results, we were able to describe how changes in molecular species prevalent in SSA are connected to changes in seawater biological activity. Throughout the research intensive, significant fluctuations in the distribution of particle types occurred, which were explained with the rise and fall of phytoplankton and heterotrophic bacteria populations within the seawater.

Finally, I present results of single particle Raman analysis of residual ice nucleating particles (INP) collected during the IMPACTS experiment and a prior mesocosm experiment using a Marine Aerosol Reference Tank (MART). Raman spectra of INP showed that two unique marine INP populations exist, composed of dissolved organic carbon INPs comprised of IN-active molecules and particulate organic carbon INPs existing as intact cells or fragments of IN-active microbes. Overall, this chapter provides an important ocean-climate connection by linking water-side chemical transformation, as driven by ocean biology, to SSA particle composition and climate relevant properties.

2.2 Introduction

Sea spray aerosol (SSA) is a major contributor to the total global aerosol mass budget.^{1,2,3} As discussed in Chapter 1, primary SSA is formed at the air-sea interface upon the bursting of air bubbles that are entrained in the water column through the breaking of waves.⁴ As with all aerosols, SSA particles impact climate by directly scattering or absorbing radiation, and indirectly by altering the microphysics of clouds through their ability to serve as CCN and IN. To better determine their climate relevant properties, an improved understanding of SSA chemical and physical characteristics and their controls is needed. Furthermore, to determine the extent to which anthropogenic aerosols perturb the global aerosol budget, a better understanding of the contributions from natural sources is required.

SSA consists of a mixture of inorganic salts, particulate biological components, and organic matter.^{1-3,5} Previous studies have given limited information regarding the organic component of SSA. For example, studies have shown that the organic matter present in submicron SSA particles is dominated by water soluble organic matter, while supermicron SSA organic matter is water soluble.⁵⁻¹¹ Broad particle classifications have also been given, showing that oxygen rich organic fractions of particles contain signatures of saccharides,⁹ carboxylic acids,¹⁰ and alkanes.¹² However, improved understanding of the complex molecular composition of SSA is still needed, specifically at the single-particle level. While past studies have analyzed the chemical properties of SSA using bulk methods, it has been shown that individual particles within the total SSA ensemble differ internally.^{4,13,14} For this reason, single particle measurements of SSA are necessary to attain a clearer understanding of the total aerosol population and its impact on climate.

As the ocean's biological activity is known to alter the chemical composition of SSA, attempts have been made to use simple biological tracers (e.g., chl-a) to predict SSA composition and organic fraction. To date, these attempts have been met with limited success. In some cases, a weak correlation has been found between organic fraction of SSA and chl-a concentrations for monthly and seasonal time scales,^{15,11} while other studies have found no differences in SSA composition with changing chl-a concentration.^{12,16} These conflicting results suggest a gap in the understanding of how ocean biology controls SSA composition. Despite its shortcomings, the chl-a tracer method is still used in several large-scale climate models.^{17,18,6} To improve the accuracy of such models, it is crucial to better understand the link between the molecular composition of SSA and the ocean's biological activity.

As may be expected, the poor understanding of SSA chemical composition has led to deficiencies in the prediction of their climate relevant properties. For example, there is only limited knowledge regarding which SSA behave as ice nucleation particles (INP). INP are quite rare (1 in

10^5 aerosol particles), and yet are critical to several cloud processes (e.g., precipitation, lifetime, optical properties) as they are required for heterogeneous ice nucleation in clouds through immersion freezing of supercooled droplets. While number concentrations of INP associated with SSA are typically low relative to terrestrial sources such as mineral dust,¹⁹ the presence of INPs in remote marine regions is nonetheless important due to the lack of alternative INP sources.²⁰ Furthermore, lab and field studies have suggested that IN capability of SSA is enhanced during periods of high ocean biological activity.^{21,22}

Few studies have attempted to identify the types of SSA particles that contribute to heterogeneous ice nucleation and the mechanisms that control their emission rates from the surface ocean. As such, the chemical identity of the INP remains largely unknown. This lack of understanding of marine INP identity has led to their poor representation in global climate models in remote regions.^{23,24} For this reason, investigations into the types of SSA that behave as efficient INP are needed to aid future efforts to improve numerical models.

To address these and other gaps in SSA knowledge, the Investigation into Marine Particle Chemistry and Transfer Science (IMPACTS) research intensive was conducted during the summer of 2014. The intensive made use of an isolated ocean-atmosphere facility, located at Scripps Institution of Oceanography, which consisted of a wave flume filled with 3,400 gallons of natural seawater that was spiked with nutrients. SSA were tracked throughout the bloom and analyzed with a suite of off-line and on-line instruments. This chapter will focus on the results obtained using single particle Raman spectroscopy to analyze the chemical composition of generated SSA. In Section 2.3, I describe the IMPACTS experiment and the associated experimental methods employed for SSA analysis. Section 2.4 presents the results obtained from Raman spectroscopy to measure the vibrational spectra of individual SSA particles generated via wave breaking throughout the blooms lifetimes. By comparing the spectra of SSA with the spectra of simple model systems,

we were able to go beyond functional group analysis to gain insights into the major classes of organic molecules that constitute SSA. Having accomplished this, we were next able to determine the ways in which ocean biology influenced the types of molecular species found in SSA. Finally, we were also able to link these changes to changes in climate relevant properties (i.e., IN capability).

2.3 Methods

2.3.1 IMPACTS Experiment and Generation of an Indoor Phytoplankton Bloom

The Investigation into Marine PArticle Chemistry and Transfer Science (IMPACTS) research intensive took place from July 3 through August 6, 2014 at the Scripps Institute of Oceanography in La Jolla, CA.²⁵ The goal of the intensive was to better understand the link between ocean biological activity and the chemical composition and climate relevant properties of sea spray aerosols. To this end, a mesocosm experiment was performed using an indoor ocean-atmosphere facility which enabled the replication of ocean seawater conditions representative of typical oceanic phytoplankton blooms and the generation of authentic SSA.

The 40-m long channel was filled with 3,400 gallons of filtered (50 μm mesh) natural seawater obtained from Scripps Pier (La Jolla, CA). To replicate ocean biological activity, the seawater was spiked with *f/2* algae growth medium (Proline, Aquatic Eco-Systems, Apopka, FL) in addition to solutions of sodium metasilicate and 9 μM of sodium phosphate (on 7/25/14). A hydraulic paddle was used to generate breaking waves with bubble distributions similar to those found in the ocean. The aerosols formed upon bubble bursting were sampled at a manifold using both on-line and off-line instruments. A schematic of the ocean-atmosphere facility and the instruments used is shown in Figure 2.1 and in-depth details of the facility can be found in the literature.^{4,25}

2.3.1.1 Bulk seawater measurements and monitoring of biological activity during IMPACTS

A number of metrics were monitored throughout the intensive to determine the biological activity of the seawater, the details of which are explained elsewhere.²⁵ Briefly, bulk chl-a concentrations were measured fluorometrically using a Wetlabs ECO BBFL2 sensor and a Turner AquaFluor handheld unit. Heterotrophic bacteria and viruses were counted via epifluorescence microscopy with SYBR Green-I nucleic acid gel stain (Life Technologies, S-7563). Enzyme activities of lipase, protease, alkaline phosphatase and chitinase were also monitored.

2.3.2 Collection of SSA for Off-Line Analysis

SSA formed upon the breaking of waves within the wave flume were analyzed using a suite of off-line and on-line instruments. Here I focus on results from the use of off-line techniques to monitor the chemical composition of SSA particles, specifically Raman spectroscopy. For off-line spectroscopic analysis, individual SSA particles were collected directly from the wave flume at RH ~68-76% onto quartz coverslips (Ted Pella Inc., part no 26016) using the fourth and sixth stages of a Micro-Orifice Uniform Deposition Impactor (MOUDI, MSP Corp. Model 110) operating at a flow rate of 30 lpm. Stage four of the MOUDI collected particles with aerodynamic diameters between 1.8-3.2 μm , while stage 6 collected particles with diameters between 0.56-1 μm . After collection, samples were sealed with PTFE tape, and then stored at room temperature until analysis.

2.3.3 Generation of Aerosol Standards from Aqueous Solution

Model system aerosol particles were generated for comparison with authentic SSA generated in the wave flume by atomizing (TSI Inc., Model 3076) aqueous solutions (see below) or suspensions of a standard that was prepared in Optima-grade water (Fisher Scientific). Upon exiting the atomizer, aerosols were passed through 2 diffusion dryers (TSI Inc., Model 3062) at a flow rate of 1.5 lpm. The resulting RH of the stream was reduced to <5%. A quartz disc was placed

in the path of the aerosol flow after the diffusion dryers for 2-30 min to impact particles for subsequent Raman analysis.

2.3.4 Chemicals and standards used in the spectroscopic analysis of individual SSA Particles

Sodium chloride ($\geq 99\%$) was purchased from Fisher Scientific. Lipopolysaccharides (LPS) of *Escherichia coli* (E. coli) 0111:B4, galactose (Pharmacopeia Reference Standard), arabinose ($\geq 99\%$), rhamnose (99%), fucose ($\geq 99\%$), arabitol ($\geq 98\%$), mannitol ($\geq 98\%$), sucrose ($\geq 99\%$), dodecanoic acid ($\geq 98\%$), tetradecanoic acid ($\geq 99\%$), hexadecanoic acid ($\geq 99\%$), octadecanoic acid ($\geq 99.5\%$), pentanoic acid ($\geq 99\%$), hexanoic acid ($\geq 99.5\%$), heptanoic acid ($\geq 97\%$), octanoic acid ($\geq 98\%$), nonanoic acid ($\geq 97\%$), decanoic acid ($\geq 98\%$) and 1-docosanol (98%) were purchased from Sigma-Aldrich. Glucose (99%), N-acetylneuraminic (sialic) acid (97%), glucosamine (98%), 1hexadecanol (98%) were purchased from Alfa Aesar. 1,2-dipalmitoylsn-glycero-3-phosphocholine (DPPC) and 1,2dihexadecanoyl-sn-glycero-3-phosphate (sodium salt) (DPPA) were purchased from Avanti Polar Lipids. All chemicals were used without further purification. Polydimethylsiloxane solution was purchased from Rain-X (ITW Global Brands, Houston, TX, USA). PRO-REEF©Sea Salt was purchased from Tropic Marin (Wartenberg, Germany).

2.3.5 Raman Spectra Collection

Raman spectroscopy of both individual lab-generated aerosol model systems and wave flume authentic SSA particles was performed using a LabRam HR Evolution Raman spectrometer (Horiba) that was equipped with an Olympus BX41 optical microscope with 100X magnification lens. Raman spectra were collected by taking the average of two 5-10 s exposures in the range of 100-4000 cm^{-1} and were generated using a 532 nm laser.

2.3.6 Compound Identification in SSA

For quantitative comparison of the spectra from SSA with model systems, χ^2 errors between two spectra were calculated. The χ^2 error is defined as the square of the difference between the

spectrum of the SSA and the spectrum of the standard at a particular wavenumber, summed over a chosen range of wavenumbers, and divided by the number of data points:

$$\chi^2 = \frac{\sum_{v_1}^{v_2} (SSA - Standard)^2}{N} \quad (\text{Eq2.1})$$

The spectral region between 100 and 550 cm^{-1} was excluded in the calculation to avoid discrepancies associated with quartz substrate peak at 400 cm^{-1} .

2.3.7 Analysis of Chemical Composition of IN Particles

To determine which particles served most effectively as INP, a Continuous Flow Diffusion Chamber (CFDC) was used to measure number concentrations of INPs associated with SSA from the MART and IMPACTS blooms.¹⁹ Briefly, dry particles entered an ice thermal diffusion chamber that was set to expose the aerosol to supersaturation RH, driving droplet activation and ice nucleation via condensation and immersion freezing. Number concentrations of activated ice crystals were then counted using an optical particle counter, where ice crystals were determined based on their larger sizes ($>4 \mu\text{m}$ geometric diameter) relative to liquid cloud droplets. Resulting ice crystals were then collected for off-line analysis using a single jet impactor (2.9 μm , 50% aerodynamic cutoff diameter) placed at the base of the CFDC.

To allow for direct measurement of the composition of molecular species found in SSA that nucleated ice following condensation of droplets and immersion freezing at $-30 \text{ }^\circ\text{C}$ (aerodynamic particle diameter, $D < 1.5 \mu\text{m}$), ice crystal residuals (i.e., evaporated ice crystals) collected during the IMPACTS experiment and an additional MART mesocosm experiment from 6-27 January 2014 were analyzed using Raman spectroscopy. Raman analysis was conducted on ICRs with diameter $\sim 1 \mu\text{m}$ collected during days 20 and 21 of the January MART experiment and days 26 and 28 of the IMPACTS experiment. These days were chosen as they followed a period of elevated number concentrations of INPs active between -25 and $-15 \text{ }^\circ\text{C}$.²⁶

2.4 Results

2.4.1 Identifying the Molecular Diversity of SSA

As explained above, SSA particles generated during the IMPACTS mesocosm experiment were analyzed using Raman microspectroscopy and compared with the spectra of more than 25 model systems to identify their molecular composition. Analysis revealed that SSA particles collected from the wave flume could be divided into two broad categories. The first category did not exhibit any Raman spectral signature associated with organic molecules and was thereby assigned as being composed of mainly sea salt (SS) (below 500 cm^{-1} , all spectral signals were attributed to the quartz substrate). The second category exhibited Raman signatures associated with C-H vibrations, indicating a mixture of organic material with sea salt.

Within this second category, five main particle types were identified as shown in Figure 2.2. The types include (1) long-chain saturated fatty acids ($\text{C}_{12}\text{-C}_{18}$), (2) short-chain saturated fatty acids ($\text{C}_5\text{-C}_{10}$), (3) saccharides (including oligosaccharides and polysaccharides), (4) mono- and disaccharides, which we refer to as free saccharides and amino sugars that contain hydroxyl groups that are substituted with amine, amide, carboxylate, sulfate and other functional groups, and (5) siliceous material that originates from biosilica structures such as exoskeletons or frustules. Additionally, a small fraction (1-27% of submicron and 7-23% of supermicron) of particles were either highly fluorescent or pyrolyzed during analysis and therefore were unable to be categorized.

An in-depth analysis of the spectra of each particle type is now presented in comparison to the spectra of relevant model systems. Figures 2.3-2.8 show the comparison of all model systems to each type of SSA spectrum observed. As explained above, sodium chloride has no first order vibrational transitions in the $100\text{-}4000\text{ cm}^{-1}$ range. The spectrum classified as chloride salts (Figure 2.2A) is therefore assigned based on the lack of peaks in this region. For particles categorized as short chain fatty acids in Figure 2.2B, there are multiple overlapping peaks in the C-H stretching

region, leading to a broad characteristic feature between 2850 and 2950 cm^{-1} . These peaks are assigned the CH_2 symmetric stretching (2853 cm^{-1}), CH_2 asymmetric stretching (2904 cm^{-1}), and CH_3 symmetric stretching (2927 cm^{-1}). In addition, the spectra also show a broad peak at 1068 cm^{-1} due to C-C stretching, as well as additional peaks at 1303 cm^{-1} and 1444 cm^{-1} due to CH_2 twisting and bending modes, respectively.^{27,28-31} Comparison of this particle type's spectrum with those of authentic standards of short chain fatty acids is shown in Figure 2.3A. Spectra of pentanoic (C_5), hexanoic (C_6), heptanoic (C_7), octanoic (C_8), nonanoic (C_9) and decanoic (C_{10}) acids also feature broad peaks in the CH stretching region. The SSA spectrum in Figure 2.2B has the best overlap with spectra of nonanoic acid (C_9), as indicated by the lowest χ^2 error. This result is consistent with the observation of nonanoic acid (C_9) during analysis of SSA by high resolution mass spectrometry.³²

SSA categorized as long chain fatty acids (Figure 2.2C) have prominent peaks in the C-H stretching region at 2846 cm^{-1} and 2880 cm^{-1} , corresponding to the symmetric and asymmetric stretches of the CH_2 group, respectively. The fingerprint region from 1050-1500 cm^{-1} also shows lower intensity peaks. These modes are associated with the vibration of CH_2 groups (i.e., C-C stretching at 1062 cm^{-1} and 1129 cm^{-1}), CH_2 twisting (1295 cm^{-1}) and CH_2 bending (1439 cm^{-1} and 1461 cm^{-1}).^{27-31,33} This spectrum was compared with the spectra of authentic standards of saturated fatty acids with even-numbered carbon chain lengths between 12 and 18, fatty alcohols with carbon chain lengths between 16 and 22, and with two different species of phospholipids: 1,2-dipalmitoyl-sn-glycero-3-phosphate (DPPA) and 1,2-dipalmitoyl-sn-glycero-3-phosphocholine (DPPC)(Figure 2.4A). The spectra of standard acids, alcohols, and phospholipids are very similar. Comparison using χ^2 errors (Figure 2.4B) shows a good match between spectra of SSA and the various fatty acid standards. High resolution mass spectrometry of SSA further supported the presence of long-chain fatty acids.³² These results are in agreement with previous studies that found SSA over the Pacific Ocean to contain long chain organics.³⁴

The SSA spectrum categorized as free monosaccharides (Figure 2.2D) features four peaks in the CH stretching region (2915, 2936, 2985, 2998 cm^{-1}), a large peak at 3408 in the OH, stretching region, a peak from the stretching vibration of the C-O bond at 1097 cm^{-1} , bending deformations of a COH group at 867 cm^{-1} , vibration of CH_2 and CH_2OH groups (1310, 1363, 1428, 1452, 1475 cm^{-1}) as well as the vibration of an amide group (amide I band) at 1640 cm^{-1} .³⁵⁻³⁸ The peak at 3275 cm^{-1} may also be due to the overtone of the amide I band. The spectrum from Figure 2.2D has been compared with the spectrum of the aged LPS (aged by storing quartz discs that contained aqueous LPS aerosols for 1 month at 20°C and 17-20% RH) as well as spectra obtained from the analysis of free saccharides representative of marine biology (Figure 2.5A).^{9,10,39-42} Most of the model systems and aged LPS have similar peaks in the C-H stretching region (2800-3000 cm^{-1}). However, the relative intensities vary between the free monosaccharide standards and the SSA spectra, resulting in negative χ^2 values. The best fit is observed between the spectra of SSA and that of aged LPS, despite differences in relative intensities of the ring (1000-1100 cm^{-1}) and CH (2900-3000 cm^{-1}) stretching vibrations.

Comparisons between the other free saccharide standards show similar discrepancies. Additionally, the OH stretch vibration in SSA is higher and broader than in the free saccharide standards. This could be due to water within the SSA particles that gives an overlap of OH stretching vibration of water and structural OH vibration of the molecule. Peaks at 1009 cm^{-1} and 1037 cm^{-1} in SSA that are not present in the spectra of model saccharides, resulting in positive χ^2 values in that region, are associated with sulfates (indicated in Figure 2.5B), with 1009 cm^{-1} corresponding to SO_4^{2-} and 1037 cm^{-1} to HSO_4^- symmetric stretches, respectively.^{43,44} The hydroxyl groups of saccharides can be substituted with sulfate groups. Better overlap of the SSA shown in Figure 2.2D can be achieved by mixing representative free saccharides. A mixture (denoted in Figures 2.5A,B as “Mix of Saccharides”) consisting of 40% fructose, 40% sucrose, 15% arabitol and 10% glucose (mixed computationally) gives the lowest χ^2 error and better overlaps with spectra

of SSA shown in Figure 2.2D. A recent study of SSA collected over the Antarctic identified a similar spectrum as belonging to the simple amino acid magnesium alanine.⁴⁵ Based on our analysis and taking into account results from recent literature, we posit the SSA shown in Figure 1D can be associated with aged LPS or with a mixture of free saccharides/amino sugars.

The SSA spectrum categorized as siliceous material (Figure 2.2E) has a peak at 791 cm^{-1} corresponding to a Si-C asymmetric stretching mode. Additional peaks at 862, 1260, and 1408 cm^{-1} correspond to rocking as well as symmetric and asymmetric bending of CH_3 groups, respectively.⁴⁶ This spectrum has been compared to the spectrum of a diatom collected from a marine biofilm (siliceous material), as well as the spectrum of a hydrophobic coating containing polydimethylsiloxane (PDMS) as a main component (Figure 2.6A). All three spectra (of SSA, diatom siliceous material and PDMS) exhibit two large peaks at 2906 and 2967 cm^{-1} . The relative intensities for these two Raman modes are slightly different between the spectra, resulting in a positive χ^2 error at 2906 cm^{-1} (Fig. 2.6B). The peaks in the 550-1500 cm^{-1} region overlap well, leading to a subtraction spectrum close to that of quartz (quartz signature is present due to a low signal of a diatom). Diatoms are known to have rigid cell walls (frustules) composed of amorphous silica (SiO_2) and various polysaccharides which is released upon cell lysis.^{47,48}

The SSA spectrum categorized as polysaccharides (Figure 2.2F) features skeletal C-C, C-O and stretching C-C-O bands at 991 and 1044 cm^{-1} , CH_2 bending vibration that typically appears at 1459 cm^{-1} in lipids, a peak at 1642 cm^{-1} that can be either C=O stretching in carbohydrates or C=C stretching vibration of unsaturated fatty acid chains and a broad peak at 2929 cm^{-1} identified as the C-H stretching modes of -CH-, methylene (- CH_2 -) and terminal methyl (CH_3) groups of fatty acid chains.^{49,50} This spectrum obtained from SSA was compared with the spectrum of commercially available standards representative of cellular polysaccharides: lipopolysaccharide (LPS) from *E. coli*, laminarin, inulin, sodium alginate and peptidoglycan (Figure 2.7A). For a

quantitative comparison of the spectra from SSA with the spectra obtained from the standards of cellular polysaccharides, χ^2 errors between two spectra were determined for the 550–4000 cm^{-1} spectral range (see Figure 2.7B).

As can be seen in the χ^2 errors shown in Figure 2.7B, the spectra of *E. coli* LPS features similarly shaped broad peak in C-H stretching region that is only slightly shifted from that of the SSA spectrum, resulting in a slight deviation in the subtraction spectrum around the baseline. Low χ^2 error (~ 0.01 for spectra normalized at 1) indicates a good match between the spectra of SSA and LPS of *E. coli*. Figure 2.7B also shows a good fit between the spectra of SSA and sodium alginate. It is well known that diatoms exude adhesive polymers similar to sodium alginate in order to adhere to surfaces that are polysaccharides cross-linked via O-glycosidic sugar-protein linkages into large proteoglycan assemblages.⁵¹ Therefore, it can be proposed that diatoms exude adhesive polysaccharide polymers (extracellular polymeric substances, EPS) to adhere to the walls of the wave channel, and are then transferred to the water and then eventually to the aerosol phase. In the mesocosm experiment described in this paper, the walls of the wave channel are the most important surfaces. In the open ocean, micelles, gels and colloids formed at high concentrations can provide adsorption surfaces for other dissolved organic matter.⁵² Due to the similarities between the spectra of the cellular polysaccharide standards, it is difficult to explicitly indicate the specific polysaccharide species present in the SSA. However, dissimilarities exist between the spectra of known polysaccharides and those of a mixture of free saccharides (Figure 2.5A).

2.4.2 Connection Between Biological Activity and SSA Composition

Having identified the molecular composition of SSA produced during the IMPACTS experiment, the next goal was to analyze time and size-dependent changes to SSA composition and connect them to the biological activity of the seawater. Throughout the 29-day experiment, two successive, yet distinct, phytoplankton blooms occurred in the wave channel, as evidenced by chl-

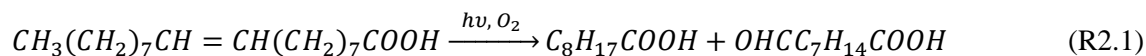
a, bacteria, and ectoenzyme activities (Figure 2.8C).²⁵ The molecular diversity of SSA particles was found to change in response to the biological activity; specifically, in response to the phytoplankton (autotrophs) and heterotrophic bacteria. Figure 2.8 shows the changes with time in the distribution of major organic classes as determined by single-particle Raman analysis of SSA collected from the wave flume as well as concentrations of chl-a, heterotrophic bacteria, and online measurements of the size-resolved bulk chemical composition by AMS.

Prior to the first bloom, only 32% of submicron particles contained long-chain fatty acid Raman signatures. Smaller fractions of other particle types included signatures from polysaccharides (14%), siliceous material (13%), and a mixture of free saccharides and short chain fatty acids (17%). During the first bloom (i.e., chl-a maximum, ~Day 13), the fraction of submicron particles featuring long-chain fatty acid Raman signatures increased significantly (up to 75%). While Raman analysis showed that the relative fraction of these aliphatic-rich particles enhanced during both of the two blooms (67% during bloom two), AMS indicated a rapid decrease in the relative mass fraction of the aliphatic-rich species as defined by mass spectra dominated by hydrocarbon peaks from 0.64 to 0.22 over a 1 day period at the end of the first bloom.²⁵ The unique trends between individual and bulk SSA chemical signatures points towards the fact that normalized organic mass fraction of bulk SSA are not reflected in the external mixing state of individual SSA. This result could also suggest that the SSA particle-size range responsible for the decrease in aliphatic-rich components in bulk submicron SSA (i.e., particles with aerodynamic diameters between 0.06 and 1.5 μm at RH of 80%) could differ from those evaluated using Raman spectroscopy (between 0.56 and 1.0 μm at 80% RH). Raman analysis of SSA during the second bloom revealed a trend similar to the first bloom, in that submicron particles featuring long-chain fatty acids increased significantly and then rapidly decreased as chl-a dropped. However, for bulk submicron SSA analyzed with AMS, the aliphatic rich signal did not change significantly (0.14 and 0.16).²⁵

Supermicron SSA were found to have differences between the first and second blooms. During the first bloom, the distribution between classes of oxygen-rich species changed only slightly, with only a small fraction of aliphatic rich compounds and larger fractions of free saccharides/amino sugars and polysaccharides. The second bloom however, featured supermicron SSA particles dominated largely by polysaccharides but with smaller fractions of other oxygen-rich particle types such as free saccharides/amino sugars and siliceous material.

Free fatty acids have been observed to be a major fraction of the organic compounds present in the ocean, and are produced by the heterotrophic breakdown of lipid-containing cellular components of microorganisms such as phospholipids, glycolipids, and triacylglycerides.^{53–57} Relative to other classes of molecules identified in this work, long chain fatty acids exhibited significantly increased surface activity, leading to their enrichment in the sea-surface microlayer, which likely allowed for their efficient transfer into film drops during the bubble-bursting process. This physicochemical behavior explains the consistently significant fraction of submicron SSA particles that feature long-chain fatty acid Raman signatures.

Similarly, short chain fatty acids with even carbon numbers (C₈, C₁₀) have also been observed to occur from biological sources.⁵⁵ Nonanoic acid has been suggested to occur mainly due to the oxidation of C₁₈ unsaturated fatty acids.⁵⁸



The siliceous material observed in SSA particles is suggested here to result from the presence of diatoms, which are known to be one of the largest groups of silicifying organisms. Diatoms take up silica and bioprocess it into useful biosilica structures such as exoskeletons or frustules.⁴⁸ Upon cell lysis, the frustule releases siliceous material into the water column, which is either transferred

into SSA, further transformed through heterotrophic processing, or sinks to the ocean floor as diatomaceous material.

Saccharides have been previously observed in the SML and marine aerosols, and are thought to exist in polymeric or oligomeric form^{10,39-41} as cellular polysaccharides (e.g., laminarin, chrysolaminarin, chitin, lipopolysaccharides LPS, alginic acid, dextrose) or extracellular polymeric substances (EPS).^{7,59,40,47,60} While cellular polysaccharides have a more defined structure, the structure of EPS is seen as either a polysaccharide or a glycoconjugate (viscous or gelatinous mixture of saccharides) and is therefore difficult to identify explicitly.^{47,61} The enrichment of such species in supermicron particles is due to their enhanced water-solubility, leading to their transfer into SSA via jet drop formation.

Figure 2.9 shows a comprehensive and dynamic pathway linking ocean biology and SSA particle composition and explains the differences in SSA composition between the two blooms. Upon the death of phytoplankton, particulate forms of lipids, polysaccharides, and siliceous material are released into the bulk seawater. Enzyme digestions from autotrophs release fatty acids from higher order lipids, while generating smaller fragments of cellular poly- and oligosaccharides and amino sugars. Together with the surface-active properties of the various molecules, these factors explain the findings from Raman and AMS analysis during the first bloom, in which submicron aerosol are dominated by surf-active, aliphatic rich organic species, while supermicron SSA is dominated by more oxidized, water-soluble saccharides and amino sugars representative of phytoplankton.

The changes in aerosol composition during the second bloom can be explained by the increase in heterotrophic bacteria, as seen in Figure 2.8C. First, the increase in bacteria helps to explain the increase in polysaccharides in supermicron SSA, as gram-negative bacteria are known to contain cell wall lipopolysaccharides. The release of bacterial enzymes that are capable of

digesting phytoplankton and bacterial components into smaller oligosaccharide fragments was likely also a contributing factor in the increase of saccharides in supermicron SSA.⁶²⁻⁶⁶ While Raman analysis revealed long-chain fatty acid contributions remained elevated, the relative aliphatic-rich mass fraction as determined by AMS remained low. The lack of FA enrichment during the second bloom seen by AMS is explained by the increase in bacterial enzymes that are also capable of hydrolyzing aliphatic, surface-active fatty acids into more water-soluble components, leading to a decrease in their efficiency of transfer to the submicron SSA by film drops. Indeed, there was an increase in lipase, a bacterial enzyme, during the second bloom. As described above, the discrepancy between Raman and AMS detection of aliphatic-rich species during the second bloom highlights the possibility that normalized organic mass fraction of bulk SSA are not reflected in the external mixing state of individual SSA.

2.4.3 Connection to Climate: IN Properties of SSA

The goal of this experiment was to see how ocean biological activity changes SSA chemical composition, and how that subsequently leads to changes in the climate relevant properties of SSA. To this end, we monitored the number and composition of INPs associated with SSA formed in the wave flume during the IMPACTS experiment and during a separate mesocosm experiment using a MART. The number concentration of activated ice crystals was determined by sending SSA to a CFDC.²⁶ To identify the molecular species found within SSA particles responsible for ice nucleation, ice crystal residuals (ICRs) collected on a single jet impactor at the base of the CFDC were analyzed using Raman spectroscopy.

ICRs of emitted IN that originated from the wave flume were collected on Day 26 of the IMPACTS experiment, which was the conclusion of a peak in INPs observed at temperatures between -25 and -15 °C from days 17-23 (Figure 2.10). ICRs of IN emitted during the separate mesocosm experiment using a MART were collected on Days 20 and 21 following a period of

elevated INP number concentrations between -25 and -15 °C on Days 15-18 (Figure 2.11). Raman analysis of the IMPACTS ICRs revealed over 40% of ICRs (N=165) contained siliceous material, indicative of diatomaceous cellular material (Figure 2.10A). Additional ICRs were collected from a MART that ran coincidentally during the IMPACTS study and contained fresh seawater and no additional nutrients. The siliceous material in the fresh-water MART ICRs were similar to those from the IMPACTS wave flume. Additionally, polysaccharides, as well as long and short chain fatty acids were observed. Analysis of INEs with diameters $>2 \mu\text{m}$ collected from bulk seawater from the wave flume revealed that 80% were from frustules, further indicating that IN active microbial material (e.g., diatoms) are an important source of INPs. Raman analysis of the separate MART mesocosm ICRs showed that over 90% (N = 50) of the ICR spectral signatures contained long chain fatty acids (Figure 2.10B). This contrasted with the composition of the total submicron aerosol particle population on Day 18 which was dominated by polysaccharides and long and short chain fatty acids (Figure 2.10B), further highlighting the rarity of such INP.

In summary, the results obtained with Raman spectroscopy in conjunction with results from other methods including scanning electron microscopy energy dispersive x-ray (SEM-EDX), and aerosol time-of-flight mass spectrometry (ATOFMS),²⁶ showed that marine INPs consist of two distinct populations: 1) dissolved organic carbon INPs composed of composed of IN-active molecules such as long-chain fatty acids and 2) particulate organic carbon INPs attributed to intact cells or fragments from microbes. These results aid in furthering our knowledge of the chemical identities of marine INPs as well as the mechanisms controlling their transfer from bulk water to SML to aerosol.

2.5 Conclusions

This chapter describes the contribution of Raman spectroscopy of single-particle SSA collected during the 2014 IMPACTS experiment to three manuscripts that were conducted to

determine the molecular species found within SSA, unravel the complex ways in which ocean biology alters the SSA chemical composition, and investigate how these changes are manifest in the climate relevant properties of SSA, such as their ability to serve as INP.

Analysis found that SSA particles in the submicron are mainly long chain fatty acids, from phytoplankton. Supermicron consisted of more oxygenated species, including free saccharides/amino sugars and polysaccharides. Analysis of the changing abundances of molecular species with time and particle size revealed the link between ocean biological activity and the organic fraction of SSA. Specifically, we presented a comprehensive way of explaining how phytoplankton and bacteria in the seawater interact to produce the observed species. Finally, the understanding of the mechanisms for the production of IN material and the subsequent release of INPs from the ocean as well as their chemical composition was improved. With this improved understanding of SSA, the door is opened to focus more directly on specific aging mechanisms of SSA containing relevant molecular species. This is the focus of the following chapters.

2.6 Acknowledgements

The author would like to thank all CAICE collaborators involved during the 2014 IMPACTS experiment. The studies in this chapter were funded by the Center for Aerosol Impacts on the Chemistry of the Environment (CAICE), an NSF-funded Center for Chemical Innovation (CHE-1305427).

Chapter 2 is reproduced with permission from the American Chemical Society: Wang, X., Sultana, C. M., Trueblood, J. V., Hill, T. C. J., Malfatti, F., Lee, C., Laskina, O., Moore, K. A., Beall, C. M., McCluskey, C. S., Cornwell, G. C., Zhou, Y., Cox, J. L., Pendergraft, M. A., Santander, M. V., Bertram, T. H., Cappa, C. D., Azam, F., DeMott, P. J., Grassian, V. H., Prather, K. A. Microbial Control of Sea Spray Aerosol Composition: A Tale of Two Blooms, ACS Central

Science, 1 (3), 124-131, 2015. The dissertation author was an investigator and co-author of this paper.

Cochran, R. E., Laskina, O., Trueblood, J. V., Estillore, A. D., Morris, H. S., Jayarathne, T., Sultana, C. M., Lee, C., Lin, P., Laskin, J., Laskin, A., Dowling, J. A., Qin, Z., Cappa, C. D. Bertram, T. H., Tivanski, A. V., Stone, E. A., Prather, K. A., Grassian, V. H. Molecular Diversity of Sea Spray Aerosol Particles: Impact of Ocean Biology on Particle Composition and Hygroscopicity, *Chem*, 2 (5), 655-667, 2017. The dissertation author was an investigator and co-author of this paper.

McCluskey, C. S., Hill, T. C. J., Sultana, C. M., Laskina, O., Trueblood, J. V., Santander, M. V., Beall, C. M., Michaud, J. M., Kreidenweis, S. M., Prather, K. A., Grassian, V. H., DeMott, P. J. A Mesocosm Double Feature: Insights into the Chemical Make-up of Marine Ice Nucleating Particles, *Journal of the Atmospheric Sciences*, 75 (7), 2405-2423, 2018. The dissertation author was an investigator and co-author of this paper.

2.7 Figures

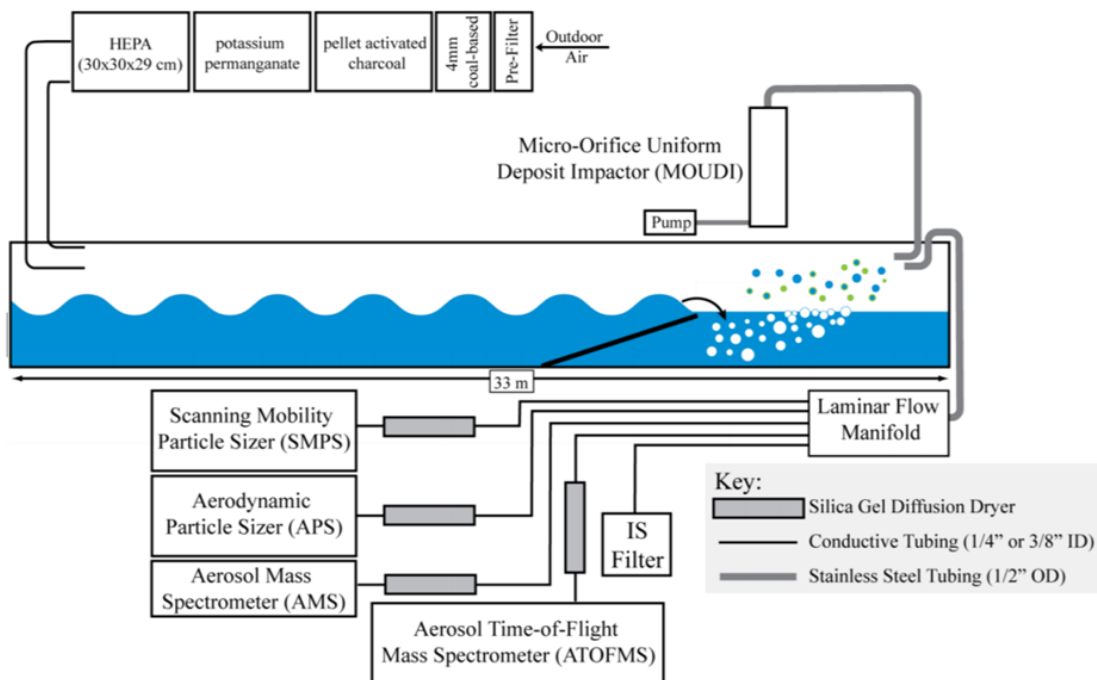


Figure 2.1: Experimental setup during the IMPACTS research intensive. Image adapted from Collins, D. B. B.; Zhao, D. F. F.; Ruppel, M. J. J.; Laskina, O.; Grandquist, J. R. R.; Modini, R. L. L.; Stokes, M. D. D.; Russell, L. M.; Bertram, T. H.; Grassian, V. H.; Deane, G. B.; Prather, K. A. Direct Aerosol Chemical Composition Measurements to Evaluate the Physicochemical Differences between Controlled Sea Spray Aerosol. *Atmos. Meas. Tech.* **2014**, 7 (11), 3667–3683.

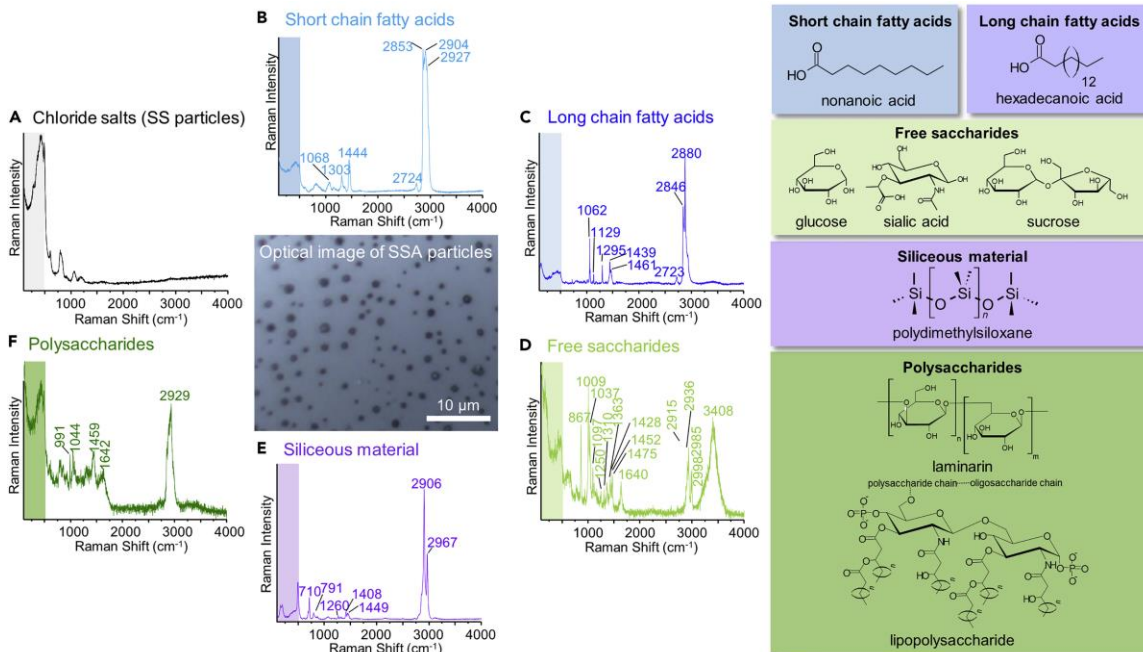


Figure 2.2: Six types of Raman signatures observed for 560-1000 nm and 1.8-3.2 μm sized SSA particles collected on a quartz substrate during the month-long IMPACTS mesocosm experiment. Organic components include B) short chain fatty acids, C) long chain fatty acids, D) free saccharides/amino sugars, E) siliceous material, and F) polysaccharides. Each spectrum was collected from a single particle within the SSA ensemble, averaging two separate exposures at 5-10 s each and recorded in the region 100-4000 cm^{-1} . The spectral region below 500 cm^{-1} (shaded) contains significant contributions from background spectral features that are attributes to either NaCl or quartz substrates and were not considered when determining the identity of the class of organic molecules.

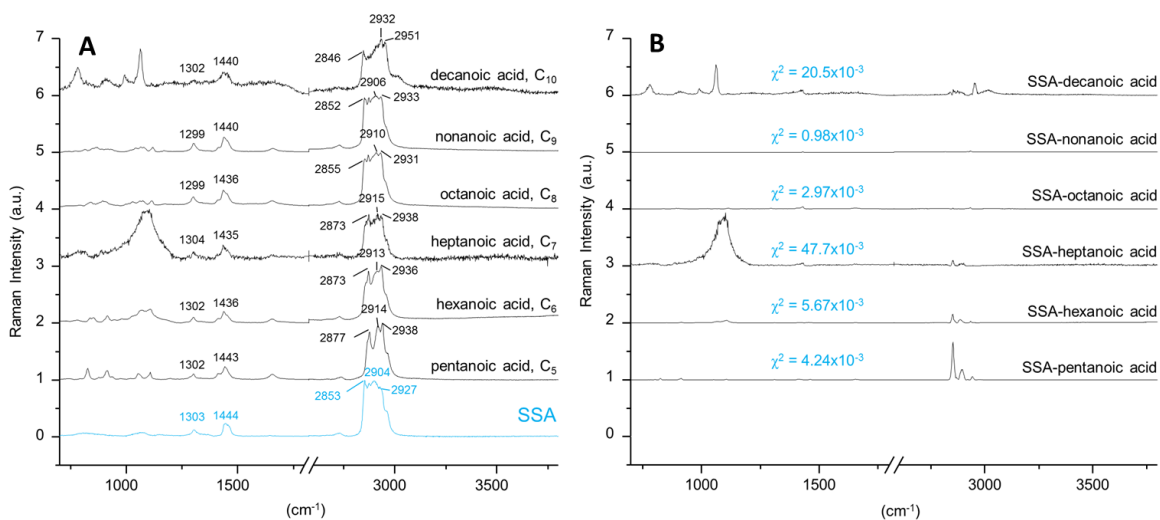


Figure 2.3: A) Raman spectra obtained for standards of short-chain fatty acids. Spectra obtained from a single SSA particle collected during the mesocosm that is proposed to contain a significant fraction of short-chain saturated fatty acids is shown for reference. B) χ^2 plots showing the statistical relationship between each standard spectra of short-chain saturated fatty acids to that of a representative SSA particle collected during the mesocosm.

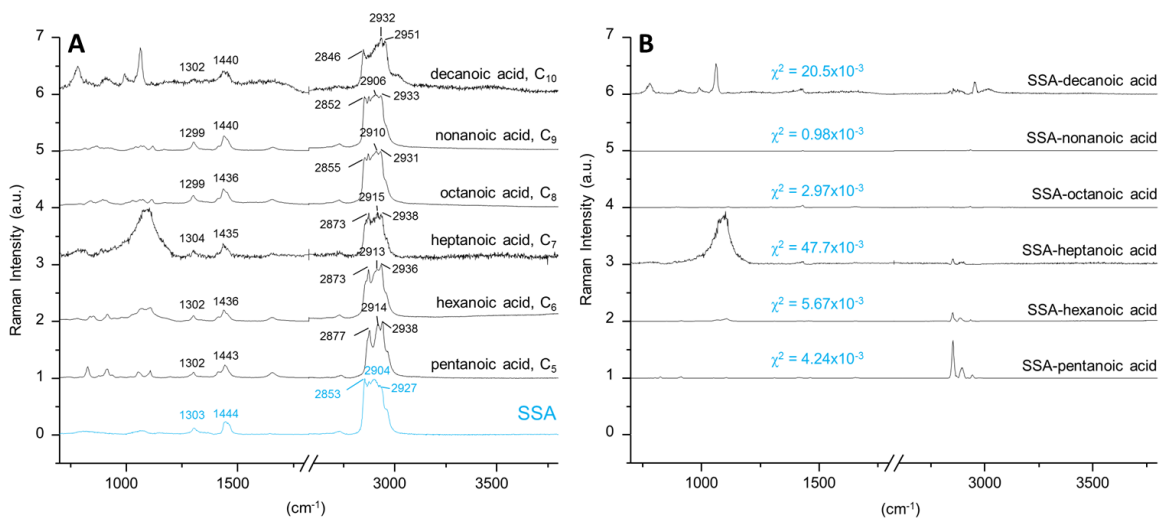


Figure 2.4: A) Raman spectra obtained for standards of long-chain saturated and unsaturated fatty acids, linear alkyl alcohols as well as phospholipids containing hexadecanoic acid ester chains (1,2-dipalmitoyl-sn-glycero-3-phosphatidic acid, DDPA; 1,2-dipalmitoyl-sn-glycero-3-phosphocholine, DPPC). Spectra obtained from a single SSA particle collected during the mesocosm that is proposed to contain a significant fraction of long-chain saturated fatty acids is shown for reference. B) χ^2 plots showing the statistical relationship between each standard spectra of long-chain saturated fatty acids and alcohols and phospholipids to that of the single SSA particle collected during the mesocosm.

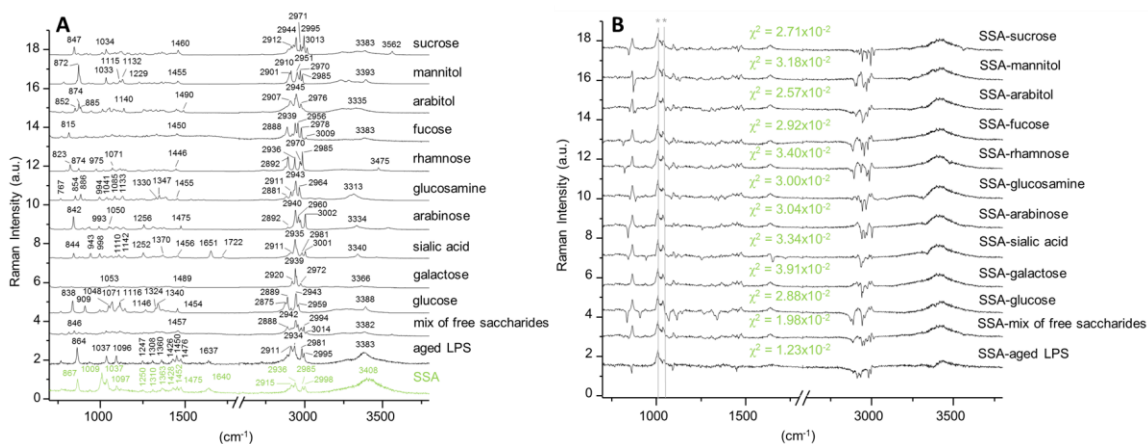


Figure 2.5: A) Raman spectra obtained for standards of free saccharides and amino sugars. Spectra obtained from a single SSA particle collected during the mesocosm that is proposed to contain a significant fraction of saccharides is shown for reference. The mixture of saccharides (denoted as “Mix of Saccharides”) consisted of 40% fucose, 40% sucrose, 15% arabinol and 5% glucose (mixed computationally). B) χ^2 plots showing the statistical relationship between each standard spectra of free saccharides to that of the single SSA particle collected during the mesocosm (shown in Figure S6 and Figure 1d). The mixture of saccharides (denoted as “Mix of Saccharides”) consisted of 40% fructose, 40% sucrose, 15% arabinol and 10% glucose (mixed computationally). Signatures labelled with “*” are due to sulfate signatures present in the SSA spectra.

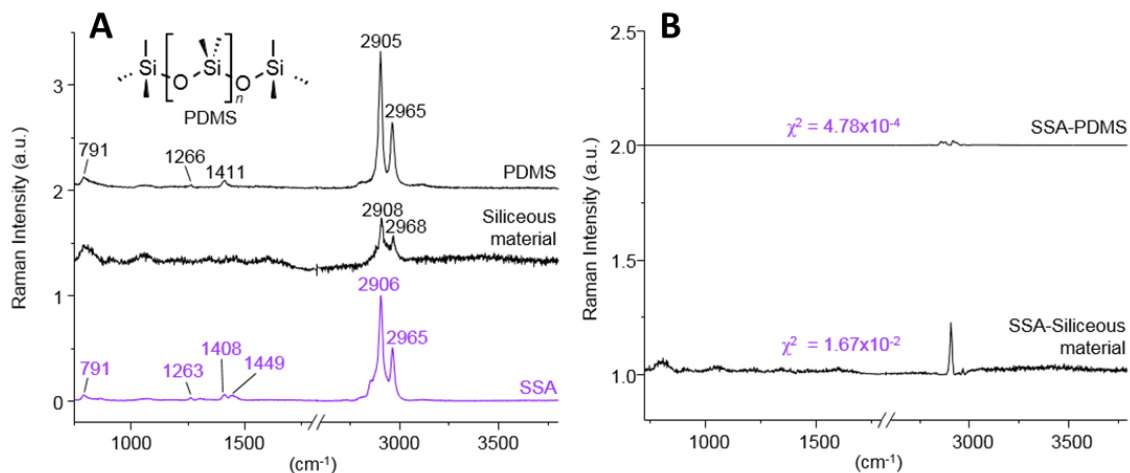


Figure 2.6: A) Comparison of Raman spectra obtained from the analysis of biofilm collected from the mesocosm and that for a single particle from SSA collected during the mesocosm with Raman spectra resembling that of siliceous material (Figure 2.2e). B) χ^2 plot showing the statistical relationship between the standard spectra of the biofilm and that of the single SSA particle collected during the mesocosm.

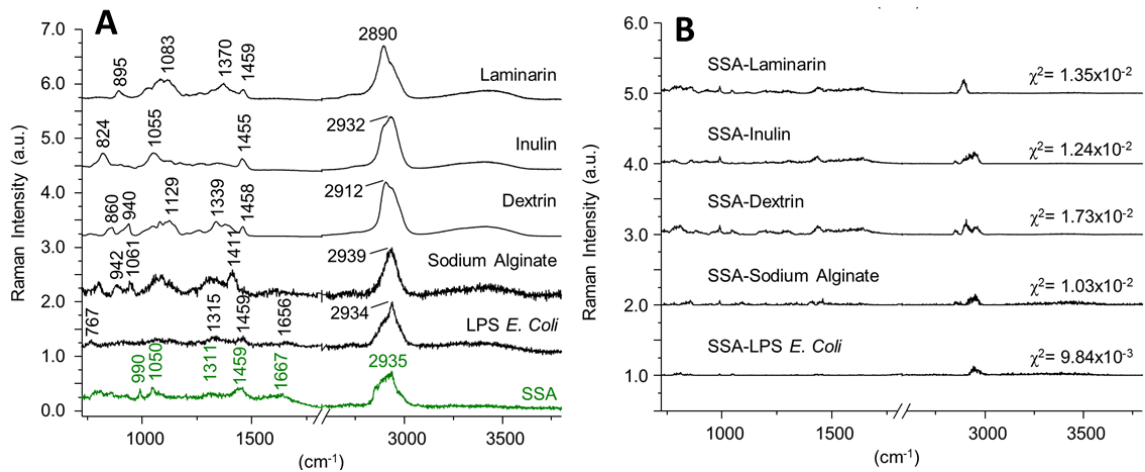


Figure 2.7: A) Comparison of Raman spectra obtained from the analysis of a standard of lipopolysaccharide (LPS; from *Escherichia coli* bacteria) and a single particle from SSA collected during the mesocosm with Raman spectra resembling that of polysaccharides (Figure 2.2F). B) χ^2 plot showing the statistical relationship between the standard spectra of LPS and sodium alginate to that of the single SSA particle collected during the mesocosm.

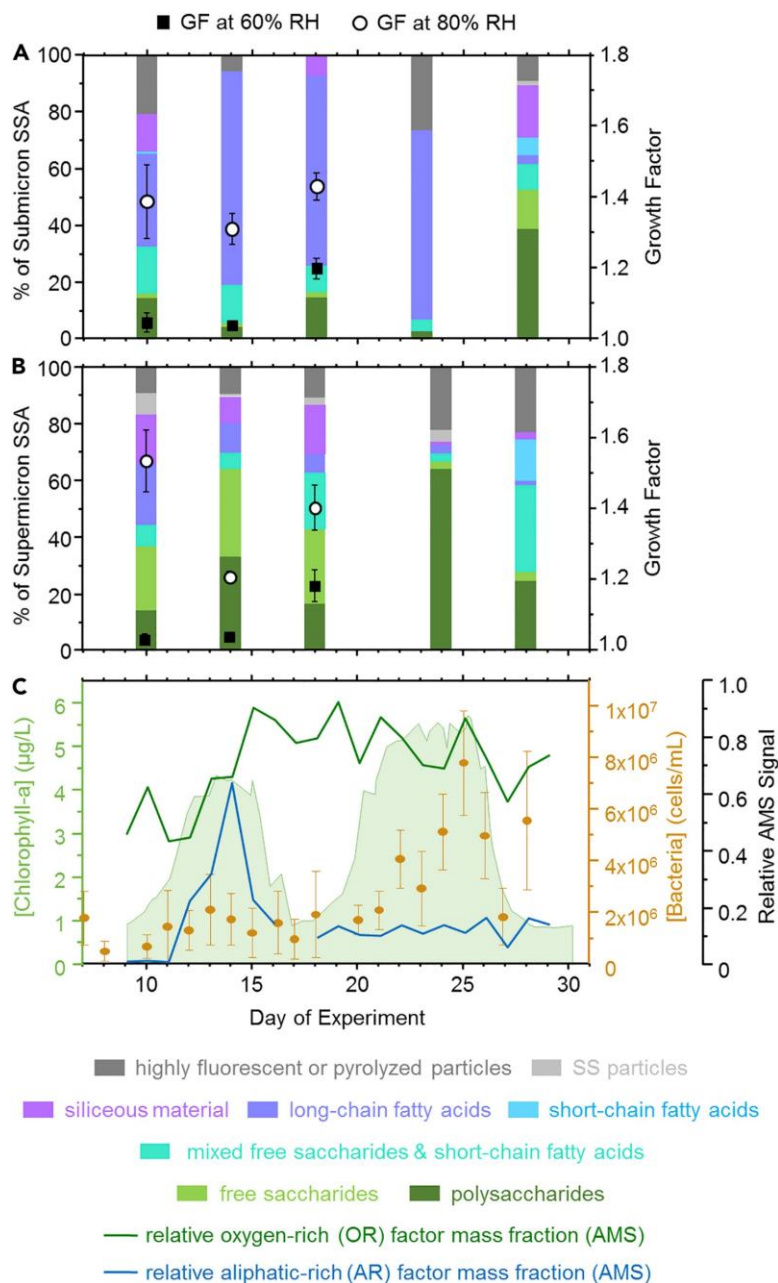


Figure 2.8: Changes in the composition of individual (a) submicron (0.56–1.00 μm) and (b) supermicron (1.8–3.2 μm) particles within SSA collected on different days throughout the mesocosm. Each class of organic and inorganic compounds are shown as a percentage of particles within the SSA ensemble that exhibit Raman signatures for that particular class. The remaining fraction of particles were highly fluorescent or pyrolyzed during Raman analysis. The average hygroscopicity (\pm one standard deviation) of individual submicron (0.5–1.0 μm) and supermicron (>1.0 μm) SSA particles collected from the wave flume as determined by offline AFM analysis are also shown in both (a) and (b). The measurements of chlorophyll-a and heterotrophic bacteria concentrations in the seawater of the wave flume are shown in (c) along with aliphatic-rich and oxygen-rich factor mass fractions as determined through the online measurement of the size-resolved bulk chemical composition of SSA by AMS.

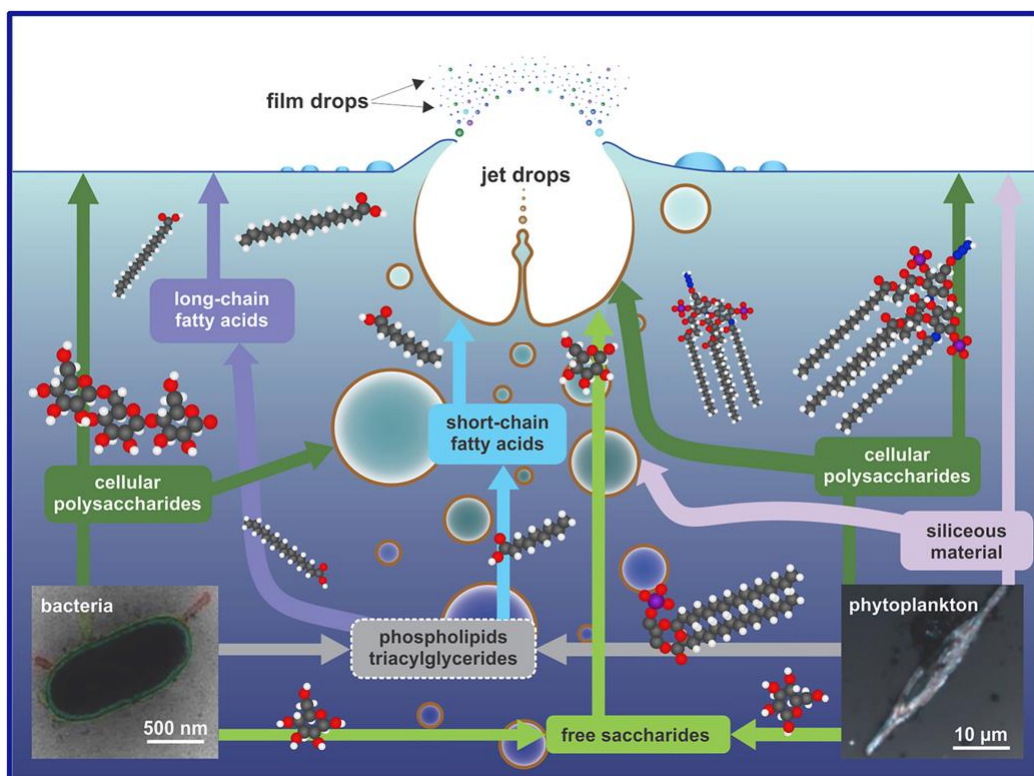


Figure 2.9: Degradation pathways of diatoms and bacteria leading to organic species that are transported from seawater to SSA particles as either film or jet drops. Boxes with a dashed outline were not directly observed in this work, but are shown here as a precursor to classes of compounds that were observed.

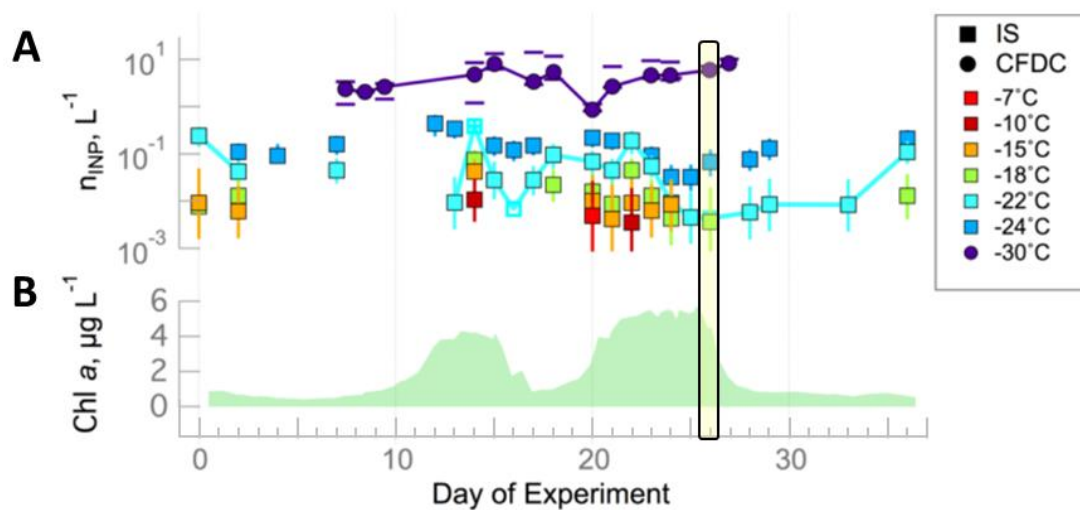


Figure 2.10: Timeline of A) ice nucleating particle (INP) number concentrations and B) chlorophyll-a concentrations. The yellow highlighted region indicates the day when ICR were collected for Raman analysis.

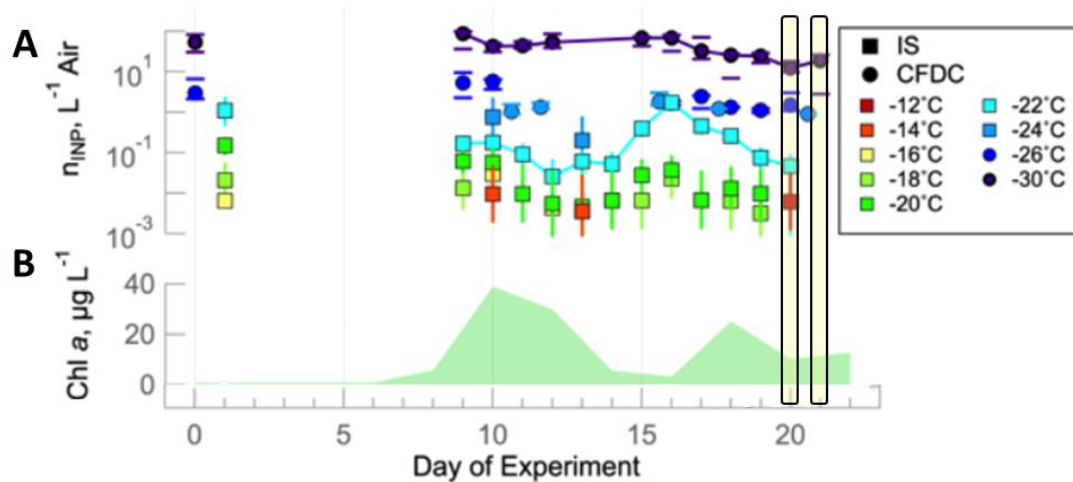


Figure 2.11: Timeline of A) ice nucleating particle (INP) number concentrations and B) chlorophyll-a concentrations. The yellow highlighted regions indicates the days when ICR were collected for Raman analysis.

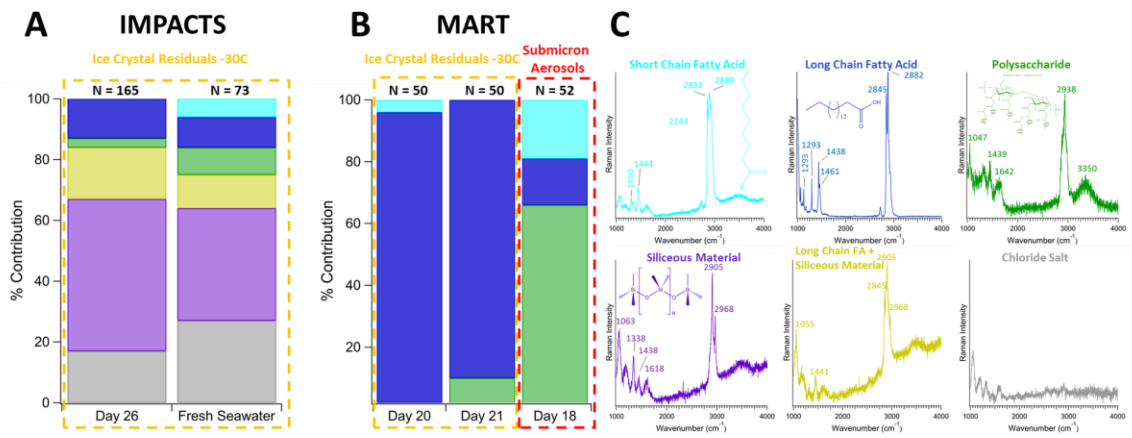


Figure 2.12: Relative contributions of particle types for ice crystal residuals (ICR) on specific days of A) IMPACTS experiment B) MART experiment. C) Shows the corresponding spectra for each particle type.

2.8 References

- (1) Quinn, P. K.; Collins, D. B.; Grassian, V. H.; Prather, K. A.; Bates, T. S. Chemistry and Related Properties of Freshly Emitted Sea Spray Aerosol. *Chem. Rev.* **2015**, *115* (10), 4383–4399.
- (2) Leeuw, G. De; Andreas, E. L.; Anguelova, M. D.; Fairall, C. W.; Lewis, E. R.; Dowd, C. O.; Schulz, M.; Schwartz, S. E. Production Flux of Sea Spray Aerosol. **2011**, No. 2010, 1–39.
- (3) Gantt, B.; Meskhidze, N.; Meskhidze, B. G. and N. The Physical and Chemical Characteristics of Marine Primary Organic Aerosol : A Review. *Atmos. Chem. Phys.* **2013**, *13* (8), 3979–3996.
- (4) Prather, K. A.; Bertram, T. H.; Grassian, V. H.; Deane, G. B.; Stokes, M. D.; Demott, P. J.; Aluwihare, L. I.; Palenik, B. P.; Azam, F.; Seinfeld, J. H.; Moffet, R. C.; Molina, M. J.; Cappa, C. D.; Geiger, F. M.; Roberts, G. C.; Russell, L. M.; Ault, A. P.; Baltrusaitis, J.; Collins, D. B.; Corrigan, C. E.; Cuadra-Rodriguez, L. A.; Ebben, C. J.; Forestieri, S. D.; Guasco, T. L.; Hersey, S. P.; Kim, M. J.; Lambert, W. F.; Modini, R. L.; Mui, W.; Pedler, B. E.; Ruppel, M. J.; Ryder, O. S.; Schoepp, N. G.; Sullivan, R. C.; Zhao, D. Bringing the Ocean Into the Laboratory to Probe the Chemical Complexity of Sea Spray Aerosol. *Proc. Natl. Acad. Sci. U. S. A.* **2013**, *110* (19), 7550–7555.
- (5) Cavalli, F.; Facchini, M. C. C.; Decesari, S.; Mircea, M.; Emblico, L.; Fuzzi, S.; Ceburnis, D.; Yoon, Y. J.; O'Dowd, C. D.; Putaud, J. P.; Dell'Acqua, A. Advances in Characterization of Size-Resolved Organic Matter in Marine Aerosol over the North Atlantic. *J. Geophys. Res. D Atmos.* **2004**, *109* (24), 1–14.
- (6) Vignati, E.; Facchini, M. C.; Rinaldi, M.; Scannell, C.; Ceburnis, D.; Sciare, J.; Kanakidou, M.; Myriokefalitakis, S.; Dentener, F.; Dowd, C. D. O. Global Scale Emission and Distribution of Sea-Spray Aerosol : Sea-Salt and Organic Enrichment. *Atmos. Environ.* **2010**, *44* (5), 670–677.
- (7) Facchini, M. C.; Rinaldi, M.; Decesari, S.; Carbone, C.; Finessi, E.; Mircea, M.; Fuzzi, S.; Ceburnis, D.; Flanagan, R.; Nilsson, E. D.; de Leeuw, G.; Martino, M.; Woeltjen, J.; O'Dowd, C. D. Primary Submicron Marine Aerosol Dominated by Insoluble Organic Colloids and Aggregates. *Geophys. Res. Lett.* **2008**, *35*, 1–5.
- (8) Russell, L. M.; Bahadur, R.; Ziemann, P. J. Identifying Organic Aerosol Sources by Comparing Functional Group Composition in Chamber and Atmospheric Particles. **2011**, *108* (9).
- (9) Russell, L. M.; Hawkins, L. N.; Frossard, A. A.; Quinn, P. K.; Bates, T. S. Carbohydrate-like Composition of Submicron Atmospheric Particles and Their Production from Ocean Bubble Bursting. *Proc. Natl. Acad. Sci.* **2010**.
- (10) Hawkins, L. N.; Russell, L. M. Polysaccharides, Proteins, and Phytoplankton Fragments: Four Chemically Distinct Types of Marine Primary Organic Aerosol Classified by Single Particle Spectromicroscopy. *Adv. Meteorol.* **2010**, *2010*, 1–14.
- (11) O'Dowd, C. D.; Facchini, M. C.; Cavalli, F.; Ceburnis, D.; Mircea, M.; Decesari, S.; Fuzzi, S.; Yoon, Y. J.; Putaud, J.-P. Biogenically Driven Organic Contribution to Marine Aerosol. *Nature* **2004**, *431* (7009), 676–680.

- (12) Quinn, P. K.; Bates, T. S.; Schulz, K. S.; Co, D. J.; Frossard, A. A.; Russell, L. M.; Keene, W. C.; Kieber, D. J. Contribution of Sea Surface Carbon Pool to Organic Matter Enrichment in Sea Spray Aerosol. *2014*, 7 (March), 228–232.
- (13) Collins, D. B. B.; Zhao, D. F. F.; Ruppel, M. J. J.; Laskina, O.; Grandquist, J. R. R.; Modini, R. L. L.; Stokes, M. D. D.; Russell, L. M.; Bertram, T. H.; Grassian, V. H.; Deane, G.; Prather, K. A. Direct Aerosol Chemical Composition Measurements to Evaluate the Physicochemical Differences between Controlled Sea Spray Aerosol. *Atmos. Meas. Tech.* **2014**, 7 (11), 3667–3683.
- (14) Dowd, C. D. O.; Langmann, B.; Varghese, S.; Scannell, C.; Ceburnis, D.; Facchini, M. C. A Combined Organic-Inorganic Sea-Spray Source Function. *Geophys. Res. Lett.* **2008**, 35, 1–5.
- (15) Rinaldi, M.; Decesari, S.; Finessi, E.; Giulianelli, L.; Carbone, C.; Fuzzi, S.; Dowd, C. D. O.; Ceburnis, D.; Facchini, M. C. Primary and Secondary Organic Marine Aerosol and Oceanic Biological Activity : Recent Results and New Perspectives for Future Studies. *Adv. in Met.* **2010**, 2010.
- (16) Bates, T. S.; Quinn, P. K.; Frossard, A. A.; Russell, L. M.; Hakala, J.; Petäjä, T.; Kulmala, M.; Covert, D. S.; Cappa, C. D.; Li, S.; Hayden, K. L.; Nuaaman, I.; McLaren, R.; Massoli, P.; Canagaratna, M. R.; Onasch, T. B.; Sueper, D.; Worsnop, D. R.; Keene, W. C. Measurements of Ocean Derived Aerosol off the Coast of California. *J. Geophys. Res.* **2012**, 117, 1–13.
- (17) Partanen, A.; Dunne, E. M.; Bergman, T.; Laakso, A.; Kokkola, H.; Ovadnevaite, J.; Sogacheva, L.; Baisnée, D. Global Modelling of Direct and Indirect Effects of Sea Spray Aerosol. *Atmos. Chem. Phys.* **2014**, 11731–11752.
- (18) Spracklen, D. V.; Arnold, S. R.; Sciare, J.; Carslaw, K. S.; Pio, C. Globally Significant Oceanic Source of Organic Carbon Aerosol. *Geophys. Res. Lett.* **2008**, 35, 1–5.
- (19) DeMott, P. J.; Hill, T. C. J.; McCluskey, C. S.; Prather, K. A.; Collins, D. B.; Sullivan, R. C.; Ruppel, M. J.; Mason, R. H.; Irish, V. E.; Lee, T.; Sultana, C. M.; Ault, A. P.; Axson, J. L.; Martinez, M. D.; Venero, I.; Santos-Figueroa, G.; Stokes, M. D.; Deane, G. B.; Mayol-Bracero, O. L.; Grassian, V. H.; Bertram, T. H.; Bertram, A. K.; Moffett, B. F.; Franc, G. D. Sea Spray Aerosol as a Unique Source of Ice Nucleating Particles. *Proc. Natl. Acad. Sci.* **2016**, 113 (21), 5797–5803.
- (20) Burrows, S. M.; Hoose, C.; Pöschl, U.; Lawrence, M. G. Ice Nuclei in Marine Air: Biogenic Particles or Dust? *Atmos. Chem. Phys.* **2013**, 13 (1), 245–267.
- (21) Bigg, E. K. Ice Nucleus Concentrations in Remote Areas. *J. Atmos. Sci.* **1973**, 30, 1153–1157.
- (22) Schnell, R. C.; Vali, G. Biogenic Ice Nuclei: Part I. Terrestrial and Marine Sources. *Journal of the Atmospheric Sciences.* **1976**, 1554–1564.
- (23) Franklin, C. N.; Sun, Z.; Bi, D.; Dix, M.; Yan, H.; Bodas-Salcedo, A. Evaluation of Clouds in Access Using the Satellite Simulator Package Cosp: Global, Seasonal, and Regional Cloud Properties. *J. Geophys. Res. Atmos.* **2013**, 118 (2), 732–748.
- (24) McCoy, D. T.; Hartmann, D. L.; Zelinka, M. D.; Ceppi, P.; Grosvenor, D. P. Journal of Geophysical Research : Atmospheres. *J. Geophys. Res. Atmos.* **2015**, 120, 9539–9554.

- (25) Wang, X.; Sultana, C. M.; Trueblood, J.; Hill, T. C. J.; Malfatti, F.; Lee, C.; Laskina, O.; Moore, K. A.; Beall, C. M.; McCluskey, C. S.; Cornwell, G.; Zhou, Y.; Cox, J.; Pendergraft, M.; Santander, M.; Bertram, T.; Cappa, C. D.; Azam, F.; DeMott, P.; Grassian, V. H.; Prather, K. A. Microbial Control of Sea Spray Aerosol Composition: A Tale of Two Blooms. *ACS Cent. Sci.* **2015**, *1* (3), 124–131.
- (26) McCluskey, C. S.; Hill, T. C. J.; Sultana, C. M.; Laskina, O.; Trueblood, J.; Santander, M. V.; Beall, C. M.; Michaud, J. M.; Kreidenweis, S. M.; Prather, K. A.; Grassian, V. H.; DeMott, P. J. A Mesocosm Double Feature: Insights into the Chemical Make-up of Marine Ice Nucleating Particles. *J. Atmos. Sci.* **2018**, JAS-D-17-0155.1.
- (27) Joke De Gelder, Kris De Gussem, Peter Vandenabeele, L. M. Reference Database of Raman Spectra of Biological Molecules. *J. Raman Spectrosc.* **2007**, *38* (April), 1133–1147.
- (28) Hill, I. R.; Levin, I. W. Vibrational Spectra and Carbon-Hydrogen Stretching Mode Assignments for a Series of N-Alkyl Carboxylic Acids. *J. Chem. Phys.* **1979**, *70* (2), 842–851.
- (29) Gomes, H.; Rosina, P.; Holakoei, P.; Solomon, T.; Vaccaro, C. Identification of Pigments Used in Rock Art Paintings in Gode Roriso-Ethiopia Using Micro-Raman Spectroscopy. *J. Archaeol. Sci.* **2013**, *40* (11), 4073–4082.
- (30) Spiker, R. C.; Levin, I. W. Raman Spectra and Vibrational Assignments for Dipalmitoyl Phosphatidylcholine and Structurally Related Molecules. *Biochim. Biophys. Acta (BBA)/Lipids Lipid Metab.* **1975**, *388* (3), 361–373.
- (31) Haggerty, J. A.; Fisher, J. B. Short-Chain Organic Acids in Interstitial Waters from Mariana and Bonin Forearc Serpentine; Leg 125. *Proceedings of the Ocean Drilling Program, Scientific Results* **1992**, *125* (5), 387–395.
- (32) Cochran, R. E.; Laskina, O.; Trueblood, J. V.; Estillore, A. D.; Morris, H. S.; Jayarathne, T.; Sultana, C. M.; Lee, C.; Lin, P.; Laskin, J.; Laskin, A.; Dowling, J. A.; Qin, Z.; Cappa, C. D.; Bertram, T. H.; Tivanski, A. V.; Stone, E. A.; Prather, K. A.; Grassian, V. H. Molecular Diversity of Sea Spray Aerosol Particles: Impact of Ocean Biology on Particle Composition and Hygroscopicity. *Chem* **2017**, *2* (5), 655–667.
- (33) Pemberton, J. E.; Chamberlain, J. R. Raman Spectroscopy of Model Membrane Monolayers of Dipalmitoylphosphatidic Acid at the Air-Water Interface Using Surface Enhancement from Buoyant Thin Silver Films. *Biopolym. - Biospectroscopy Sect.* **2000**, *57* (2), 103–116.
- (34) Deng, C.; Brooks, S. D.; Vidaurre, G.; Thornton, D. C. O. Using Raman Microspectroscopy to Determine Chemical Composition and Mixing State of Airborne Marine Aerosols over the Pacific Ocean. *Aerosol Sci. Technol.* **2014**, *48* (2), 193–206.
- (35) She, C. Y.; Dinh, N. D.; Tu, A. T. Laser Raman Scattering of Glucosamine N-Acetylglucosamine, and Glucuronic Acid. *BBA - Gen. Subj.* **1974**, *372* (2), 345–357.
- (36) Wu, H.; Volponi, J. V.; Oliver, A. E.; Parikh, A. N.; Simmons, B. A.; Singh, S. In Vivo Lipidomics Using Single-Cell Raman Spectroscopy. *Proc. Natl. Acad. Sci.* **2011**, *108* (9), 3809–3814.
- (37) Amharref, N.; Beljebbar, A.; Dukic, S.; Venteo, L.; Schneider, L.; Pluot, M.; Manfait, M. Discriminating Healthy from Tumor and Necrosis Tissue in Rat Brain Tissue Samples by Raman Spectral Imaging. *Biochim. Biophys. Acta - Biomembr.* **2007**, *1768* (10), 2605–2615.

- (38) Lin, V. J. C.; Koenig, J. L. Raman Studies of Bovine Serum Albumin. *Biopolymers* **1976**, *15* (1), 203–218.
- (39) Compiano, A.-M. M.; Romano, J.-C. C.; Garabetian, F.; Laborde, P.; de la Giraudièrea, I. Monosaccharide Composition of Particulate Hydrolysable Sugar Fraction in Surface Microlayers from Brackish and Marine Waters. *Mar. Chem.* **1993**, *42* (3–4), 237–251.
- (40) Gao, Q.; Leck, C.; Rauschenberg, C.; Matrai, P. A. On the Chemical Dynamics of Extracellular Polysaccharides in the High Arctic Surface Microlayer. *Ocean Sci.* **2012**, *8* (4), 401–418.
- (41) van Pinxteren, M.; Müller, C.; Iinuma, Y.; Stolle, C.; Herrmann, H. Chemical Characterization of Dissolved Organic Compounds from Coastal Sea Surface Microlayers (Baltic Sea, Germany). *Environ. Sci. Technol.* **2012**, *46* (19), 10455–10462.
- (42) Cunliffe, M.; Engel, A.; Frka, S.; Gašparović, B. Ž.; Guitart, C.; Murrell, J. C. C.; Salter, M.; Stolle, C.; Upstill-Goddard, R.; Wurl, O. Sea Surface Microlayers: A Unified Physicochemical and Biological Perspective of the Air-Ocean Interface. *Prog. Oceanogr.* **2013**, *109*, 104–116.
- (43) Wang, A.; Freeman, J. J.; Jolliff, B. L.; Chou, I. M. Sulfates on Mars: A Systematic Raman Spectroscopic Study of Hydration States of Magnesium Sulfates. *Geochim. Cosmochim. Acta* **2006**, *70* (24), 6118–6135.
- (44) Zhang, Y. H.; Chan, C. K. Study of Contact Ion Pairs of Supersaturated Magnesium Sulfate Solutions Using Raman Scattering of Levitated Single Droplets. *J. Phys. Chem. A* **2000**, *104* (40), 9191–9196.
- (45) Eom, H. J.; Gupta, D.; Cho, H. R.; Jin Hwang, H.; Do Hur, S.; Gim, Y.; Ro, C. U. Single-Particle Investigation of Summertime and Wintertime Antarctic Sea Spray Aerosols Using Low-Z Particle EPMA, Raman Microspectrometry, and ATR-FTIR Imaging Techniques. *Atmos. Chem. Phys.* **2016**, *16* (21), 13823–13836.
- (46) Shahzad, M. I.; Giorcelli, M.; Shahzad, N.; Guastella, S.; Castellino, M.; Jagdale, P.; Tagliaferro, A. Study of Carbon Nanotubes Based Polydimethylsiloxane Composite Films. *J. Phys. Conf. Ser.* **2013**, *439* (1).
- (47) Gügi, B.; Costaeuec, T. Le; Burel, C.; Lerouge, P.; Helbert, W.; Bardor, M. Diatom-Specific Oligosaccharide and Polysaccharide Structures Help to Unravel Biosynthetic Capabilities in Diatoms. *Mar. Drugs* **2015**, *13* (9), 5993–6018.
- (48) Marron, A. O. O.; Alston, M. J. J.; Heavens, D.; Akam, M.; Caccamo, M.; Holland, P. W. H. W. H.; Walker, G. A Family of Diatom-like Silicon Transporters in the Siliceous Loricatae Choanoflagellates. *Proc. R. Soc. B Biol. Sci.* **2013**, *280* (1756), 20122543.
- (49) Laucks, M. L.; Sengupta, A.; Junge, K.; Davis, E. J.; Swanson, B. D. Comparison of Psychro-Active Arctic Marine Bacteria and Common Mesophilic Bacteria Using Surface-Enhanced Raman Spectroscopy. **2005**, *59* (10).
- (50) Kamnev, A. A.; Tarantilis, P. A.; Antonyuk, L. P.; Bespalova, L. A.; Polissiou, M. G.; Colina, M.; Gardiner, P. H. E.; Ignatov, V. V. Fourier Transform Raman Spectroscopic Characterisation of Cells of the Plant-Associated Soil Bacterium *Azospirillum Brasilense* Sp7. *J. Mol. Struct.* **2001**, *563–564*, 199–207.

- (51) Wustman, B. A.; Lind, J.; Wetherbee, R.; Gretz, M. R. Extracellular Matrix Assembly in Diatoms (Bacillariophyceae) . III. Organization of Fucoglucuronogalactans within the Adhesive Stalks of *Achnanthes Longipes*. *Plant Physiol.* **1998**, *116*, 1431–1441.
- (52) Verdugo, P.; Alldredge, A. L.; Azam, F.; Kirchman, D. L.; Passow, U.; Santschi, P. H. The Oceanic Gel Phase: A Bridge in the DOM-POM Continuum. *Mar. Chem.* **2004**, *92* (1–4), 67–85.
- (53) Jeffrey, L. M. M. Lipids in Sea Water. *J. Am. Oil Chem. Soc.* **1966**, *43* (4), 211–214.
- (54) Marty, J. C. C.; Saliot, A.; Buat-Ménard, P.; Chesselet, R.; Hunter, K. a. A. Relationship between the Lipid Compositions of Marine Aerosols, the Sea Surface Microlayer, and Subsurface Water. *J. Geophys. Res.* **1979**, *84* (C9), 5707.
- (55) Osterroht, C. Extraction of Dissolved Fatty Acids from Sea Water. *Fresenius. J. Anal. Chem.* **1993**, *345* (12), 773–779.
- (56) Slowey, J. F. F.; Jeffrey, L. M. M.; Hood, D. W. W. The Fatty-Acid Content of Ocean Water. *Geochim. Cosmochim. Acta* **1962**, *26* (6), 607–616.
- (57) Gagosian, R. B. R. B.; Peltzer, E. T. E. T.; Zafiriou, O. C.; Zafirioui, O. C. Atmospheric Transport of Continentally Derived Lipids to the Tropical North Pacific. *Nature* **1981**, *291* (5813), 312–314.
- (58) Ziemann, P. J. Aerosol Products, Mechanisms, and Kinetics of Heterogeneous Reactions of Ozone with Oleic Acid in Pure and Mixed Particles. *Faraday Discuss.* **2005**, *130*, 469–490.
- (59) Granum, E.; Kirkvold, S.; Myklestad, S. M. Cellular and Extracellular Production of Carbohydrates and Amino Acids by the Marine Diatom *Skeletonema Costatum*: Diel Variations and Effects of N Depletion. *Mar. Ecol. Prog. Ser.* **2002**, *242* (Werner 1977), 83–94.
- (60) Waterkeyn, L.; Bienfait, A. Localization and Function of Beta 1,3-Glucans (Callose and Chrysolaminarin) in *Pinnularia* Genus (Diatoms). *Cell.* **1987**, *74*, 199–226.
- (61) Aslam, S. N.; Cresswell-Maynard, T.; Thomas, D. N.; Underwood, G. J. C. Production and Characterization of the Intra- and Extracellular Carbohydrates and Polymeric Substances (Eps) of Three Sea-Ice Diatom Species, and Evidence for a Cryoprotective Role for Eps. *J. Phycol.* **2012**, *48* (6), 1494–1509.
- (62) Boman, H. G.; Monner, D. a. Characterization of Lipopolysaccharides From *Escherichia Coli* K-12 Mutants. *J. Bacteriol.* **1975**, *121* (2), 455–464.
- (63) Zarrouk, H.; Karibian, D.; Bodie, S.; Perry, M. B.; Richards, J. C.; Caroff, M. Structural Characterization of the Lipids A of Three *Bordetella Bronchiseptica* Strains: Variability of Fatty Acid Substitution. *J. Bacteriol.* **1997**, *179* (11), 3756–3760.
- (64) Carlson, R. W.; Kalembasa, S.; Turowski, D.; Pachori, P.; Noel, K. D. Characterization of the Lipopolysaccharide From a *Rhizobium Phaseoli* Mutant That Is Defective in Infection Thread Development. *J. Bacteriol.* **1987**, *169* (11), 4923–4928.
- (65) Marvasi, M.; Visscher, P. T.; Casillas Martinez, L. Exopolymeric Substances (EPS) From *Bacillus Subtilis*: Polymers and Genes Encoding Their Synthesis. *FEMS Microbiol. Lett.* **2010**, *313*, 1–9.

- (66) Kumar, A. S.; Mody, K.; Jha, B. Bacterial Exopolysaccharides - A Perception. *J. Basic Microb.* **2007**, *47*, 103–117.

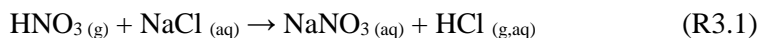
Chapter 3 Heterogeneous Chemistry of Lipopolysaccharides with Gas-Phase Nitric Acid: Reactive Sites and Reaction Pathways

3.1 Synopsis

Recent studies have shown that sea spray aerosol has a size-dependent, complex composition consisting of biomolecules and biologically-derived organic compounds as well as salts. This additional chemical complexity most likely influences the heterogeneous reactivity of SSA, as these other components will have different reactive sites and reaction pathways. In this study, we focus on the reactivity of a class of particles derived from some of the biological components of sea spray aerosol, including lipopolysaccharides (LPS), that undergo heterogeneous chemistry within the reactive sites of the biological molecule. Examples of these reactions and the relevant reactive sites are proposed as follows: $\text{R-COONa}_{(s)} + \text{HNO}_{3(g)} \rightarrow \text{NaNO}_3 + \text{R-COOH}$ and $\text{R-HPO}_4\text{Na}_{(s)} + \text{HNO}_{3(g)} \rightarrow \text{NaNO}_3 + \text{R-H}_2\text{PO}_4$. These reactions may not only be a heterogeneous pathway for sea spray aerosol, but for a variety of other types of atmospheric aerosol as well.

3.2 Introduction

The heterogeneous chemistry of sea spray aerosol (SSA) particles with nitrogen-oxides has been studied extensively in both laboratory and field studies.¹⁻³ These reactions play an important role in atmospheric chemistry by controlling the loss of nitrogen-oxide species from the gas phase into the aerosol phase, in addition to causing important changes to SSA physicochemical properties.^{4,5} For example, a current paradigm for the formation of particulate nitrate in the marine boundary layer involves the well-known reaction of nitric acid gas with sodium chloride in sea spray aerosol, as shown in Reaction 3.1:



However, this reaction represents the reactivity of only one of the components of sea spray aerosol. As shown in Chapter 2, SSA particles are quite chemically diverse with different types of particles containing a vast array of other constituents besides salts; including biological particles such as whole bacteria, as well as various biomolecules like lipopolysaccharides, lipids, and carbohydrates.^{4,6-12} With this in mind, we set out to investigate different reaction pathways that may occur in the heterogeneous reactivity of some of these different components of SSA, as well as other types of aerosols present in the troposphere, with gas phase nitric acid, an important trace acidic atmospheric gas.

As discussed below, micro-Raman spectroscopy of individual particles was used to identify different particle types within SSA and the different reaction chemistry associated with them.¹³ We show the importance of heterogeneous chemistry of gas-phase nitric acid with biologically derived components of SSA. In particular, we show that some bacterial degradation products, which includes lipopolysaccharides (LPS), the major component of the outer membrane of Gram-negative bacteria, can get into the atmosphere and undergo heterogeneous chemistry with nitric acid to form nitrate salts in a new heterogeneous reaction pathway that involves reactive sites on the biological molecule. Examples of these types of reactions are shown in Reactions 3.2 and 3.3:



The protonation of LPS is shown above for the sodium cation, but other cations including divalent calcium and magnesium can be involved as well. We surmise that this chemistry involving atmospheric inorganic acidic gases with deprotonated carboxylate and phosphate groups within biological molecules may be relevant not only for SSA, but for a variety of atmospheric particle types including biomass burning particles and other bioaerosols that contain amino acids, proteins, and nucleic acids.

3.2. Experimental Methods

3.2.1 Sources and Purity of Compounds.

Commercially available compounds were used as model systems in this study and included NaCl (99.8%, Fischer Scientific), LPS from *E. coli* (L4130, extracted from *Escherichia coli* 0111:B4, purified by trichloroacetic acid extraction), palmitic acid ($\geq 99.0\%$, Sigma-Aldrich), magnesium nitrate (99%, Sigma-Aldrich), potassium nitrate ($\geq 99.0\%$, Sigma-Aldrich), sodium nitrate ($\geq 99.0\%$, Sigma-Aldrich), calcium nitrate ($\geq 99.0\%$, Sigma-Aldrich), DPPA (sodium salt, Sigma-Aldrich), Lipid A (ammonium salt, Avanti Lipids), and Kdo₂-Lipid A (sodium salt, Cayman Chemical).

3.2.2 Model Systems Sample Preparation

Single component model system aerosol particles were generated by atomizing (TSI Inc., model 3076) aqueous solutions (Optima water, Fischer Scientific) of the compounds listed above. Aerosol particles were then sent through two diffusion dryers (TSI Inc., model 3062) at a flow rate of 1.5 lpm to reduce humidity (RH) to ca. 5%. Quartz substrates (Ted Pella Inc., part no. 16001-1) were then used to collect the aerosol particles by mounting the quartz substrate on an impactor installed in front of a differential mobility analyzer (DMA) for 1 to 25 min.

3.2.3 Reaction of Sea Spray Aerosol and Model Systems with Nitric Acid Vapor

Authentic SSA particles generated during the 2014 Investigation into Marine Particle Chemistry and Transfer Science (IMPACTS) mesocosm experiments¹⁴ were reacted on-the-fly with ~1 ppm of HNO₃ using a 5L flow tube reactor at a relative humidity of ~60% and temperature 30-35°C. Model system LPS particles were also reacted on-the-fly by atomizing (Collison) an aqueous solution of 50 mg of commercial LPS in 200 mL of ultrapure water. Resulting particles were generated at a relative humidity of >90% (Vaisala, HMP110). An aerosol flow tube (1.5 m length, 4.8 cm i.d.) equipped with a movable injector (reactive trace gas entry position range of 0

to 0.88 m from the end) was used for the heterogeneous reaction of model system LPS particles with HNO₃ gas. The inside of the flow tube was coated with inert halocarbon wax (Halocarbon Production, Halocarbon Wax 600) to minimize wall-loss of the reactive gases. The injector position was set at its maximum extension, allowing for a reaction residence time inside the flow tube of ~1.8 min. Dry nitrogen gas (N₂) was used to deliver HNO₃ gas at a concentration of ~10 ppb into the flow tube, with an HNO₃ permeation tube (KIN-TEC, HRT-010.00 -2022/60) as the source of the HNO₃ gas. LPS particles entered the flow cell and mixed with the reactive gas at a relative humidity of 55±3%. Particles exiting the flow tube were then dried using two diffusion driers prior to entering an aerosol time of flight mass spectrometer (ATOFMS).

For offline reactions of substrate deposited model system and authentic SSA particles,¹⁵ the substrate deposited particles were loaded into a reaction chamber that allowed introduction of HNO₃ acid and water vapor for RH studies. Samples were exposed to ~1 ppm of HNO₃ at 20% RH for 10 minutes.

3.2.4 Micro-Raman Spectroscopy of Authentic Sea Spray Aerosols and Model System Particles

Substrate deposited model system aerosol particles were analyzed before and after exposure to HNO₃ using a LabRam HR Evolution Raman spectrometer (Horiba) equipped with an Olympus BX41 optical microscope. Spectra were obtained using the 100× microscope objective with a working distance of 7.6 mm and laser wavelength of 532 nm. Similar settings were used for the authentic sea spray aerosol (SSA) particles collected from the ocean-atmosphere facility at the Scripps Institute of Oceanography. Unless otherwise noted, spectra were collected at ca. 20% RH at 298 K.

3.2.5 Verification of Model System LPS Reactivity Using ATOFMS and XPS

Verification of the reactivity of pure model system LPS particles was accomplished using aerosol time-of-flight mass spectrometry (ATOFMS). Detailed information on the ATOFMS

instrumentation can be found elsewhere.¹⁶ Model system LPS particles were reacted on-the-fly as described above and sent through the ATOFMS.

In addition, the reaction of model system LPS with HNO₃ was investigated with an X-Ray photoelectron spectroscopy (XPS) system. Detailed information on the instrument can be found elsewhere.¹⁷ For this study, lyophilized powder samples of LPS were pressed onto indium foil and mounted onto a copper stub. The X-ray gun was operated with a 10 mA emission current at an accelerating voltage of 15 kV. Low energy electrons were used to compensate for charging of the sample. Survey scans were first collected followed by high resolution scans in regions of interest including the C1s, Ca2p, Mg2p, N1s, Na1s, O1s, P2p, and S2p binding energy regions. The absolute energy scale was calibrated to the C1s peak binding energy of 285 eV.

3.2.6 Determination of Relative Reactivities for LPS and NaCl with HNO₃

To investigate the relative rates of reaction for LPS and NaCl with HNO₃, pure LPS particles and pure NaCl particles of diameter ~2 μm were simultaneously exposed to ~20 mT of HNO₃ at ~15% RH for a total of ten minutes. Raman spectra of particles were collected after total exposure times of 1, 3, 6, and 10 minutes. The extent of reaction was then determined by summing the total counts in the nitrate ν₁ stretching region (1040-1070 cm⁻¹).

3.3 Results and Discussion

3.3.1 Reaction of Authentic SSA Particles

Authentic particles of SSA were generated under real-world conditions using natural seawater in a unique ocean-atmosphere facility that has been described in detail previously.¹⁴ Before collection by impaction onto substrates, particles were exposed to HNO₃ in an in-situ flow tube at 1 ppm and a relative humidity (RH) of ~60%. Spectral analysis of these reacted particles and comparison with the spectra from model systems (*vide infra*) indicates that these particles can be assigned to particles that contain mainly sodium chloride, which is highly reactive,

lipopolysaccharides, which is also reactive, and protonated long chain carboxylic acids (e.g., palmitic acid), which are not reactive (see Figure 3.8 in Section 3.7.6 Supporting Information Figures for spectra of all three particle types). An optical microscope image of the substrate-deposited particles and a Raman spectrum focused on a particle identified as containing lipopolysaccharide shows that there is a Raman peak near ca. 1068 cm^{-1} associated with this particle (Figure 3.1). The peak occurs upon exposure to nitric acid and is assigned to the symmetric stretch (ν_1) of the nitrate ion, indicating the particle has reacted.

3.3.2 Reaction of LPS Particles

To better understand the reactivity of LPS, a commercial source of LPS was purchased from Sigma-Aldrich and then reacted with gas-phase nitric acid in a method similar to the SSA particles shown above. Different experiments and techniques were employed to verify this heterogeneous chemistry with LPS.

Using micro-Raman spectroscopy, spectra of the LPS model system particles were collected before and after exposure to nitric acid vapor (10 mTorr) at ~20% RH (Figure 3.2A). LPS particle spectra following exposure to nitric acid showed an intense nitrate peak nearly identical to the reacted sea spray aerosol particles originating from the more complex sea spray (Figure 3.9 in Section 3.7.6 Supporting Information Figures shows a direct comparison of the reactivity of model system aerosols with the authentic sea spray particles). Further demonstration of the reactivity of LPS with gas-phase HNO_3 was accomplished by investigating LPS powder reactivity with X-Ray photoelectron spectroscopy (XPS) and LPS aerosol reactivity using aerosol time-of-flight mass spectrometry (ATOFMS) as shown in Figures 3.2B and 3.2C, respectively.

Figure 3.2B shows the N1s region for the unreacted LPS has two peaks at 400.1 and 402.7 eV corresponding to amide groups from peptide linkages and protonated nitrogen respectively, in agreement with previous analysis of bacterial cell walls using XPS.¹⁸ Upon exposure of LPS

powder to HNO₃, a third peak in the N1s region became evident with a binding energy of 406.6 eV, indicating the presence of nitrate ions. Figure 3.2C shows the average ATOFMS spectra of over 4,000 unreacted and reacted LPS particles. Peaks at 62 and 46 m/z, corresponding to NO₃⁻ and NO₂⁻, respectively, were observed in the reacted LPS spectra. In all three of these very different experiments, a nitrate peak was present in the relevant wavenumber, binding energy, and mass to charge ratio regions following exposure of LPS to nitric acid vapor. Taken together, these results show that LPS itself can undergo reaction with gas-phase nitric acid to form a nitrate salt.

3.3.3 Investigation of LPS Reactive Sites

Considering relevant reactive sites within LPS, we turn to its structure, which can be divided into three main components: 1) Lipid A 2) core oligosaccharide, which is comprised of an inner and outer core, and 3) O-antigen. Previous studies have shown that the binding of mono and divalent cations at the inner core and Lipid A portions is crucial to the structural integrity of the bacterial outer cell wall membrane.

Figure 3.3 shows a detailed view of the Lipid A and inner core oligosaccharide regions of LPS, with phosphate and carboxylate regions highlighted in red and blue, respectively. As shown, phosphate is present in the Lipid A region, while both phosphate and carboxylate groups are found in the inner core oligosaccharide portion. We hypothesize that the presence of these basic sites results in the observed LPS reactivity, as described in reactions (2) and (3).

To further elucidate the reactivity of LPS, different components of LPS were prepared and exposed to nitric acid vapor. In particular, particles were generated from three separate standards of Lipid A, Kdo₂-Lipid A, and a solution of LPS that was hydrolyzed to remove the Lipid A component, thus leaving only the core oligosaccharide and O-antigen regions.^{19,20} Chemical structures for these components serving as different model systems are shown in Figure 3.10 (Section 3.7.6 Supporting Information Figures).

Figure 3.4 shows the resulting spectra from these components before and after reaction with nitric acid vapor at 20% RH. The formation of nitrate, as indicated by the ingrowth of the ν_1 nitrate peak, verifies both Lipid A and the core oligosaccharide components are reactive sites within LPS. Interestingly, the resulting spectrum for each sample produced a ν_1 nitrate peak at slightly different frequency and intensity. For reacted particles in general, the exact position of the ν_1 peak varied from particle to particle between values of 1045 and 1068 cm^{-1} . This is due to the fact that the exact frequency of this band depends on the amount of water associated with the LPS particle as well as the cation present.^{13,21,22} As these reactions all took place at the same relative humidity (~20%), the frequency difference is most likely a result of the different cations present. The influence of the local environment, water content, and cation present on the frequency of this band is shown in Figures 3.11 and 3.12 (Section 3.7.6 Supporting Information Figures), respectively. The differences in intensity following the same exposure to nitric acid in these different experiments suggest either different rates of reaction for the different reactive sites within these molecules, and/or differences in relative site concentration. These differences may be related to the gas-phase basicity of these groups, an issue that future studies will further explore.

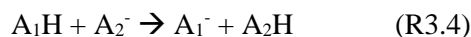
3.3.4 Extension of Reaction Mechanism to other Aerosol Types

To attain a better understanding of functional group reactivity within sea spray and other aerosol types involving deprotonated carboxylate and phosphate groups, four additional model systems were investigated as shown in Figure 3.5. The left side of the figure shows spectra for atomized and substrate deposited A) DPPA (1,2-dihexadecanoyl-*sn*-glycero-3-phosphate sodium) and sodium carboxylate salts, sodium palmitate, sodium nonanoate, and sodium butyrate, B-D, before exposure to gas-phase nitric acid, while the right side shows the particle spectra upon exposure to HNO_3 at 20% RH.

DPPA has only one phosphate group available for reaction and Figure 3.5A verifies the potential of this phosphate as a reactive group. Figure 3.5 B-C also shows that carboxylate salts become readily protonated (as highlighted in Figure 3.5D) along with the formation of sodium nitrate upon exposure to nitric acid vapor (full spectra from 500 to 4000 cm^{-1} are shown in Figure 3.13 of Section 3.7.5). These carboxylate salts represent deprotonated carboxylic acids that are prevalent in the atmosphere.²³

3.3.5 Acid/Base Properties of LPS

Gas-phase thermochemical parameters represent the pure Bronsted basicity properties since no solvent molecules are involved.²⁴ For this reason, detailed knowledge on the acid/base characteristics of sites in gas-phase molecules is useful for predicting sites of protonation, relative reactivities, and likely structural conformations. For example, the reactions proposed in Reactions 3.2 and 3.3 involving LPS reactive sites and HNO_3 can be thought of as simple proton transfer reactions according to the following generic equation:



The thermodynamic driving force for this reaction can then be examined using the gas phase acidity (GA) of the species involved:²⁵



$$\text{GA}(\text{AH}) = \Delta_{\text{acid}}G^\circ \quad (\text{R3.6})$$

$$\Delta_{\text{rxn}}G^\circ = \text{GA}(\text{A}_1\text{H}) - \text{GA}(\text{A}_2\text{H}) \quad (\text{R3.7})$$

where $\Delta_{\text{acid}}G^\circ$ is the Gibbs free energy of the deprotonation reaction of an acid, and $\Delta_{\text{rxn}}G^\circ$ is the Gibbs free energy of the overall proton transfer reaction shown in Reaction 3.5.

To date, no studies have been conducted to assess the gas phase acidity/basicity of LPS molecules. Given the structural complexity and large molecular weight (1.6×10^8 Da) of LPS,²⁶ several structural conformations likely exist, making it challenging to assay the exact value of its gas phase acid/base properties. However, biomolecules with similar structure and reactive groups (e.g., mono/oligosaccharides and phospholipids) to LPS can be used as estimates in place of experimental data. Unfortunately, the choices were limited due to the small number of studies conducted on the gas phase basicity of oligosaccharides and phospholipids relative to those for amino acids, peptides, and nucleobases.²⁷ Table 3.1 (Section 3.7.7) gives the gas phase acidity values and molecular structure for the biomolecules we chose to act as proxies for the reactive sites of LPS.

As shown in Figure 3.3, Kdo₂ sugars in the inner core region contain COOH functional groups. To test the reactivity of COOH sites on LPS, we used gentisic acid, glucuronic acid, sucrose, sialyllactose, and ethanone as model estimates. Table 3.1 shows that for COOH groups on gentisic acid, glucuronic acid, and sucrose, the reaction with nitric acid is spontaneous, with $\Delta_{\text{rxn}}G^\circ$ ranging from -0.7 to -43.3 kJ/mol. Conversely, $\Delta_{\text{rxn}}G^\circ$ for nitric acid with sialyllactose and ethanone are 66.7 and 5.7 kJ/mol, respectively.

While a study on the gas phase acidity/basicity of phospholipids has been carried out previously, the lack of reference acids meant only relative values could be determined.²⁸ For this reason, we used the values for isolated phosphoric acid and its conjugate bases. As seen in Table S1, the phosphates become weaker acids as their charge becomes more negative (i.e., they become stronger bases), with $\Delta_{\text{rxn}}G^\circ$ values of -21.3, -553.3, and -1072.3 kJ/mol for H₃PO₄, H₂PO₄⁻, and HPO₄²⁻, respectively. Given these values, along with the parallel argument found in peptides which states that gas-phase basicity increases with increasing chain length,²⁹ the reaction of nitric acid with phosphate groups found on LPS is likely spontaneous.

Unlike the gas phase, the acid/base behavior of LPS molecules in aqueous solution has been studied more extensively.^{30,31} A recent study conducted acid-base titrations on LPS strains to calculate the expected pKa of the various reactive groups of the LPS molecule. The reported pKa value of 5 for carboxyl groups and 6-8 for the phosphoryl groups³² agrees with the results from our preliminary gas-phase calculations above, indicating that both groups could potentially take part in the reaction. Given the fact that aerosols containing LPS likely occur somewhere between the completely water-free gas phase and the aqueous phase, research spotlight should be focused to further the understanding of the thermodynamic properties of LPS in both phases. Furthermore, given the increasingly known importance of LPS in different research areas, studies should be conducted to ascertain its changes in structural conformation, water uptake properties under varying environmental conditions, and whether the LPS remains intact when transported to the atmosphere.

3.3.6 Relative Product Formation and Rates NaCl Compared to LPS

To contextualize our newly proposed pathway for the formation of particulate nitrate in relation to the conventional NaCl method, we simultaneously exposed NaCl and pure LPS particles to HNO₃ for ten minutes and monitored the extent of reactions as a function of exposure time. Figure 3.6 shows the Raman spectra for A) NaCl and B) LPS particles as a function of increasing HNO₃ exposure time.

The nitrate peak areas (1050-1070 cm⁻¹) showed linear growth as a function of time and therefore the relative slopes can provide information about relative rates of nitrate formation for NaCl compared to LPS particles. This comparison shows that the rate of reaction for LPS is three to four times slower than that of NaCl particles, indicating this newly proposed mechanism, albeit slower than the NaCl reaction, may still serve as a relevant pathway for the formation of particulate nitrate in the atmosphere. Previous studies have indicated that SSA particles of decreasing size contain increasing amounts of organic matter, with particles below 200 nm in diameter existing as

external mixtures of organic species completely devoid of NaCl.⁹ The traditional reaction pathway of nitric acid with NaCl is likely irrelevant for these particles in that crucial submicron size range. As such, this new reaction pathway involving organic SSA with HNO₃ is significant in that it demonstrates the reactivity of a class of SSA that was previously overlooked, and could be used to better correlate particulate nitrate and sea salt observations with chemical model predictions.

Furthermore, recent studies have provided evidence that weak acids can react with NaCl and NaNO₃ to produce gaseous HCl and HNO₃.³³ While this reaction is the reverse of the reaction shown here, there is most likely an equilibrium between them. This suggests that additional studies focused on the reaction kinetics of both mechanisms are needed to assess the exact nature of this equilibrium. However, given the relatively short period of time required for our proposed reaction to occur (~10 minutes), in comparison to the reverse pathway (~15-24 hours), it is safe to assume that this mechanism is still relevant for nascent SSA.

3.4 Conclusions

Here we have shown a previously unrecognized pathway for the reaction of biologically derived components of sea spray aerosol consisting of LPS molecules. This newly identified chemistry involving basic groups present due to biological components of SSA in the particulate phase and its reactivity with acidic gases is summarized in Figure 3.7. This type of chemistry has not been shown before for any type of aerosol to date, and may serve as another mechanism for nitrate salt formation in the atmosphere that hitherto has been unrecognized. Furthermore, these reactions may be important for other atmospheric aerosols besides SSA (e.g., biomass burning aerosols).

Future studies should use micro-Raman spectroscopic mapping and atomic force microscopy³⁴ to address the connection between particle morphology, hydration state, and reactivity. In addition to studying the climate relevant effects, kinetics of these reactions as a

function of relative humidity are also needed. Studies of the reaction of homologous series of sodium carboxylate salts, as well as reactions with divalent carboxylate salts, will also be carried out to further understand the heterogeneous proton transfer type chemistry described herein.

Finally, the reactivity of these biological components of SSA with other trace gases will potentially unravel additional new and important chemical pathways in ocean-derived bioaerosols and other atmospheric aerosols as well.³⁵ This represents a paradigm shift from earlier studies that focused only on the salt component of SSA and ignored the biological components that are commonly present.

3.5 Acknowledgements

This work was funded by Center for Aerosol Impacts on Climate and the Environment (CAICE), a National Science Foundation Center for Chemical Innovation under grant number CHE1305427. The author would like to thank all collaborators involved with the 2014 CAICE intensive campaign (IMPACTS) and the SIO Hydraulics Laboratory staff. In addition, the author would like to thank Professors Amnon Kohen and Christopher Cheatum of the University of Iowa for the helpful discussions on the reactivity of LPS.

Chapter 3 is reproduced with permission from: Trueblood, J. V., Estillore, A. D., Lee, C., Dowling, J. A., Prather, K. A., Grassian, V. H. Heterogeneous Chemistry of Lipopolysaccharides with Gas-Phase Nitric Acid: Reactive Sites and reaction Pathways, *JPC A*, 120 (32), 6444-6450, 2016. The dissertation author was the primary investigator and author of this paper.

3.6 Figures

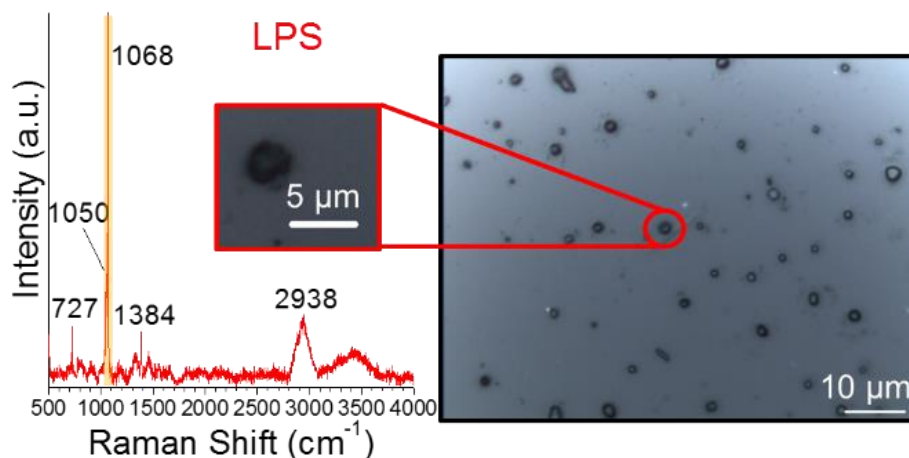


Figure 3.1: Optical image of SSA particles collected on a substrate following exposure to HNO₃. Besides particles identified as reacted salt particles, another class was identified as a nitric acid reacted lipopolysaccharide (LPS) particle from micro-Raman spectroscopy. Efforts to understand reactive sites within LPS for heterogeneous reactivity involve model system studies (See text for further details).

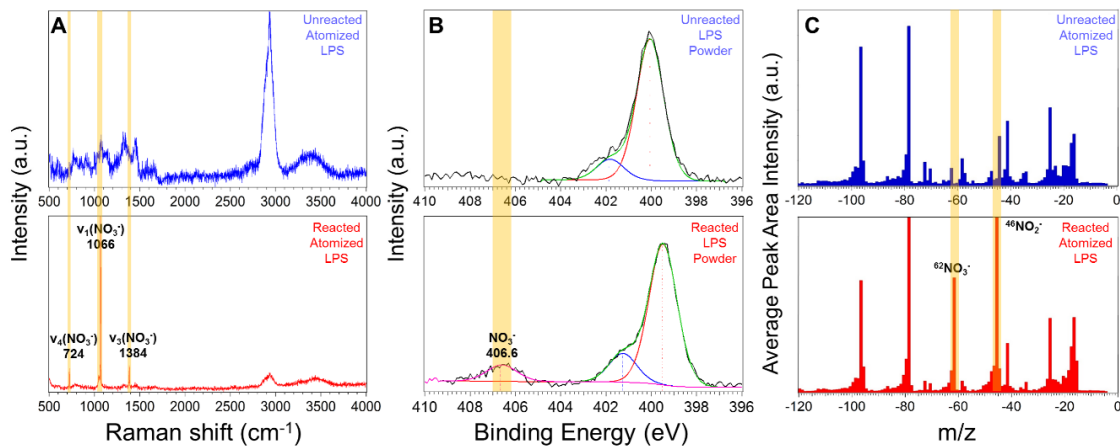


Figure 3.2: Experimental data for liposaccharide exposed to gas phase nitric acid in three different experiments. A) micro-Raman spectroscopy of substrate deposited LPS aerosol particles from aqueous solution, B) XPS data of the N1s binding energy region for LPS powder, and C) ATOFMS average spectra of atomized aqueous solutions of LPS.

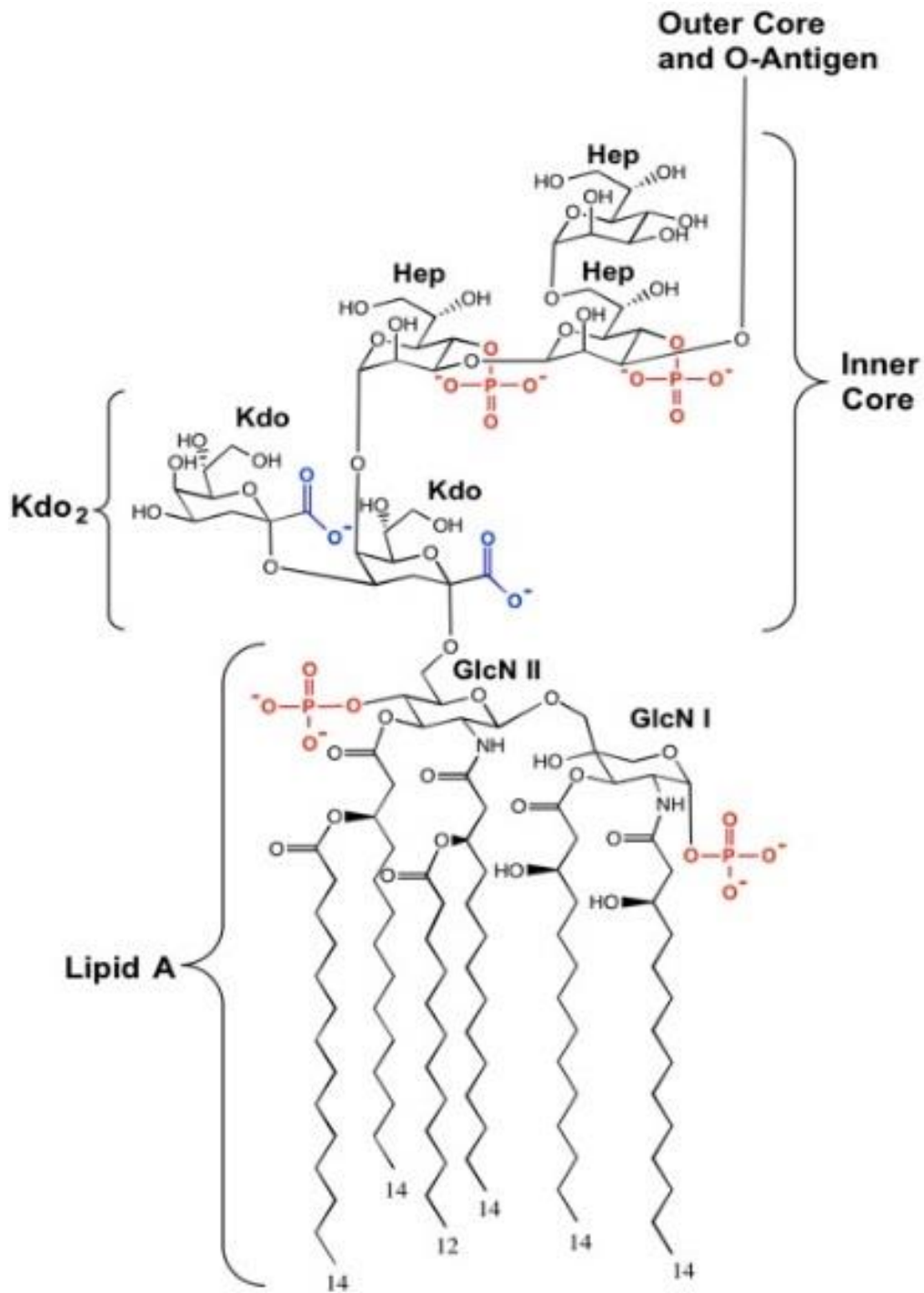


Figure 3.3: Basic components of LPS that could react with gas phase nitric acid. The phosphate and carboxylate sites are highlighted red and blue, respectively, and are found in the Lipid A and inner core oligosaccharide regions. The inner core consists of Kdo₂ and three heptose sugars. Abbreviations: Kdo: 3-deoxy-D-manno-oct-2-ulosonic acid; Hep: L-glycero-D-manno-heptose; GlcN: glucosamine.

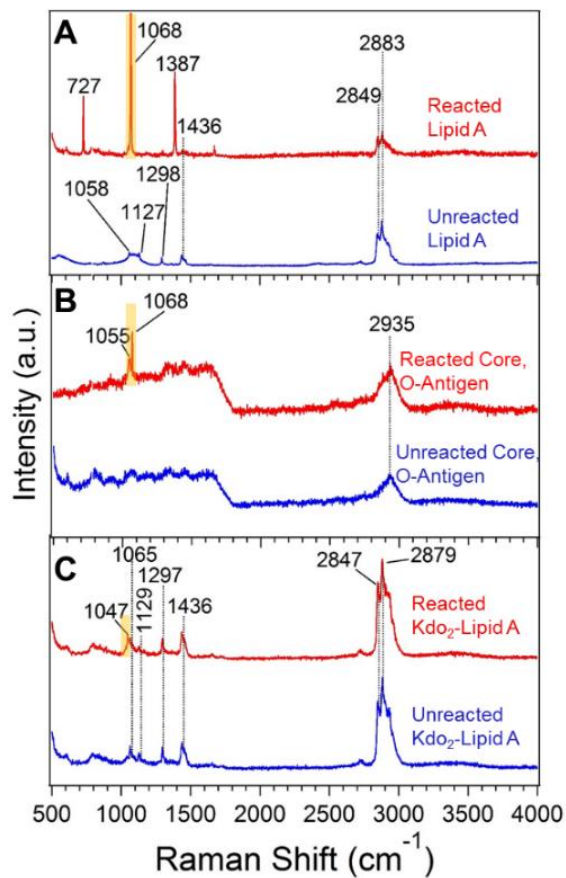


Figure 3.4: Raman spectra of different isolated portions of LPS before (blue) and after (red) exposure to HNO_3 . The yellow highlighted peak represents the ν_1 stretch for the nitrate ion. After HNO_3 exposure, A) Lipid A, B) core oligosaccharide and O-antigen, and C) Kdo₂-Lipid A each feature the presence of the ν_1 nitrate anion peak, indicating they all contribute to the reactivity of LPS. The existence of two nitrate peaks in the reacted Core, O-Antigen particle suggests the presence of different cations.

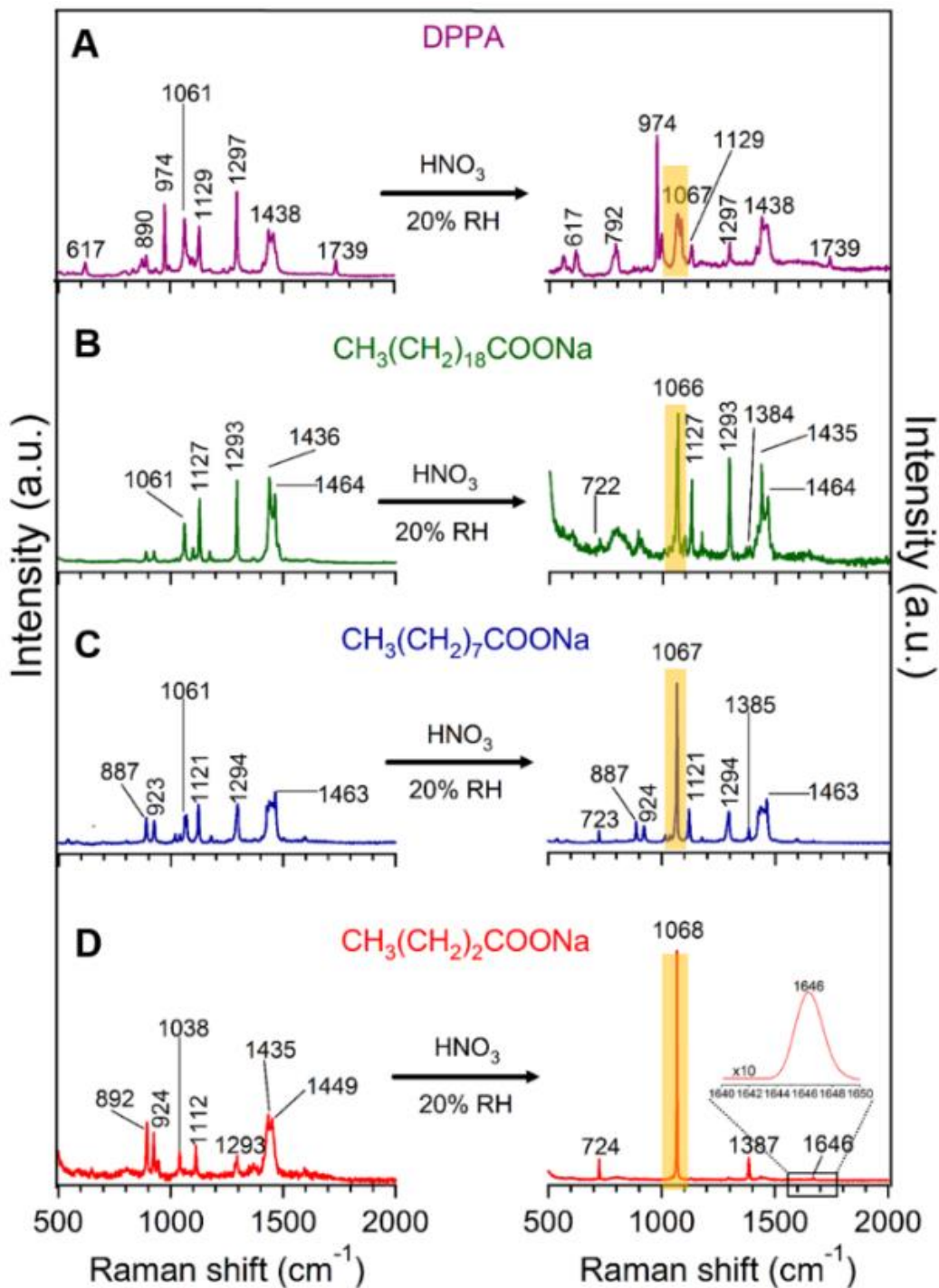


Figure 3.5: Raman spectra of individual particles composed of A) DPPA, B) sodium palmitate, C) sodium nonanoate, and D) sodium butyrate before (left) and after (right) exposure to HNO_3 . The yellow highlighted peak represents the ν_1 stretch for the nitrate ion, indicating the phosphate group and carboxylate groups of DPPA and sodium carboxylate salts are reactive.

NaCl + HNO₃

LPS + HNO₃

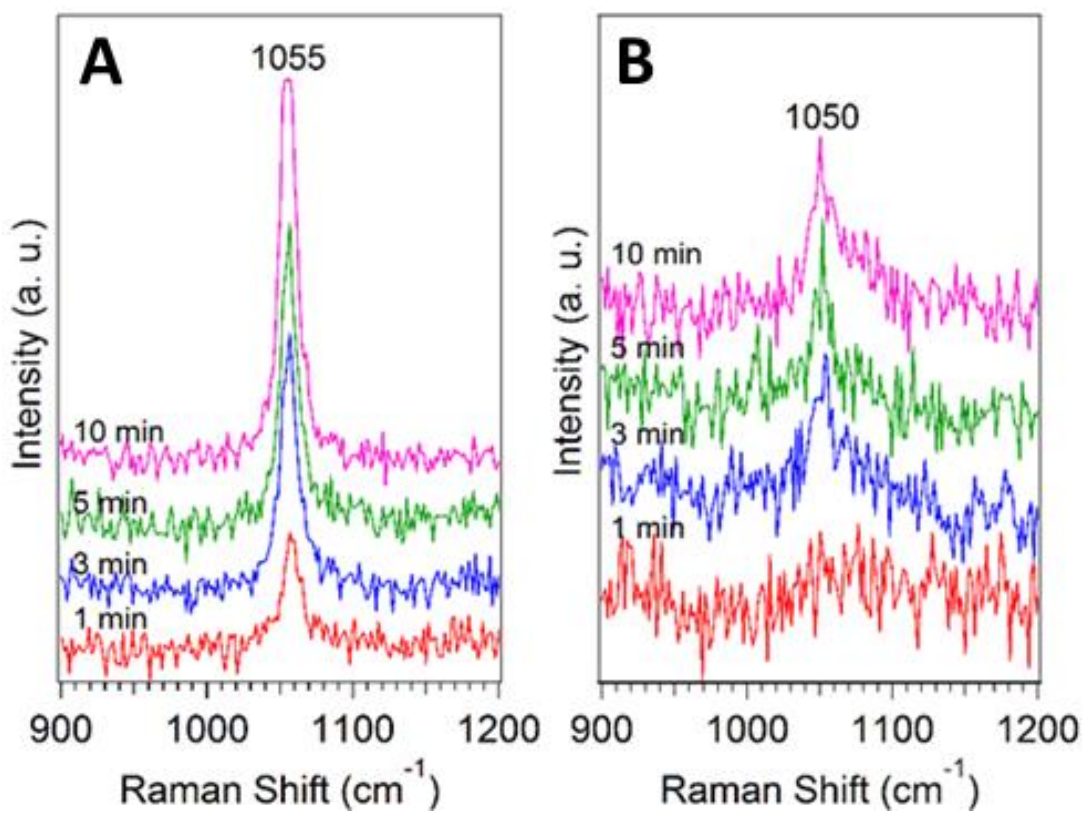


Figure 3.6: A) NaCl and B) LPS particle Raman spectra of the ν_1 nitrate stretching region as a function of HNO₃ exposure time. The nitrate peak increased with time for both particle types.

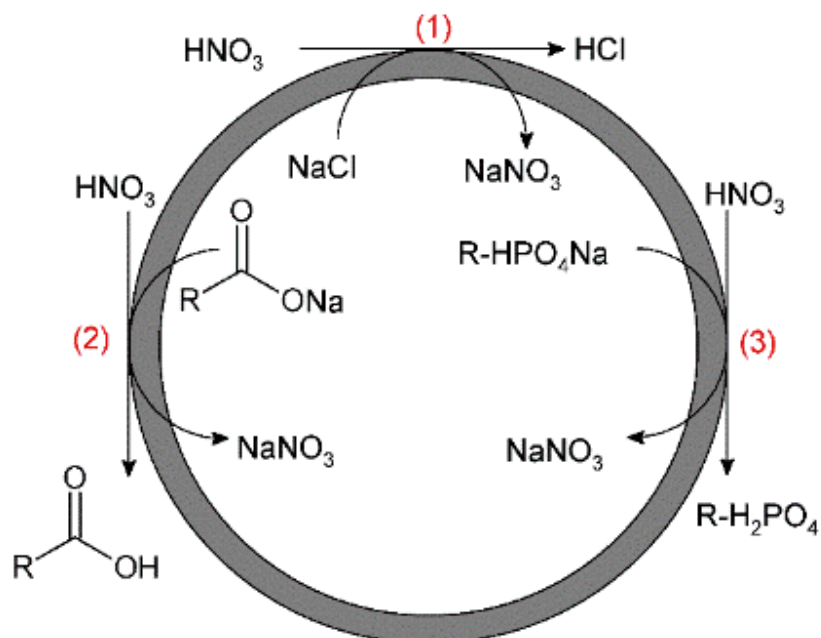


Figure 3.7: Nitric acid can react with different components of SSA as summarized above. (1) is the well-known chloride displacement reaction. Other reactive sites within the bioaerosols, in particular that of LPS, include carboxylate (2) and phosphate (3) groups.

3.7 Supporting Information

3.7.1 Micro-Raman Spectroscopy of Authentic SSA and Model System Particles

Figure 3.8 shows an optical image along with spectra of the three particle types identified (i.e., lipopolysaccharides, sea salt, and long chain carboxylic acid). A direct comparison of the micro-Raman spectroscopy signatures of the online HNO₃ reacted authentic SSA particles with the offline reacted model system particles is shown in Figure 3.8.

3.7.2 Molecular Structure and Reactivity of LPS and its Constituents

Figure 3.9 shows the structure of LPS as well as the structures of the Lipid A, Kdo₂-Lipid A, and DPPA standards that were used in this study. Additionally, particles containing only the saccharide portion of LPS (i.e., inner core, outer core, and O-antigen; denoted as the unreacted and reacted core, O-antigen in Figure 3.4 of the main text) were prepared and exposed to nitric acid. The particles were prepared by hydrolyzing LPS to cleave the Lipid A from the parent molecule.²⁰

3.7.3 Micro-Raman Spectroscopy of Nitrate Salts

Nitrate salts form in the reaction of carboxylate and phosphate groups with gas-phase nitric acid. The exact frequencies of the vibrational mode of the nitrate anion will depend on the counter cation (NaNO₃, KNO₃, Mg(NO₃)₂ and Ca(NO₃)₂) and relative humidity (20% versus 76% RH) as shown in Figures 3.11 and Figure 3.12, respectively. As seen, the exact positions of the peaks depend on the type of cation present^{13,21,22} and relative humidity.³⁶

3.7.4 Reactivity of Carboxylate and Phosphate Groups

The full Raman spectra for reacted carboxylate model systems and DPPA are shown in Figure 3.13. These spectra complement Figure 3.5 in the main text which only shows the spectra from 500 to 2000 cm⁻¹.

3.7.5 Gas Phase Acid/Base Characteristics of Selected Proxy Molecules

For thermodynamic analysis of the proton transfer reaction between HNO_3 and LPS, molecules similar in structure to the reactive regions of LPS were chosen to act as proxies. Table 3.1 gives a list of the molecules chosen, along with their structures, gas-phase acidity (GPA) and the calculated $\Delta_{\text{rxn}}G^\circ$ for reaction with nitric acid.

3.7.6 Supporting Information Figures

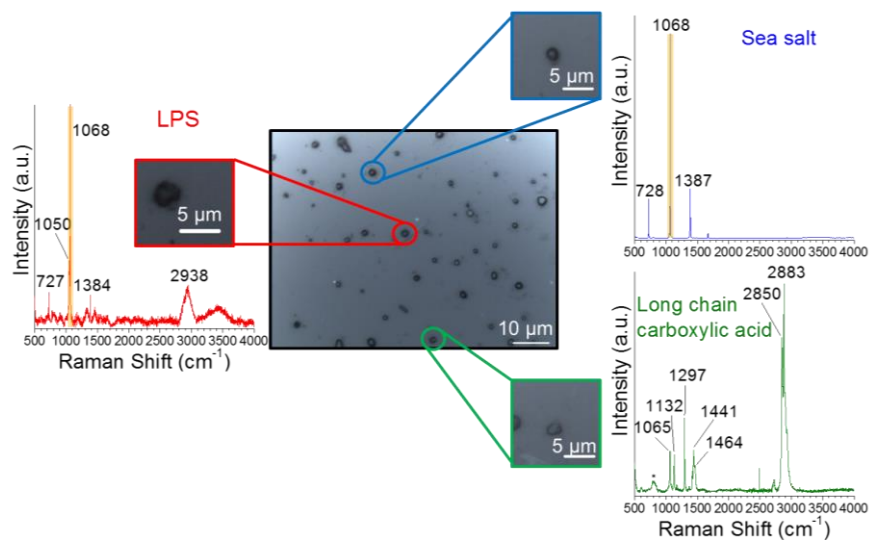


Figure 3.8: Optical image of SSA particles collected on a substrate following exposure to HNO₃. Raman spectra are shown for three of these particles. The yellow highlighted peak represents the symmetric stretch for the nitrate ion. Based on these spectra and model systems, different reactivity are seen for LPS (red), sea salt (blue) compared to the long chain carboxylic acids (green) which is non-reactive. (Note the band at 1065 cm⁻¹ is due to the C-O stretch of the carboxylic acid group.)

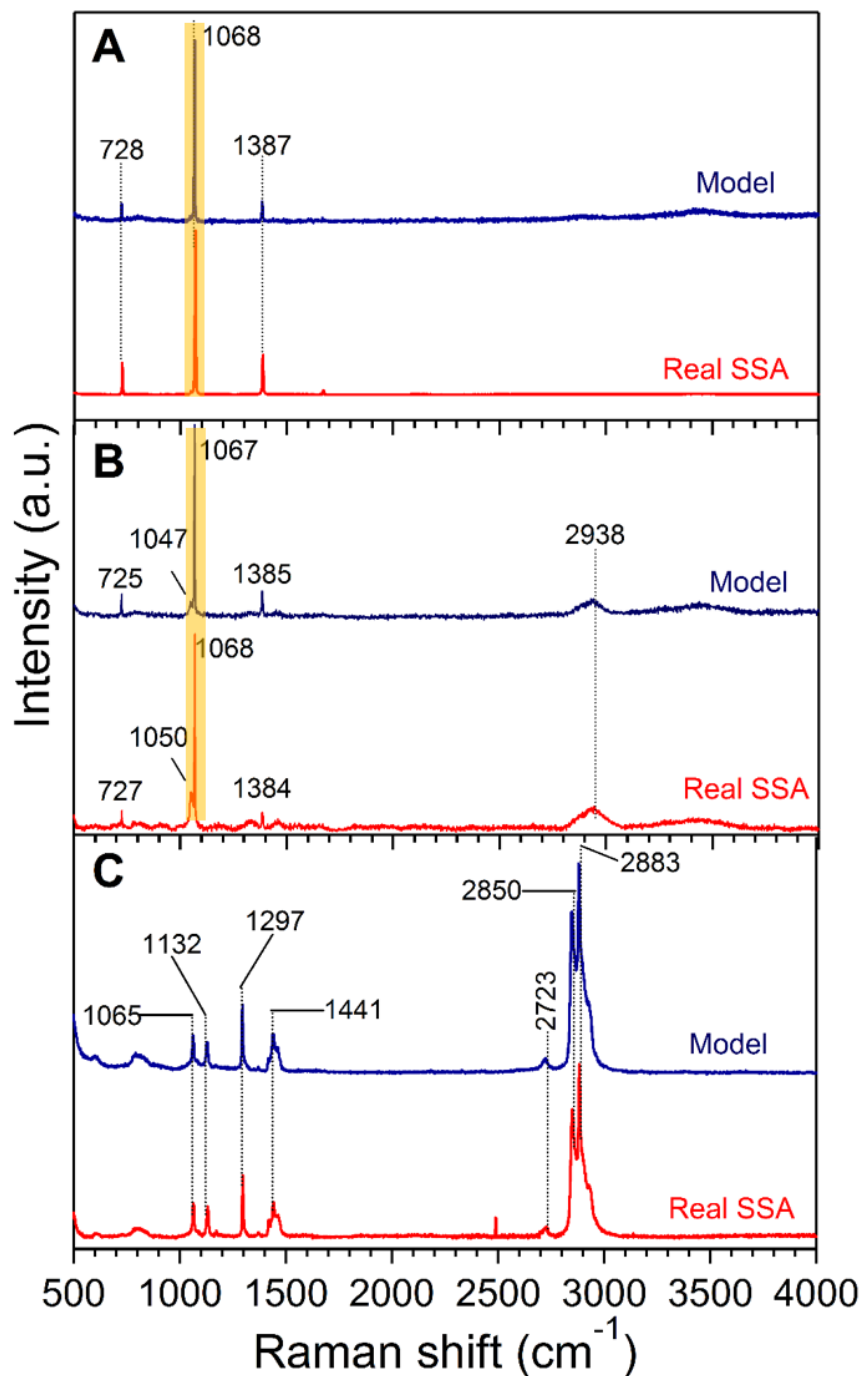


Figure 3.9: Raman spectra of the three HNO_3 reacted model systems (blue) compared to reacted real sea spray aerosol (red). The model systems are aerosolized samples of A) NaCl, B) LPS, and C) palmitic acid. Note that the band at 1065 cm^{-1} in the palmitic acid model and real SSA sample is due to the C-O stretch of the protonated carboxylic acid group. This peak does not change, as palmitic acid does not react upon exposure to HNO_3 .

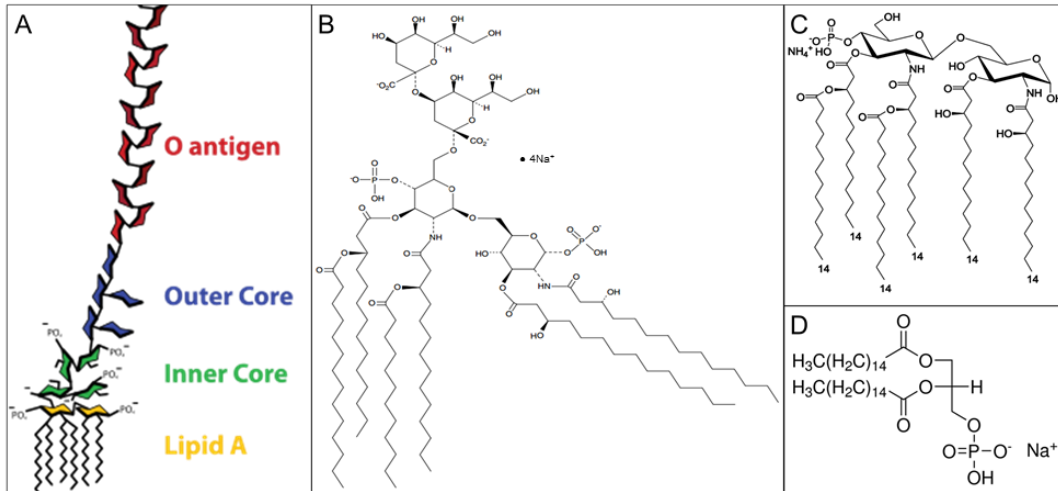


Figure 3.10: Chemical structure of model systems used A) lipopolysaccharide, B) Kdo₂-Lipid A, C) Lipid A, and D) DPPA.

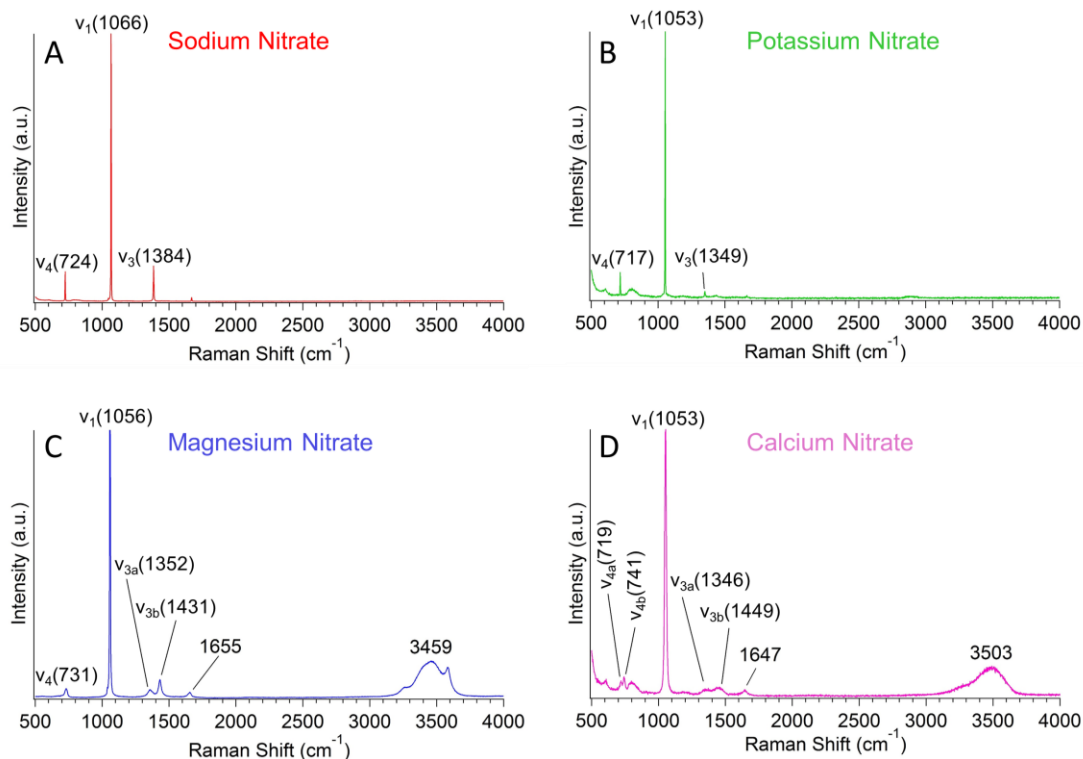


Figure 3.11: Raman spectra of atomized A) sodium nitrate, B) potassium nitrate, C) magnesium nitrate, and D) calcium nitrate from aqueous solutions. The frequency of specific vibrational modes depends on the cation present. In particular, the ν_1 mode shifts between 1053 and 1066 cm^{-1} . For both $\text{Mg}(\text{NO}_3)_2$ and $\text{Ca}(\text{NO}_3)_2$, water bands remain present due to the formation of stable amorphous hydrates that form for these divalent cation nitrate salts.^{37,38}

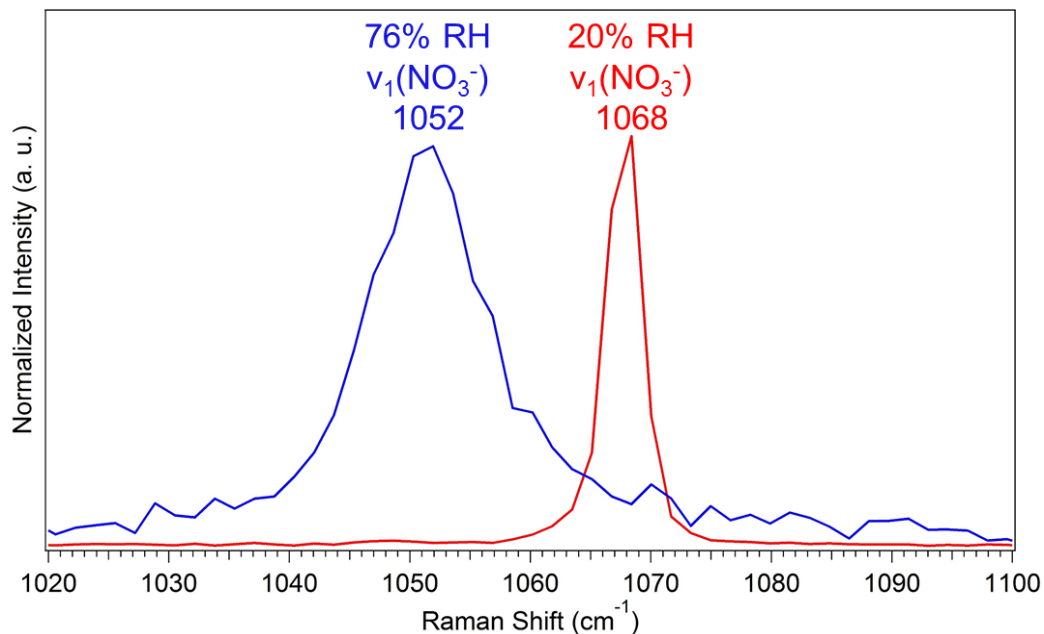


Figure 3.12: Raman spectra of a sodium nitrate particle at 20% and 76% relative humidity. The frequency of the $\nu_1(\text{NO}_3^-)$ vibrational mode changes from 1068 at 20% RH to 1052 cm^{-1} at 76% RH. The shift is due to interactions between the nitrate anion and water molecules.³⁶

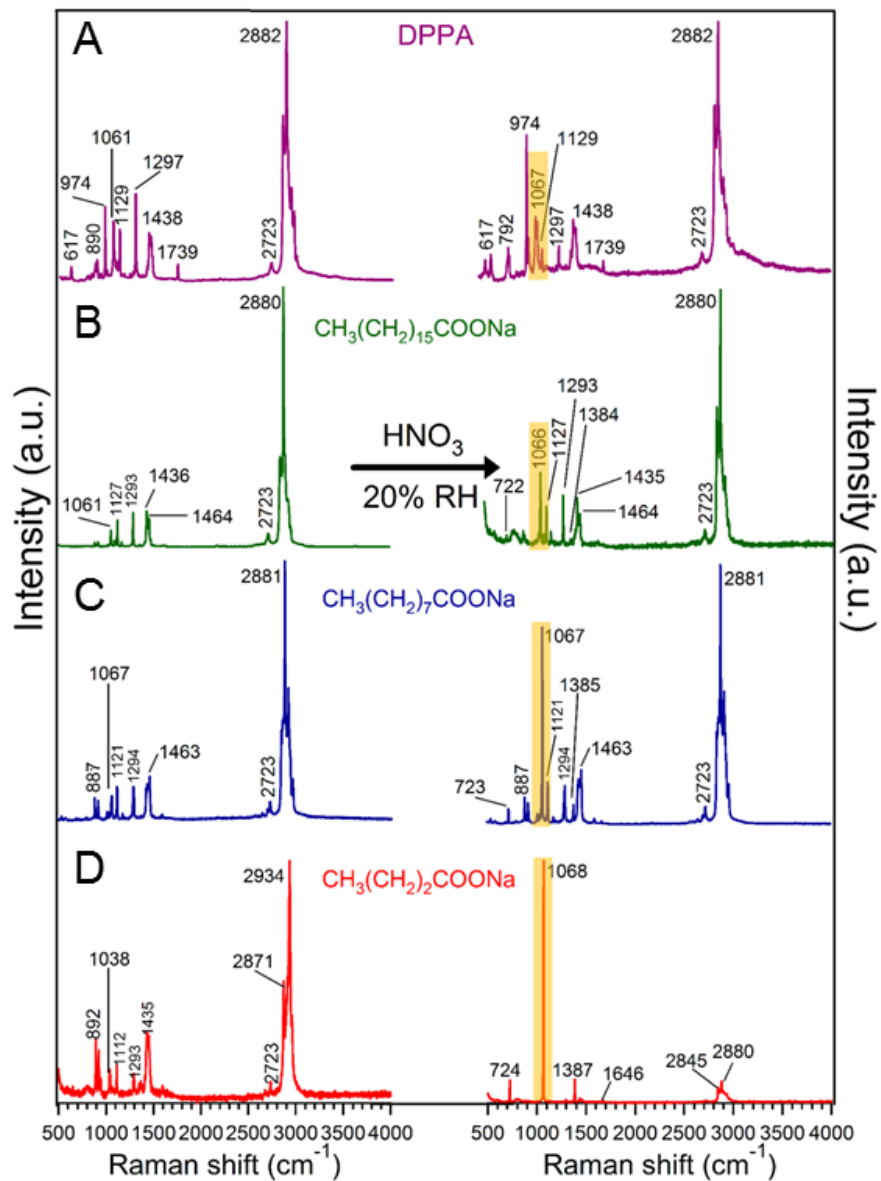
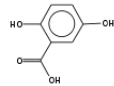
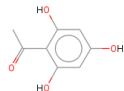
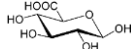
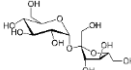
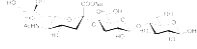
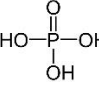
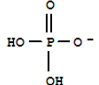
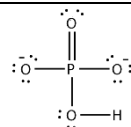


Figure 3.13: Full Raman spectra collected following reaction of HNO₃ with DPPA and three carboxylate model systems.

3.7.7 Supporting Information Tables

Table 3.1: Thermodynamic Properties and Molecular Structures of Chosen LPS Proxy Biomolecules.

Molecule	GPA kJ/mol	Structure	^a Calculated $\Delta_{\text{rxn}}G^\circ$ (kJ/mol)
Gentisic acid	1329 ³⁹		-0.7
Ethanone	1324 ³⁹		5.7
D-glucuronic acid	1331 ⁴⁰		-1.3
Sucrose	1373 ⁴⁰		-43.3
3-sialyllactose	1265 ⁴⁰		66.7
H ₃ PO ₄	1351 ⁴¹		-21.3
H ₂ PO ₄ ⁻	1883 ⁴¹		-553.3
HPO ₄ ²⁻	2402 ⁴¹		-1072.3

3.8 References

- (1) Rossi, M. J. Heterogeneous Reactions on Salts. *Chem. Rev.* **2003**, *103* (12), 4823–4882.
- (2) Finlayson-Pitts, B. J. Reactions at Surfaces in the Atmosphere: Integration of Experiments and Theory as Necessary (but Not Necessarily Sufficient) for Predicting the Physical Chemistry of Aerosols Barbara. *Phys. Chem. Chem. Phys.* **2009**, *11* (36), 7760.
- (3) Abbatt, J. P. D.; Lee, A. K. Y.; Thornton, J. A. Chem Soc Rev Quantifying Trace Gas Uptake to Tropospheric Aerosol : Recent Advances and Remaining Challenges W. **2012**, 6555–6581.
- (4) Quinn, P. K.; Collins, D. B.; Grassian, V. H.; Prather, K. A.; Bates, T. S. Chemistry and Related Properties of Freshly Emitted Sea Spray Aerosol. *Chem. Rev.* **2015**, *115* (10), 4383–4399.
- (5) Quinn, P. K.; Bates, T. S. The Case against Climate Regulation via Oceanic Phytoplankton Sulphur Emissions. *Nature* **2011**, *480* (7375), 51–56.
- (6) O’Dowd, C. D.; Facchini, M. C.; Cavalli, F.; Ceburnis, D.; Mircea, M.; Decesari, S.; Fuzzi, S.; Yoon, Y. J.; Putaud, J.-P. Biogenically Driven Organic Contribution to Marine Aerosol. *Nature* **2004**, *431* (7009), 676–680.
- (7) Jaenicke, R. Abundance of Cellular Material and Proteins in the Atmosphere. *Science* (80-.). **2005**, *308* (5718), 73.
- (8) Hawkins, L. N.; Russell, L. M. Polysaccharides, Proteins, and Phytoplankton Fragments: Four Chemically Distinct Types of Marine Primary Organic Aerosol Classified by Single Particle Spectromicroscopy. *Adv. Meteorol.* **2010**, *2010*, 1–14.
- (9) Prather, K. A.; Bertram, T. H.; Grassian, V. H.; Deane, G. B.; Stokes, M. D.; Demott, P. J.; Aluwihare, L. I.; Palenik, B. P.; Azam, F.; Seinfeld, J. H.; Moffet, R. C.; Molina, M. J.; Cappa, C. D.; Geiger, F. M.; Roberts, G. C.; Russell, L. M.; Ault, A. P.; Baltrusaitis, J.; Collins, D. B.; Corrigan, C. E.; Cuadra-Rodriguez, L. A.; Ebben, C. J.; Forestieri, S. D.; Guasco, T. L.; Hersey, S. P.; Kim, M. J.; Lambert, W. F.; Modini, R. L.; Mui, W.; Pedler, B. E.; Ruppel, M. J.; Ryder, O. S.; Schoepp, N. G.; Sullivan, R. C.; Zhao, D. Bringing the Ocean Into the Laboratory to Probe the Chemical Complexity of Sea Spray Aerosol. *Proc. Natl. Acad. Sci. U. S. A.* **2013**, *110* (19), 7550–7555.
- (10) Carpenter, L. J.; Nightingale, P. D. Chemistry and Release of Gases from the Surface Ocean. *Chem. Rev.* **2015**, *115* (10), 4015–4034.
- (11) Patterson, J. P.; Collins, D. B.; Michaud, J. M.; Axson, J. L.; Sultana, C. M.; Moser, T.; Dommer, A. C.; Conner, J.; Grassian, V. H.; Stokes, M. D.; Deane, G. B. Evans, J. E.; Burkart, M. D.; Prather, K. A.; Gianneschi, N. C. Sea Spray Aerosol Structure and Composition Using Cryogenic Transmission Electron Microscopy. *ACS Cent. Sci.* **2016**, *2* (1), 40–47.

- (12) Russell, L. M.; Hawkins, L. N.; Frossard, A. A.; Quinn, P. K.; Bates, T. S. Carbohydrate-like Composition of Submicron Atmospheric Particles and Their Production from Ocean Bubble Bursting. *Proc. Natl. Acad. Sci.* **2010**.
- (13) Ault, A. P.; Guasco, T. L.; Baltrusaitis, J.; Ryder, O. S.; Trueblood, J. V.; Collins, D. B.; Ruppel, M. J.; Cuadra-Rodriguez, L. A.; Prather, K. A.; Grassian, V. H. Heterogeneous Reactivity of Nitric Acid with Nascent Sea Spray Aerosol: Large Differences Observed between and within Individual Particles. *J. Phys. Chem. Lett.* **2014**, *5* (15), 2493–2500.
- (14) Wang, X.; Sultana, C. M.; Trueblood, J.; Hill, T. C. J.; Malfatti, F.; Lee, C.; Laskina, O.; Moore, K. A.; Beall, C. M.; McCluskey, C. S.; Cornwell, G.; Zhou, Y.; Cox, J.; Pendergraft, M.; Santander, M.; Bertram, T.; Cappa, C. D.; Azam, F.; DeMott, P.; Grassian, V. H.; Prather, K. A. Microbial Control of Sea Spray Aerosol Composition: A Tale of Two Blooms. *ACS Cent. Sci.* **2015**, *1* (3), 124–131.
- (15) Laskina, O.; Morris, H. S.; Grandquist, J. R.; Estillore, A. D.; Stone, E. A.; Grassian, V. H.; Tivanski, A. V. Substrate-Deposited Sea Spray Aerosol Particles: Influence of Analytical Method, Substrate, and Storage Conditions on Particle Size, Phase, and Morphology. *Environ. Sci. Technol.* **2015**, *49* (22), 13447–13453.
- (16) Gard, E.; Mayer, J. E.; Morrical, B. D.; Dienes, T.; Ferguson, D. P.; Prather, K. A. Real-Time Analysis of Individual Atmospheric Aerosol Particles: Design and Performance of a Portable ATOFMS. *Anal. Chem.* **1997**, *69* (20), 4083–4091.
- (17) Baltrusaitis, J.; Jayaweera, P. M.; Grassian, V. H. XPS Study of Nitrogen Dioxide Adsorption on Metal Oxide Particle Surfaces under Different Environmental Conditions. *Phys. Chem. Chem. Phys.* **2009**, *11* (37), 8295–8305.
- (18) Rouxhet, P. G.; Mozes, N.; Dengis, P. B.; Dufrière, Y. F.; Gerin, P. A.; Genet, M. J. Application of X-Ray Photoelectron Spectroscopy to Microorganisms. *Colloids Surfaces B Biointerfaces* **1994**, *2* (1), 347–369.
- (19) Boman, H. G.; Monner, D. a. Characterization of Lipopolysaccharides From Escherichia Coli K-12 Mutants. *J. Bacteriol.* **1975**, *121* (2), 455–464.
- (20) Wang, Y.; Cole, R. B. Acid and Base Hydrolysis of Lipid A from Enterobacter Agglomerans as Monitored by Electrospray Ionization Mass Spectrometry: Pertinence to Detoxification Mechanisms. *J. Mass Spectrom.* **1996**, *31* (2), 138–149.
- (21) Zangmeister, C. D.; Pemberton, J. E. Raman Spectroscopy of the Reaction of Sodium Chloride with Nitric Acid: Sodium Nitrate Growth and Effect of Water Exposure. *J. Phys. Chem. A* **2001**, *105* (15), 3788–3795.
- (22) Xu, M.; Tang, C. Y.; Jubb, A. M.; Chen, X.; Allen, H. C. Nitrate Anions and Ion Pairing at the Air # Aqueous Interface. *J. Phys. Chem. C* **2009**, *113* (6), 2082–2087.
- (23) Chebbi, a; Carlier, P. Carboxylic Acids in the Troposphere, Occurrence, Sources and Sinks:

- A Review. *Atmos. Environ.* **1996**, *30* (24), 4223–4249.
- (24) Bouchoux, G. GAS-PHASE BASICITIES OF POLYFUNCTIONAL MOLECULES. PART 1: THEORY AND METHODS. *Mass Spectrom. Rev.* **2007**, *26*, 775–835.
- (25) Hunter, Edward P. L.; Lias, S. G. Evaluated Gas Phase Basicities and Proton Affinities of Molecules; Heats of Formation of Protonated Molecules. *J. Phys. Chem. Ref. Data* **1998**, *27*, 413.
- (26) Hartley, J. L.; Adams, G. L.; Tornabene, T. G. Chemical and Physical Properties of Lipopolysaccharide of Yersinia Pestis. *J. Bacteriol.* **1974**, *118* (3), 848–854.
- (27) Raczyńska, E. D.; Gal, J. F.; Maria, P. C.; Zientara, K.; Szlag, M. Application of FT-ICR-MS for the Study of Proton-Transfer Reactions Involving Biomolecules. *Anal. Bioanal. Chem.* **2007**, *389* (5), 1365–1380.
- (28) Thomas, M. C.; Mitchell, T. W.; Blanksby, S. J. A Comparison of the Gas Phase Acidities of Phospholipid Headgroups: Experimental and Computational Studies. *J. Am. Soc. Mass Spectrom.* **2005**, *16* (6), 926–939.
- (29) Hoaglund-Hyzer, C. S.; Counterman, A. E.; Clemmer, D. E. Anhydrous Protein Ions. *Chem. Rev.* **1999**, *99* (10), 3037–3080.
- (30) Din, Z.; Mukerjee, P.; Kastowsky, M.; Takayama, K. Effect of pH on Solubility and Ionic State of Lipopolysaccharide Obtained from the Deep Rough Mutant of Escherichia Coli. *Biochemistry* **1993**, *32* (17), 4579–4586.
- (31) Borrok, D.; Turner, B. F.; Fein, J. B.; Hall, F.; Dame, N. A Universal Surface Complexation Framework for Modeling Proton Binding onto Bacterial Surfaces in Geologic Settings. **2005**, *305*, 826–853.
- (32) Phoenix, V. R.; Korenevsky, A. A.; Ferris, F. G.; Gorby, Y. A.; Beveridge, T. J. Influence of Lipopolysaccharide on the Surface Proton-Binding Behavior of Shewanella Spp. *Curr. Microbiol.* **2007**, *55* (2), 152–157.
- (33) Wang, B.; O'brien, R. E.; Kelly, S. T.; Shilling, J. E.; Moffet, R. C.; Gilles, M. K.; Laskin, A. Reactivity of Liquid and Semisolid Secondary Organic Carbon with Chloride and Nitrate in Atmospheric Aerosols. *J. Phys. Chem. A* **2015**, *119* (19), 4498–4508.
- (34) Morris, H. S.; Estillore, A. D.; Laskina, O.; Grassian, V. H.; Tivanski, A. V. Quantifying the Hygroscopic Growth of Individual Submicrometer Particles with Atomic Force Microscopy. *Anal. Chem.* **2016**, *88* (7), 3647–3654.
- (35) Pöschl, U.; Shiraiwa, M. Multiphase Chemistry at the Atmosphere-Biosphere Interface Influencing Climate and Public Health in the Anthropocene. *Chem. Rev.* **2015**, *115* (10), 4440–4475.

- (36) Liu, Y. J.; Zhu, T.; Zhao, D. F.; Zhang, Z. F. Investigation of the Hygroscopic Properties of Ca(NO₃)₂ and Internally Mixed Ca(NO₃)₂/CaCO₃ Particles by Micro-Raman Spectrometry. *Atmos. Chem. Phys.* **2008**, *8* (23), 7205–7215.
- (37) Al-Abadleh, H. A.; Grassian, V. H. Phase Transitions in Magnesium Nitrate Thin Films: A Transmission FT-IR Study of the Deliquescence and Efflorescence of Nitric Acid Reacted Magnesium Oxide Interfaces. *J. Phys. Chem. B* **2003**, *107* (39), 10829–10839.
- (38) Schuttlefield, J.; Al-Hosney, H.; Zachariah, A.; Grassian, V. H. Attenuated Total Reflection Fourier Transform Infrared Spectroscopy to Investigate Water Uptake and Phase Transitions in Atmospherically Relevant Particles. *Appl. Spectrosc.* **2007**, *61* (3), 283–292.
- (39) Linstrom, P.; Mallard, W. NIST Standard Reference Database Number 69. In *National Institute of Standards and Technology*; Gaithersburg, MD, 2003.
- (40) Cai, Y.; Jiang, Y.; Cole, R. B. Anionic Adducts of Oligosaccharides by Matrix-Assisted Laser Desorption / Ionization Time-of-Flight Mass Spectrometry. *Anal. Chem.* **2003**, *75* (7), 1638–1644.
- (41) Moser, A.; Range, K.; York, D. M. Accurate Proton Affinity and Gas-Phase Basicity Values for Molecules Important in Biocatalysis. *J. Phys. Chem. B* **2010**, *114* (43), 13911–13921.

Chapter 4 The Old and the New: Aging of Sea Spray Aerosols and Formation of Secondary Marine Aerosol Through OH Oxidation Reactions

4.1 Synopsis

Marine aerosols (MA) are classified into two broad categories: primary sea spray aerosols (SSA) produced upon the breaking of waves, and secondary marine aerosol (SMA) produced upon the oxidation of gas phase species. Regarding SSA, heterogeneous oxidation reactions initiated by gas-phase hydroxyl radicals (OH) have been shown in some cases to cause a decrease in the amount of particulate carbon present in aerosol particles through fragmentation reactions that produce volatile product species, which are subsequently lost to the gas phase. The importance of these reactions on sea spray aerosol (SSA) is largely unknown. As SSA has a complex chemical composition consisting of a mixture of salts and organic compounds that changes as a function of ocean biology, it is likely that OH-initiated oxidation reactions of SSA will be different from that of aerosols from terrestrial sources because of differences in their molecular compositions. OH is also believed to be an important reactive gas in the formation of SMA through its oxidation of volatile organic compounds (VOCs) released by oceanic phytoplankton. In this study, we have investigated the effect of OH oxidation reactions on the formation and chemical composition of marine-derived aerosols using a Marine Aerosol Reference Tank (MART) filled with water from a lab-grown phytoplankton bloom to produce SSA particles and volatile organic compounds (VOCs) representative of those found over the ocean. We then used on-line and off-line methods to compare unreacted nascent marine aerosols to the marine aerosols that resulted from MART headspace and SSA being sent through a Potential Aerosol Mass (PAM) reactor and exposed to OH radicals. Several single particle methods of analysis were used, including micro-Raman spectroscopy and atomic force microscopy (AFM) coupled to photothermal infrared spectroscopy (PTIR) to

investigate composition and size of substrate deposited particles, and *in situ* particle mass measurements using an aerosol mass spectrometry (AMS) to understand marine aerosol chemistry. Raman spectra of resulting SSA showed that heterogeneous OH oxidation reactions significantly lower the amount of organic matter found in supermicron SSA particles, which are dominated, in part, by nitrogen containing species (e.g., amino sugars/amino acids) during periods of high biological productivity. Furthermore, AFM and AMS analyses showed the formation of secondary marine aerosols (SMA) in the submicron size regime due to oxidation of biologically produced VOCs. These results provide important insights into how the combined effects of ocean biological activity and OH oxidation reactions determine the overall chemical composition of marine aerosols (SMA and SSA) across multiple size regimes and formation mechanisms.

4.2 Introduction

Atmospheric aerosols are an important part of the Earth's system, influencing biogeochemical cycles, air quality, human health, and climate.¹ Aerosols formed in marine regions (hereafter termed marine aerosols) include primary sea spray aerosol (SSA) particles generated upon the breaking of waves, as well as secondary marine aerosols (SMA) formed upon the oxidation of VOCs (e.g., alkenes, dimethyl sulphide, isoprene, monoterpenes) released from the surface ocean during periods of biological activity.² As roughly two thirds of the Earth's surface are covered by oceans, marine aerosols are an important contributor to the total global aerosol inventory.^{2,3}

With respect to climate impacts, aerosols are known to alter the amount of radiation that reaches the Earth's surface both directly by scattering and absorbing processes, as well as indirectly by serving as cloud condensation nuclei (CCN) upon which water vapor condenses to form cloud droplets. A critical factor in determining the behavior of aerosols as CCN is their physicochemical properties, which are a function of their source and formation mechanisms. Furthermore, the

properties of aerosols can change drastically as a result of atmospheric aging processes such as heterogeneous photochemical and homogenous oxidation reactions.⁴ As such, a better understanding of these processes is needed to reduce the uncertainties associated with aerosols and their impacts on climate.

It has long been known that OH radicals react with gas-phase volatile organic compounds (VOCs) over terrestrial regions to produce secondary organic aerosol (SOA).^{5,6} However, less known is regarding the impact of OH radical initiated reactions of VOCs emitted during periods of high oceanic biological activity in marine regions, and the resulting secondary marine aerosols that are formed. Perhaps the most well known VOC involved in secondary aerosol formation in marine regions is methanesulfonic acid (MSA), which is formed upon the atmospheric oxidation of dimethylsulfide (DMS). However, other formation processes involving different VOCs such as biogenically formed isoprene and alkyl amines have also begun to receive more attention.⁷ Despite this, the formation of secondary marine aerosols in marine regions remains largely unexplained.⁷

Furthermore, only recently has attention been given to the impact of OH reactions on condensed phase organic aerosols consisting mainly of simple hydrocarbons.⁸ It is currently understood that the OH-initiated oxidation of hydrocarbons begins with hydrogen abstraction, followed by the formation of reactive oxygenated species (ROS). From there, functionalization reactions can lead to the formation of oxygenated low volatility species with a concomitant increase in particle mass, density, and hygroscopicity. Alternatively, fragmentation reactions via C-C bond scission can lead to the formation of higher volatility species and subsequent reduction in particle mass due to volatilization. However, attempts to determine the importance of each pathway have produced varying results. Some studies have found the functionalization reactions are the dominant pathway^{9,10} while others indicate the fragmentation pathway to be of greater importance.^{11,12,9,13,14,15}

As such, the extent to which fragmentation reactions dominate varies, is difficult to predict, and is most likely dependent on chemical speciation and specific molecular species involved.

To date, studies examining the heterogeneous OH-oxidation of aerosols have focused largely on systems that are representative of terrestrial aerosols (e.g., secondary organic aerosols, particulate organic aerosols, and biomass burning aerosols).⁸ As previous studies have shown that the chemical composition of SSA is unique from terrestrial aerosols and changes based on ocean biological activity,^{16,17} SSA particles are expected to exhibit different reactivities than their terrestrial counterparts. As such, there is a need for experiments that investigate the effects of OH-oxidation on authentic SSA particles that accounts for their dynamic and complex chemical composition.

In this study, we investigated the combined impact of heterogeneous OH-oxidation reactions on authentic SSA and of homogeneous OH-oxidation reactions on VOCs generated during a phytoplankton bloom on the overall chemical composition of marine aerosols. Our findings suggest that the fragmentation reactions by OH-oxidation are highly efficient for supermicron SSA particles composed of amino sugars/amino acids, which ultimately leads to losses in their particulate organic carbon mass. In addition, oxidation of VOCs was found to lead to formation of SMA, the extent of which depends on ocean biology. These results help to explain how the OH-oxidation of biologically produced VOCs and SSA control the physicochemical properties of the overall marine aerosol budget.

4.3 Methods

4.3.1 Mesocosm Experiment

To replicate the chemical complexity of the ocean, an algae bloom was grown outdoors in a 2,400 L tank filled with Pacific Ocean water collected from Scripps Pier (32.86 N, -117.25 W). Phytoplankton growth was stimulated by spiking the system with an f/100 nutrient mixture

(Proline, Aquatic Eco-Systems, Apopka, FL), which was diluted from the typical f/2 used in algae growth studies to generate a more realistic bloom cycle. Details of the bloom can be found in Mayer et al. (to be submitted). The bloom was tracked by monitoring chlorophyll-a (chl-a) concentration, dissolved organic carbon (DOC), and bacteria counts. Chl-a concentration was determined using a Turner AquaFluor handheld unit, while bacteria concentrations were determined by collecting samples onto 0.02 μm filters and then staining them with SYBR green dye for analysis with an epifluorescence microscope (Keyence BZ-X700).

When chl-a levels began to rise, authentic SSA was generated by transferring 120 L of the water to a Marine Aerosol Reference Tank (MART) during each day of the experiment. Detailed information on the MART can be found in elsewhere.¹⁸ Briefly, the system uses a plunging waterfall to generate bubbles with a size distribution that accurately mimics that of breaking waves in the ocean. Upon the bursting of surface bubbles, primary SSA were produced and then either sent directly for on-line and off-line analysis (nascent SSA) or were sent along with the MART headspace through a PAM for exposure to OH radicals (PAM-derived MA) (see next section) before being analyzed.

4.3.2 Oxidation of SSA and VOCs via OH Exposure

To simulate the aging of aerosols and formation of SMA through oxidation of VOCs by OH radicals, SSA and headspace from the MART were passed through a Potential Aerosol Mass oxidative flow reactor (PAM-OFR). The PAM uses UV lamps with wavelengths of $\lambda=185$ nm and 254 nm (OFR185 mode) to produce OH radicals. OH exposure was calibrated by introducing SO_2 (30 ppb) into the PAM at the same air flow rate and relative humidity used during the sampling experiments. SO_2 concentration was calculated after being passed through the PAM, and was used to calculate the OH exposure based on SO_2 -OH-oxidation kinetics. The residence time of air flow in the PAM-OFR was 160 seconds. The OH exposure was set to be $\sim(4.3\pm 1.3)\times 10^{11}$ molecules x

sec/cm³, which is equivalent to $\sim 3.3 \pm 0.5$ days of aging under a typical atmospheric condition where OH concentrations are on the order of $\sim 1.5 \times 10^6$ molecules/cm³.

4.3.3 Off-line sampling of Nascent SSA and Marine Aerosols Exposed to OH Radicals (PAM-Derived MA)

For off-line analysis, individual nascent SSA particles exiting directly from the MART and PAM-derived MA (i.e., secondary marine aerosols formed through OH oxidation of VOCs and OH-aged SSA) were impacted onto separate quartz and silicon wafers using stages 4 and 7 of a micro-orifice uniform deposition impactor (MOUDI, MSP Corp. Model 110), operating at a flow rate of 10 lpm for 30 minutes. Stage four of the MOUDI collected particles with an aerodynamic diameter between 1.8 to 3.2 μm , while stage seven sampled particles between 0.32 to 0.56 μm . Samples were transferred to containers and sealed with PTFE tape inside a nitrogen purged glove box and then stored at room temperature until analysis.

4.3.4 Micro-Raman Spectroscopy of Supermicron Nascent SSA and PAM-Derived MA

Raman spectra of individual supermicron aerosol particles were collected using a LabRam HR Evolution Confocal Raman Spectrometer (Horiba). The spectrometer was equipped with an Olympus BX41 optical microscope with 100X magnification lens. Spectra were collected between 100-4000 cm^{-1} with a 532 nm laser. Two exposures of 10 second exposure time were averaged to obtain the resulting spectra. Each particle was then classified by comparing its spectrum to a spectral database of over 100 model systems, as done in previous studies.¹⁷ If the Raman signal from organics in a given aerosol particle was too low, the particle was classified as sea salt (SS).

4.3.5 Atomic Force Microscopy-Photo-Thermal Infrared Spectroscopy of Submicron Nascent SSA and PAM-Derived MA

Off-line analysis via atomic force microscopy-photo-thermal infrared spectroscopy (AFM-PTIR) of submicron marine aerosol particles impacted on silicon wafers was conducted using a commercial nanoIR2 microscopy system (Bruker, Santa Barbara, CA, USA). AFM imaging of the

particles was conducted at 298 K and a relative humidity (RH) of ~30% at ambient pressure. Images were scanned at a rate of 0.5 Hz using a gold-coated silicon nitride probe (tip radius <30 nm) with 1-7 N m⁻¹ spring constant and 75 ± 15 kHz resonant frequencies in tapping mode. Particle counts and their spherical volume equivalent diameter were then acquired from 20x20 μm² images (N = 9) of the particle-coated substrate. Photo-thermal infrared spectra were collected across the spectral range (2500-3600 cm⁻¹) with a spectral resolution of 4 cm⁻¹ and by averaging 1024 laser pulses per wavenumber. Chemical maps were collected at a scan rate of 0.1 Hz, averaging 8 times per pixel.

4.3.6 Online sampling of Submicron Nascent SSA and PAM-Derived MA

Aerosol mass was determined using a high-resolution time-of-flight aerosol mass spectrometer (HR-ToF-AMS), which characterizes non-refractory aerosol components. Briefly, dried aerosol entered the AMS through an aerodynamic focusing lens, forming a narrow particle beam which was then collected by a hot vaporizer. Non-refractory materials were then vaporized and ionized by electron impact. Finally, a high-resolution time-of-flight mass spectrometer was used to detect the generated ions. A capture vaporizer was used in the AMS and its temperature was set to 650°C to vaporize non-refractory aerosol mass. AMS signals were calibrated by known mass concentration of NH₄NO₃ particles, which were produced from an atomizer. The mass size distribution was determined using AMS particle time of flight (PToF) mode, which separated aerosol particles based on their vacuum aerodynamic size. The detailed description of this process can be found elsewhere.¹⁹

4.4 Results and Discussion

4.4.1 Biological Activity of Seawater

Figure 4.1 shows the changing bloom conditions over time as tracked by chl-a, DOC, and bacteria concentration. At the start of the experiment, chl-a was at elevated levels as the bloom had already begun before transfer of the water to the MART. Chl-a then reached a maximum on a

specific date 9/2 (all experiments done in 2016) as biological activity was at a maximum, and then dropped again as the bloom died on 9/5. DOC largely correlated with chl-a concentrations, while bacteria counts lagged chl-a slightly, peaking two days after the chl-a maximum on 9/4.

4.4.2 Formation of Secondary Marine Aerosols (SMA)

Figure 4.2 shows the AMS determined mass size distributions of organic signals and their respective curve fits for nascent SSA and PAM-derived MA (OH-exposed SSA and MART headspace). PAM-derived MA mass shows a significant mode that peaks at around 200 nanometers, which we attribute to the formation of SMA. Figure 4.3 shows the curve fits of AMS-derived mass size distributions of organic signals for PAM-derived MA as a function of bloom age. The SMA mode at ca. 200 nm was significant at the beginning of the bloom and decreased with bloom age towards the end of the experiment. This trend suggests that the SMA formation was associated with phytoplankton concentration in seawater. Indeed, it is well known that VOCs such as dimethyl sulfide (DMS) can form sulfate or methanesulfonic acid (MSA) secondary aerosols.

Figure 4.4 shows particle counts of substrate-impacted particles as well as amplitude images (20 μm x 20 μm) of substrate deposited PAM-derived MA taken by AFM on two different days during the bloom (9/01 and 9/05). Particle counts reveal a larger number of particles in the smallest size ranges for PAM-derived MA particles at the beginning of the bloom (9/01) vs the end (9/05), in agreement with the data shown by AMS. This further indicates that SMA formation was linked to the biological activity of the seawater.

Spectral analysis by AFM-PTIR of two submicron PAM-derived MA particles is shown in Figure 4.5. Figure 4.5A shows the AFM amplitude of a particle with a volume equivalent diameter of 250 nm, which according to AMS data is within the size range dominated by SMA. PTIR spectra taken at the particle core and shell (Fig. 4.5B) further confirm the presence of organics, with peaks at 2940 and 2972 cm^{-1} attributed to C–H stretching modes of organic species. Comparison of a 3D

height map of a different particle with volume equivalent diameter of 70 nm (4.5C) and its corresponding chemical map at 2930 cm^{-1} in Figure 4.5D reveals the particle shell is composed largely of organics. Together, these results confirm the presence of organics in particles at both upper and lower ends of the size range determined by AMS to be attributed largely to SMA.

4.4.3 Fragmentation Reactions and Loss of Organic Matter in PAM-Derived MA

In addition to the formation of SMA, Raman spectroscopy of supermicron-sized PAM-derived MA particles (wet diameter = 1.8 to 3.2 μm) showed evidence of fragmentation reactions due to heterogeneous OH reactions with SSA, resulting in significant losses of particulate organic matter. Figure 4.6 shows the relative fractions of particles that were classified as organic, burnt/fluorescing, or sea salt (SS) according to Raman spectroscopy across all days for supermicron nascent SSA and PAM-derived MA. The particle classification method is carried out as in previous studies.¹⁷ As previously noted, particles were classified as sea salt if the organic signature was low. It is important to point out that this does not mean the particle was purely sea salt, but that the contribution of organics in the particle was too low for detection with Raman. Particles classified as burnt/fluorescing have highly fluorescent spectra and are likely due to the presence of humic-like substances as well as organic components, including biological materials.²⁰ Nascent SSA summed across all days contained 23% more organic particles than PAM-derived MA (83% vs 60%, respectively), and 26% fewer sea salt particles (10 vs 36%, respectively). The remaining 3% difference between nascent SSA and PAM-derived MA is due to a decrease in burnt/fluorescing particles from 7% to 4% between nascent SSA and PAM-derived MA, respectively.

To further explain the changes seen in supermicron particles, we examined the Raman spectra of the most common particle type in supermicron nascent SSA and PAM-derived MA particles across all days. This particle type has previously been identified as either free saccharides/amino sugars or as an alpha-amino acid such as magnesium alanine.^{17,21} Figure 4.10 in

the Supporting Information Figures Section 4.8.1 compares a representative spectrum of this particle type with spectra of model system sialic acid and the amino acid alanine. Further discussion of this particle type and its assignment can be found in the literature.¹⁷ Figure 4.7 shows the integrated area of the CH stretching region (2700 to 3100 cm^{-1}) for all nascent SSA and PAM-derived MA particles belonging to this particle type across all days. The clear drop in integrated area from nascent SSA to PAM-derived MA suggests that the amount of organic matter present in these particles was reduced due to OH exposure as volatile product species were lost to the gas phase. Previous studies have found that fragmentation reactions dominate in particles with $\text{O/C} > 0.4$.¹⁵ Considering alanine has an O/C ratio of 0.66, and sialic acid, a model system for amino sugars, has an O/C ratio of 0.82, it is reasonable that this particle type would be highly susceptible to fragmentation reactions due to exposure to OH radicals.

4.4.4 Proposed Reaction Mechanism

A simple reaction mechanism for OH oxidation of aerosols consisting of simple hydrocarbon species has previously been proposed.⁸ The first two steps of this mechanism consist of hydrogen abstraction and subsequent formation of an alkyl radical, which then reacts with O_2 to form an alkylperoxy radical (RO_2). Next, either an RO alkoxy radical is formed through self-reaction, or one of several other pathways involving reaction with HO_2 , NO_x occurs. Upon formation of RO alkoxy radicals, lower-volatility oxygenated species are then either generated via isomerization reaction with O_2 and chain propagation, or lower molecular weight, higher volatility species are formed via decomposition through C-C scission.

For the chemically distinct SSA observed in our study, we propose a similar mechanism by OH radicals for an SSA particle containing amino acids such as alanine (Figure 4.8). This mechanism is based on previous studies of OH-initiated reactions of simple alpha-amino acids.^{22,23} Possible products formed include CO_2 , ammonia (NH_3), ammonium (NH_4^+), as well as

formaldehyde (HCHO) and other radical species. Interestingly, the formation of HCHO could help to explain discrepancies seen in previous studies between HCHO observations and models.²⁴

Spectroscopic evidence for this reaction mechanism is shown in the difference spectrum (PAM-derived MA – Nascent SSA) of the average of normalized Raman spectra of the most common particle type across all days (Figure 4.9). The effect of the loss of organics due to fragmentation and subsequent volatilization is seen in the negative peaks from 2800 to 3000 cm^{-1} which are due to symmetric and asymmetric CH stretches. Furthermore, positive peaks indicate a greater relative contribution from ammonia, ammonia salt complexes, and NH_2 containing species as other volatile product species are lost. Positive peaks located in the regions 1035 to 1070, 1550 to 1650, and 3000 to 3400 cm^{-1} are due to symmetric deformation, degenerate deformation, and antisymmetric and symmetric stretching of NH_3 , respectively. These regions are highlighted in Figure 4.9, with the specific location of the peaks within each region based on the surrounding environment.^{25,26} Finally, evidence for the formation of ammonium can be seen in the shift of the SO_4^{2-} symmetric stretching peak in the Figure 4.9. As ammonium ions are formed, it is expected that ammonium sulfate will be formed at the expense of other species (e.g., sodium sulfate, calcium sulfate, magnesium sulfate). The positive going peak at lower wavenumber 977 cm^{-1} is due to SO_4^{2-} symmetric stretching of ammonium sulfate, while negative peaks at 992 and 1016 cm^{-1} are due to lower contributions of sodium sulfate and calcium sulfate, respectively, as the relative number of cation species is shifted.^{27,28,29}

It should be noted that the efficiency of the reaction mechanism presented in Figure 4.8 will depend on the pH of the aerosol particle. If the aerosol is acidic, the nitrogen will remain protonated and the initial attack of the OH radical will occur on the carbon chain. Under more basic conditions, the nitrogen becomes de-protonated and competition will exist between the nitrogen and the alpha carbon for the initial step.³⁰ Above pH 6, the mechanism shown will be expected to

dominate, and CO₂ yield will increase. At lower pH, this reaction may not be as important, and thus this mechanism may be most important during the early stages of aerosol lifetime as aged aerosol may have different reactivities. Further studies of these reactions at different aerosol pH are needed.

4.5 Conclusions

In this chapter, we presented results from a study examining the impact of OH oxidation reactions on the composition of authentic, lab generated marine aerosol. We found that fragmentation reactions of supermicron particles composed of amino acids/amino sugars led to decreases in carbon content and subsequent increases in relative contribution of nitrogen containing species (e.g., ammonia and ammonium). AFM-PTIR analysis and AMS-derived mass analysis of submicron particles showed the formation of SMA due to oxidation of VOCs released during bloom activity. Taken together, these results help to explain the complex interplay between the ocean's biological activity and of certain atmospheric aging processes in determining the chemical composition of marine aerosol across different size-regimes. These findings will help climate modelers create better algorithms for identifying marine aerosol speciation and CNN/IN activity.

4.6 Acknowledgments

The author of this dissertation would like to gratefully acknowledge all co-authors as well as all CAICE researchers that took part in the summer 2016 research intensive. This study was funded by the Center for Aerosol Impacts on the Chemistry of the Environment (CAICE), an NSF-funded Center for Chemical Innovation under Grant CHE1305427.

Chapter 4 is in preparation: Trueblood, J. V., Wang, X., Or, V. W., Alves, M. R., Santander, M., Prather, K. A., Grassian, V. H. The Old and the New: Aging of Sea Spray

Aerosols and Formation of Secondary Marine Aerosol Through OH Oxidation Reactions. The dissertation author was the primary investigator and author of this paper.

4.7 Figures

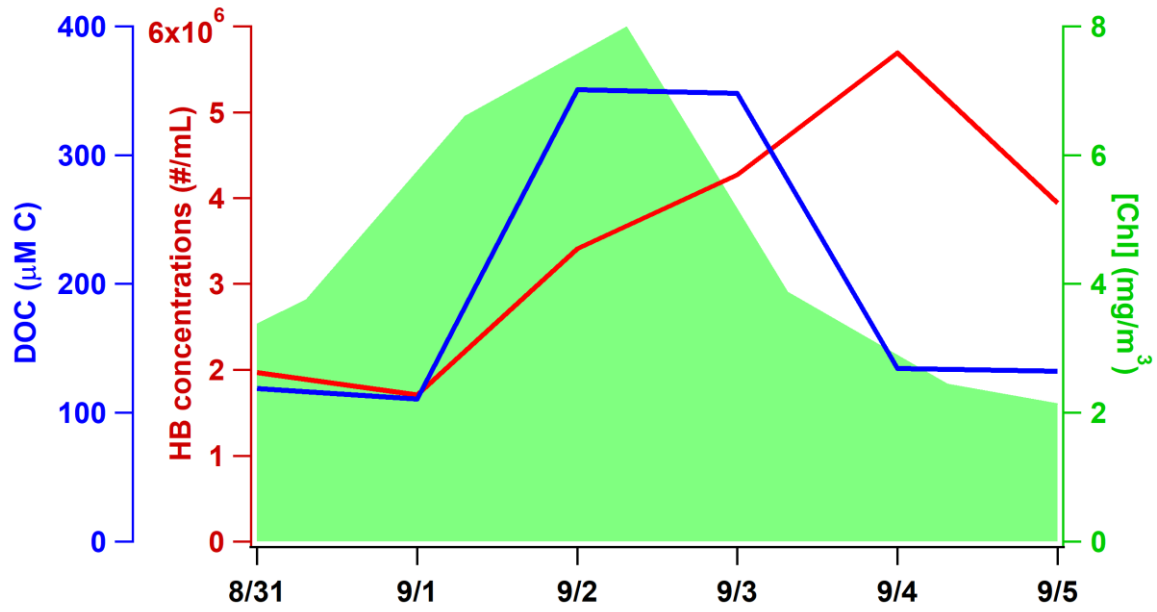


Figure 4.1: Dissolved organic carbon (DOC), heterotrophic bacteria counts, and chlorophyll-a (Chl) throughout the bloom.

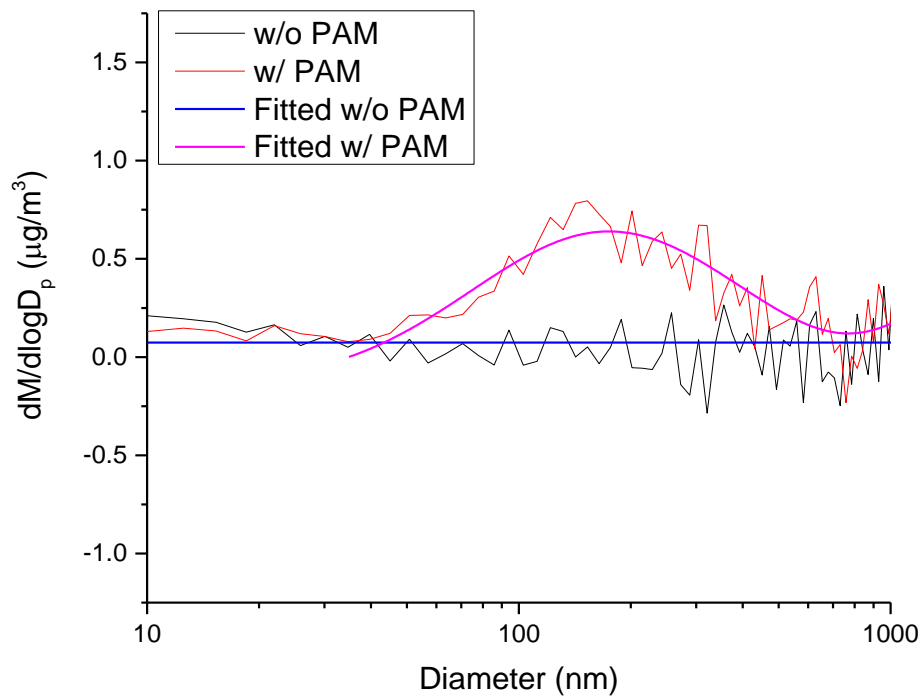


Figure 4.2: AMS-derived mass size distributions and corresponding curve fits for nascent and PAM-derived marine aerosol. Results show that PAM-derived marine aerosol have a greater contribution of particles in the size range from ~50 to 500 nm, indicating the formation of SMA.

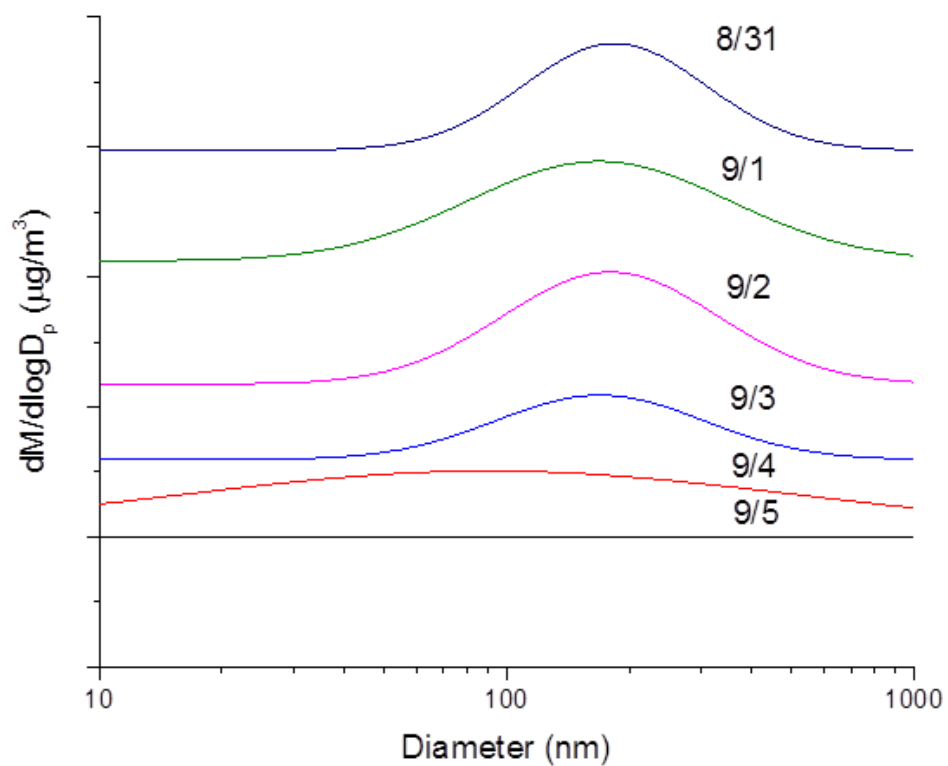
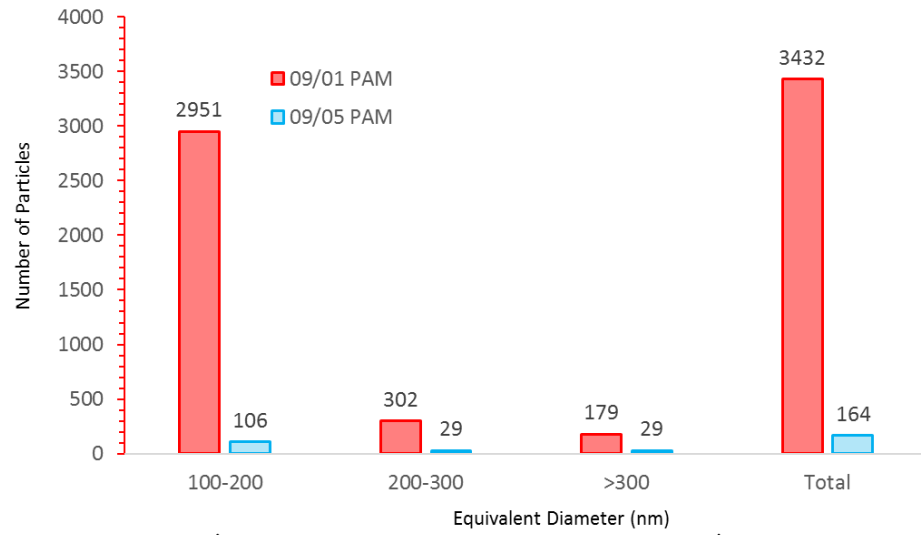


Figure 4.3: Curve fits of the AMS-derived mass size distributions of organic signals for PAM-derived marine aerosol on different days of the experiment.

AFM Particle Counts



09/01 PAM

09/05 PAM

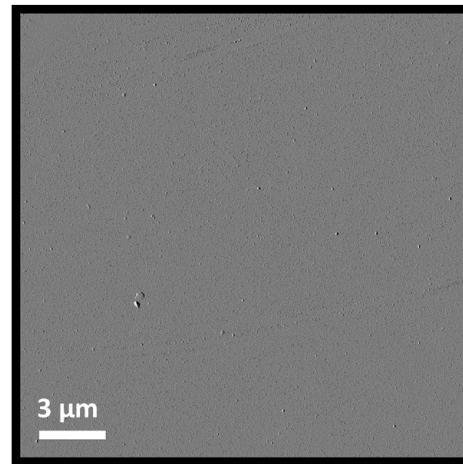
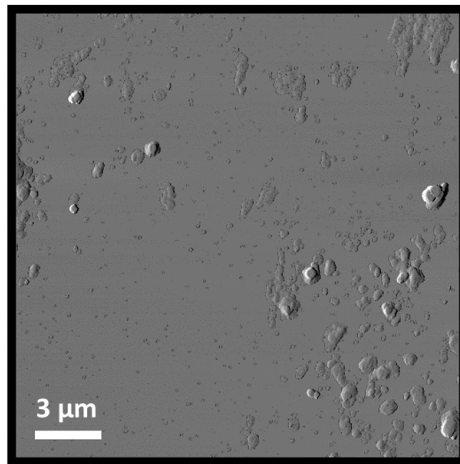


Figure 4.4: Particle counts (top) and amplitude images (bottom) as carried out by AFM for PAM-derived marine aerosol on 9/01 and 9/05.

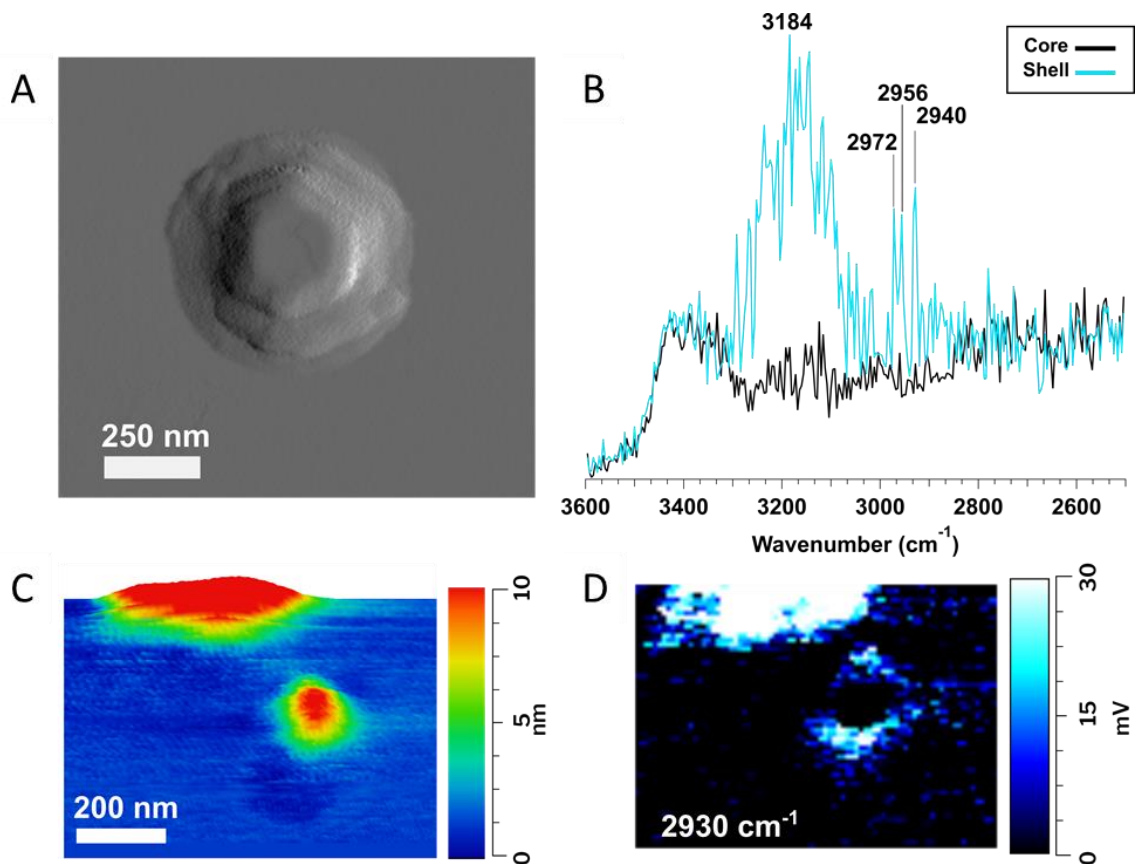


Figure 4.5: A) AFM amplitude image of a particle with a volume equivalent diameter of 250 nm. B) PTIR spectra taken at the particle core (black) and on the shell (blue). C) 3D height image of a particle with a volume equivalent diameter of 70 nm. D) Chemical map of the particle in panel C taken at 2930 cm^{-1} .

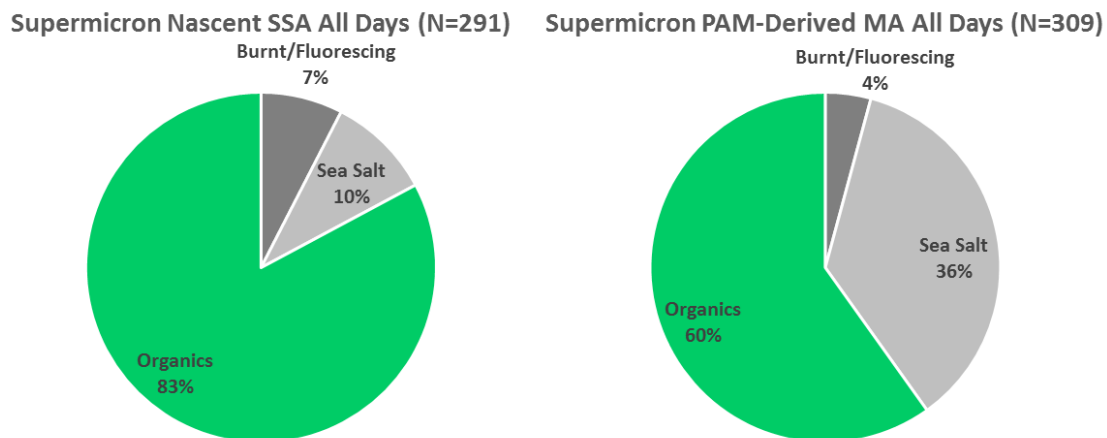


Figure 4.6: Relative fractions of particles that were identified as organic, burnt/fluorescing, or sea salt across all days for particles ranging from 1.8-3.2 μm , classified using Raman spectroscopy. Particles were classified according to a method previously described in literature. Particles that had such a small organic signature that no reasonable identification could be made were classified as salt particles.

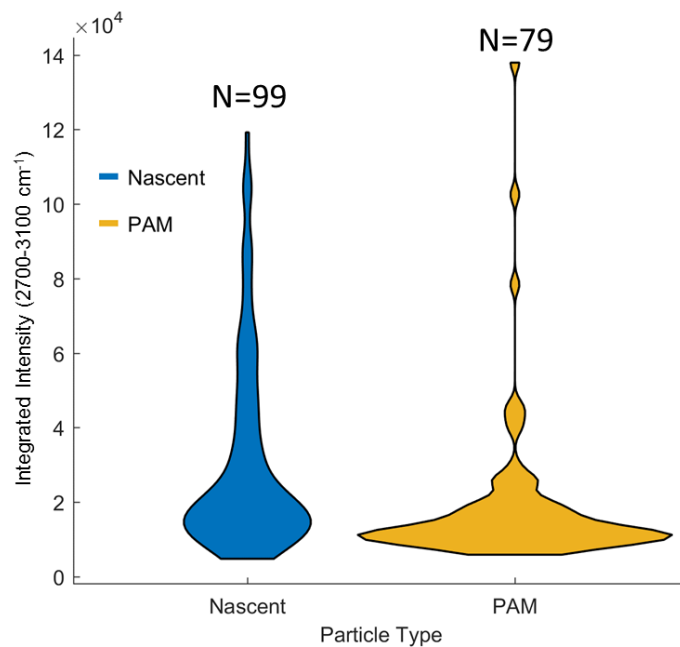


Figure 4.7: Violin plot of the integrated area from 2700 to 3100 cm^{-1} for of all particles classified as the most common particle type in nascent SSA and PAM-derived MA. The width of each plot represents the number of particles with a given integrated area intensity.

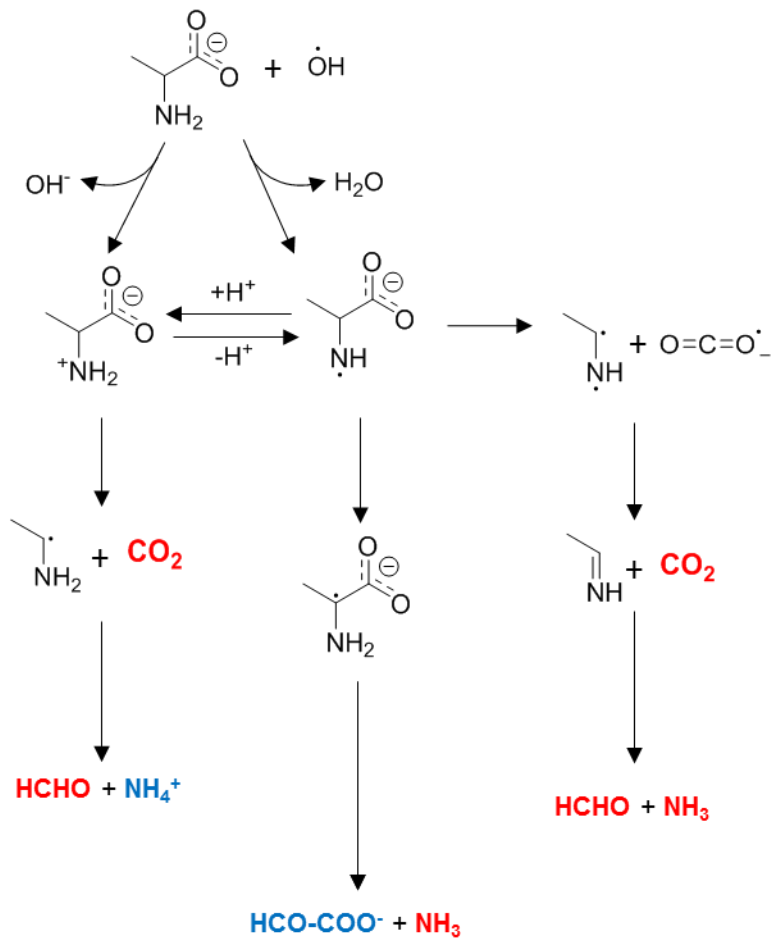


Figure 4.8: Proposed reaction mechanism for loss of organic mass from marine aerosols containing simple amino sugars and amino acids such as alanine upon exposure to OH radicals. Gaseous products are highlighted in red while condensed phase products are in blue. This mechanism is based on previous studies of OH initiated reactions of simple alpha-amino acids.^{22,23}

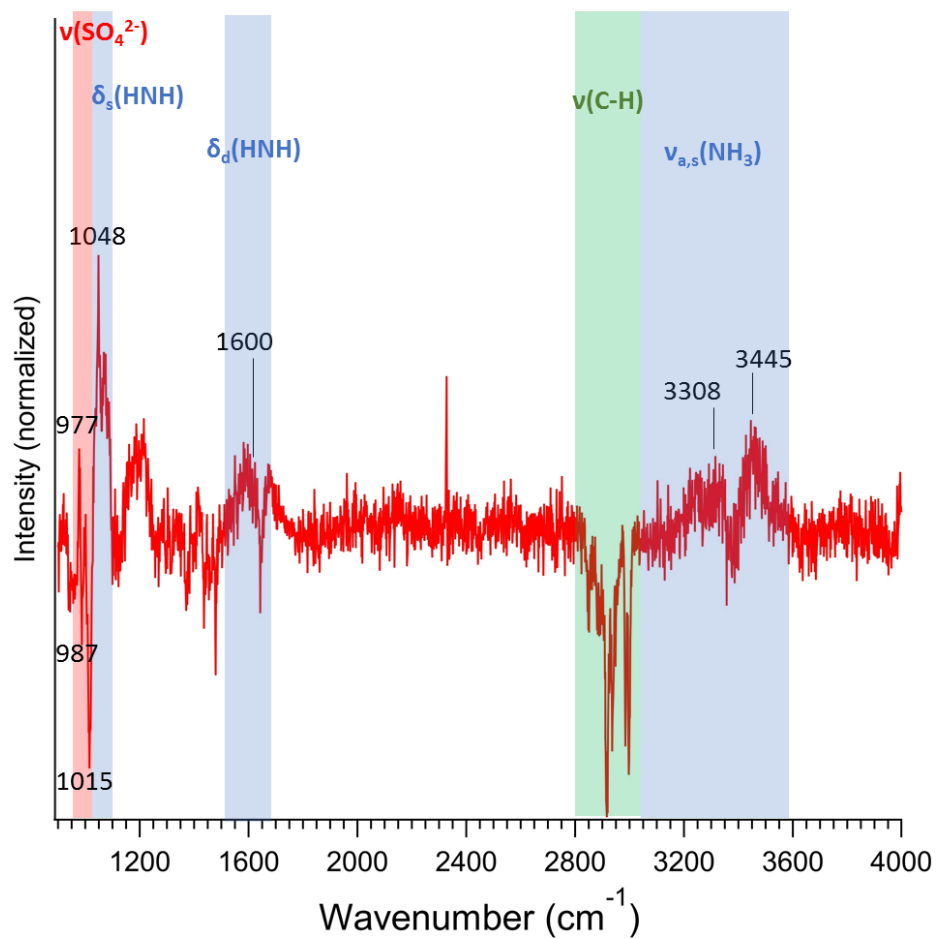


Figure 4.9: Difference spectrum (PAM versus non-PAM marine aerosol) of the average of the normalized spectra of the most abundant particle type for supermicron SSA across all days analyzed. Inspection reveals that the SO_4^{2-} peak due to calcium sulfate decreases at 1015 cm^{-1} , while the increase in ammonium sulfate and decrease in sodium sulfate leads to a shift in the SO_4^{2-} stretch from 985 to 980 cm^{-1} .

4.8 Supporting Information

4.8.1 Supporting Information Figures

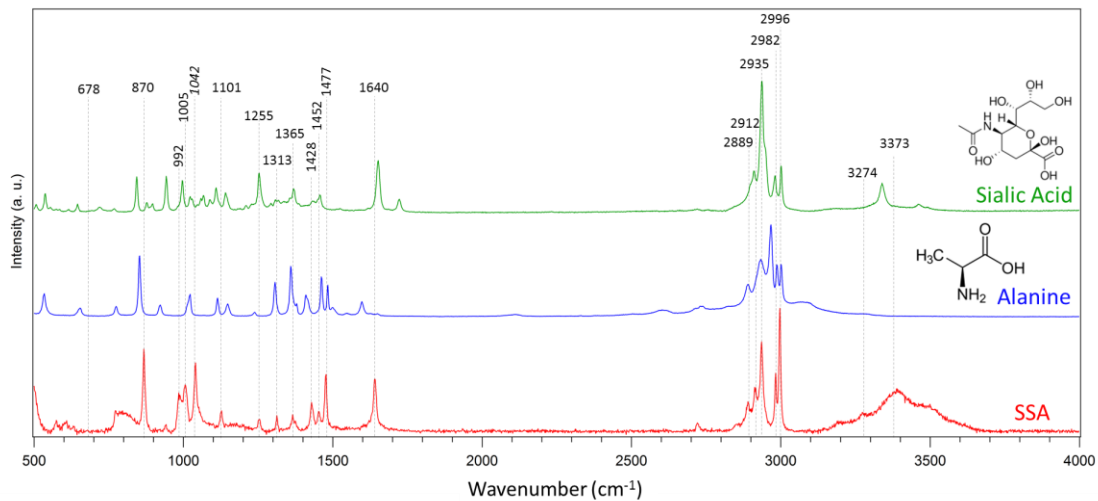


Figure 4.10: Comparison of spectra of the most common particle type in supermicron particles across all days (red) with alanine (blue) and sialic acid (green).

4.9 References

- (1) Pöschl, U. Atmospheric Aerosols: Composition, Transformation, Climate and Health Effects. *Angew. Chemie - Int. Ed.* **2005**, *44* (46), 7520–7540.
- (2) Myriokefalitakis, S.; Vignati, E.; Tsigaridis, K.; Papadimas, C.; Sciare, J.; Mihalopoulos, N.; Facchini, M. C.; Rinaldi, M.; Dentener, F. J.; Ceburnis, D.; Hatzianastasiou, N.; O'Dowd, C.; Van Weele, M.; Kanakidou, M. Global Modeling of the Oceanic Source of Organic Aerosols. *Adv. Meteorol.* **2010**, *2010*, 1–16.
- (3) Leeuw, G. De; Andreas, E. L.; Anguelova, M. D.; Fairall, C. W.; Lewis, E. R.; Dowd, C. O.; Schulz, M.; Schwartz, S. E. Production Flux of Sea Spray Aerosol. *Rev. Geophys.* **2011**, No. 2010, 1–39.
- (4) George, C.; Ammann, M.; D'Anna, B.; Donaldson, D. J.; Nizkorodov, S. A. Heterogeneous Photochemistry in the Atmosphere. *Chem. Rev.* **2015**, *110* (10), 4218–4258.
- (5) Lim, Y. Bin; Ziemann, P. J. Chemistry of Secondary Organic Aerosol Formation from OH Radical-Initiated Reactions of Linear, Branched, and Cyclic Alkanes in the Presence of NO_x. *Aerosol Sci. Technol.* **2009**, *43* (6), 604–619.
- (6) Lim, Y. Bin; Ziemann, P. J. Products and Mechanism of Secondary Organic Aerosol Formation from Reactions of N-Alkanes with OH Radicals in the Presence of NO_x. *Environ. Sci. Technol.* **2005**, *39* (23), 9229–9236.
- (7) Rinaldi, M.; Decesari, S.; Finessi, E.; Giulianelli, L.; Carbone, C.; Fuzzi, S.; Dowd, C. D. O.; Ceburnis, D.; Facchini, M. C. Primary and Secondary Organic Marine Aerosol and Oceanic Biological Activity: Recent Results and New Perspectives for Future Studies. **2010**, *2010*.
- (8) George, I. J.; Abbatt, J. P. D. Heterogeneous Oxidation of Atmospheric Aerosol Particles by Gas-Phase Radicals. *Nat. Chem.* **2010**, *2* (9), 713–722.
- (9) Kessler, S. H.; Nah, T.; Daumit, K. E.; Smith, J. D.; Leone, S. R.; Kolb, C. E.; Worsnop, D. R.; Wilson, K. R.; Kroll, J. H. OH-Initiated Heterogeneous Aging of Highly Oxidized Organic Aerosol. *J. Phys. Chem. A* **2012**, *116* (24), 6358–6365.
- (10) George, I. J.; Vlasenko, A.; Slowik, J. G.; Broekhuizen, K.; Abbatt, J. P. D. Heterogeneous Oxidation of Saturated Organic Aerosols by Hydroxyl Radicals: Uptake Kinetics, Condensed-Phase Products, and Particle Size Change. *Atmos. Chem. Phys.* **2007**, *7* (16), 4187–4201.
- (11) Molina, M. J.; Ivanov, A. V.; Trakhtenberg, S.; Molina, L. T. Atmospheric Evolution of Organic Aerosol. *Geophys. Res. Lett.* **2004**, *31* (22), 1–5.
- (12) Kroll, J. H.; Donahue, N. M.; Jimenez, J. L.; Kessler, S. H.; Canagaratna, M. R.; Wilson, K. R.; Altieri, K. E.; Mazzoleni, L. R.; Wozniak, A. S.; Bluhm, H.; Mysak, E.; Smith, J.; Kolb, C.; Worsnop, D. Carbon Oxidation State as a Metric for Describing the Chemistry of Atmospheric Organic Aerosol. *Nat. Chem.* **2011**, *3* (2), 133–139.
- (13) Kessler, S. H.; Smith, J. D.; Che, D. L.; Worsnop, D. R.; Wilson, K. R.; Kroll, J. H. Chemical Sinks of Organic Aerosol: Kinetics and Products of the Heterogeneous Oxidation of Erythritol and Levoglucosan. *Environ. Sci. Technol.* **2010**, *44* (18), 7005–7010.

- (14) Lim, C. Y.; Browne, E. C.; Sugrue, R. A.; Kroll, J. H. Rapid Heterogeneous Oxidation of Organic Coatings on Submicron Aerosols. *Geophys. Res. Lett.* **2017**, *44* (6), 2949–2957.
- (15) Kroll, J. H.; Smith, J. D.; Che, D. L.; Kessler, S. H.; Worsnop, D. R.; Wilson, K. R. Measurement of Fragmentation and Functionalization Pathways in the Heterogeneous Oxidation of Oxidized Organic Aerosol. *Phys. Chem. Chem. Phys.* **2009**, *11*, 8005–8014.
- (16) Wang, X.; Sultana, C. M.; Trueblood, J.; Hill, T. C. J.; Malfatti, F.; Lee, C.; Laskina, O.; Moore, K. A.; Beall, C. M.; McCluskey, C. S.; Cornwell, G.; Zhou, Y.; Cox, J.; Pendergraft, M.; Santander, M.; Bertram, T.; Cappa, C. D.; Azam, F.; DeMott, P.; Grassian, V. H.; Prather, K. A. Microbial Control of Sea Spray Aerosol Composition: A Tale of Two Blooms. *ACS Cent. Sci.* **2015**, *1* (3), 124–131.
- (17) Cochran, R. E.; Laskina, O.; Trueblood, J. V.; Estillore, A. D.; Morris, H. S.; Jayarathne, T.; Sultana, C. M.; Lee, C.; Lin, P.; Laskin, J.; Laskin, A.; Dowling, J. A.; Qin, Z.; Cappa, C. D.; Bertram, T. H.; Tivanski, A. V.; Stone, E. A.; Prather, K. A.; Grassian, V. H. Molecular Diversity of Sea Spray Aerosol Particles: Impact of Ocean Biology on Particle Composition and Hygroscopicity. *Chem* **2017**, *2* (5), 655–667.
- (18) Stokes, M. D.; Deane, G. B.; Prather, K.; Bertram, T. H.; Ruppel, M. J.; Ryder, O. S.; Brady, J. M.; Zhao, D. A Marine Aerosol Reference Tank System as a Breaking Wave Analogue for the Production of Foam and Sea-Spray Aerosols. *Atmos. Meas. Tech.* **2013**, *6* (4), 1085–1094.
- (19) Decarlo, P. F.; Kimmel, J. R.; Trimborn, A.; Northway, M. J.; Jayne, J. T.; Aiken, A. C.; Gonin, M.; Fuhrer, K.; Horvath, T.; Docherty, K. S.; Worsnop, D.; Jimenez, J. Aerosol Mass Spectrometer. *Anal. Chem.* **2006**, *78* (24), 8281–8289.
- (20) Ivleva, N. P.; McKeon, U.; Niessner, R.; Pöschl, U. Raman Microspectroscopic Analysis of Size-Resolved Atmospheric Aerosol Particle Samples Collected with an ELPI: Soot, Humic-like Substances, and Inorganic Compounds. *Aerosol Sci. Technol.* **2007**, *41* (7), 655–671.
- (21) Eom, H. J.; Gupta, D.; Cho, H. R.; Jin Hwang, H.; Do Hur, S.; Gim, Y.; Ro, C. U. Single-Particle Investigation of Summertime and Wintertime Antarctic Sea Spray Aerosols Using Low-Z Particle EPMA, Raman Microspectrometry, and ATR-FTIR Imaging Techniques. *Atmos. Chem. Phys.* **2016**, *16* (21), 13823–13836.
- (22) Karpel Vel Leitner, N.; Berger, P.; Legube, B. Oxidation of Amino Groups by Hydroxyl Radicals in Relation to the Oxidation Degree of the α -Carbon. *Environ. Sci. Technol.* **2002**, *36* (14), 3083–3089.
- (23) Bonifačić, M.; Štefanić, I.; Hug, G. L.; Armstrong, D. A.; Asmus, K. D. Glycine Decarboxylation: The Free Radical Mechanism. *J. Am. Chem. Soc.* **1998**, *120* (38), 9930–9940.
- (24) Riedel, K.; Allan, W.; Weller, R.; Schrems, O. Discrepancies between Formaldehyde Measurements and Methane Oxidation Model Predictions in the Antarctic Troposphere: An Assessment of Other Possible Formaldehyde Sources. *J. Geophys. Res. D Atmos.* **2005**, *110* (15), 1–14.
- (25) Ujike, T.; Tominaga, Y. Raman Spectral Analysis of Liquid Ammonia and Aqueous Solution of Ammonia. *J. Raman Spectrosc.* **2002**, *33* (6), 485–493.

- (26) Sexton, B. A.; Mitchell, G. E. VIBRATIONAL SPECTRA OF AMMONIA CHEMISORBED ON PLATINUM (111) I. Identification of Chemisorbed States. *Surf. Sci.* **1980**, *99*, 523–538.
- (27) Jordanov, N.; Zellner, R. Investigations of the Hygroscopic Properties of Ammonium Sulfate and Mixed Ammonium Sulfate and Glutaric Acid Micro Droplets by Means of Optical Levitation and Raman Spectroscopy. *Phys. Chem. Chem. Phys.* **2006**, *8*, 2759-2764.
- (28) Mabrouk, K. Ben; Kauffmann, T. H.; Fontana, M. D. Raman Study of Cation Effect on Sulfate Vibration Modes in Solid State and in Aqueous Solutions. *J. Raman Spectrosc.* **2013**, *44*, 1603–1608.
- (29) Ault, A. P.; Zhao, D.; Ebben, C. J.; Tauber, M. J.; Geiger, F. M.; Prather, K. A.; Grassian, V. H. Raman Microspectroscopy and Vibrational Sum Frequency Generation Spectroscopy as Probes of the Bulk and Surface Compositions of Size-Resolved Sea Spray Aerosol Particles. *Phys. Chem. Chem. Phys.* **2013**, *15* (17), 6206–6214.
- (30) Vi, T.; Hayon, E.; Ibata, T.; Lichtin, N. N.; Simic, M. Sites of Attack of Hydroxyl Radicals on Amides in Aqueous Solution. *JACS*, **1970**, *92* (13), 3898–3903.

Chapter 5 Shedding Light on Photosensitized Reactions within Marine-Relevant Organic Thin Films

5.1 Synopsis

Photochemical processes drive much of the daytime gas phase chemistry in the atmosphere. Within condensed phases such as aerosol particles and thin films enriched in organics, much less is understood about these processes. This chapter describes a series of experiments aimed at better understanding the photosensitized reactions that can occur within marine-relevant systems. In particular, we investigated photosensitized reactions between a fatty acid model system and different photosensitizers in thin organic films representative of molecular species found in the sea surface microlayer (SML) and sea spray aerosols (SSA). Photosensitized reactions of thin films containing nonanoic acid and three different photosensitizers, including 4-benzoyl benzoic acid (BBA), humic acid (HA), and marine-derived dissolved organic matter (m-DOM), were probed using a suite of analytical techniques, including vibrational spectroscopy, excitation emission matrix spectroscopy (EEMS), and ultra-high-resolution mass spectrometry. Considerable differences were found in the photosensitizing capability for each of these systems. We also present an analysis of the molecular differences between the different photosensitizers to explain their unique characteristics and light absorbing properties. This study begins to shed light on the relevance of such reactions in the marine environment.

5.2 Introduction

Air-water interfaces are ubiquitous throughout the Earth system, existing in lakes, ocean, rivers, and at the surface of aerosols. An important property of the air-water interface is its ability to concentrate chemical species relative to the underlying bulk water, thereby exposing them to conditions ripe for chemical and physical processing. One such species found in elevated

concentrations at air-water interfaces is dissolved organic matter (DOM), which is operationally defined as the elemental organic matter content of natural waters that passes through 0.45 or 0.22 μm filters.¹

In general, the portion of DOM that interacts with light ranging from ~300-800 nm is known as chromophoric dissolved organic matter (CDOM).² Upon excitation through absorption of radiation, CDOM can proceed through a variety of photochemical pathways. Following excitation into the first-excited singlet state, intersystem crossing to an excited triplet state is a particularly important photochemical pathway for CDOM.³ As a result of its relatively long lifetime, photoexcited triplet state CDOM is known to efficiently degrade and react with organic compounds and contaminants in the aqueous phase. Such reactions occur either directly through H-abstraction and charge transfer reactions, or indirectly through the formation of other photochemically produced reactive intermediate species (PPRI) (e.g., HO, H₂O₂, peroxy radicals, singlet oxygen) which then react with organic substrates.^{4,5} Such reactions in the bulk phase have been extensively studied and are known to form various saturated alcohols, aldehydes, and ketones.⁶

Recently, studies using simple CDOM mimics and model systems (e.g., benzoyl benzoic acid (BBA), commercial humic acid) and single component organic substrates (e.g., nonanoic acid, octanol) placed at the air-water interface have highlighted the role of a previously unknown class of photosensitized reactions in the formation of unsaturated and functionalized volatile organic compounds (VOCs) and condensed phase products, including hexene, hexenal, heptadiene, and octenal, among others.^{7,8,9,10} Such reactions are thought to serve as a source of secondary organic aerosol (SOA) precursors and are unique to the air water interface due to its concentrating ability which allows for efficient interaction between formed radical species.

As two thirds of the Earth is covered in oceans, photosensitized reactions may be of great importance either at the sea surface microlayer (SML) or at the surface of sea spray aerosols (SSA), which are known to be enriched with DOM. Indeed, the total pool of DOM in marine environments (termed m-DOM) accounts for one of the largest carbon reservoirs on Earth (662 Pg).¹¹ Since a portion of this large m-DOM pool consists of light absorbing chromophoric components, termed m-CDOM, there is an abundance of molecules available to serve as photosensitizers in such regions. However, experiments investigating potential photosensitized reactions within marine environments have to date used simple photosensitizer model systems (e.g. BBA), leaving the question of how effective m-DOM, and its associated fraction of m-CDOM, behaves as a photosensitizer unanswered.

Currently, the main chromophores in m-CDOM remain poorly defined in comparison to their terrestrial counterparts.² In addition to lignin phenols from terrestrial runoff, m-CDOM is thought to acquire its photoactive properties from aromatic amino acids and a large class of poorly defined marine humic substances produced by the microbial and photochemical processing of phytoplankton exudates.^{12,13} Because of its unique formation mechanism and molecular structure (*vide infra*), m-CDOM is therefore expected to have different photochemical properties than the terrestrially derived humic acid and simple model systems used in previous studies investigating photosensitized reactions.⁶ For this reason, more complex and authentic photosensitizing systems need to be analyzed to determine the relevance of these photosensitizers at the organic-rich air-water interfaces of the SML and SSA.

This chapter presents the results from studies comparing the ability of three different photosensitizing systems to initiate photosensitized reactions with nonanoic acid at the organic-rich air-water interface: 1) the simple model system molecule 4-benzoylbenzoic acid (BBA); 2) commercially purchased terrestrial humic acid (HA) and; 3) authentic m-DOM, which includes m-

CDOM, grown from a phytoplankton lab culture. The goal of this study was to better understand the role of m-CDOM in this new class of photosensitizing reactions in hopes of better determining the relevancy of these reactions in the marine environment.

5.3 Experimental Methods

5.3.1 Chemicals and Production of m-DOM

Nonanoic acid (NA), a fatty acid commonly found in the SML and SSA, was used as the organic substrate. Three different systems of increasing complexity were used as photosensitizers: a well-known photosensitizer molecule 4-benzoylbenzoic acid (BBA) (Sigma Aldrich), humic acid (Sigma Aldrich), and authentic m-CDOM as discussed below.

To produce authentic m-DOM, which contains m-CDOM, three liters of seawater were taken from Scripps Institution of Oceanography pier and placed into a large Erlenmeyer flask. The seawater was spiked with Guillard's *f/2* medium to induce a phytoplankton bloom. A fluorescent tube (Full Spectrum Solutions, model 205457; T8 format, color temperature 5700 K, 2950 lumens) above the flask was used to promote the growth of phytoplankton. The progress of the phytoplankton bloom was occasionally monitored by measuring *in vivo* chlorophyll fluorescence using a handheld fluorimeter (Turner Designs, Aquafuor).

After approximately 3-4 weeks, the m-DOM material was extracted based on a styrene divinyl benzene polymer (PPL) solid phase extraction (SPE) procedure described previously.¹⁴ Briefly, the acidified cultured seawater (pH 2) was filtered first with 0.7 μm Whatman glass filter (GF/F) followed by a 0.2 μm GTTP filter to remove organisms. The SPE filters were pre-rinsed once with methanol, three times with dilute acid, three times with Milli-Q water, and three times with methanol. Filtered seawater was then passed through the SPE cartridges, followed by further rinsing with dilute acid three times (0.01 M HCl), Milli-Q water three times, and then dried under

N₂. m-DOM was then extracted from the SPE cartridge by rinsing three times with methanol. The m-DOM methanol solution was then rotovapped and the dried sample was stored in a freezer.

5.3.2 TOC Analysis

To aid in comparison of humic acid and m-DOM, aliquots of each sample in Milli-Q water were sent to Nelson Labs for total organic carbon (TOC) analysis. A solution of 3.5 mg/mL of HA in methanol was prepared and sonicated for 10 minutes. 500 µl of the HA/methanol solution was then extracted, evaporated, and then reconstituted in 40mL of Milli-Q water. For TOC analysis of m-DOM, 5 mL of methanol was mixed with the dry m-DOM sample, sonicated for 10 minutes, and then 500 µl was extracted and evaporated and reconstituted with 40 mL of Milli-Q water. Both solutions were further sonicated for 10 minutes after addition of H₂O and sent to Nelson Labs for TOC analysis.

5.3.3 Analysis of Photosensitized Reactions with Nonanoic Acid

5.3.3.1 Attenuated Total Reflectance-Fourier Transform Infrared Spectroscopy (ATR-FTIR)

Attenuated total reflectance-Fourier transform infrared (ATR-FTIR) spectroscopy was used to monitor the condensed phase of irradiated and non-irradiated NA in the presence of various photosensitizer systems. To mimic the organic-rich interface of the SML and SSA particles, 400 µl of NA was placed on top of a thin film of photosensitizer that was formed on the surface of an AMTIR crystal. The thin photosensitizer films were made by first creating a solution of the photosensitizer species in ethanol: 15.9 M for BBA, 3500 mg/L for humic acid or (136.8 mg C/L based on TOC analysis), and reconstituting the m-DOM in 5 mL ethanol for a concentration of 640 mg C/L. 450 µl of the photosensitizer/ethanol solution was then placed onto the AMTIR crystal, and dry air was passed over it for ~60 minutes to ensure solvent evaporation. Evaporation was assumed complete when subsequent ATR-FTIR scans revealed no further spectral changes or contributions from ethanol.

After evaporation of ethanol and formation of the photosensitizer thin film, 400 μl of nonanoic acid was placed on top of the thin photosensitizer film. To reduce evaporative losses, the AMTIR crystal was then covered using a trough plate fitted with a UV port window to allow light onto the sample. After 10 minutes of equilibration time, the solar simulator was either turned on for irradiation experiments or remained off for non-irradiation experiments. Spectra were then collected every 10 minutes for the next 60 minutes. The spectral resolution of the ATR-FTIR was set to 8, with 128 scans averaged per scan across a range of 800-4000 cm^{-1} .

5.3.3.2 Ultra High Resolution Mass Spectrometry of Reaction Products.

For further analysis of light and dark reactions, the solution from the AMTIR crystal was extracted and stored at $-20\text{ }^{\circ}\text{C}$ before analysis via ultra-performance liquid chromatography tandem heated electrospray-linear ion trap Orbitrap high resolution mass spectrometer (UPLC-HESI-LIT-Orbitrap, ThermoFisher) as adopted from the literature.¹⁰ In brief, samples were analyzed by a reverse phase (Hypersil GOLD™ aQ, ThermoFisher) UPLC-HESI-LIT-Orbitrap. Peaks were detected in both positive and negative mode at a capillary voltage set to 2.8 kV at $325\text{ }^{\circ}\text{C}$ and separated using a water and acetonitrile solvent gradient. The heated electrospray ionization (HESI) source was operated at $50\text{ }^{\circ}\text{C}$. The HESI-LIT-Orbitrap was calibrated the day of sample analysis for each experiment. Samples run in positive mode were derivatized with PFBHA for aldehyde and ketone detection prior to analysis in a similar manner as Tinel and coworkers.¹⁰ Samples run in negative mode were not derivatized. All extracts were prepared by diluting 25 μl of the sample to 1 mL with a 1:1 acetonitrile:water mixture. Aliquots were then analyzed after a 24 hour-period.

5.3.4 Analysis of Molecular Composition of Photosensitizers

5.3.4.1 Ultra High Resolution Mass Spectrometry

To determine the chromophores found within, and hence better understand the photochemical properties of, complex photosensitizers (HA and m-DOM), ultra-high resolution

mass spectrometry was again utilized. Extracts of each photosensitizer were introduced into a heated electrospray ionization linear ion trap Orbitrap (HESI-LIT-Orbitrap) mass spectrometer via direct injection at a flow rate of 5 $\mu\text{L min}^{-1}$. Chromatographic separation was not used in this case due to the difficulty in separating components in DOM, which is known to contain tens of thousands of unique molecular species.

Utilizing the ability of HESI-LIT-Orbitrap to separate complex mixtures, thousands of molecular signatures were detected. Molecular formula assignments were performed using the Xcalibur software (ThermoFisher) with the following element ranges: ^{12}C , 0-30; ^1H , 0-50; ^{16}O , 0-30; ^{14}N , 0-5; ^{32}S , 0-2; ^{23}Na , 0-1 (sodium adduct for positive mode species only). Compositions including phosphorus (P) were excluded in this analysis due to the uncertainty of their presence in our samples.^{15,16} Formulas with a relative double bond greater than 15 and/or with an O/C ratio less than zero or greater than 2.5 were rejected. Additionally, peaks were chosen with a mass error of less than 5 ppm and with a relative intensity greater than 0.05% of the largest detected peak. The majority of ions in both photosensitizers (HA and m-DOM) were found in positive mode and the previously stated parameters set for composition analysis resulted in ~40-66% of ions being successfully characterized for both modes.

Assigned formulas were next categorized by compound class based upon elemental stoichiometries as done previously.¹⁷ Modified aromaticity index (AI_{mod}) was calculated according to Equation 4.1:

$$\text{AI}_{\text{mod}} = (1 + \text{C} - 0.5\text{O} - \text{S} - 0.5\text{H}) / (\text{C} - 0.5\text{O} - \text{S} - \text{N} - \text{P}) \quad (\text{Eq. 4.1})$$

Where $\text{P} = 0$ for our identified compounds. Compound classes were then identified as follows: $\text{AI}_{\text{mod}} 0.5$ to 0.67 = aromatic, $\text{AI}_{\text{mod}} > 0.67$ = condensed aromatic, highly unsaturated = $\text{AI}_{\text{mod}} < 0.5$, $\text{H}/\text{C} < 1.5$; aliphatics = H/C 1.5 to 2.0, $\text{O}/\text{C} < 0.9$, $\text{N} = \text{O}$; peptide = H/C 1.5 to 2.0, $\text{O}/\text{C} < 0.9$, $\text{N} > 0$.

As noted in previous work, compounds identified as peptides have molecular formulas of peptides, but the actual structure may differ.¹⁷

5.3.4.2 Fluorescence excitation-emission matrices (EEMs)

Fluorescence excitation-emission matrices (EEMS) of HA and m-DOM were obtained using a spectrofluorometer (Horiba Scientific, Aqualog with extended range). Dry samples were resuspended in 5 ml of ultrapure water. A small aliquot (1.5 ml) was then used to obtain EEMs. Excitation wavelengths ranged from 235-450 nm. Emission ranged from 250-800 nm. A background spectrum acquired with ultrapure water was then subtracted from all EEMs. EEMs were corrected for inner-filter effects based on absorbance spectra measured simultaneously. Finally, Rayleigh scattering (1st and 2nd order) was removed.

5.4 Results

5.4.1 Analysis of Photosensitized Reactions of Three Different Photosensitizers with NA

Analysis of products formed during irradiated and non-irradiated NA with three different photosensitizers was conducted using ATR-FTIR spectroscopy and UPLC-HESI-LIT-Orbitrap MS. As mentioned, a thin film of the photosensitizer was first formed on an AMTIR ATR-FTIR crystal. Individual spectra of thin films of each of the three photosensitizers is shown in Figure 5.5 (5.9.1 Supporting Information Figures). After creation of the photosensitizer thin film, NA was placed on top. The full signal spectrum of each photosensitizer with NA system was largely dominated by NA as shown in Figure 5.6 (5.9.1 Supporting Information Figures).

After preparation of the NA and photosensitizer thin film, the system was then either kept in the dark for one hour or irradiated with a solar simulator, with spectra collected every ten minutes. Figure 5.1A-C shows ATR-FTIR difference spectra (final-initial) of irradiated and non-irradiated NA in the presence of each of the three photosensitizers as a function of time over one hour. Increasingly bright colored lines correspond to increasing irradiation time, while gray lines

show the difference spectra for dark samples (i.e., no irradiation). After irradiation and analysis by ATR-FTIR, samples were extracted, derivatized, and analyzed using UPLC-HESI-LIT-Orbitrap MS for identification of specific molecular species. Table 5.1 shows signal strength and ratio (irradiated/non-irradiated) of counts of select products found upon analysis in positive and negative mode, respectively. It should be noted that the analysis of mixtures via HRMS ESI mass spectrometry is not entirely quantitative due to differences in ionization efficiencies of the samples. To comparatively assess the photochemical production of identified species between experiments, four thresholds relative to the signal of the HRMS's total ion count (TIC) spectra were calculated and used to create four categories to describe the relative intensities of each product. The categories were assigned in a manner similar to previous studies,¹⁸ and are calculated as follows. First, "below threshold" was determined as ten times greater than the average noise for that system. The following three categories (termed "weak," "medium" and "strong") were then each identified as being an order of magnitude higher than the previous threshold. For example, for the system of NA in the presence of BBA, the noise average was 10^2 counts, giving a "below threshold" value of 10^3 counts. "Weak" signals then had intensities greater than 10^4 counts, "medium" signals had intensities greater than 10^5 counts, and strong signals had intensities greater than 10^6 counts. Light:Dark ratios counts were also calculated, indicating the extent to which irradiation produced observed products. Graphs showing ion counts for each system as well as water blanks in irradiated and non-irradiated conditions are shown in Figure 5.7 of Section 5.9.1 Supporting Information. An in-depth discussion of the findings for each system is now given.

5.4.1.1 BBA and Nonanoic Acid

Fig. 5.1A shows the difference spectra in the fingerprint region from $1300\text{-}1500\text{ cm}^{-1}$ and the region from $3200\text{-}3500\text{ cm}^{-1}$ for the system consisting of NA and BBA photosensitizer. Considering the expected products based upon previous results in the literature, we attribute the broad negative-going peak centered at $\sim 1310\text{ cm}^{-1}$ to C-O stretching of nonanoic acid.^{19,20,21} The

broad positive region with a maximum at 1399 cm^{-1} is due to a combination of C-H bending and O-H in-plane bending from the formation of aldehydes and oxygenated species, respectively.²¹ The negative peak centered at 1430 cm^{-1} is due to the loss of O-H in-plane bending modes of nonanoic acid.^{20,21} It should be noted this peak also overlaps with a peak in the BBA spectrum. While BBA is not expected to undergo direct photolysis, it is possible that the formation of combination products of BBA with various radicals may be responsible for some of the changes in the spectra at this wavenumber.

The two positive peaks at 1633 and 1663 cm^{-1} are assigned as stretching of C=C alkenes and C=O stretching of unsaturated aldehydes, respectively.²² The large negative peak at 1701 cm^{-1} is due to the loss of C=O groups as nonanoic acid is consumed. The band of positive-going peaks from 1711 - 1800 cm^{-1} are likely C=O stretches due to the formation of multiple aliphatic ketone/aldehyde species.²¹ It is possible these peaks are also caused by changes in the hydrogen-bonding state of the nonanoic acid. Loss of carboxylic acid dimers due to hydrogen bond disruption has been shown to cause the C=O peak to increase in wavenumber.²⁰ It is possible that even with an IR filter in place, irradiation of the sample by the solar simulator may cause changes in hydrogen bonding state. Nonetheless, in light of the other changes to the spectra, we are confident that the changes are not exclusively a result of changes in the hydrogen bonding state. Finally, further evidence for the formation of oxygenated species is seen in the broad positive band caused by O-H stretching, with peaks at 3333 and 3381 cm^{-1} .

The results from MS analysis of this system (Table 5.1) generally agree with the results from the ATR-FTIR spectra. Looking at the signal strength for irradiated systems in conjunction with the light:dark ratio gives an indication as to which products were most abundant and whether they were formed through thermal dark reactions or light induced reactions. The combination product NA+BBA had a strong signal and was largely produced as a result of irradiation. Saturated

and unsaturated fatty acids (e.g., octenoic, nonenoic, heptanoic) acids only had weak to medium signal but were highly enriched relative to the non-irradiated experiments. Finally, oxygenated C8/C9 acids as well as saturated and unsaturated C8 ketones/aldehydes exhibited strong signals in both irradiated and non-irradiated, but their production was clearly increased upon irradiation, with production ratios ranging from 3.26 for octenal and 1.79 for octanal to 42.8 for oxo-nonanoic acid. Overall, these results are in agreement with previous studies of this photosensitizer with NA that found small production of carboxylic acids, and strong production of saturated/unsaturated oxygenated species.¹⁰

5.4.1.2 Humic Acid and Nonanoic Acid

Figure 5.1B shows the irradiated and non-irradiated ATR-FTIR difference spectra for the system consisting of NA and the photosensitizer humic acid over 1 hour. Similar to the system of NA in the presence of BBA, Fig. 5.1B shows that irradiated NA with HA has positive-going peaks found at 1401 cm^{-1} which we again assign to aldehydic C-H deformation and in plane O-H bending of alcohol functional groups.²¹ The negative-going peak at 1429 cm^{-1} and 1470 cm^{-1} are again attributed to the O-H in plane bending associated with nonanoic acid.^{21,22} Fig. 5.1B shows a negative peak at 1696 cm^{-1} presumably due to loss of C=O stretching groups associated with nonanoic acid, and a positive band centered at 1752 cm^{-1} due to C=O stretching of various formed aldehydes and ketones. In contrast to the NA with BBA system, the NA with HA system has much smaller changes in the C=C and C=O region from $1630\text{-}1660\text{ cm}^{-1}$, indicating it less efficiently produces unsaturated species. Finally, Figure 5.1B shows a broad positive band from $3100\text{-}3500\text{ cm}^{-1}$ due to the formation of OH groups.

Table 5.1 shows the strength of signal and ratio of counts (irradiated:non-irradiated) for select products from MS analysis of the system consisting of NA in the presence of HA. Unsurprisingly, the BBA+NA combination product ion is absent. Carboxylic acids are only slightly

enriched in the irradiated systems (1.07 Light:Dark for octanoic acid, 1.09 for heptanoic acid). Interestingly, the main ketone/aldehyde enriched in irradiated samples is octanal (9828.14), with lower values for nonanedial (1.26) and hexenal (1.24) and no enrichment for octenal (0.99). This perhaps indicates a specific pathway is favored for this system. Finally, the production of oxygenated acids is favored only slightly in irradiated systems, with oxononanoic acid at 1.11 and hydroxy-nonanoic acid at 1.07. Overall, HA appears to be a less efficient photosensitizing system than BBA.

5.4.1.3 *m*-DOM and Nonanoic Acid.

ATR-FTIR difference spectra of *m*-DOM and NA in Figure 5.1C show that *m*-DOM is a poor photosensitizer, as indicated by the presence of only slightly negative-going peaks, possibly due to evaporation of high volatility species from *m*-DOM. Figure 5.1C has no positive going peaks and instead features only a broad decrease at 1650 cm^{-1} . Given the complicated chemical nature of *m*-DOM, this peak could be due to any number of functional groups and their combinations, including C=C, C=O, N=C, and N-H. The peak that is unaffected at 1713 cm^{-1} is likely due to the presence of nonanoic acid which does not appear to be reacting. The negative-going peak at 1731 cm^{-1} indicates the loss of C=O species in the *m*-DOM. Further, the large losses centered at 3337 cm^{-1} in Fig. 5.1C indicate loss of O-H species. The peaks lost in Fig. 5.1C seem to indicate *m*-DOM could be undergoing direct photolysis and subsequent evaporation of low-volatility products.

Ion counts in Table 5.1 show little to no enhancement in irradiated *m*-DOM and NA relative to non-irradiated samples for most products. Indeed, many systems feature an enrichment ratio of ~ 1 or less than 1, including octenal and octanal, which were highly enriched in systems containing either BBA or HA. The overall findings therefore are that BBA is an efficient photosensitizer, producing oxygenated species and unsaturated ketones/aldehydes, humic acid to a lesser extent,

while m-CDOM appears to be exhibited no photosensitizing capability with the nonanoic acid substrate.

5.4.2 Comparison of m-DOM and Humic Acid Molecular Composition and Chromophores

To better understand the differences between humic acid and m-DOM as they compare to BBA, we conducted a series of experiments to better understand their molecular structure and associated chromophores.

5.4.2.1 EEMS.

Figure 5.2 A,B shows the EEMS spectra of humic acid and m-DOM, respectively. The EEMS spectrum of HA shown in Figure 5.2A has a main peak centered at $\lambda_{\text{ex}}/\lambda_{\text{em}} = 250/500$ nm that stretches into higher excitation wavelengths up to 450/500 nm. Comparison with literature¹³ reveals this is due contributions from terrestrial fulvic and humic acids. Furthermore, the excitation at longer wavelengths is indicative of highly aromatic species. The EEMS spectrum for m-DOM shown in Figure 5.2B, has a peak at $\lambda_{\text{ex}}/\lambda_{\text{em}} = 250-280/350$ nm and a band that stretches to higher excitation wavelengths from 300-400/450 nm. Comparison with literature reveals the m-DOM sample contains proteins and marine humic substances with a lower degree of aromaticity relative to terrestrial humic acids.

5.4.2.2 ATR-FTIR Spectroscopy

Figure 5.3 A,B shows the ATR-FTIR spectra of HA and m-DOM, respectively. Due to the complex nature of these systems, the resulting spectra are broad, with each peak likely a composite of multiple vibrating functional groups. For this reason, a broad description of each region is given, with possible assignments for peaks in each region shown in Table 5.2.

Fig. 5.3A shows the ATR-FTIR spectrum of commercial HA with assignments based upon relevant literature.²¹⁻²⁶ The broad peak in region 1 ranging from 3400-2500 cm^{-1} is due to O-H and

N-H stretching. The shape of the peak and the fact that it extends to 2500 cm^{-1} is evidence that this peak is associated mainly with the presence of carboxylic acids. The strong peaks of region II at 2920 cm^{-1} and 2850 cm^{-1} are indicative of large contributions from aliphatic CH_2 and CH_3 stretching, respectively. The peak in region III at 1709 cm^{-1} is due to $\text{C}=\text{O}$ vibrations of carboxylic acids, aldehydes, and ketones. Region IV has a peak at 1593 cm^{-1} that can be attributed to a number of species and combinations thereof, including aromatic and olefinic $\text{C}=\text{C}$ and $\text{C}-\text{C}$ vibrations, $\text{C}=\text{N}$ aliphatic imines, and $\text{C}=\text{O}$ stretching of quinones. The low wavenumber seen for HA (i.e. $<1630\text{ cm}^{-1}$), however, suggests the presence of aromatic moieties. The cluster of peaks surrounding 1408 cm^{-1} in region V also indicate aromaticity, as they can be attributed to ring breathing modes, as well as deformation of aliphatic $\text{C}-\text{H}$, $\text{O}-\text{H}$ stretching of phenols and alcohols. The broad doublet of Region VI around 1227 cm^{-1} is possibly due to $\text{O}-\text{H}$ stretching of phenols and alcohols, as well as $\text{C}-\text{O}$ stretching and $\text{O}-\text{H}$ deformation of carboxylic acids. Region VII has a cluster of peaks around 1032 cm^{-1} from $\text{C}-\text{O}$ stretching of polysaccharide-like structures and in plane $\text{C}-\text{H}$ bending of benzene ring as well as peaks at $\sim 915\text{ cm}^{-1}$ due to aromatic out-of-plane $\text{C}-\text{H}$ bends.

Generally speaking, the same analysis for humic acid can be applied to m-DOM (Figure 5.3B). However, the relative contributions and presence or absence of key peaks reveal molecular differences compared to humic acid. First, there is a larger contribution at 3279 cm^{-1} in region I compared to the HA spectrum, indicating a greater contribution of $\text{O}-\text{H}$ and $\text{N}-\text{H}$ groups. Furthermore, the aliphatic $\text{C}-\text{H}$ stretching peaks in region II are smaller relative to peaks in Region III indicating a greater degree of oxygenation. The peak at 1707 cm^{-1} is broader, representative of a greater variety of species containing the carbonyl group. Unlike HA, there is no isolated peak at 1629 cm^{-1} . Instead, the peak at 1709 is broadened with a shoulder extending into Region IV. This shift, in addition to the larger peak in region I, points towards the presence of nitrogen-containing groups, such as amides and amines. Furthermore, the blue-shifting of the peak ($>1630\text{ cm}^{-1}$) could be due to a greater contribution of olefinic $\text{C}=\text{C}$ rather than aromatic species. Taken together, these

results indicate that the m-DOM sample is more oxidized, non-aromatic, and has an abundance of nitrogen-containing functional groups, while HA contains an abundance of aromatic species with high degrees of carboxylic acid functional groups. These results are in general agreement with the EEMS analysis.

5.4.2.3 *M.S Analysis.*

Figure 5.4 shows the contribution of molecular species in humic acid and m-DOM based on analysis upon direct injection of each sample into HESI-LIT-Orbitrap M/S. Immediately apparent is the fact that the m-DOM sample is much more chemically complex than the HA sample. A total of 3,496 species were identified for m-DOM, compared to just 684 for humic acid. The O/C ratio of m-DOM is 0.301 compared to .2795 for HA. Figure 5.5 also shows that m-DOM has more nitrogen containing species than HA (59.73% vs 38.89%, respectively), and is less aromatic (12% vs 38%). Interestingly, both m-DOM and HA have high percentages of highly unsaturated species (36% and 41%). Previous studies have identified the main contributors to the “highly unsaturated” category as either carboxylic rich alicyclic molecules (CRAM) formed from autochthonous microbial sources or as aromatic lignin from terrestrial sources.¹⁷ Given that the m-DOM was produced in a laboratory without input from terrestrial sources, it is more likely the highly unsaturated species are due to CRAM molecules, while the highly unsaturated species in HA is from lignin. This would again explain the differences in the impact of m-DOM as a photosensitizer, as CRAM is less photo-active than lignin, which is highly aromatic. Overall, the results from M/S analysis agree with the ATR-FTIR and EEMS spectra of these two complex systems, which show that m-DOM is more oxygenated, less aromatic, and has more nitrogen-containing species.

5.5 Conclusions

In this study, we compared the ability of three different potential photosensitizers with increasing chemical complexity (i.e., BBA, HA, m-DOM) to initiate photosensitized reactions with

the fatty acid nonanoic acid in an organic rich environment. ATR-FTIR and M/S results revealed that BBA is an efficient photosensitizer, leading to the production of several unsaturated and functionalized products, including saturated and unsaturated C8 aldehydes/ketones, combination products (BBA+NA), and hydroxy-nonanoic acid. HA was found to be a less efficient photosensitizer than BBA, yet still produced unsaturated and functionalized products. Irradiation of NA in the presence of m-DOM led to no enrichment of products, indicating the m-DOM and associated chromophores produced by marine microbes appear to be less efficient photosensitizers within a rich organic layer.

Analysis of HA and m-DOM by EEMS, ATR-FTIR, and HESI-LIT-Orbitrap M/S reveal that HA was photoactive due to its presence of aromatic species, while m-DOM was less photoactive due to its high abundance of CRAM, which is less aromatic. The lower photosensitizing capability m-DOM is in agreement with a recent study which found less than 10% of DOC in a phytoplankton dominated lake was photo-labile.²⁷ Interestingly, despite its poor photosensitizing capability, the m-DOM still appeared to undergo photochemistry itself, an avenue that should be investigated in future studies.

It should be noted that while this study points towards the low photosensitizing capability of microbially produced DOM, it does not preclude the importance of such reactions in the open ocean or SSA surfaces altogether, as other sources of CDOM in these regions exist. For example, previous work has shown that highly chromophoric dissolved polycyclic aromatics are formed thermogenically in the deep ocean.²⁸ Furthermore, terrestrial input of photo-active lignin-type molecules can also add to the number of chromophores found at the air-water interface of the ocean in coastal regions.²⁹ Future studies should investigate the photosensitizing ability of freshly upwelled deepwater DOM and coastal region DOM.

The findings in this study are important in that they lend further knowledge of the variability of DOM from various sources (here, marine derived DOM) to serve as a photosensitizer. Furthermore, these results point towards the need for studies using complex, authentic model systems in such experiments.

5.6 Acknowledgements

The author of this dissertation would like to thank Professor Michael Tauber and Samantha Doyle for m-DOM sample preparation and extraction. This study was supported by the National Science Foundation through the Centers for Chemical Innovation Program under Grant CHE1305427

Chapter 5 is in preparation: Trueblood, J. V., Alves, M., Power, D., Santander, M., Cochran, R., Prather, K. A., Grassian, V. H. Shedding Light on Photosensitized Reactions within Marine-Relevant Organic Thin Films. The dissertation author was the primary investigator and author of this paper.

5.7 Figures

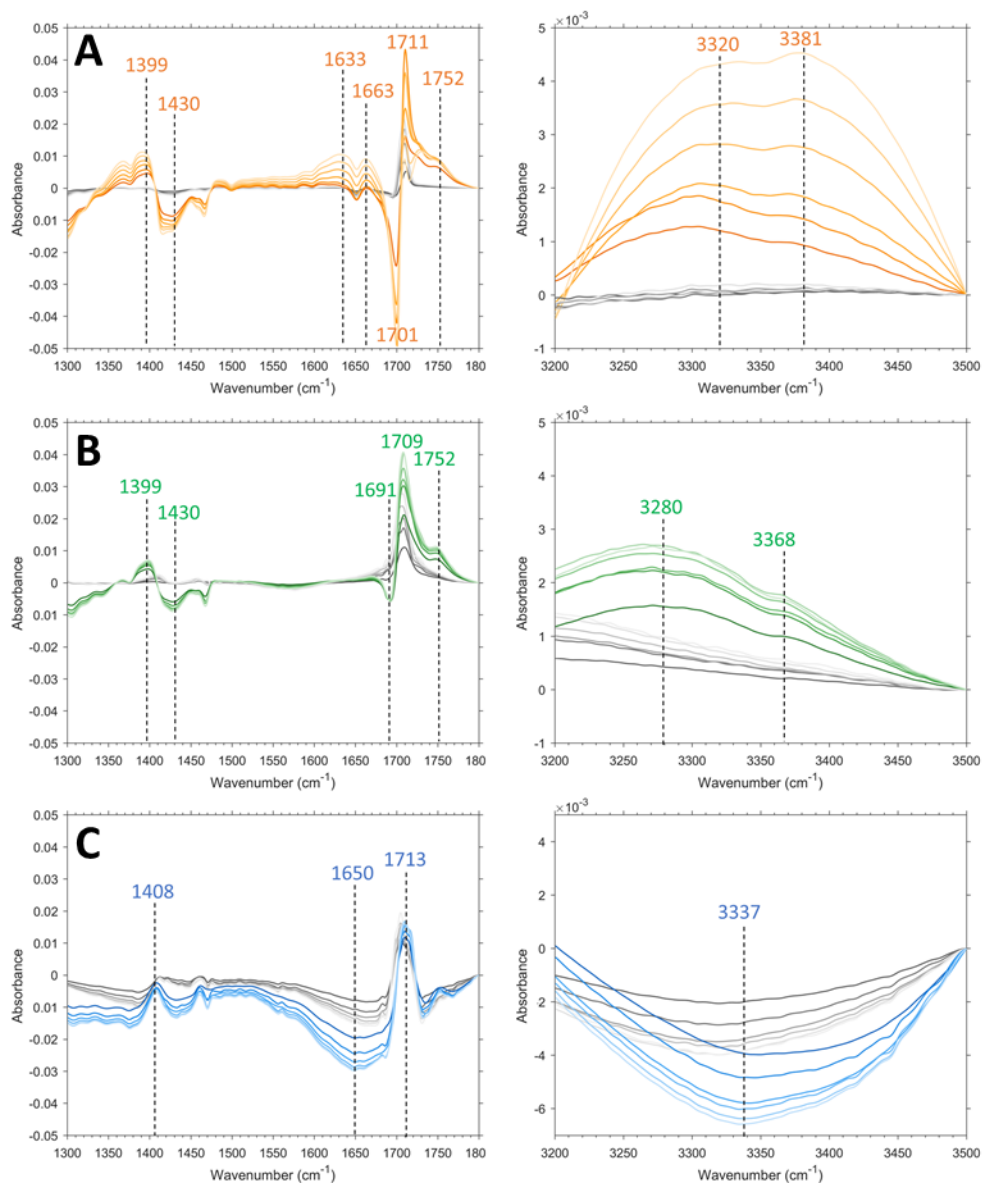


Figure 5.1: Select regions of ATR-FTIR difference spectra (final-initial) of 60-minute non-irradiated (gray lines) and irradiated (colored lines) NA in the presence of A) BBA; B) HA and C) m-DOM. Spectra were collected every 10 minutes. Lines become increasingly light with increased time.

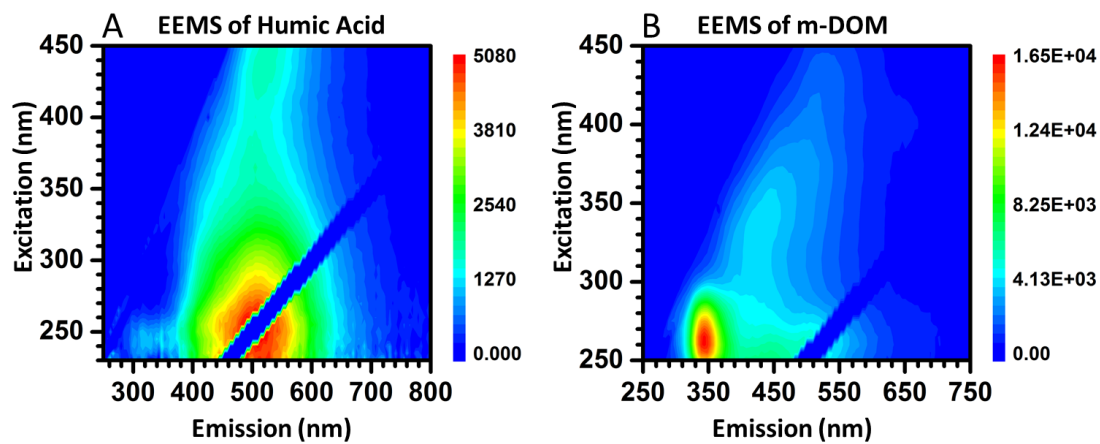


Figure 5.2: Excitation-emission matrices of A) humic acid and B) m-DOM.

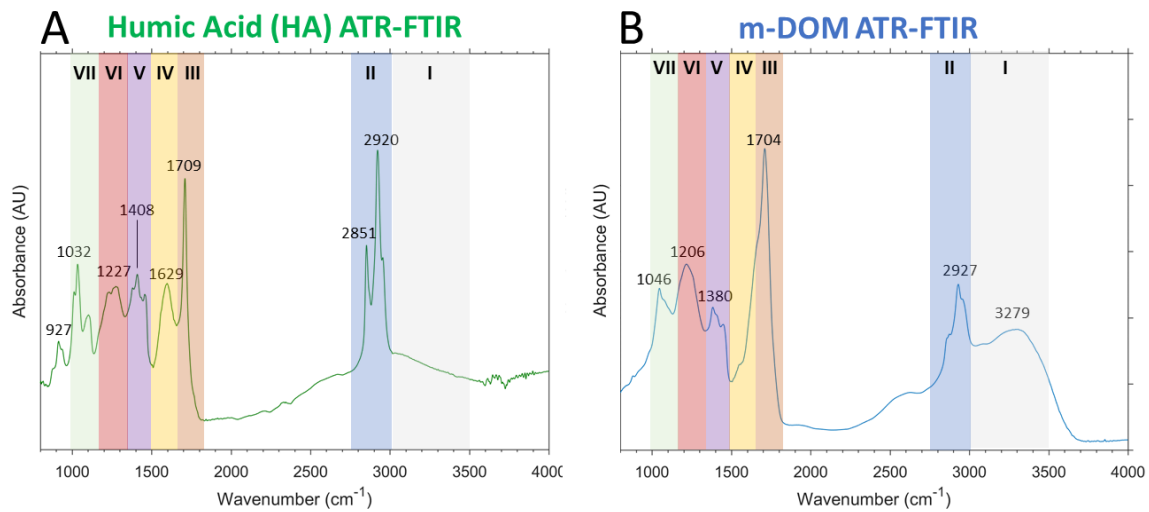


Figure 5.3: ATR-FTIR spectra of A) humic acid and B) m-DOM extracted from a lab-grown phytoplankton culture. Peak assignments are listed in Table 4.1.

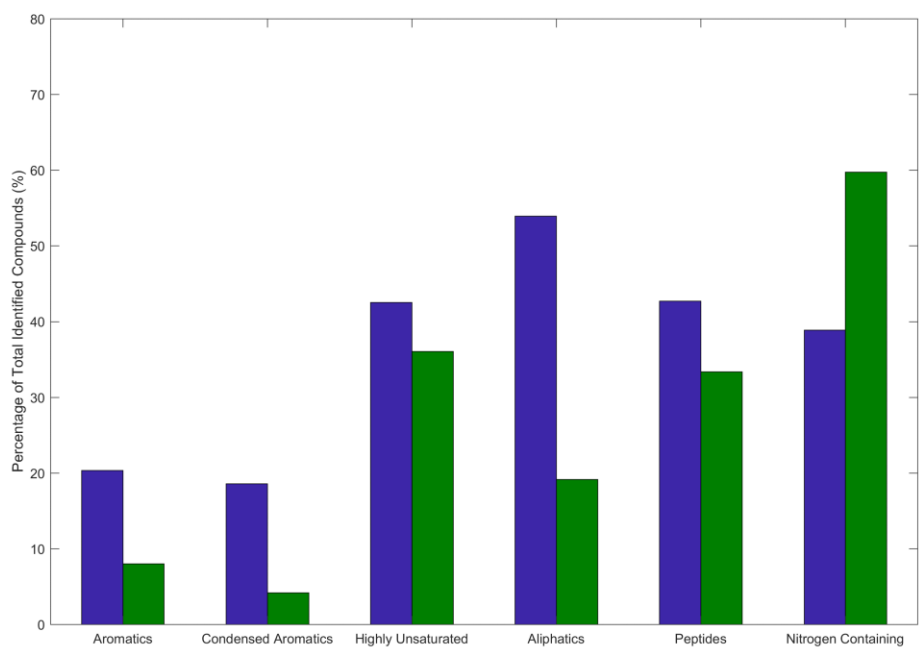


Figure 5.4: Relative abundance of each molecular class in humic acid and m-DOM as determined by HESI-LIT-Orbitrap MS analysis calculated according to Section 4.3.4.

5.8 Tables

Table 5.1 Signal strength and enrichment ratios for select products as detected by MS analysis for samples of various photosensitizers in the presence of NA.

Molecular Formula	Assigned Structure ^a	Irradiated BBA	BBA Light:Dark	Irradited HA	HA Light:Dark	Irradiated m-DOM	m-DOM Light:Dark
Combination Products							
C ₂₃ H ₂₈ O ₅	NA+BBA ^c	strong	>200000	below threshold	NA	below threshold	NA
C ₁₈ H ₃₄ O ₄	2NA-2H ^c	medium	>100	below threshold	NA	medium	0.92
Carboxylic Acids							
C ₈ H ₁₆ O ₂	Octanoic acid	medium	>200000	medium	1.07	strong	1.02
C ₈ H ₁₄ O ₂	Octenoic acid	weak	>10000	below threshold	NA	below threshold	NA
C ₉ H ₁₆ O ₂	Nonenoic acid	weak	>10000	below threshold	NA	below threshold	NA
C ₇ H ₁₄ O ₂	Heptanoic acid	weak	1.5	medium	1.09	medium	1.02
Oxygenated Acids							
C ₉ H ₁₆ O ₃	Oxo-NA	strong	42.81	strong	1.11	strong	0.93
C ₉ H ₁₆ O ₄	Hydroxy-oxo-NA	medium	22.27	strong	1.01	strong	0.99
C ₉ H ₁₈ O ₃	Hydroxy-NA	medium	5.77	strong	1.07	strong	1.12
C ₆ H ₁₀ O ₄	Hydroxy-oxo-octanoic acid	medium	1.73	strong	1.02	medium	1.02
Aldehydes/Ketones							
C ₇ H ₁₂ O ₂	Heptanedial	weak	11.53	below threshold	NA	below threshold	NA
C ₆ H ₁₀ O ₂	Hexanedial	weak	7.75	below threshold	NA	below threshold	NA
C ₈ H ₁₄ O	Octenal	strong	3.26	medium	0.99	strong	1
C ₉ H ₁₆ O	Nonenal	weak	2.14	below threshold	NA	weak	0.96
C ₈ H ₁₆ O	Octanal	strong	1.79	medium	9828.14	strong	1.04
C ₉ H ₁₆ O ₂	Nonanedial	medium	1.21	medium	1.26	strong	0.99
C ₉ H ₁₈ O	Nonanal	weak	1.2	weak	0.48	strong	0.71
C ₆ H ₁₀ O	Hexenal	medium	1.19	weak	1.24	medium	0.97
C ₇ H ₁₄ O	Heptanal	weak	1.17	below threshold	NA	medium	1.04
C ₆ H ₁₂ O	Hexanal	medium	1.1	below threshold	NA	below threshold	NA
C ₅ H ₈ O	Pentenal	below threshold	NA	medium	1.26	below threshold	NA

Table 5.2: Peak assignments of ATR-FTIR spectra of humic acid and m-DOM.

Region	Assignment
I	O-H, N-H stretches
II	Aliphatic C-H stretches
III	C=O of carboxylic acids,, aldehydes, and ketones
IV	C=O of quinones and amide I, C=N of imines, C=C and C-C of alkenes or aromatics
V	Ring breathing of aromatics, C-H deformation, O-H deformation of phenols and alcohols
VI	O-H stretching of phenols and alcohols, C-O stretching and O-H deformation of carboxylic acids
VII	C-O stretching of polysaccharide-like substances, C-H in plane bending of rings, C-H out-of-plane bends of aromatics

Table 5.3: Molecular characteristics of humic acid and m-DOM as determined by HESI-LIT-Orbitrap MS analysis.

	m-DOM	Humic Acid
All Formulas	3496	684
Average AI	0.1361	0.1927
Average H/C	1.567	1.5587
Average O/C	0.301	0.2795

5.9 Supporting Information

5.9.1 Supporting Information Figures

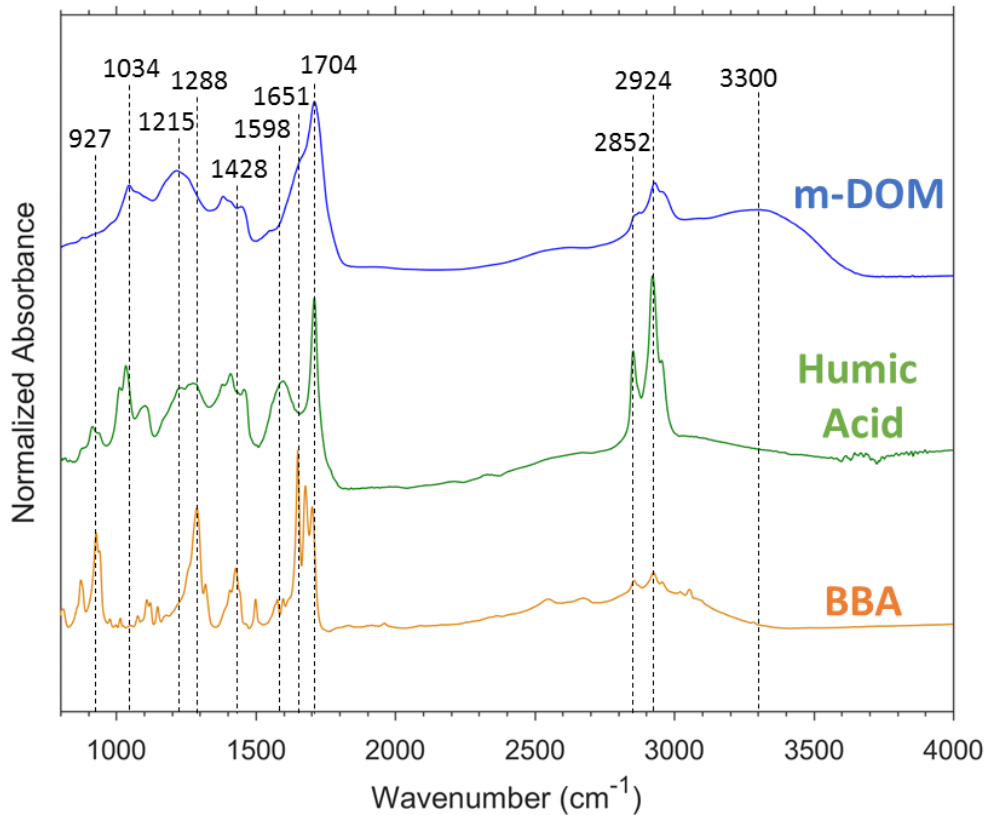


Figure 5.5: ATR-FTIR spectra of thin films of each of the photosensitizer model systems studied in this experiment. An in-depth analysis of the humic acid and m-DOM spectra is given in Section 4.4.2.

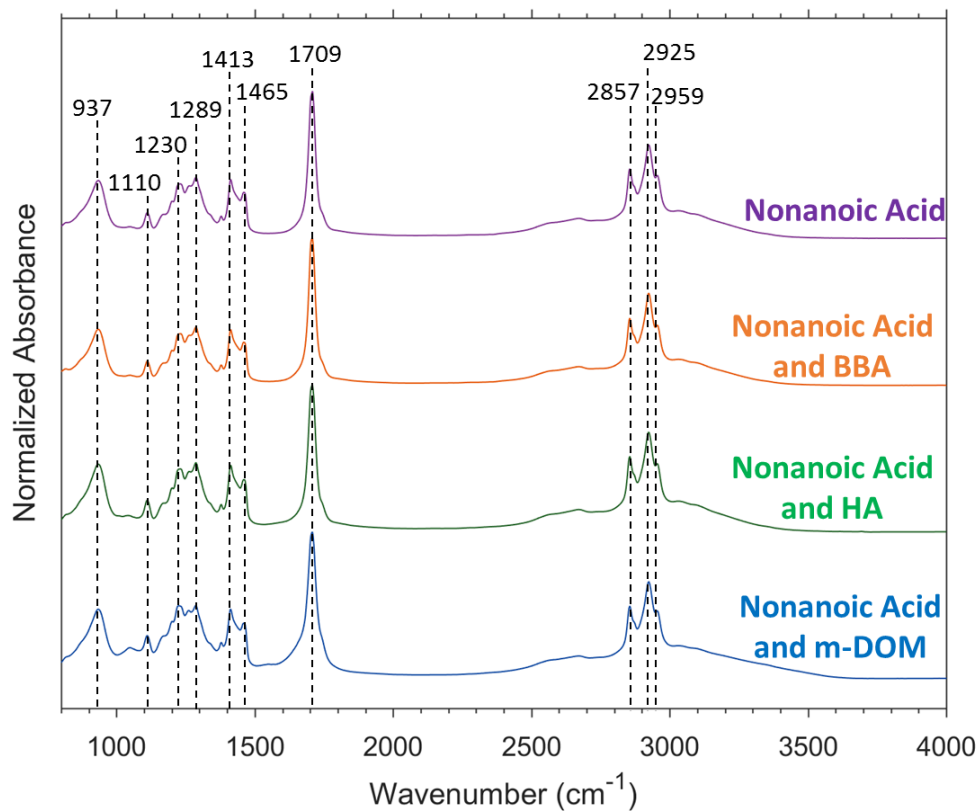


Figure 5.6: ATR-FTIR spectra of nonanoic acid and each of the systems containing a thin film of photosensitizer with nonanoic acid. Peak assignments for nonanoic acid are shown in Table 5.4.

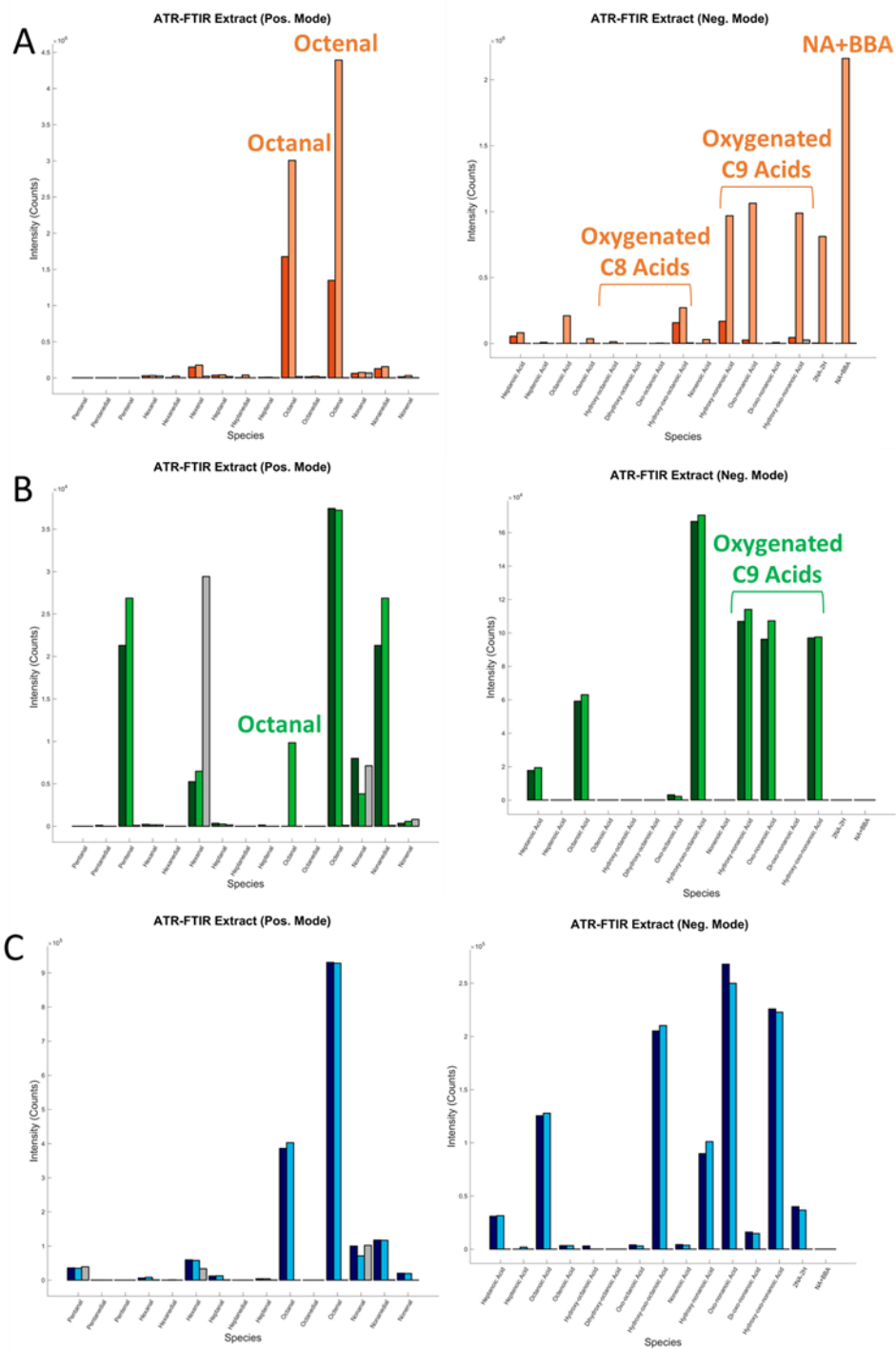


Figure 5.7: Signal detected (counts) for select products upon analysis by HESI-LIT-Orbitrap MS analysis in positive (left) and negative (right) mode of irradiated (light colored), non-irradiated (dark colors), and water blanks (grey) of A) NA in the presence of BBA, B) NA in the presence of humic acid, and C) NA in the presence of m-DOM.

5.9.2 Supporting Information Tables

Table 5.4: Peak assignments of nonanoic acid.³⁰

Peak (cm⁻¹)	Assignment
937	O-H bending
1285	CO stretching
1413,1462	OH bending, CH ₂ scissoring
1708	C=O stretching
2856	Symmetric CH stretching
2926	Asymmetric CH stretching
2500-3400	OH stretching

5.10 References

- (1) Thurman, E. M. Organic Geochemistry of Natural Waters. *Usgs* **1985**, 497.
- (2) Timko, S. A.; Maydanov, A.; Pittelli, S. L.; Conte, M. H.; Cooper, W. J.; Koch, B. P.; Schmitt-Kopplin, P.; Gonsior, M. Depth-Dependent Photodegradation of Marine Dissolved Organic Matter. *Front. Mar. Sci.* **2015**, *2*, 1–13.
- (3) Vione, D.; Calza, P. Chapter 1: Introduction. In *Surface Water Photochemistry*; 2016; pp 1–15.
- (4) Canonica, S. Oxidation of Aquatic Organic Contaminants Induced by Excited Triplet States. *Chimia (Aarau)*. **2007**, *61* (61), 641–644.
- (5) McNeill, K.; Canonica, S. Triplet State Dissolved Organic Matter in Aquatic Photochemistry: Reaction Mechanisms, Substrate Scope, and Photophysical Properties. *Environ. Sci. Process. Impacts* **2016**, *18* (11), 1381–1399.
- (6) Clark, C.; Zika, R. Marine Organic Photochemistry: From the Sea Surface to Marine Aerosols. *Mar. Chem.* **2000**, *5*, 1–33.
- (7) Ciuraru, R.; Fine, L.; Van Pinxteren, M.; D’Anna, B.; Herrmann, H.; George, C. Photosensitized Production of Functionalized and Unsaturated Organic Compounds at the Air-Sea Interface. *Sci. Rep.* **2015**, *5* (March), 1–10.
- (8) Ciuraru, R.; Fine, L.; Pinxteren, M. Van; D’Anna, B.; Herrmann, H.; George, C. Unravelling New Processes at Interfaces: Photochemical Isoprene Production at the Sea Surface. *Environ. Sci. Technol.* **2015**, *49* (22), 13199–13205.
- (9) Fu, H.; Ciuraru, R.; Dupart, Y.; Passananti, M.; Tinel, L.; Rossignol, S.; Perrier, S.; Donaldson, D. J.; Chen, J.; George, C. Photosensitized Production of Atmospherically Reactive Organic Compounds at the Air/Aqueous Interface. *J. Am. Chem. Soc.* **2015**, *137* (26), 8348–8351.
- (10) Tinel, L.; Rossignol, S.; Bianco, A.; Passananti, M.; Perrier, S.; Wang, X.; Brigante, M.; Donaldson, D. J.; George, C. Mechanistic Insights on the Photosensitized Chemistry of a Fatty Acid at the Air/Water Interface. *Environ. Sci. Technol.* **2016**, *50* (20), 11041–11048.
- (11) Hansell, D.; Carlson, C.; Repeta, D.; Schlitzer, R. Dissolved Organic Matter in the Ocean: A Controversy Stimulates New Insights. *Oceanography* **2009**, *22* (4), 202–211.
- (12) Nelson, N. B.; Siegel, D. A. The Global Distribution and Dynamics of Chromophoric Dissolved Organic Matter. *Ann. Rev. Mar. Sci.* **2013**, *5* (1), 447–476.
- (13) Coble, P. G. Marine Optical Biogeochemistry: The Chemistry of Ocean Color. *Chem. Rev.* **2007**, *107* (2), 402–418.
- (14) Dittmar, T.; Koch, B.; Hertkorn, N.; Kattner, G. OCEANOGRAPHY : METHODS A Simple and Efficient Method for the Solid-Phase Extraction of Dissolved Organic Matter (SPE-DOM) from Seawater. **2008**, 230–235.

- (15) Boris P. Koch, Matthias Witt, Ralph Engbrodt, Thorsten Dittmar, G. K. Molecular Formulae of Marine and Terrigenous Dissolved Organic Matter Detected by Electrospray Ionization Fourier Transform Ion Cyclotron Resonance Mass Spectrometry. *Geochimica et Cosmochimica Acta* **2005**, 69 (13), 3299–3308.
- (16) Kujawinski, E. B.; Longnecker, K.; Blough, N. V.; Del, R.; Finlay, L.; Kitner, J. B.; Giovannoni, S. J. Identification of Possible Source Markers in Marine Dissolved Organic Matter Using Ultrahigh Resolution Mass Spectrometry. *Geochim. Cosmochim. Acta* **2009**, 73 (15), 4384–4399.
- (17) Stubbins, A.; Dittmar, T. Illuminating the Deep: Molecular Signatures of Photochemical Alteration of Dissolved Organic Matter from North Atlantic Deep Water. *Mar. Chem.* **2015**, 177, 318–324.
- (18) Rapf, R. J.; Perkins, R. J.; Carpenter, B. K.; Vaida, V. Mechanistic Description of Photochemical Oligomer Formation from Aqueous Pyruvic Acid. *J. Phys. Chem. A* **2017**, 121 (22), 4272–4282.
- (19) Wang, Z.; Sun, J.; Xie, S.; Ma, G.; Jia, Y. Thermal Properties and Reliability of a Lauric Acid/Nonanoic Acid Binary Mixture as a Phase-Change Material for Thermal Energy Storage. *Energy Technol.* **2017**.
- (20) Stuart, B. H. *Infrared Spectroscopy: Fundamentals and Applications*.
- (21) Smith, B. *Infrared Spectral Interpretation: A Systematic Approach*; CRC Press: Boca Raton, Florida, 1999.
- (22) Coates, J. Interpretation of Infrared Spectra, A Practical Approach. In *Encyclopedia of Analytical Chemistry*; 2006.
- (23) Pospíšilová, L.; Fasurova, N. Spectroscopic Characteristics of Humic Acids Originated in Soils and Lignite. *Soil Water Res.* **2009**, 4 (4), 168–175.
- (24) Tatzber, M.; Stemmer, M.; Spiegel, H.; Katzlberger, C.; Haberhauer, G.; Mentler, A.; Gerzabek, M. H. FTIR-Spectroscopic Characterization of Humic Acids and Humic Fractions Obtained by Advanced NaOH, Na₄P₂O₇, and Na₂CO₃ Extraction Procedures. *J. Plant Nutr. Soil Sci.* **2007**, 170 (4), 522–529.
- (25) Ribeiro, J. S.; Ok, S. S.; Garrigues, S.; De la Guardia, M. FTIR Tentative Characterization of Humic Acids Extracted from Organic Materials. *Spectrosc. Lett.* **2001**, 34 (2), 179–190.
- (26) Alberola, C.; Lichtfouse, E.; Navarrete, M.; Debaeke, P.; Souchère, V. Elemental Analysis, FTIR, and C-NMR of Humic Acid from Sewage Sludge Composting. *Agron.* **2004**, 24 (1), 13-18.
- (27) Obernosterer, I.; Benner, R.; Carolina, S. Competition between Biological and Photochemical Processes in the Mineralization of Dissolved Organic Carbon. *Limnol. Oceanog.* **2004**, 49 (1), 117–124.
- (28) Dittmar, T. The Molecular Level Determination of Black Carbon in Marine Dissolved

Organic Matter. *Org. Geochem.* **2008**, *39* (4), 396–407.

- (29) Stubbins, A.; Spencer, R. G. M.; Chen, H.; Hatcher, P. G.; Mopper, K.; Hernes, P. J.; Mwamba, V. L.; Mangangu, A. M.; Wabakanghanzi, J. N.; Six, J. Illuminated Darkness: Molecular Signatures of Congo River Dissolved Organic Matter and Its Photochemical Alteration as Revealed by Ultrahigh Precision Mass Spectrometry. *Limnol. Oceanogr.* **2010**, *55* (4), 1467–1477.
- (30) Robert M. Silverstein, Francis X. Webster, D. J. K. Spectrometric Identification of Organic Compounds. *Journal of Molecular Structure*. 2005, p 512.

Chapter 6 Design and Validation of an LED Incoherent Broadband Cavity Enhanced Absorption Spectrometer (LED-IBCEAS) for the Detection of Nitrogen Oxides

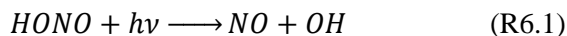
6.1 Synopsis

Nitrous acid is an important trace gas due to its role in the formation of reactive hydroxyl (OH) radicals as well as its deleterious health impacts. Known pathways for the formation of HONO include direct emissions, homogenous gas-phase reactions, heterogeneous reactions, surface photolysis, and biological processes. Despite decades of research, the observed concentrations of HONO, especially during the daytime, have yet to be explained. Recent research has indicated that photosensitized reactions involving various organic species such as humic acid with NO_2 may be an important source of HONO. Furthermore, studies have shown that direct photolysis of particulate nitrate or adsorbed HNO_3 on aerosol particles could also explain the observed concentrations of HONO over marine regions. To conduct laboratory experiments aimed at investigating the various sources of daytime HONO, we designed and constructed an LED incoherent broadband cavity enhanced absorption spectrometer (LED-IBCEAS) that allows for detection of gas-phase nitrogen oxides including HONO and NO_2 through differential optical absorption spectroscopy (DOAS). This chapter summarizes the theory behind LED-IBCEAS, describes the design and construction of a new instrument, and shows preliminary results from a validation experiment of the instrument in which a DOAS fit of NO_2 in the gas phase was performed.

6.2 Introduction

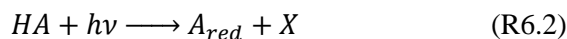
6.2.1 Sources of Atmospheric Nitrous Acid

Nitrous acid (HONO) is an important trace gas due to its harmful health effects¹⁻³ and its considerable role in the formation of hydroxyl (OH) radicals in both indoor and outdoor environments, as shown in Reaction 6.1:⁴⁻⁶



There are currently five known pathways for the formation of HONO in the atmosphere: direct emission, homogeneous gas-phase reactions, heterogeneous reactions, surface photolysis, and biological processes.⁷ However, despite being the focus of much research since the 1970s, atmospheric scientists have yet to fully explain the observed concentrations of HONO, particularly during the daytime.^{7,8} Depending on the environment, studies have indicated that an unknown source of HONO still exists that accounts for anywhere between 2 and 600 ppb/hr.⁷ Such a sizable gap points to the need for studies that will further investigate alternative pathways for HONO formation and the concomitant renoxification of the atmosphere.

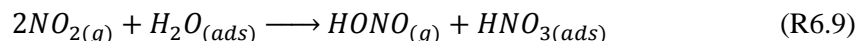
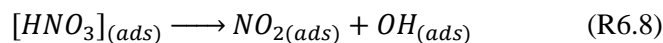
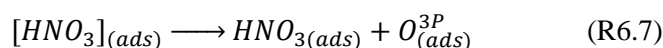
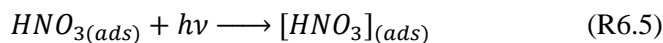
Heterogeneous reactions and surface photolysis are currently considered the most important sources of HONO, accounting for up to 86% of predicted HONO.⁹ Recently, this pathway has been extended to photosensitized heterogeneous reactions that take place on organic aerosol surfaces. For example, recent studies have proposed the following HONO formation mechanism involving photosensitized reduction of NO₂ on humic acid (HA):¹⁰



In the proposed mechanism, humic acid is first activated (R6.2), and then either deactivates with an oxidant (X) via R6.3 or reduces gaseous NO₂ to form HONO (R6.4). The exact nature of the

organic chemicals that participate in the HONO formation remain poorly defined and uncharacterized.

In addition to photosensitized reactions, direct photolysis pathways for HONO formation involving inorganic species have also been proposed.¹¹⁻¹³ For example, the following mechanism involving photolysis of adsorbed HNO₃ or particulate nitrate has been identified as an important daytime HONO and NO_x source in rural environments:



These two pathways for HONO formation (i.e., photosensitized reactions of NO₂ with various organic photosensitizers, photolysis of adsorbed HNO₃/NO₃⁻) require further characterization at aerosol surfaces to enhance agreement between modeled and observed HONO concentrations, particularly in marine regions.¹⁴ Specifically, studies investigating the impact of surface water content, chemical composition of organic photosensitizers, aerosol aging, emission of VOCs from aerosol surfaces, pH, and varying irradiation regimes (i.e., UVA vs UVB) on relevant HONO formation mechanisms are needed.

6.2.2 Methods for HONO Detection

Adding to the difficulty in discovering HONO formation pathways is the fact that HONO is inherently difficult to measure due to the lack of HONO reference systems caused by its unstable nature and high solubility. Currently, HONO is detected using either spectroscopic or wet chemical techniques. Wet chemical techniques work by collecting gaseous HONO through a device (e.g., wet effluent denuder, rotated denuder, bubbler) that are wetted with suitable solutions. The solutions are then either directly analyzed for HONO or the HONO is converted into a more stable species for subsequent analysis. Detection methods include ion chromatography (IC), fluorescence,

chemiluminescence, high performance liquid chromatography (HPLC), and spectrophotometry, among others. Wet chemical methods are simple and relatively inexpensive and are known to provide high sensitivity (i.e., minimum detection limit of ~pptv). However, the drawback to these methods is that their time resolution is on the order of minutes to hours. Furthermore, they suffer from unquantified chemical interferences and sampling artifacts due to the high potential for heterogeneous formation of HONO on the aqueous surfaces.^{15,16}

6.2.3 Long Path Absorption Based Spectroscopic methods

Optical spectroscopic techniques are favorable as they do not require chemical extraction, are non-intrusive, require no additional sample preparation such as trapping, separations, chemical conversion, pre-concentration, and they have minimal sampling artifacts.¹⁷ Spectroscopic techniques detect HONO either indirectly and directly. Indirect spectroscopic detection of HONO includes the use of photofragmentation laser-induced fluorescence, chemical ionization mass spectrometry, and thermal dissociation chemiluminescence. Direct spectroscopic detection of gas phase HONO is based upon the Beer-Lambert law and makes use of long path-lengths to establish the required absorbance signal. Direct spectroscopic methods can take several forms, including differential optical absorption spectroscopy (DOAS), tunable laser absorption spectroscopy (TLAS), cavity ringdown spectroscopy (CRDS), Fourier transform infrared spectroscopy (FTIR), and cavity enhanced absorption spectroscopy (CEAS).

We chose to develop an LED incoherent broadband cavity enhanced absorption spectrometer (LED-IBCEAS) for detection of trace gas HONO to conduct experiments aimed at the uncertainties described in the previous section. The following section gives an in-depth description of the theoretical principle of LED-IBCEAS. Section 6.4 gives a description of the design and construction of our system as well as results from the validation of the system by performing a DOAS fit for NO₂.

6.3 Theory of LED-IBCEAS

As discussed in Section 6.2.3, direct spectroscopic detection of gas-phase HONO based upon the Beer-Lambert law requires long path lengths to establish absorbance signals. To conduct experiments using this method without the use of instruments that are kilometers in length, cavity-based techniques make use of a passive optical resonator equipped with mirrors to achieve the required path lengths across a small sample volume. To design an effective LED-IBCEAS, the relevant theoretical considerations must be known, thereby allowing for informed decisions regarding parts and design. I begin with a brief description of the theoretical considerations of LED-IBCEAS, beginning with Beer's Law. Next, a description of the DOAS technique is presented. Finally, LED-IBCEAS is described, which is a variant on the DOAS technique.

6.3.1 Absorption Spectroscopy and Beer's Law

As light passes through a medium, some of its energy is absorbed by the various molecular species, resulting in the reconfiguration of their outer electron shells and formation of electronically excited states. UV-Vis Absorption spectroscopy is based upon this interaction, allowing target molecules to be identified based on their characteristic interactions with light at specific wavelengths. The Beer-Lambert law equation allows for determination of the concentration of a given species based on the change in intensity of light as it passes through the sample according to Equation 6.1:

$$I(\lambda) = I_o(\lambda) \cdot \exp(-\sigma(\lambda) \cdot c \cdot L) = I_o(\lambda) \cdot \exp(-\alpha(\lambda) \cdot L) \quad (\text{Eq6.1})$$

where I_o is the initial intensity of light emitted by a source of radiation, I is the intensity of radiation after passing through a medium of thickness L , σ is the absorption cross section of the absorbing species, and c is the concentration. The right-hand side of Equation 6.1 is described in terms of the absorption coefficient (α), which is defined as:

$$\alpha(\lambda) = \sigma(\lambda) \cdot c \quad (\text{Eq6.2})$$

Taking the natural log of the ratio of I_o/I gives optical depth (D). If the absorption cross section and path length are known, the concentration of the species can be determined:

$$D = \ln\left(\frac{I_o(\lambda)}{I(\lambda)}\right) = \alpha(\lambda) \cdot L = \sigma(\lambda) \cdot c \cdot L \quad (\text{Eq6.3})$$

6.3.2 Differential Optical Absorption Spectroscopy (DOAS)

Differential optical absorption spectroscopy, first introduced in 1979 by Perner and Platt,¹⁸ uses Beer's law over long path lengths and broad spectral bandwidth to simultaneously detect multiple trace gas species in the atmosphere. The DOAS algorithm can be described by first expanding the extinction coefficient to account for all the possible ways in which light is lost as it passes through the atmosphere in addition to absorption:

$$\alpha(\lambda) = \alpha_{Abs}(\lambda) + \alpha_{Mie}(\lambda) + \alpha_{Ray}(\lambda) \quad (\text{Eq6.4})$$

where α_{Abs} is absorption, α_{Mie} is scattering by aerosols, and α_{Ray} is scattering by gas molecules. This expanded extinction coefficient is then plugged into Eq6.1, yielding:

$$I(\lambda) = I_o(\lambda) \cdot \exp(-L \cdot [\sum_j(\sigma_j(\lambda) \cdot c_j) + \alpha_{Mie} + \alpha_{Ray}]) \quad (\text{Eq6.5})$$

In Eq6.4, the absorption coefficient, α_{Abs} , is defined in terms of cross section, $\sigma(\lambda)$, and concentration, c , and includes contributions from the j absorbing species that are present.

Since the Earth's atmosphere cannot be removed, and attempts to do so are generally frowned upon, determination of radiation intensity in the absence of the various absorbing species (I_o) in the atmosphere poses a challenge. However, this difficulty is overcome by separating the rapidly varying differential absorption structures from the slowly varying broadband absorption or extinction processes. This process is the hallmark of *differential* optical absorption spectroscopy, and leads to the following equation:

$$I(\lambda) = I_o(\lambda) \exp(-L \cdot [\sum_j(\sigma'_j(\lambda) \cdot c_j) + \sum_j(\sigma_j^B(\lambda) \cdot c_j) + \alpha_{Mie} + \alpha_{Ray}]) = I_o(\lambda) \exp(-L \cdot [\sum_j(\sigma'_j(\lambda) \cdot c_j) + \text{polynomial}]) \quad (\text{Eq6.6})$$

In Eq6.6, the absorption cross section has now been separated into broadband and differential portions, with the broadband structures being accounted for by a polynomial in the right-hand side of the equation. Rearranging Eq6.6 and taking the natural log gives the optical density:

$$D = \ln \left(\frac{I_o(\lambda)}{I(\lambda)} \right) = L \cdot (\sum_j (\sigma_j'(\lambda) \cdot c_j) + polynomial) = D' + D_B \quad (\text{Eq6.7})$$

Where the optical density is now recognized to consist of a differential component (D') and a broadband component (D_B):

$$D' = (\sum_j \sigma_j'(\lambda) \cdot c_j \cdot L - polynomial) \quad (\text{Eq6.8})$$

$$D_B = L \cdot (\sum_j (\sigma_j^B(\lambda) \cdot c_j) + \alpha_{Mie} + \alpha_{Ray}) \quad (\text{Eq6.9})$$

The absorber concentration can then be calculated by first subtracting the polynomial from the optical density and then fitting the calculated differential absorption cross section to the measured differential optical depth using a non-linear minimization method.

6.3.3 LED-IBCEAS

Controlled experiments in laboratory settings cannot use the DOAS algorithm due to size constraints. Cavity enhanced absorption spectroscopy overcomes this difficulty by making use of an optical cavity to artificially increase the light's path-length. In CEAS experiments, light is coupled into a cavity that has highly reflective mirrors at each end. The light then circulates inside the cavity from mirror to mirror, creating a much longer path length and allowing the light to interact with the sample enough to create an absorption spectrum. The absorption/extinction coefficient can then be calculated using the following equation:¹⁹

$$\alpha(\lambda) = \left(\frac{I_o(\lambda)}{I(\lambda)} - 1 \right) \cdot \left(\frac{1-R(\lambda)}{L} \right) = \sum_i \sigma_i'(\lambda) \cdot N_i + polynomial \quad (\text{Eq6.10})$$

Here, I_o is the light intensity upon exiting the cavity filled with non-absorbing species (e.g., nitrogen) I is the light intensity exiting the cavity filled with an absorbing sample, L is the cavity length, and R is the mirror reflectivity which changes as a function of wavelength. Mirror

reflectivity can be calculated by introduction of known concentrations of gases with different Rayleigh scattering coefficients (here, nitrogen and helium) and the use of the following equation:²⁰

$$R(\lambda) = 1 - L \frac{\left(\frac{I_{N_2}(\lambda)}{I_{He}(\lambda)}\right) \alpha_{Ray}^{N_2}(\lambda) - \alpha_{Ray}^{He}(\lambda)}{1 - \left(\frac{I_{N_2}(\lambda)}{I_{He}(\lambda)}\right)} \quad (\text{Eq6.11})$$

Once the absorption coefficient has been calculated, the DOAS fitting procedure can be employed as described in Section 6.3.2 to attain gas concentrations.

6.4 Design and Validation of LED-IBCEAS

6.4.1 Design and Hardware

For detection of gas phase nitrogen oxides (NO₂ and HONO), we designed and constructed an LED-IBCEAS. A block diagram of the instrument is shown in Figure 6.1. The light source consists of a high-power UV LED (Nichia, NVSU333A, 3.640 Watt, peak wavelength $\lambda = 365$ nm) mounted onto a copper printed circuit board (Cree XHP-70 MCPB). The light source was then mounted to a heatsink block which consists of a copper plate attached to a heatsink (ARCTIC, Alpine 11 plus) with a Peltier cooler sandwiched between the two for temperature control. The Peltier cooler and LED are separately powered using two power supplies (Mouser, TDK-Lambda Z36-12-U). A custom-built circuit board was constructed to allow for constant current output to the LED. To monitor the temperature of the system, thermocouple probes were placed at the LED and the heatsink. Readout of the temperature probes and control of the power supplies is accomplished using a custom built Labview program that communicates with the hardware through a MyRIO (Figure 6.2).

The LED and heatsink block is held in place using a custom-built mount consisting of an aluminum base tooling plate that can be swiveled in x and y directions (Figure 6.3). The mount has a cavity that holds a lens tube containing an aspheric condenser lens (Thorlabs, ACL25416U-A, diameter = 1 inch, NA = 0.79). Collimated light is then directed into an optical cavity (CRD optics, length = 1 m, diameter = 2.54 cm) with high reflectivity mirrors at each end (CRD Optics, Model

Number 901-0010-0370, 99.99% reflectivity at 370 nm, ROC = 1 meter, diameter = 2.54 cm). Mirrors are held in place using purgeable mirror mounts (CRD Optics, 902-8010) that connect to the cavity through conflat flanges. Adjustment of each mirror is accomplished using three alignment screws that press against a brass backing ring fit onto the back surface of the mirror. Mirrors are given a constant purge flow of N₂ to prevent deposition of contaminants.

Collimated light exiting the cavity is collected and focused using a plano-convex fused silica lens (Thorlabs, LA4380-UV, diameter = 1 inch, AR coated 245-400 nm, f/3.93, focal length = 100 mm). Out of band light is removed using a bandpass filter (Semrock, FF01-370/36-25, 25 mm) and the remaining light is fed into a round to keyed linear fiber optic cable (Ocean optics, PL100-2-UV-VIS) connected to a fiber adapter (Thorlabs, SM1SMA SMA). The focusing lens, bandpass filter, and fiber adapter are all held in-line using a lens tube (Thorlabs, SM1M20 SM1) with an adjustable length to allow the maximum amount of light into the fiber optic cable.

Light exiting the fiber optic cable is then fed into the slit inlet (25 μm) of a fiber-coupled spectrometer (Ocean Optics, QEPRO). The spectrometer optical bench consists of a Symmetrical Crossed Czerny Turner monochromator with a 101 mm focal length (f/# = f/4). Light is dispersed using an H3 grating (600 mm⁻¹ groove density) and detected using a back-thinned, thermo electric cooled CCD detector (Hamamatsu, S7031-1006S). The resulting spectral range of the system is 300-680 nm with a spectral resolution of ~0.96 nm. The QEPro is controlled using the Ocean Optics software.

For assistance with LED alignment, a laser diode module (CPS405 Thorlabs, λ = 402.6, 4.4mW, 30 mA) was purchased. The laser diode is powered using a LDS5 5-volt linear regulated power supply (Thorlabs) and is held in place using an SM2A6 adapter with external SM2 threads and internal SM1 threads (Thorlabs) and an AD11F SM1 threaded adapter placed into slotted lens tube equipped with an SM2D25 lever-actuated iris diaphragm (Thorlabs).

6.4.2 Validation of Instrument

As mentioned previously, the absorption coefficient of an absorbing species in CEAS can be calculated according to:

$$\alpha(\lambda) = \left(\frac{I_o(\lambda)}{I(\lambda)} - 1 \right) \cdot \left(\frac{1-R(\lambda)}{L} \right) = \sum_i \sigma'_i(\lambda) \cdot N_i + polynomial \quad (\text{Eq6.12})$$

In this section we present the validation of our LED-IBCEAS system by performing a DOAS fit of NO₂ and comparing the results with literature. Figure 6.4 shows the flow diagram of the steps of a DOAS fit using LED-IBCEAS.

6.4.1.1 Calculation of Mirror Reflectivity

As shown by Equation 6.12, mirror reflectivity is necessary to calculate accurate absorption coefficients. The mirror reflectivity equation is given as follows:

$$R(\lambda) = 1 - L \frac{\left(\frac{I_{N_2}(\lambda)}{I_{He}(\lambda)} \cdot \alpha_{Ray}^{N_2}(\lambda) \right) - (\alpha_{Ray}^{He}(\lambda))}{1 - \left(\frac{I_{N_2}(\lambda)}{I_{He}(\lambda)} \right)} \quad (\text{Eq6.13})$$

To determine the Rayleigh scattering coefficient for He and N₂, first the Rayleigh scattering cross section (α_{Ray}) for each gas was determined using Equation 6.14:²¹

$$\sigma_{Ray}(\lambda) = \frac{24\pi^3}{N^2\lambda^4} \left(\frac{n_\lambda^2 - 1}{n_\lambda^2 + 2} \right)^2 F_k(\lambda) \quad (\text{Eq6.14})$$

Here, N is the number density of the gas ($N = 2.546899 \times 10^{19}$ molecules cm⁻³), n is the index of refraction and F_k is the King correction factor. The index of refraction of each gas was calculated according to:²⁰

$$(n - 1) \times 10^8 = A + \frac{B}{C - \nu^2} \quad (\text{Eq6.15})$$

where ν is the wavenumber in cm⁻¹ and A and B are taken from the literature and are $A_{He} = 2283$, $A_{N_2} = 5677.465$, $B_{He} = 1.8102 \times 10^{13}$ cm⁻¹, $B_{N_2} = 318.81874 \times 10^{12}$ cm⁻¹, $C_{He} = 1.5342 \times 10^{10}$ cm⁻¹, and $C_{N_2} = 14.4 \times 10^9$ cm⁻¹.²⁰ F_k is the king correction factor and is equal to 1 for He and calculated for N₂ using Equation 6.16:²¹

$$F_k(\nu) = 1.034 + 3.17 \times 10^{-12} \cdot (\nu)^2 \quad (\text{Eq6.16})$$

It should be noted that the constants used for this calculation assume a temperature of 288.15 K and 1 atm of pressure as done in previous studies.^{20,22} To determine the error in calculated mirror reflectivity due to this assumption, pressure and temperature inside the cavity should be monitored in future experiments.

Using the Rayleigh scattering cross sections, the Rayleigh scattering coefficient (α_{Ray}) for each gas was calculated according to:

$$\alpha_{Ray} = N \cdot \sigma_{Ray} \quad (\text{Eq6.17})$$

The resulting Rayleigh scattering coefficients for helium and nitrogen are given in Figure 6.5A and Figure 6.5B, respectively. The LED light intensity transmitted when the cavity was filled with He and N₂ (Figure 6.6) was used then to calculate the mirror reflectivity (Figure 6.7).

6.4.1.2 Calculation and DOAS Fitting of the CEAS Absorption Coefficient for NO₂

The system was validated by performing a DOAS fit on CEAS spectra obtained from filling the cavity with 8 ppm of NO₂. The high resolution reference spectrum of the absorption cross section for NO₂ was taken from the literature²³ and convoluted to the resolution of our spectrometer. Figure 6.8A,B shows the NO₂ absorption cross section in our specific region of interest before and after convolution. The full spectrum is shown in Figure 6.11 (Supporting Information Figures Section 6.8.1). The absorption cross section spectrum of NO₂ has an asymmetric bellshape with a maximum at about 400 nm and is separated into two broad regions: a region below 250 nm due to D-X electronic transitions and a region between 300 and 790 nm due to B-X and A-X electronic transitions.^{24,25} Superimposed onto the broad spectrum are densely packed, fine-structure peaks, many of which lack definite spectroscopic assignment.^{25,26} The high density of peaks are due to the existence of strong vibronic interactions between the electronic ground state (²A₁) and the three excited doublet states (²B₁, ²B₂, ²A₂),^{27,28} leading to the existence of thousands of reproducible peaks near the dissociation limit at 400nm.²⁹ The strongest vibronic interaction occurs as a result of the conical intersection between the potential energy surfaces of the two lowest electronic states (²A₁

and 2B_2).^{25,26,30,31} Additional peaks are also present due to rovibronic interactions.²⁸ It is this unique fine structure that allows NO_2 to be detected using DOAS methods.

Next, the N_2 and NO_2 intensity spectra were obtained and are shown in Figure 6.9. The absorption coefficient was then calculated from intensity data using the CEAS equation:

$$\alpha(\lambda) = \left(\frac{I_o(\lambda)}{I(\lambda)} - 1 \right) \cdot \left(\frac{1-R(\lambda)}{L} \right) \quad (\text{Eq6.18})$$

The differential structure of the absorption coefficient and the convoluted NO_2 absorption cross section were obtained by employing a low pass filter to the spectra and then subtracting the resulting broadband spectra from the original. DOASIS software³² was then used to fit the observed differential absorption spectrum with a nonlinear least squares method and a polynomial of the 6th order. Figure 6.10 shows a comparison of our fit of the calculated absorption coefficient with a fit from the literature of a sample containing both NO_2 and HONO.³³ Absorption features are in general agreement in terms of relative peak positions. The calculated concentration is $2.23 \times 10^7 \pm 1.03 \times 10^7$ molecules cm^{-3} , which falls within the range of the expected 1.97×10^{14} molecules cm^{-3} based on the concentration of the NO_2 reference gas (8 ppm).

6.5 Conclusions and Future Work

In this chapter we reviewed the current state of HONO chemistry in the atmosphere and the need for more experiments to determine unknown sources. We then discussed various methods to detect HONO, leading to the decision to use CEAS. After a description of the theory, we presented the design and construction of an LED-IBCEAS system. Validation of the system was done by performing a DOAS fit of the calculated absorption spectrum of a gas sample consisting of 8 ppm NO_2 . Comparison with the literature yielded good agreement.

Future work will involve improvement of the signal to noise ratio, removal of etalon structures from the LED light, and observation of HONO. Correct temperature and pressure measurements will also allow for the determination of error in mirror reflectivity, which will allow

for improved concentration calculations. Furthermore, experiments will be conducted to determine the missing sources of HONO.

6.6 Acknowledgements

The author of this dissertation gratefully acknowledges Mike Alves for help throughout the design, construction, and validation of the instrument, Frank Cardon for design and construction of the LED circuit and control system, Mark Young for his valuable discussion of design considerations, Kristin Wall for calculation of Rayleigh scattering cross sections, and Joe Mayer for construction of the LED housing.

6.7 Figures

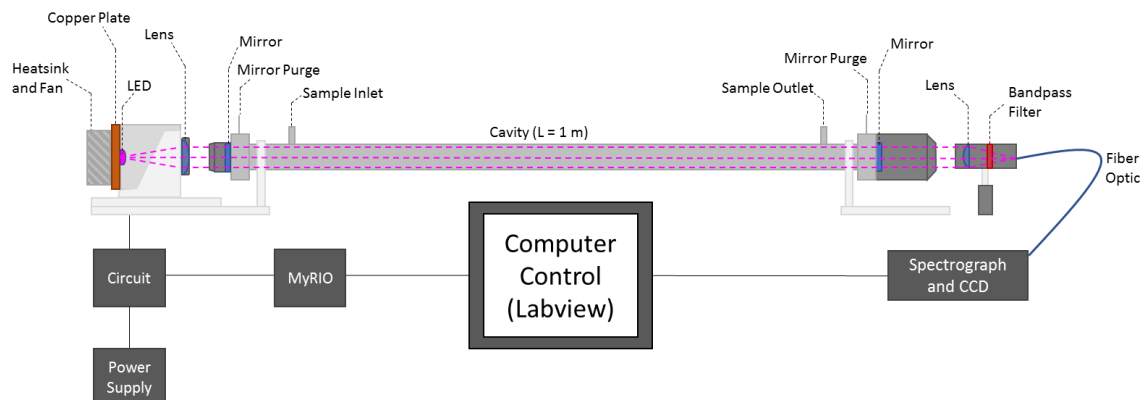
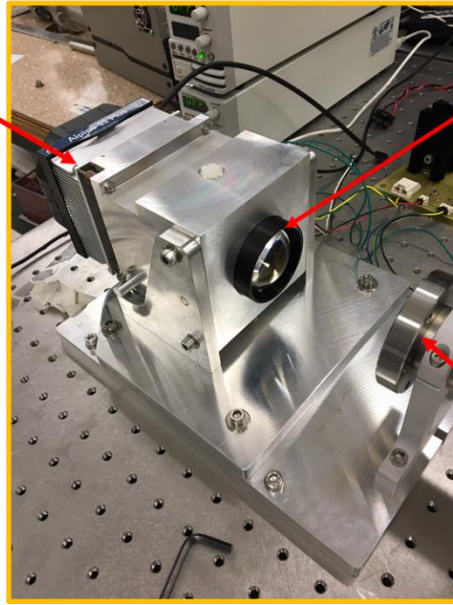


Figure 6.1: Block diagram of the LED incoherent broadband cavity enhanced absorption spectrometer constructed for detection of gas-phase nitrogen oxides.



Figure 6.2: Schematic of the circuit board, power supplies, and MyRIO control. The computer interacts with the MyRIO through Labview to control the power supply of the LED and Peltier cooler and to give temperature readout of the thermocouples.

Heatsink,
Peltier
Cooler,
Copper
Block, LED



Lens tube,
collimating
lens

Cavity entrance

Figure 6.3: Image of the custom-built mount consisting of an aluminum base tooling plate that can be swiveled in x and y directions. The mount has a cavity filled with lens tube and a lens for collimation of LED light not the optical cavity.

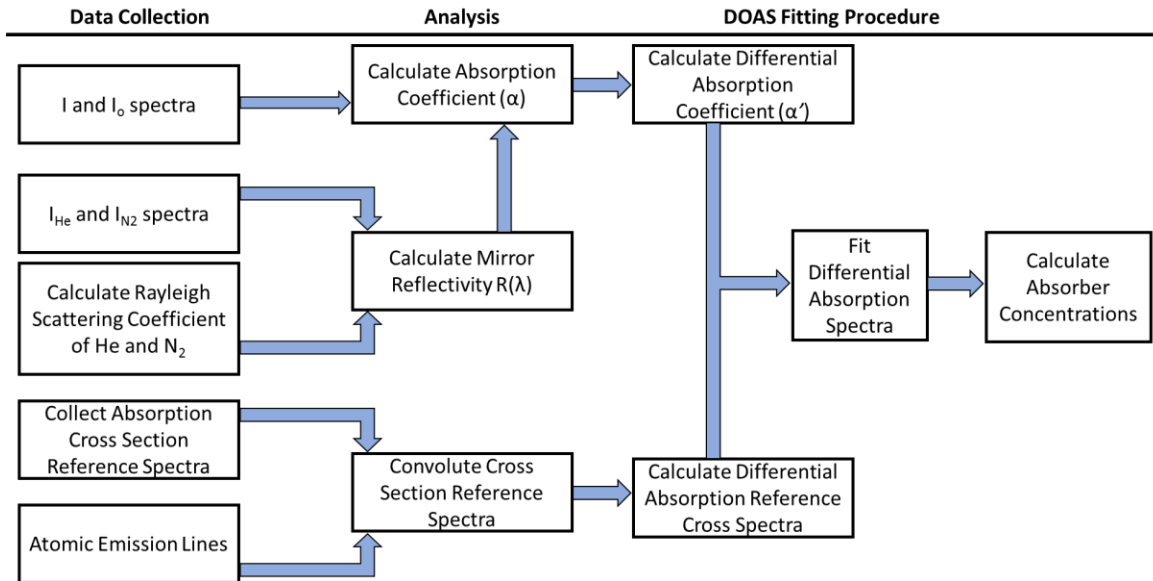


Figure 6.4: Flow chart for determination of differential absorption coefficients and absorber concentrations using the LED-IBCEAS-DOAS method.

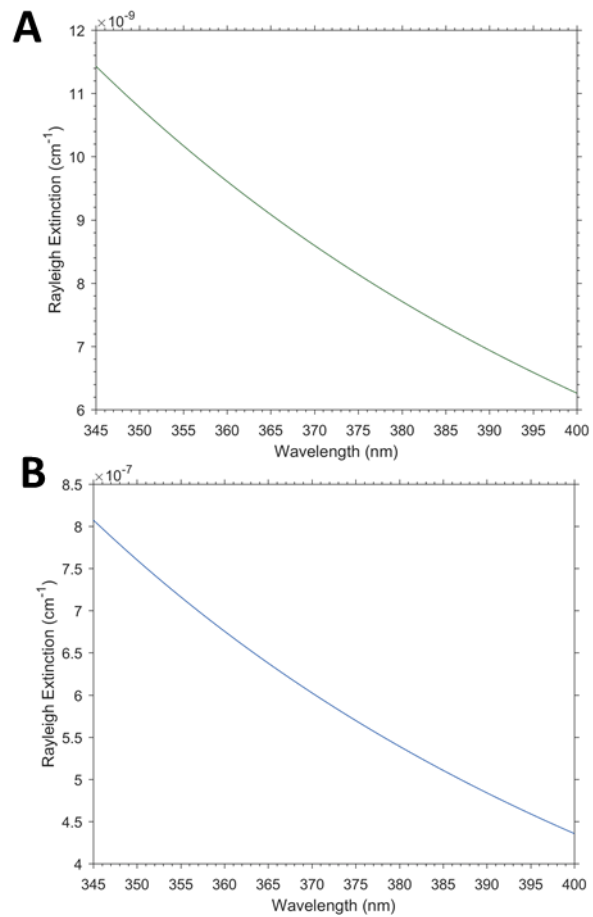


Figure 6.5: Calculated Rayleigh extinction coefficient for A) helium and B) nitrogen.

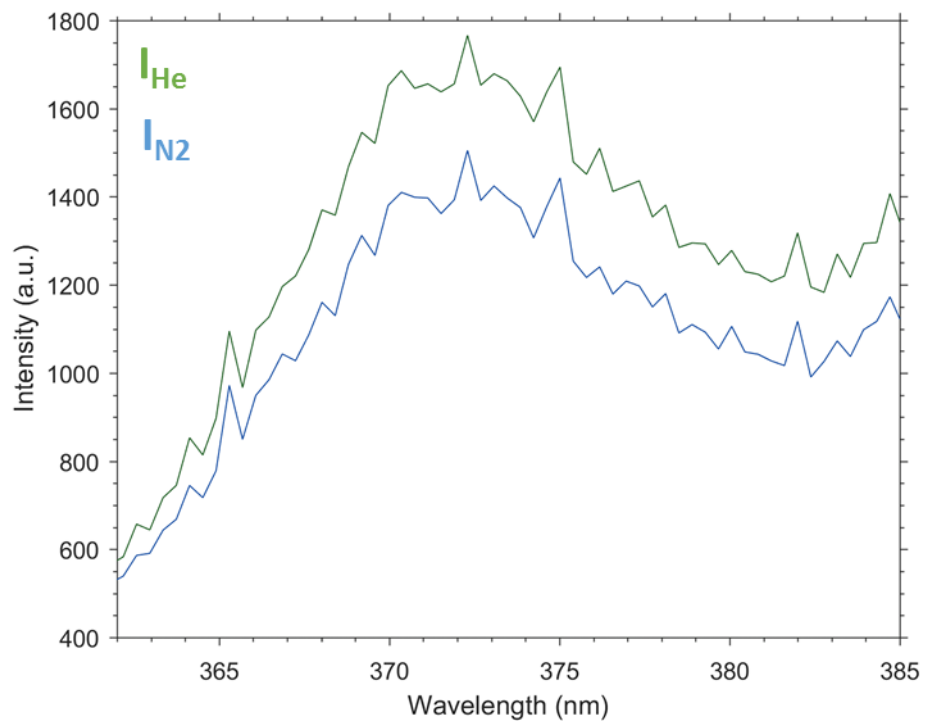


Figure 6.6: LED transmitted intensity through the cavity filled with helium and with nitrogen.

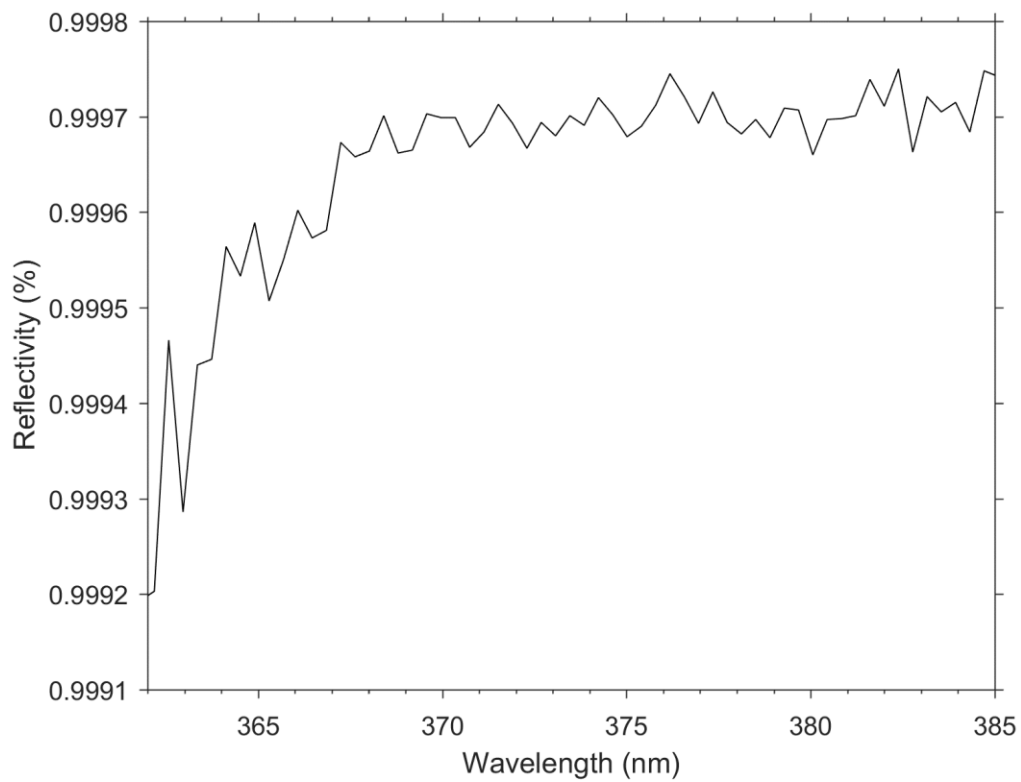


Figure 6.7: Calculated mirror reflectivity as a function of wavelength.

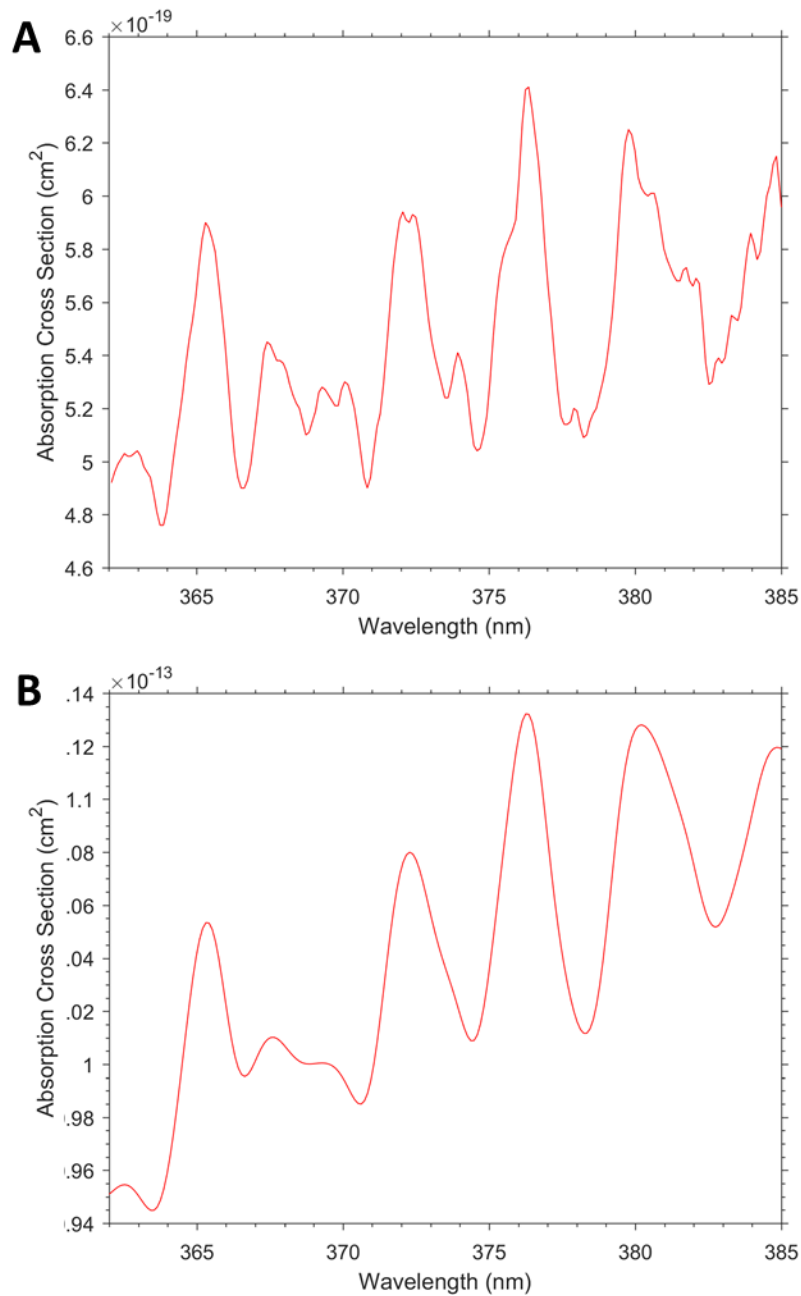


Figure 6.8: A) Literature NO₂ absorption cross section before and B) after convolution to the resolution of our spectrometer. Data in A) reprinted from Burrows, J. P.; Dehn, A.; Deters, B.; Himmelmann, S.; Richter, A.; Voigt, S.; Orphal, J. Atmospheric Remote-Sensing Reference Data from GOME: Part 1. Temperature-Dependent Absorption Cross-Sections of NO₂ in the 231-794 nm Range, *J. Quant. Spectrosc. Radiat. Transf.* **1998**, *60* (6), 1025–1031.

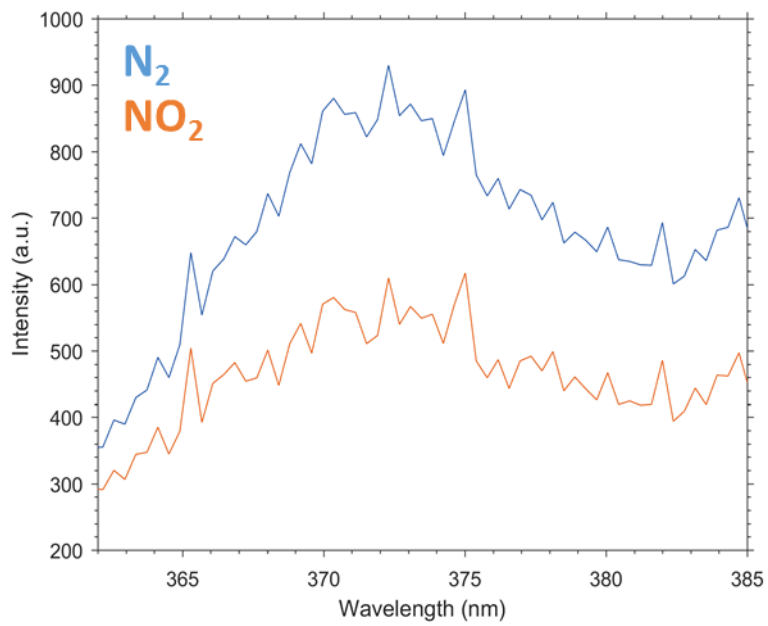


Figure 6.9: LED transmitted intensity through the optical cavity filled with nitrogen or NO₂.

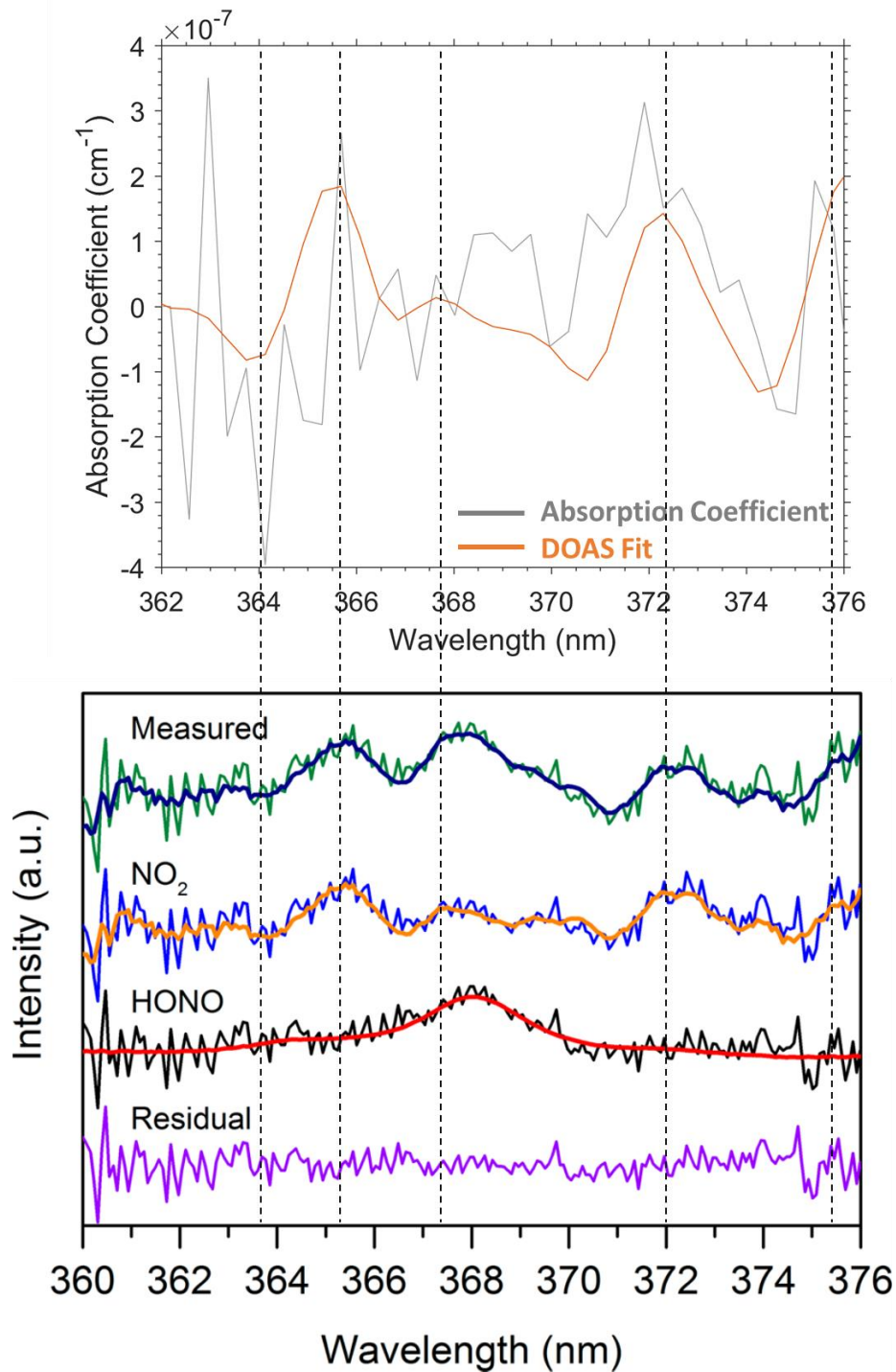


Figure 6.10: (Top) Resulting fit of the measured absorption coefficient for NO₂ compared with the results from the literature of a mixture of NO₂ with HONO (bottom). Bottom figure reprinted from Scharko, N. K.; Berke, A. E.; Raff, J. D. Release of Nitrous Acid and Nitrogen Dioxide from Nitrate Photolysis in Acidic Aqueous Solutions. *Environ. Sci. Technol.* **2014**, *48* (20), 11991–12001.

6.8 Supporting Information

6.8.1 Supporting Information Figures

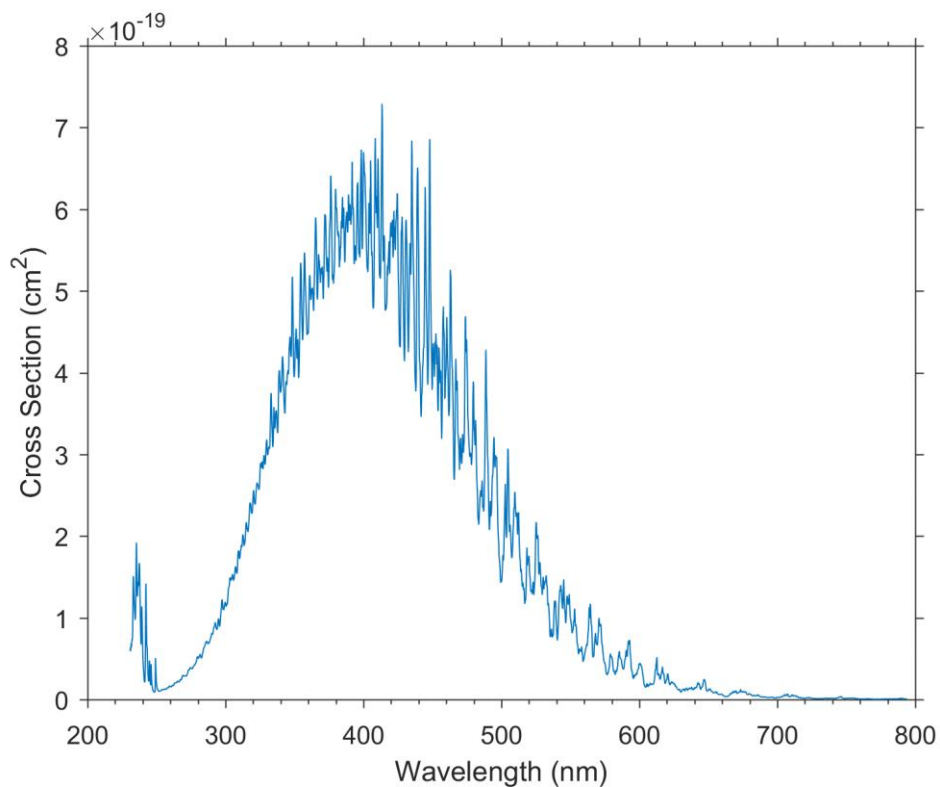


Figure 6.11: High resolution absorption cross section of NO₂ from literature. Data from Burrows, J. P.; Dehn, A.; Deters, B.; Himmelmann, S.; Richter, A.; Voigt, S.; Orphal, J. Atmospheric Remote-Sensing Reference Data from GOME: Part 1. Temperature-Dependent Absorption Cross-Sections of NO₂ in the 231-794 nm Range, *J. Quant. Spectrosc. Radiat. Transf.* **1998**, *60* (6), 1025–1031.

6.9 References

- (1) Sleiman, M.; Gundel, L. A.; Pankow, J. F.; Jacob, P.; Singer, B. C.; Destailats, H. Formation of Carcinogens Indoors by Surface-Mediated Reactions of Nicotine with Nitrous Acid, Leading to Potential Thirdhand Smoke Hazards. *Proc. Natl. Acad. Sci.* **2010**, *107* (15), 6576–6581.
- (2) Rasmussen, T. R.; Brauer, M.; Kjaergaard, S. Effects of Nitrous Acid Exposure on Human Mucous Membranes. *Am. J. Crit. Care. Med.* **1995**, *151* (5), 1504–1511.
- (3) Pitts, J. N.; Grosjean, D.; Cauwenberghe, K. Van; Schmid, J. P.; Fitz, D. R. Photooxidation of Aliphatic Amines Under Simulated Atmospheric Conditions: Formation of Nitrosamines, Nitramines, Amides, and Photochemical Oxidant. *Environ. Sci. Technol.* **1978**, *12* (8), 946–953.
- (4) Kleffmann, J. Daytime Sources of Nitrous Acid (HONO) in the Atmospheric Boundary Layer. *ChemPhysChem* **2007**, *8* (8), 1137–1144.
- (5) Kleffmann, J.; Gavriloaiei, T.; Hofzumahaus, A.; Holland, F.; Koppmann, R.; Rupp, L.; Schlosser, E.; Siese, M.; Wahner, A. Daytime Formation of Nitrous Acid: A Major Source of OH Radicals in a Forest. *Geophys. Res. Lett.* **2005**, *32* (5), 1–4.
- (6) Acker, K.; Möller, D.; Wieprecht, W.; Meixner, F. X.; Bohn, B.; Gilge, S.; Plass-Dülmer, C.; Berresheim, H. Strong Daytime Production of OH from HNO₂ at a Rural Mountain Site. *Geophys. Res. Lett.* **2006**, *33* (2), 2–5.
- (7) Spataro, F.; Ianniello, A. Sources of Atmospheric Nitrous Acid: State of the Science, Current Research Needs, and Future Prospects. *J. Air Waste Manage. Assoc.* **2014**, *64* (11), 1232–1250.
- (8) Czader, B. H.; Rappenglück, B.; Percell, P.; Byun, D. W.; Ngan, F.; Kim, S. Modeling Nitrous Acid and Its Impact on Ozone and Hydroxyl Radical during the Texas Air Quality Study 2006. *Atmos. Chem. Phys.* **2012**, *12* (15), 6939–6951.
- (9) Sarwar, G.; Roselle, S. J.; Mathur, R.; Appel, W.; Dennis, R. L.; Vogel, B. A Comparison of CMAQ HONO Predictions with Observations from the Northeast Oxidant and Particle Study. *Atmos. Environ.* **2008**, *42* (23), 5760–5770.
- (10) Stemmler, K.; Ndour, M.; Elshorbany, Y.; Kleffmann, J.; D’Anna, B.; George, C.; Bonn, B.; Ammann, M. Light Induced Conversion of Nitrogen Dioxide into Nitrous Acid on Submicron Humic Acid Aerosol. *Atmos. Chem. Phys.* **2007**, *7* (16), 4237–4248.
- (11) Ye, C.; Zhang, N.; Gao, H.; Zhou, X. Photolysis of Particulate Nitrate as a Source of HONO and NO_x. *Environ. Sci. Technol.* **2017**, *51* (12), 6849–6856.
- (12) Ye, C.; Gao, H.; Zhang, N.; Zhou, X. Photolysis of Nitric Acid and Nitrate on Natural and Artificial Surfaces. *Environ. Sci. Technol.* **2016**, *50* (7), 3530–3536.
- (13) Zhou, X.; Zhang, N.; Teravest, M.; Tang, D.; Hou, J.; Bertman, S.; Alaghmand, M.; Shepson, P. B.; Carroll, M. A.; Griffith, S.; Dusanter, S.; Stevens, P. S. Nitric Acid

Photolysis on Forest Canopy Surface as a Source for Tropospheric Nitrous Acid. *Nat. Geosci.* **2011**, 4 (7), 440–443.

- (14) Ye, C.; Zhou, X.; Pu, D.; Stutz, J.; Festa, J.; Spolaor, M.; Tsai, C.; Cantrell, C.; Mauldin, R. L.; Campos, T.; Weinheimer, A.; Hornbrook, R. S.; Apel, E. C.; Guenther, A.; Kaser, L.; Yuan, B.; Karl, T.; Haggerty, J.; Hall, S.; Ullmann, K.; Smith, J. N.; Ortega, J.; Knute, C. Rapid Cycling of Reactive Nitrogen in the Marine Boundary Layer. *Nature* **2016**, 532 (7600), 489–491.
- (15) Acker, K.; Möller, D.; Auel, R.; Wieprecht, W.; Kalaß, D. Concentrations of Nitrous Acid, Nitric Acid, Nitrite and Nitrate in the Gas and Aerosol Phase at a Site in the Emission Zone during ESCOMPTE 2001 Experiment. *Atmos. Res.* **2005**, 74 (1–4), 507–524.
- (16) Febo, A.; Perrino, C.; Cortiello, M. A Denuder Technique for the Measurement of Nitrous Acid in Urban Atmospheres. *Atmos. Environ. Part A, Gen. Top.* **1993**, 27 (11), 1721–1728.
- (17) Chen, W.; Maamary, R.; Fertein, E. Photonic Sensing of Environmental Gaseous Nitrous Acid (HONO): Opportunities and Challenges. 693–737.
- (18) Perner, D.; Platt, U. Detection of Nitrous Acid in the Atmosphere by Differential Optical Absorption. **1979**, 6 (12), 917–920.
- (19) Fiedler, S. E.; Hoheisel, G.; Ruth, A. A.; Hese, A. Incoherent Broad-Band Cavity-Enhanced Absorption Spectroscopy of Azulene in a Supersonic Jet. *Chem. Phys. Lett.* **2003**, 382 (3–4), 447–453.
- (20) Thalman, R.; Zarzana, K. J.; Tolbert, M. A.; Volkamer, R. Rayleigh Scattering Cross-Section Measurements of Nitrogen, Argon, Oxygen and Air. *J. Quant. Spectrosc. Radiat. Transf.* **2014**, 147, 171–177.
- (21) Sneep, M.; Ubachs, W. Direct Measurement of the Rayleigh Scattering Cross Section in Various Gases. *J. Quant. Spectrosc. Radiat. Transf.* **2005**, 92 (3), 293–310.
- (22) Bodhaine, B. A.; Wood, N. B.; Dutton, E. G.; Slusser, J. R. On Rayleigh Optical Depth Calculations. *J. Atmos. Ocean. Technol.* **1999**, 16 (11 PART 2), 1854–1861.
- (23) Burrows, J. P.; Dehn, A.; Deters, B.; Himmelmann, S.; Richter, A.; Voigt, S.; Orphal, J. Atmospheric Remote-Sensing Reference Data from GOME: Part 1. Temperature-Dependent Absorption Cross-Sections of NO₂ in the 231–794 nm Range. *J. Quant. Spectrosc. Radiat. Transf.* **1998**, 60 (6), 1025–1031.
- (24) Orphal, J. A Critical Review of the Absorption Cross-Sections of O₃ and NO₂ in the Ultraviolet and Visible. *J. Photochem. Photobiol. A Chem.* **2003**, 157, 185–209.
- (25) Bilgehan, D.-P. Dissertation, Fachbereich Physik der Universität Bremen, **2006**.
- (26) Volkers, E. A.; Koudijzer, M. C.; Vredenburg, A.; Bulthuis, J.; Stolte, S.; Linnartz, H.; Jost, R. The A₂B₂-X₂A₁ Electronic Transition of 15NO₂: A Rovibronic Survey Covering 14,300–18,000 cm⁻¹. *J. Mol. Spectrosc.* **2006**, 2135(1), 1–17.

- (27) Kirmse, B.; Delon, A.; Jost, R. NO₂ Absorption Cross Section and Its Temperature Dependence. *J. Geophys. Res.* **1997**, *102* (D13), 89–105.
- (28) Georges, R.; Delon, A.; Bylicki, F.; Jost, R.; Campargue, A.; Charvat, A.; Chenevier, M.; Stoeckel, F. Jet Cooled NO₂ intra Cavity Laser Absorption Spectroscopy (ICLAS) between 11200 and 16150 cm⁻¹. *Chem. Phys.* **1995**, *190*, 207-229.
- (29) Nizkorodov, S. A.; Sander, S. P.; Brown, L. R. Temperature and Pressure Dependence of High-Resolution Air-Broadened Absorption Cross Sections of NO₂ (415-525 Nm). *J. Phys. Chem. A* **2004**, *108* (22), 4864-4872.
- (30) Schwartz, S. E.; Johnston, H. S. Kinetics of Nitrogen Dioxide Fluorescence. *J. Chem. Phys.* **1969**, *51* (4), 1286–1302.
- (31) Jackels, C. F.; Davidson, E. R. An Ab Initio Potential-Energy Surface Study of Several Electronic States of NO₂. *J. Chem. Phys.* **1976**, *65* (8), 2941–2957.
- (32) Kraus, S. G. *DOASIS --- A Framework Design for DOAS*; 2006.
- (33) Scharko, N. K.; Berke, A. E.; Raff, J. D. Release of Nitrous Acid and Nitrogen Dioxide from Nitrate Photolysis in Acidic Aqueous Solutions. *Environ. Sci. Technol.* **2014**, *48* (20), 11991–12001.

Chapter 7 Conclusions and Future Work

7.1 Synopsis

The overall goal of this dissertation was to determine how fundamental chemical processes alter sea spray aerosol properties in hopes of better understanding their impact on the Earth's climate. To this end, the dissertation first described experiments aimed at improving the understanding of how SSA chemical complexity is controlled by ocean biological activity, and how these chemical changes manifest in the climate relevant properties of SSA. With the improved knowledge of the molecules present in SSA, we next conducted experiments to determine how these species altered various heterogeneous and photochemical aging reactions that take place at the surface of SSA. Finally, we described the construction and validation of a cavity enhanced absorption spectrometer that will allow for detection of trace gases resulting from the various photochemical reactions that occur at the surfaces of aerosols. The following sections describe the main conclusions from each study and introduce ongoing investigations and future studies.

7.2 Chapter 2 Summary

Chapter two of this thesis presented results of studies conducted to improve the understanding of the ways in which ocean biological activity alters the chemical composition of SSA, and how those translate to changes in the climate relevant properties of SSA. The 2016 IMPACTS research intensive was a month-long collaborative effort involving several research institutions that made use of an indoor ocean-atmosphere facility to generate and monitor SSA. Over the course of two phytoplankton blooms, SSA chemical complexity and IN properties were monitored using a range of analytical methods. Single particle Raman spectroscopy of authentic SSA produced from a wave flume was compared with lab generated model systems to identify the specific molecules found within SSA.

Having identified the molecules in SSA, we then linked temporal and size resolved changes in SSA chemical complexity to the changing biological conditions in the water. The enrichment of long chain fatty acids in submicron SSA was determined to be a result of enhanced activity of autotrophic phytoplankton during the first bloom. As bacteria counts increased during the second bloom, the amount of labile, aliphatic-rich species was observed to decrease. We attributed this to the enzymatic activity of the bacteria that processed the labile, long-chain fatty acids. Furthermore, an enhancement of various saccharides was observed in supermicron SSA during the second bloom, likely due to the various secretions of bacteria. Such results illuminated the complex interaction between autotrophic and heterotrophic microbes in the ocean and the resulting impacts such microbial processes have on the chemical complexity of SSA.

Finally, a range of analytical methods were used to address how changes to chemical speciation of SSA altered their climate relevant properties—specifically IN activity. CFDC analysis of SSA found that IN counts increased during periods of high biological activity. Single particle Raman analysis of ICRs immediately following the peak in IN revealed that particles consisting of bacteria fragments and DOM were the main IN active components of SSA. This allowed us to link changes in SSA resulted in changes to ice nucleating capability of SSA.

7.3 Chapter 3 Summary

Chapter three presented results from a study aimed at attaining a better understanding of how the presence of organics altered some of the well-known heterogeneous reactions of trace gases with SSA. Off-line and on-line analysis of SSA particles reacted on-the-fly with HNO_3 during the IMPACTS experiment revealed that in addition to highly reactive SSA consisting of NaCl and unreactive SSA consisting of fatty acids, a third type of SSA derived from some of the biological components of gram-negative bacteria exhibited its own reactivity. Using model systems and employing chemical principles, we proposed a new pathway for the heterogeneous reaction of HNO_3 with SSA involving the basic groups of biological components of SSA such as

lipopolysaccharides. These previously unrecognized reactions may serve as another mechanism for nitrate salt formation and may not only be a heterogeneous pathway for sea spray aerosol, but for a variety of other types of atmospheric aerosol as well.

7.4 Chapter 4 Summary

Chapter four focused on photosensitized reactions between photosensitizer molecules and organic substrates at the organic-rich air-water interface found in marine-relevant regions. Previous studies using simple model system molecules meant to mimic the photoactive component of SSA, termed chromophoric dissolved organic matter (CDOM), showed the potential for a previously unknown class of photosensitized reactions with single component organic substrates leading to the formation of unsaturated and functionalize VOCs and condensed phase products.¹⁻³ However, as such experiments used simple photosensitizer model systems, the question of how effective marine-derived DOM was as a photosensitizer remained unanswered.

For this reason, we used a suite of analytical approaches to investigate the capability of three different photosensitizers with increasing chemical complexity to initiate photosensitized reactions with the fatty acid nonanoic acid in organic-rich environments. Analysis by ATR-FTIR and MS revealed that 4-BBA is an efficient photosensitizer, leading to the production of unsaturated and functionalized products, including C8/aldehydes/ketones, oxygenated products, and combination products (BBA and NA). However, irradiation of more environmentally relevant model systems revealed differences in the photosensitizing capability of the molecules. Terrestrially derived HA was found to be a less efficient photosensitizer than BBA, yet still produced unsaturated and functionalized products. Finally, irradiation of marine derived DOM in the presence of NA revealed no enrichment of products, indicating the m-DOM produced by marine microbes is a less efficient photosensitizer within an organic rich layer.

Using EEMS, ATR-FTIR, and HESI-LIT-ORBITRAP MS, we investigated the chemical composition and associated chromophores within the complex model systems HA and m-DOM to

explain their differences in reactivity. Despite being more chemically complex than HA, m-DOM was less reactive due to its lower degree of aromaticity and high abundance of CRAM.

7.5 Chapter 5 Summary

Chapter 5 focused on the impact of both photochemical heterogeneous and homogeneous reactions. Specifically, we investigated the formation of new secondary marine aerosol by oxidation of VOCs with OH as well as the heterogeneous aging reaction of primary SSA by OH. While numerous studies have examined the formation of SMA by various oxidation reactions, much uncertainty remains regarding the various SMA precursor gases and pathways of particle formation. Furthermore, studies on the heterogeneous aging reactions of OH with aerosols have focused specifically on terrestrially derived aerosol particles rather than SSA particles, which have unique chemical composition from their terrestrial counterparts.

For this reason, we investigated the OH oxidation reactions on the formation and chemical composition of marine-derived aerosols using a Marine Aerosol Reference Tank (MART) filled with water from a lab-grown phytoplankton bloom to produce SSA particles and volatile organic compounds (VOCs) representative of those found over the ocean. We then used on-line and off-line methods to compare unreacted nascent marine aerosols to the marine aerosols that resulted from headspace and SSA being sent through a Potential Aerosol Mass (PAM) reactor and exposed to OH radicals. Several single particle methods of analysis were used, including micro-Raman spectroscopy and atomic force microscopy (AFM) coupled to photothermal infrared spectroscopy (PTIR) to investigate composition and size of substrate deposited particles, and *in situ* particle mass measurements using an aerosol mass spectrometry (AMS) to understand marine aerosol chemistry.

We found that fragmentation reactions of supermicron particles composed of amino acids/amino sugars led to decreases in carbon content and subsequent increases in relative contribution of nitrogen containing species (e.g., ammonia and ammonium). AFM-IR analysis and AMS-derived mass analysis of submicron particles showed the formation of SMA due to oxidation

of VOCs released during bloom activity. Taken together, these results help to explain the complex interplay between the ocean's biological activity and of certain atmospheric aging processes in determining the chemical composition of marine aerosol across different size-regimes. These findings will help climate modelers create better algorithms for identifying marine aerosol speciation and CNN/IN activity.

7.6 Chapter 6 Summary

Chapter six focused on the construction of a cavity enhanced absorption spectrometer in order to detect various trace gases that result from the aging reactions of aerosols, including nitrous acid (HONO). Specifically, we designed and constructed an LED-incoherent broadband cavity enhanced absorption spectrometer (LED-IBCEAS) and validated it through detection of NO₂ using the DOAS fitting algorithm. Comparison with literature yielded good results.

7.7 Future Studies

Many questions remain regarding the connection between aerosols and climate exist^{4,5} as well as the connection between the ocean and the atmosphere.⁶ For example, work remains to be done to continue accurately representing the SSA generation process. Indeed, new studies are already underway at CAICE using a newly constructed ocean-atmosphere facility. This facility is expected to allow for conditions that are more representative of the ocean, including more realistic phytoplankton blooms as well as wind generation and solar irradiation simulation.

While the work in this thesis helped to determine the connection between ocean biology and SSA chemical complexity, much work remains to be done. For example, studies looking at other marine-relevant enzymes need to be investigated to determine their impact on resulting SSA chemical species. Future studies should also better constrain the various biogenic volatile organic compounds emitted during periods of high biological activity, and determine which of these VOCs are important secondary organic aerosol precursors. Finally, in addition to phytoplankton and bacteria, viruses are an important part of the microbial loop and should be examined.

Many questions remain regarding the aging of SSA by heterogeneous and photochemical reactions. Future studies are needed to determine the reactivity of these particles as a function of different atmospheric conditions, including water vapor content and temperature. Studies are currently underway to investigate how these types of reactions will alter the water uptake properties and IN capability of SSA particles. Ongoing work has already investigated the impact of cations on the reactivity of LPS. For instance, studies have shown that higher order structures formed from the calcium-induced aggregation of LPS can effect the reactivity of LPS. Finally, studies should examine the heterogeneous reactivity of the other biological and organic components of SSA.

The chromophoric properties of marine derived dissolved organic matter remains poorly constrained. Studies are needed to better determine the chromophores within marine DOM as well as their changing properties as a function of solar irradiation and biological processing. Work is now being conducted in the lab to investigate the role of water in altering the photosensitizing capability of m-CDOM molecules. Other organic substrates should be studied, including polysaccharides and LPS molecules. Finally, transient spectroscopy and chemical modeling is needed to explain the various pathways and excited states of chromophoric species in DOM.

The goal of Chapter 6 was to develop an LED-IBCEAS instrument and show that it works for NO_2 . Further efforts will be used to study processes in the marine boundary layer that converts NO_2 to HONO which will require calibration of HONO. Improvements to the design will also allow for better detection limits. Upon optimization of the CEAS, studies can then be conducted to determine the ability of SSA to serve as a source of nitrous acid either through photosensitized reactions of m-CDOM or HULIS or through the direct photolysis of particulate nitrate.

In conclusion, the results and future work discussed throughout this thesis provide better understanding of the controls of the chemical complexity of SSA and the associated changes to their climate relevant properties. Furthermore, these studies have improved our understanding of the reactions that change them. The overarching goal of this and other similar studies is to predict

the impact of SSA on climate in order to improve regional and global climate models. Such improvements will allow us to better determine how natural as well as anthropogenically-driven shifts in the environment are changing the Earth system.

7.8 References

- (1) Ciuraru, R.; Fine, L.; Pinxteren, M. Van; D'Anna, B.; Herrmann, H.; George, C. Unravelling New Processes at Interfaces: Photochemical Isoprene Production at the Sea Surface. *Environ. Sci. Technol.* **2015**, *49* (22), 13199–13205.
- (2) Fu, H.; Ciuraru, R.; Dupart, Y.; Passananti, M.; Tinel, L.; Rossignol, S.; Perrier, S.; Donaldson, D. J.; Chen, J.; George, C. Photosensitized Production of Atmospherically Reactive Organic Compounds at the Air/Aqueous Interface. *J. Am. Chem. Soc.* **2015**, *137* (26), 8348–8351.
- (3) Tinel, L.; Rossignol, S.; Bianco, A.; Passananti, M.; Perrier, S.; Wang, X.; Brigante, M.; Donaldson, D. J.; George, C. Mechanistic Insights on the Photosensitized Chemistry of a Fatty Acid at the Air/Water Interface. *Environ. Sci. Technol.* **2016**, *50* (20), 11041–11048.
- (4) Carslaw, K. S.; Boucher, O.; Spracklen, D. V.; Mann, G. W.; Rae, J. G. L.; Woodward, S.; Kulmala, M. And Physics A Review of Natural Aerosol Interactions and Feedbacks within the Earth System. **2010**, 1701–1737.
- (5) Quinn, P. K.; Collins, D. B.; Grassian, V. H.; Prather, K. A.; Bates, T. S. Chemistry and Related Properties of Freshly Emitted Sea Spray Aerosol. *Chem. Rev.* **2015**, *115* (10), 4383–4399.
- (6) Quinn, P. K.; Bates, T. S.; Alexander, B.; Oceanic, N. And Physics Global Distribution of Sea Salt Aerosols : New Constraints from in Situ and Remote Sensing Observations. **2011**, No. 2004, 3137–3157.